Engineering doping profiles in graphene: from Dirac fermion optics to high frequency electronics.

Quentin Wilmart

ÉCOLE NORMALE SUPÉRIEURE

Département de Physique

THÈSE de DOCTORAT de L'ÉCOLE NORMALE SUPÉRIEURE

École doctorale : "Physique en Île-de-France"

réalisée au **Laboratoire Pierre Aigrain (LPA)**

présentée par

Quentin WILMART

En vue de l'obtention du grade de
DOCTEUR de l'ÉCOLE NORMALE SUPÉRIEURE

Sujet de la thèse :

Engineering doping profiles in graphene: from Dirac fermion optics to high frequency electronics.

Presentée et soutenue le 7 décembre 2015 devant le jury composé de :

M.	Jérôme Cayssol	rapporteur
M.	Christoph Stampfer	rapporteur
M.	Lydéric Bocquet	examinateur
M.	Vincent Bouchiat	examinateur
M.	Bernard Plaçais	directeur de thèse
M.	Michael Rosticher	membre invité

Abstract

This thesis discusses the engineering of the doping profile in graphene by means of nanostructured local gates for Dirac fermion electronics. The nanostructured gates enable a full control of the graphene doping profile at the Fermi wavelength scale which is essential for Dirac Fermion optics experiments as well as for high frequency transistors.

In this work, I first present our technology based on local bottom gates and high mobility graphene on thin boron nitride. This allows the realization of sharp, tunable and ballistic p-n junctions which are the building blocks for Dirac Fermion optics. I will discuss a direct application of this technology, the Klein tunneling transistor, which takes advantage of the refractive properties of Dirac Fermions to switch ON and OFF a graphene transistor. Then this technology is implemented to equip our devices of a gate located underneath the contact area. Using this contact gate we have a full control of the contacted graphene doping and the contact junction resistance is tunable up to the gigahertz range.

The last two chapters are devoted to the study of our devices when they are driven at high bias, which is relevant for high frequency applications ; in this regime the doping profile will depend on the drain-source voltage as well. We observe and model the current saturation as a consequence of two effects: scattering by surface phonons of the hBN substrate and inhomogeneous doping profile in local gated graphene. Finally, the device performances as a radio frequency transistor are evaluated in the saturation regime, in terms of power gain cut-off frequency.

Résumé

Cette thèse traite du contrôle du profil de dopage dans le graphène au moyen de grilles locales nano-structurées, pour l'électronique des fermions de Dirac. Cette nano-structuration à l'échelle de la longueur d'onde de Fermi s'avère essentielle pour réaliser des expériences d'optique de fermion de Dirac ainsi que, dans un registre plus appliqué, pour l'électronique haute-fréquence. Dans ce travail, je commence par présenter notre technologie, qui repose sur des grilles arrières locales et du graphène haute-mobilité sur nitrure de bore hexagonal. Cela nous permet de réaliser des jonctions p-n abruptes, accordables et balistiques, qui sont l'élement de base pour l'électronique des fermions de Dirac. Je traiterai une application possible de cette technologie, le *transistor à effet tunnel de Klein*, qui utilise la réfraction des fermions de Dirac pour controler l'ouverture et la fermeture du canal d'un transistor graphène. Ensuite, cette technologie est mise en application pour équiper un transistor d'une grille placée sous le métal de contact. Cette grille de contact donne un contrôle complet du dopage du graphène contacté et permet de moduler la resistance de la jonction de contact jusque dans le gigahertz.

Les deux derniers chapitres sont dévolus au régime de fort biais qui est pertinent pour les applications hautes fréquences ; dans ce régime le profile de dopage dépend aussi de la tension drain-source appliquée. Nous observons et modélisons la saturation de courant comme la conséquence de deux effets : la diffusion par les phonons de surface du substrat hBN et l'inhomogénéité de dopage dans les dispositifs à grilles locales. Enfin, nous évaluons les performances de nos dispositifs comme transistors radio-fréquences dans ce régime de saturation, notamment en terme de fréquence de coupure du gain de puissance.

Acknowledgements

Tout d'abord je tiens à remercier Jérôme Cayssol, Christoph Stampfer, Vincent Bouchiat et Lydéric Bocquet d'avoir accepté d'être membre de mon jury de thèse et d'avoir pris le temps d'évaluer mon travail.

J'ai eu la chance d'être très bien entouré pendant ces trois années de thèse au Laboratoire Pierre Aigrain. Beaucoup de personnes ont contribué au travail présenté ici et je souhaiterais les remercier très chaleureusement. En premier lieu je veux remercier mon directeur de thèse, Bernard Plaçais, qui m'a proposé ce sujet difficile mais passionnant et qui a été présent à toutes les étapes. Merci pour ta profusion d'idées et de solutions quand on était dans une impasse, ton optimisme et ton humour. Merci pour avoir fait en sorte que tout se passe pour le mieux. On a réellement appliqué ta (ou une de tes) devise(s) "la physique en s'amusant". Merci également à Michael qui est pour beaucoup dans la mise au point des techniques de fabrication des grilles nano-structurées et qui a fabriqué d'innombrables échantillons pour ma thèse. Merci pour ton aide et tes encouragements. Merci à Pascal pour le four à recuit, pour son aide à la mise au point du montage de transfert des matériaux 2D et pour la croissance du graphène CVD. Merci à Mohamed qui a partagé avec moi les difficultés de salle blanche pour la fabrication de transistor graphène. Merci aux permanents du groupe, Gwendal et Jean-Marc pour leur accueil, pour les relectures des papiers et les répétitions de présentations. Je tiens aussi à remercier tous les thésards, stagiaires, postdocs pour les discussions enrichissantes, les conseils mais aussi pour avoir fait en sorte que le laboratoire soit toujours un endroit très agréable, où l'ambiance est bonne et où on a plaisir à aller tous les jours. Ainsi les collègues sont aussi devenus des amis avec qui on se retrouve pour boire des coups, faire de l'escalade, des ballades ou la fête. Merci donc à Andreas, Arthur, Holger, Badih, Wei ainsi qu'aux voisins de HQC, Matthieu B., Matmat, Jérémie, Laure, MaDar, Tino, Laurianne. Merci aux anciens membres de l'équipe, Emiliano, Sung Ho, David Brunel, et particulièrement à Andreas Betz qui m'a formé quand je suis arrivé en stage au LPA et dont j'ai repris le travail. Merci au autres permanents du LPA avec qui j'ai été heureux d'interagir et notamment Christophe Voisin, Takis Kontos et Audrey Cottet.

Je souhaiterais remercier le personnel technique et administratif du LPA et du Département de Physique de l'ENS et d'abord Anne Matignon et Fabienne Renia dont je salue l'efficacité remarquable. Merci également à Yann Colin pour l'informatique. Merci à Nabil Garroum pour les simulations Comsol, José Palomo pour son aide en salle blanche, David Darson pour les très appréciées illustrations 3D de dispositifs ainsi qu'avec Anne Denis et Philippe Pace pour les simulations de guide d'onde et toutes les questions d'électronique. Merci à Claude pour le logiciel du four, à l'atelier et notamment à Jules,

et merci à Olivier et Aurélien pour avoir toujours trouvé une solution pour fournir de l'hélium même quand cela semblait impossible. Un grand merci à Didier Courtiade, Catherine Gripe, Celia Ruschinzik, Romain Ferreaux, nos sauveteurs dans les situations désespérées, quand il faut déménager un cryostat ou un prober cryo à cinq bras à 6h du matin par exemple.

J'aimerais aussi remercier les personnes extérieures à l'ENS mais qui ont contribué à ce travail: Salim Berrada, Philippe Dolffus et Viet Hung pour les simulations NEGF, Stéphan Suffit pour la salle blanche de Paris 7, Loïc Becerra pour les dépts de tungsten à la salle blanche de Paris 6.

Enfin je voudrais remercier mes amis, de l'ESPCI et d'ailleurs et ma famille qui m'ont soutenu et encouragé tout au long de cette aventure.

Contents

Chapter 1

Introduction

1.1 General introduction

A decade after the discovery of graphene by A.K. Geim and K.S. Novoselov [1–3], many of its fundamental properties have been intensely studied. Indeed, the early promise of graphene has been kept, leading to a fruitful research in many fields as diverse as optics, mechanics, chemistry or electronics, and graphene still deserves the name of *wonder material* as among its attributes there is an exceptionally good conduction of heat and electricity, it is one of the strongest known material while being light and optically transparent. Its success was partly due to the easy micromechanical cleavage or scotch tape exfoliation technique accessible to any laboratory without heavy equipment, that allowed to study the properties of graphene with a wide range of experimental techniques. Following the success of graphene, other two-dimensional (2D) materials were obtained with the same technique, leading to a particularly rich physics.

In our field of interest, mesoscopic physics, there is another essential ingredient to the success of graphene: its field effect tunability. Indeed, the carrier density of graphene can be easily tuned over a large range $\sim 10^9\ cm^{-2}$-$10^{13}\ cm^{-2}$ with an electric field induced by a gate electrode. This tunability is a consequence of the band structure of graphene, but it is also due to the 2D nature of graphene as there is no charge screening in the direction perpendicular to the graphene plane. Finally, thanks to its crystal symmetry, graphene is not a regular conductor but a chiral conductor, and the charge carriers do not follow the usual Schrödinger equation but rather a Dirac-like equation (thus they are called Dirac fermions). Consequently, the electronic transport properties of graphene are controlled by the conservation of a pseudo-spin locked to the momentum, leading to an unusual behavior of electrons at potential steps. The peculiar transport properties of Dirac fermion arise when the transport is ballistic, that is to say when the impurity level

is low enough that the electrons can propagate without scattering over a distance on the order of the sample size. This is the regime of Dirac fermion optics, where electrons trajectories are similar to light rays, experiencing refraction at potential steps.

As a 2D crystal, graphene is extremely sensitive to its environment, it is therefore essential to work with a "graphene-friendly" environment. One solution is to remove the environment and to work with suspended graphene [4, 5]. However, supported graphene devices offer a better control and spatial resolution of the doping profile. The perfect environment was found by depositing graphene on top of hexagonal boron nitride (hBN) [6]. hBN is also a 2D material with a honeycomb lattice, thus atomically flat, but it is insulating with a $6\,eV$ bandgap. It appeared that using hBN as a substrate for graphene was a way to preserve the intrinsic properties of graphene while protecting it from the environment. As a result, ballistic transport up to a few microns at room temperature was demonstrated using hBN-encapsulated graphene [7, 8].

As discussed above, graphene is a very rich platform for fundamental science. It also raised a strong interest for the possible industrial applications, which opens other perspectives. From a material point of view, there is a need for a large scale and reliable graphene production. This issue is addressed for example by the development of the chemical vapor deposition (CVD) technique [9–11] which is close to reach the quality of exfoliated graphene. As a next step graphene has to be implemented in realistic devices whose performances must be compared to the existing semiconductor devices.

Regarding the possible applications of graphene in electronics, the realization of digital transistors seems elusive due to the absence of a bandgap in graphene, and the attempts to open a gap, e.g. using graphene nanoribbons, have resulted in a mobility degradation. However, the ability of graphene transistors to work as an amplifier up to hundreds of gigahertz thanks to its high electronic mobility and high Fermi velocity has been demonstrated and is still an active field of research [12–16]. The graphene radio frequency (RF) transistor is comparable to the high electron mobility transistor (HEMT) that relies on a two-dimensional electron gas at the interface of two semiconductors. In graphene and in HEMT, the field effect is very efficient thanks to the 2D nature of the electron gas, and the high mobility ensures fast operation.

In this thesis, our approach is to investigate the physics of graphene devices targeting the high frequency electronics applications. To this end we have developed, in the clean room of the Physics Department of the Ecole Normale Supérieure, a new technology based on graphene on hexagonal boron nitride, on top of nanostructured bottom gates. We call this technology GoBN for graphene on boron nitride. The use of hBN as a substrate gives access to the high mobility necessary for the ballistic transport whereas the nanostructured local gates allow us to finely control the doping profile of graphene

through the sample. Engineering the doping profile of ballistic graphene at a spatial resolution on the order of the Fermi wavelength enables the realization of devices working in the regime of Dirac fermion optics. Nevertheless, having a realistic device compatible with high frequency operations sets sharp geometrical constraints. First we work with short channel two-terminal devices for which the contact resistance dominates the device properties. It is therefore a major issue to understand and control the phenomena taking place at a metal-graphene contact. Second, a graphene RF transistor works at high bias, that is to say at high in-plane electric field in order to maximize the transconductance. In that regime the scattering by phonons is not negligible and it leads to the saturation of the current. In addition, for high biased devices equipped with a local gate, the graphene doping profile is not uniform in the channel leading to an effect similar to the "pinch-off" effect observed in semiconductor based transistors.

This thesis will be organized as follows. We begin by giving a short overview of the graphene electronics basic concepts. The main features of the Dirac equation are discussed, and we give the useful elements describing an electronic transport experiment in the diffusive regime and in the ballistic regime.

Chapter 2 introduces the fabrication techniques of our GoBN devices, presented from the Dirac fermion optics application point of view. The use of hBN as a substrate and a thin gate dielectric allows us to realize devices with a high mobility, a good doping homogeneity, a low residual doping, and to avoid gate hysteresis effects. The local bottom gates are structured prior to hBN and graphene deposition at the Fermi wavelength scale ($\sim 15 - 30\,nm$) in order to fully control the doping profile of graphene in the device. We are able to create sharp potential barriers which can be tuned electrostatically to create functionalities exploiting the optics-like properties of Dirac fermions. The chapter is concluded with the description of our measurement setup for direct current (DC) and radio frequency (RF) experiments. In particular, we introduce the RF measurement principle of the devices admittance parameters using a vector network analyser (VNA).

Chapter 3 is devoted to Dirac fermion optics. We begin with an overview of the proposals and experimental realization of devices exploiting the Dirac nature of graphene electrons. Then we give theoretical elements to describe more precisely the Klein tunneling of Dirac fermions at a potential step which is the building block for Dirac fermion optics. But the core of this chapter is our proposal of the *Klein tunneling transistor* whose working principle follows the geometrical optics analogy of a reflector. The Klein tunneling transistor is simulated using scattering theory and non equilibrium Green function (NEGF) approaches. Its potential use as a RF transistor is discussed as well.

In chapter 4 we focus on the metal-graphene contact properties. As already mentioned, this aspect is crucial for devices, and we give a short overview of the graphene contact

physics and achievements. More specifically we give theoretical elements explaining how the carrier density of contacted graphene is not solely determined by the metal induced doping but can be tuned by field effect. To this end we describe the gating effect taking into account the finite density of states of graphene close to neutrality. Our contribution is to use the GoBN technology to introduce a local gate below the metal-graphene contact area that can tune the carrier density of the contacted graphene. This contact gate is used in addition of a channel gate which tunes the doping of graphene in the channel. Both gates gives a full control of the contact junction whose transmission is modelled using the Klein tunneling equations of chapter 3. The contact gating effect is demonstrated on several devices, with exfoliated graphene flakes and with CVD. Finally, the contact gate is actuated at gigahertz frequencies, demonstrating that a graphene RF transistor can also work by modulation of the contact junction resistance.

In chapter 5, we drive our GoBN transistors at high bias and observe the current saturation. Two principal regimes are identified. At large doping the saturation is due to the scattering by optical phonons, and we are able to extract the phonon characteristic energy, which points out a scattering mechanism dominated by the remote phonons of the hBN substrate. At low doping we show that the saturation can be enhanced by a bias induced non-uniform doping in the channel. We specify that this effect is a distinctive feature of local gate devices for which the finite graphene density of states has to be taken into account.

Finally, in chapter 6 we focus on the RF properties of our GoBN devices. First, the relevant RF quantities and figures of merits are defined[1], second we present our RF experiments and attest the device performances in term of current and power gain cutoff frequencies. In particular, we show how to take advantage of the current saturation mechanisms discussed in chapter 5.

Four series of samples were fabricated and measured for the present thesis. Sample GoBN1 is the prototype of the GoBN technology and is shown in appendix B. GoBN2 is a sample made of exfoliated graphene equipped with contact gates. It is presented in chapter 4. GoBN3 is a series of samples made of CVD graphene and equipped with contact gates. It is presented in chapters 4, 5 and 6. Finally there is a series named GoAl that consists of control samples with Al_2O_3 as gate dielectric instead of hBN. They are shown in 4. All sample characteristics are summarized in table 2.1.7 and in appendix C.

[1] The reader who is not familiar with RF transistor may refer to section 6.1.2 of this chapter whenever RF properties are discussed.

1.2 Graphene electronics basic concepts

There are numerous very good introductions and seminal papers about the basics of graphene electronic properties [17–20]. Here, our objective is not a complete description of those properties but rather a quick summary of the concepts and formulas that we will need in this work.

1.2.1 From the honeycomb lattice to the Dirac equation

In graphene, the carbon atoms are arranged in a honeycomb lattice with a C-C distance of $a \approx 0.142\,nm$. In terms of Bravais lattices, graphene is generally described as the superposition of two triangular sub-lattices formed by the atoms A and B of Fig 1.1.

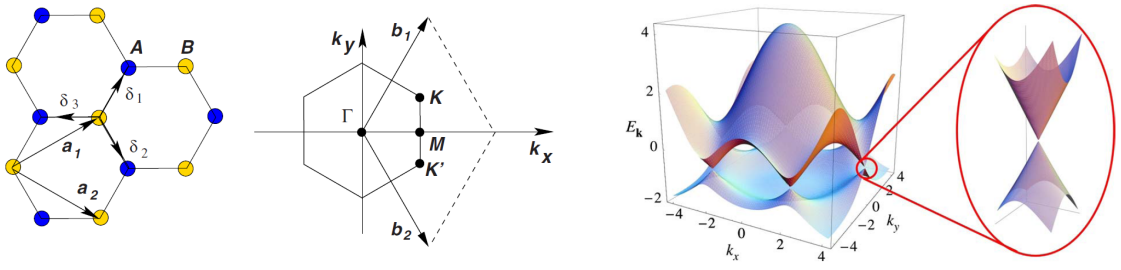

FIGURE 1.1: From left to right: graphene lattice with two unequivalent atoms A and B ; corresponding Brillouin zone ; energy dispersion with a zoom to the Dirac point. Adapted from [18].

The electronic properties of graphene are generally described by the tight binding approach within the nearest-neighbour approximation. It gives the complete electronic band structure which is plotted in Fig. 1.1. The most important features of graphene can be seen from the band structure: the conduction band and the valence band are touching at two inequivalent points at zero energy. Thus, graphene is a zero-gap semiconductor or a semi-metal, and the Fermi level lies at the intersection between valence and conduction bands. Close to the intersection points, the energy dispersion $E(\vec{k})$ has a conical shape and is linear with the wave vector k.

$$E(\vec{k}) = \pm\hbar v_F |\vec{k}|, \tag{1.1}$$

where the + sign stands for the conduction band and the - sign for the valence band. v_F is the Fermi velocity which is defined as

$$v_F = \frac{3ta}{2\hbar} \approx 10^6 ms^{-1}, \tag{1.2}$$

with the hopping energy $t \approx 2.8\,eV$ [18].

The linearity of the energy dispersion (Eq. 1.1) is a distinctive feature of graphene. Indeed, the graphene quasiparticles are not described by the usual Schrödinger equation but rather by the Dirac equation. Those quasiparticles are called Dirac fermions as they behave as massless relativistic particles (with an effective speed of light v_F) by opposition to the Schrödinger fermions in usual semiconductors which have a parabolic energy dispersion. The two points where conduction and valence band are touching are called Dirac points.

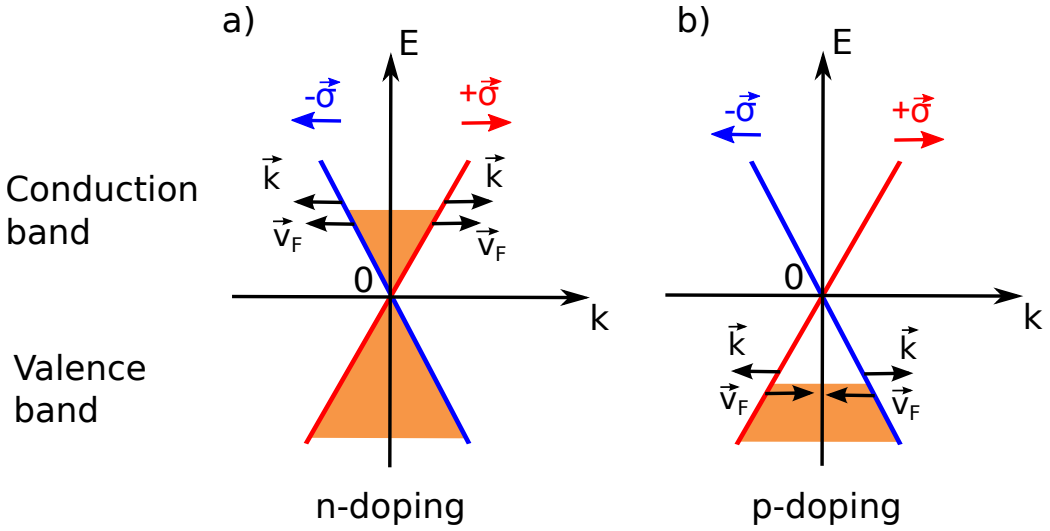

FIGURE 1.2: Energy dispersion close to the Dirac point. (a) The Fermi level is in the conduction band meaning that the graphene is n-doped. (b) The Fermi level is in the valence band meaning that the graphene is p-doped. The two branches of the band structure $+\vec{\sigma}$ and $-\vec{\sigma}$ define the pseudo-spin. The pseudo-spin is locked to the momentum, they are parallel in the conduction and anti-parallel in the valence band. The direction of motion is represented by $\vec{v_F}$. It remains constant for a given $\vec{\sigma}$.

The energy dispersion. The conical energy dispersion close to the Dirac point is shown in figure 1.2. The filled electronic levels are colored in orange, thus the Fermi level is at the orange-white limit. If the Fermi level lies in the $E > 0$ part of the cone (Fig. 1.2-a) then the doping is called n as negative charges are in excess in the graphene sheet (the charge carriers are called electrons). If the Fermi level lies in the $E < 0$ part of the cone (Fig. 1.2-b) then the doping is said p as positive charges are in excess in the graphene sheet (the carriers are called holes [2]). In the following, when we estimate carrier density values using the n notation, a positive value will indicate a n-doping (Fermi level in the conduction band) and a negative value a p-doping. On the opposite, $p > 0$ will correspond to a p-doping and $p < 0$ to a n-doping.

[2] As explained in [19], even if $E < 0$, the charge carriers still are at the Fermi level, so they are electrons. On the opposite, strictly speaking, a hole is the removal of an electron below the Fermi level. Yet a Dirac fermion in the valence band is often called hole.

A sublattice degree of freedom. There is another important consequence of the lattice symmetry on the transport properties. Due to the two-atom basis of the Bravais lattice, there is an additional degree of freedom that we call pseudo-spin. Thus, the graphene's quasiparticles are described by a two-component wave function defining the relative contribution of sublattices A and B. Consequently the conical spectrum can be seen as the intersection of two branches originating from sublattices A and B and a pseudo-spin index $\pm\vec{\sigma}$ can be attributed to each branch, as pictured in blue and red in Fig. 1.2. Electrons and holes belonging to the same branch have the same pseudo-spin $\vec{\sigma}$.

The momentum $\vec{k}$ is parallel to the pseudo-spin $\vec{\sigma}$ in the conduction band and it is anti-parallel in the valence band. Concerning the direction of propagation, it is represented as the $\vec{v_F}$ vector in Fig. 1.2. $\vec{v_F}$ is parallel to the momentum $\vec{k}$ for the electrons and anti-parallel to $\vec{k}$ for the holes, so that the direction of motion is constant for a given pseudo-spin.

To summarize, there is a degree of freedom associated with the real spin, another one associated with the two unequivalent Dirac point (valley degeneracy) [3] and that we account for by a factor 4 in this thesis. By contrast the pseudo-spin degree of freedom has a stronger impact on the transport properties.

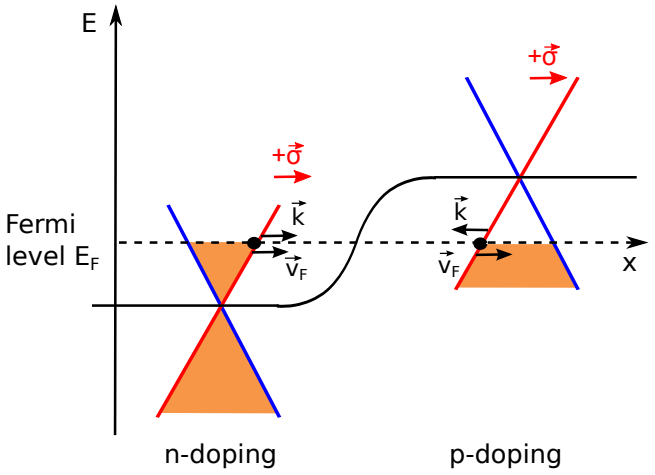

FIGURE 1.3: Energy dispersion at a potential step. The Fermi level (dotted line) is constant and the band structure is shifted. A right moving electron (black dot) in a n-doped area is transmitted to a p-doped area. The pseudo-spin $\vec{\sigma}$ is conserved, the wave vector is reversed and the direction of motion $\vec{v_F}$ is conserved. This is an example of a so-called n-p junction (the case of the p-n junction is symmetric).

Consequence of the pseudo-spin: Klein tunneling. Let us consider a quasiparticle incident on an electrostatic potential step (Fig. 1.3). The step height is chosen to inverse

[3] The inter-valley scattering can be neglected if there is no scatterer acting at the lattice constant scale.

the doping polarity, therefore it is called a n-p (or equivalently p-n) junction. The pseudo-spin has to be conserved through the barrier (a pseudo-spin-flip process would require a short range process acting differently on A and B sites - for example if the barrier transition is shorter than the lattice constant). As a consequence, a right-moving incident electron cannot be backscattered as $\vec{v_F}$ to $-\vec{v_F}$ would imply a change of branch. Therefore it is transmitted inside the barrier as a hole state. This process is also responsible for graphene's high mobility, as if the barrier is replaced by an impurity or a defect, the incident carrier is not backscattered resulting in a larger mean free path. The properties of those p-n junctions will be discussed more specifically in chapter 3.

1.2.2 Important formulas

Dispersion relation. As already introduced, the dispersion relation is

$$E_F = \hbar v_F k_F \tag{1.3}$$

Density of states. The number of states per unit area in a two-dimensional system is:

$$N = g \int_0^{k_F(E_F)} \frac{kdk}{2\pi}, \tag{1.4}$$

where $g = 4$ due to the 2-fold valley and real spin degeneracy. Thus, close to the Dirac point and using Eq. 1.3, the graphene density of states is

$$\rho = \frac{\partial N}{\partial E} = \frac{2E_F}{\pi(\hbar v_F)^2} \tag{1.5}$$

Charge carrier density. The carrier density is obtained by integrating the density of states over the whole energy range. It corresponds to the algebraic charge number per unit area in the graphene sheet, the neutrality corresponding to the Dirac point. It is equivalently referred to as doping in this thesis, and it is expressed in cm^{-2}.

$$n = \int_0^{\infty} \rho(E) f(E) dE = \frac{E_F^2}{\pi(\hbar v_F)^2}, \tag{1.6}$$

where f is the Fermi-Dirac distribution taken at zero temperature.

From Eqs. (1.6) and (1.3) one can obtain the following useful expression:

$$k_F = \sqrt{\pi n} \tag{1.7}$$

Fermi wavelength. The Fermi wavelength of the Dirac fermions is expressed as:

$$\lambda_F = \frac{2\pi}{k_F} \tag{1.8}$$

The typical carrier density in our system is $n = 1 \times 10^{12}\, cm^{-2}$. It corresponds to a Fermi energy $E_F = 116\, meV$, a wave vector $k_F = 1.77 \times 10^8\, m^{-1}$ and a Fermi wave length $\lambda_F = 35\, nm$.

1.2.3 Diffusive transport.

In opposition to the ballistic transport, in the diffusive regime, charge carriers experience elastic scattering essentially due to collision with impurities. The less there are impurities the better is the electrical conduction. In the Drude model, electrons are accelerated by an electric field $\mathcal{E}$ and are scattered at a relaxation time τ, so that the equation of motion in terms of momentum $p = \hbar k_F$ reads

$$\frac{dp}{dt} = -\frac{p}{\tau} + e\mathcal{E} \tag{1.9}$$

Which gives a steady state

$$p = \hbar k_F = e\mathcal{E}\tau \tag{1.10}$$

One defines the carrier mobility μ as

$$v_d = \mu\mathcal{E}, \tag{1.11}$$

where v_d is the carrier drift velocity, that is to say the average speed of electrons. v_d and τ are related through the mean free path $l_{mfp} = v_d\tau$ which is the mean distance between two impurities. Thus

$$l_{mfp} = \frac{\mu\hbar k_F}{e} \tag{1.12}$$

We say that the transport is diffusive when l_{mfp} is smaller than the sample length. In the opposite case the transport is ballistic.

From those quantities one can calculate the current density:

$$j = |n|ev_d, \tag{1.13}$$

and the graphene sheet conductivity

$$\sigma = |n|e\mu \tag{1.14}$$

The mobility is the main figure of merit to discuss the quality of a semiconductor. It is generally expressed in units of $cm^2V^{-1}s^{-1}$. A higher mobility implies a higher conductivity and a higher mean free path. The success of graphene in electronics is essentially based on its exceptionally large mobility. In particular, a recent experiment [8] has shown that the room temperature graphene mobility can reach $\mu \gtrsim 100000\, cm^2V^{-1}s^{-1}$ which is the limit set by phonon scattering. This corresponds to a mean free path $l_{mfp} \approx 1\,\mu m$. At cryogenic temperatures, the samples go ballistic and the mean free path is limited by the size of the sample $l_{mfp} > 15\,\mu m$.

Device geometry and gate effect. A basic transport experiment is to measure the resistance of a rectangular graphene channel between two contact electrodes that we call drain and source (the source electrode being at $0V$). The distance between source and drain electrodes is the length of the channel noted L ; the width is noted W and the dielectric thickness t_{BN} (see Fig. 1.4) . Therefore the channel resistance is

$$R = \frac{L}{W}\frac{1}{|n|e\mu}. \tag{1.15}$$

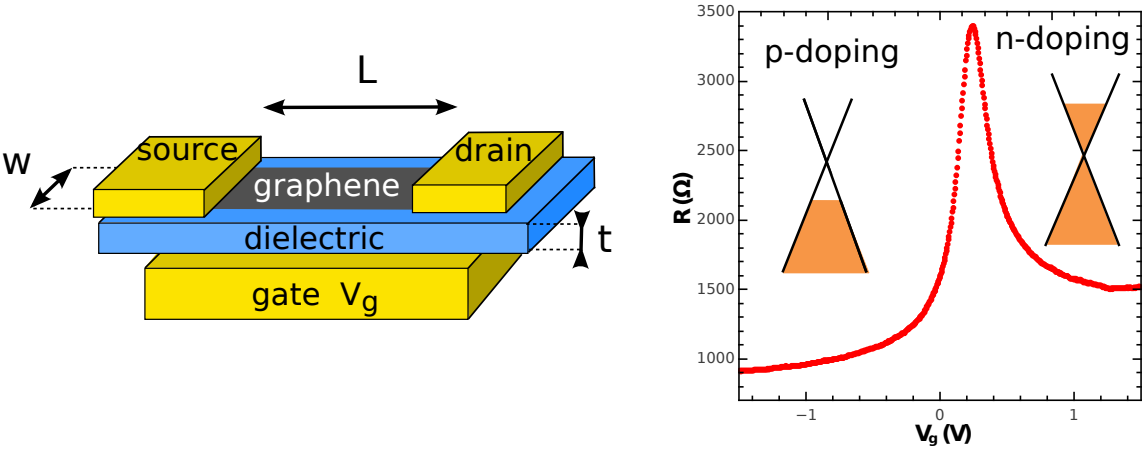

FIGURE 1.4: Left: image of a graphene transistor with a bottom gate. Right: resistance as a function of gate voltage (transfer curve) for a device similar to the sketch on the left. The dimension of the device are $L = 1.4\,\mu m$, $W = 1.6\,\mu m$. The dielectric is a hBN flake of thickness $t_{BN} = 7\,nm$.

The carrier density is tuned by a gate electrode separated from graphene by a dielectric. Within the plate capacitor model (this approximation is discussed in chapter 4) there is an equal number of charge in the graphene and in the gate electrode, leading to

$$n = \frac{CV_g}{e}, \tag{1.16}$$

where C is the gate capacitance per unit area and V_g is the gate voltage. Therefore n can be tuned from negative to positive values. The maximum accessible carrier density

is set by the breakdown voltage of the gate dielectric, the minimum n depends on the disorder and the temperature. In our experiment we can access $|n| \sim 0.1 - 10 \cdot 10^{12}\, cm^2$. The minimum carrier density is also called the residual density and is noted n_0. Thus a more accurate estimation of the graphene doping is

$$n = sign(V_g)\sqrt{\left(\frac{CV_g}{e}\right)^2 + n_0^2} \tag{1.17}$$

Consequently, the graphene resistance is tuned by the gate voltage with a maximum at the so-called Dirac point. The value of the maximum is limited by n_0 and μ in our experiments[4]. An example of transport measurement is shown in Fig. 1.4, where the resistance as a function of the local bottom gate voltage is plotted. Accordingly to equation (1.15) a bipolar behavior is observed, as well as a resistance peak which corresponds to the charge neutrality point (CNP) or Dirac point. Away from the Dirac point the $R(V_g)$ curve is not symmetric. This effect arises from additional resistance due to the contact electrodes (contact resistance) and chapter 4 will discuss this asymmetry.

1.2.4 Ballistic transport

When the mean free path is larger than the sample size, the transport is said ballistic. It cannot be described anymore by the Drude model. Instead, it is described within the Landauer-Büttiker formalism where the electronic conduction can be seen as a wave propagation in a waveguide.

The Landauer-Büttiker formalism. In this description, the conductance is quantized by the number of modes allowed in the waveguide (Fig 1.5). Each mode contributes as a quantum of conductance $2e^2/h$, where the pre-factor 2 takes into account the spin degeneracy. The conductance of ballistic graphene is given by:

$$G = \frac{4e^2}{h}M, \tag{1.18}$$

where M is the mode number and the pre-factor 4 stands for both spin and valley degeneracy. The mode number is set by the Fermi wavelength and the channel width W:

$$M\frac{\lambda_F}{2} = W \tag{1.19}$$

Therefore, the Landauer conductance of graphene reads

$$G = \frac{4e^2}{h}\frac{k_F W}{\pi} \tag{1.20}$$

[4] In cleaner systems it is on the order of $\frac{L}{W}\frac{\pi h}{4e^2}$ [21–23].

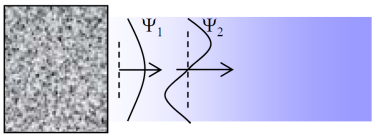

FIGURE 1.5: Sketch of the Landauer electronic modes.

For a typical carrier density $n = 10^{12} cm^{-2}$, we have $G/W \approx 9\, mS\mu m^{-1}$.

Then one may want to estimate the conductance of a junction in ballistic graphene. To this end, the Landauer-Büttiker formalism enables us to think in term of transmission T of the junction which yields for the conductance

$$G = \frac{4e^2}{h}\frac{k_F W}{\pi}T \tag{1.21}$$

This case is of great importance for the description of the graphene transistor properties and it will be treated in more detail in chapter 3.

Chapter 2

Experimental methods

The fabrication of high mobility graphene devices has been a major challenge in the past few years, and it has experienced considerable progress since the early measurements. The use of an atomically flat and inert substrate, hexagonal Boron Nitride (hBN), enables researcher to reach the ultimate phonon-limited mobility of $\mu \approx 100000\ cm^2V^{-1}s^{-1}$ at room temperature leading to a mean free path of a few μm [24]. However, the fabrication of such devices remains particularly difficult, as it requires successive and delicate transfer steps of graphene and hBN flakes. In the case of devices for Dirac Fermion optics we need even more complex architectures resulting in a more challenging fabrication. As a result a great effort in terms of fabrication processes has been made in this work, both concerning the introduction at LPA of the state of the art transfer techniques of 2D crystals (exfoliated and CVD) and in the realization of nano-patterned gate electrodes for new Dirac Fermion optics architectures. In this chapter, we will first introduce the techniques we developed in the LPA clean room that lead to the fabrication of devices for Dirac Fermion Optics. This presentation focuses on the fabrication of the Klein tunneling transistor whose working principle is introduced in Chapter 3. However, the same fabrication techniques also apply for the fabrication of the gated contact transistor whose experimental results are presented in Chapters 4, 5 and 6. In a second a part I will present the electronic setup we used to characterize the devices.

2.1 Nanofabrication : the GoBN technology

2.1.1 Technological requirements for Dirac Fermion optics

The realization of devices for Dirac Fermion optics has high requirements that introduce sharp constraints in the fabrication process. First of all, the carrier mobility has to be

high enough to reach the ballistic regime. This sets some constraints on the graphene quality, on the choice of substrate, and on the level of contamination accepted during the process. Secondly, geometrical constraints can be defined using the analogy of the equivalent optical index ñ of geometrical optics. Indeed, the building block for Dirac Fermion optics is the p-n junction. A n-p junction separates two zones of different doping, n and p, in a graphene sheet (see Fig. 2.1 and Chap. 3 for more details). And in the ballistic regime the electrons incident on that junction follow the Snell-Descartes refraction law with an equivalent optical index $\tilde{n} = -\sqrt{p/n}$. Besides, comparing the device dimensions to the electronic wavelength λ_F allows to set the limits of the geometrical optics regime. To mimic a simple geometrical optic elements as a dioptre our device should verify the requirements of 2.1.

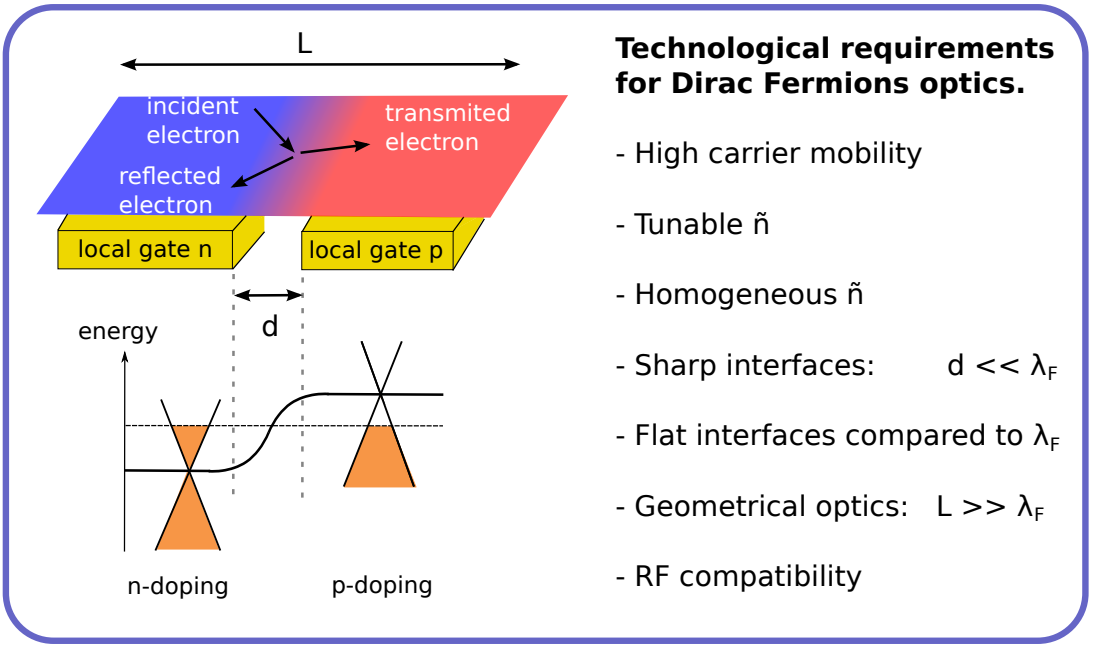

FIGURE 2.1

Obviously, in regular optics, it is difficult to tune ñ, without changing the material ! In graphene however, ñ can be tuned very easily and over a very large range with an electrostatic gate. The homogeneity of ñ over a certain area is improved by using a local metallic gate, very close to the graphene which efficiently sets the graphene electrical potential. The most simple optical device one can make is a dioptre separating two areas of different ñ. In graphene electronics this dioptre or interface is called a junction and is the result of contiguous regions with different doping. Doping can be induced either electrostatically or chemically. The optical properties of this dioptre depend on the typical length d over which ñ varies when going through the interface. We choose to work with sharp interfaces, meaning that the Fermi wavelength of the electrons stays larger than the interface length d. Typically a graphene device operates at a density

$n = 10^{12}\, cm^{-2}$ (energy: 116 meV) which corresponds to a Fermi wavelength of $\lambda_F = 35.4nm$. The condition $d \lesssim \lambda_F$ is critical to obtain a good transmission at the interfaces, and achieving the $10 - 30\, nm$ scale resolution is one of the major steps of the present thesis. Similarly the roughness of the interface between both media has to be small compared to λ_F in order to avoid scattering at the junction. By contrast, to stay within the geometrical optic regime, the size of the device needs to be much larger than λ_F , otherwise the occurrence of diffraction would blur the particular effects we investigate. In the end a compromise between mean free path and diffraction limit will have to be found. Finally, we want to characterize the dynamical properties of Dirac Fermion in the radio frequency (RF) regime, thus our device geometry has to be suitable with a $50\,\Omega$ impedance matched environment. Moreover, in order to avoid RF losses, we have to use an insulating substrate. For example SiO_2 on doped silicon is not suitable, and we have to use resistive silicon ($\rho \sim 2000\,\Omega cm$) instead.

2.1.2 The local bottom gate technology

In order to meet the requirements presented above we propose an architecture, named GoBN, that consists of a vertical stack of graphene on Boron Nitride on a set of local bottom gates. The bottom gate voltages will imprint different media of different ñ and their interfaces. The choice of bottom gates instead of the more common top gates offers some advantages: First, it is a way to avoid a complicated and risky deposition of a top dielectric on graphene followed by the evaporation of the metallic gate. As specified above we need a $10\, nm$ resolution in the gate geometry which is hardly possible using a lift off technique. Second, the use of hBN as a substrate ensures a good mobility (it is atomically flat) and good dielectric properties (no charge traps and breakdown voltage approaching $1\, V/nm$). Third, we still have a free graphene surface that can be cleaned and flattened if needed (a top dielectric could trap some impurities). Besides, access to the graphene top surface allows for opto-electronic experiments as for example photocurrent detection [25, 26], as well as gas sensitivity experiments [27]. Nevertheless, graphene easily adsorbs molecules on its surface and it is necessary to clean the sample by annealing prior to the measurement.

Stating the problem is rather simple: we need to be able to make a set of gates whose separation is less than $30\, nm$, with even smaller edge roughness. Obviously the top surface roughness of the gate has to be much smaller (ideally $< 1\, nm$), the graphene being very sensitive to the substrate's roughness while a thin hBN layer does not smooth out completely a rough surface. Moreover, as will be explained in more detail later, we need to remove the resist residues after the graphene transfer which implies an annealing

step at $300°C$ under H_2/Ar atmosphere. Thus the metal used for the gate needs to sustain such conditions.

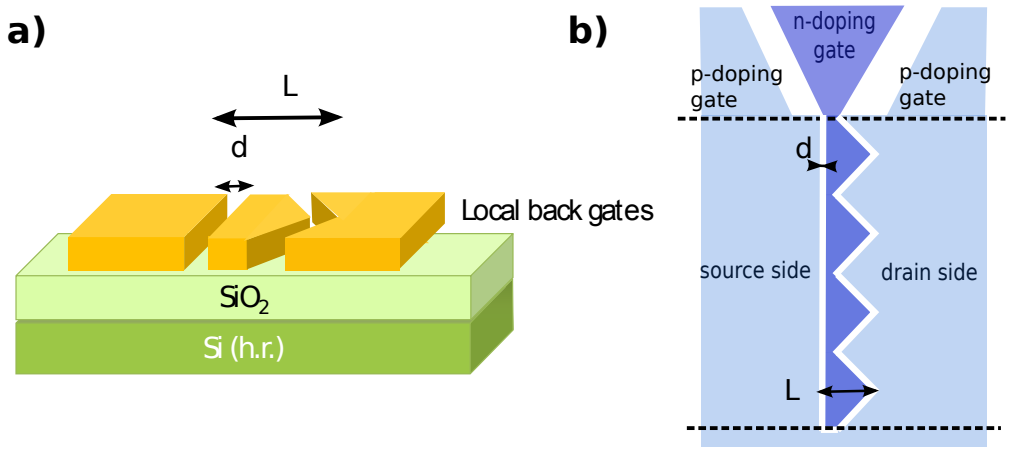

FIGURE 2.2: (a) Perspective view of the local back gates of one unit of the Klein tunneling transistor (without graphene yet). L is the total length of the device over which the transport should be ballistic. d is the inter-gate gap, it sets the smoothness of the junction. (b) Top view of the Klein tunneling transistor. Here it is composed of four elementary units.

The principles of the fabrication are described taking as an example the Klein Tunneling Transistor sketched in Fig. 2.2 and whose working principle is decribed in Chap. 3 but it is expandable to other geometries. The same technology is used for the fabrication of the devices presented in Chap. 4, 5 and 6.

As already mentioned above, a process involving standard e-beam lithography followed by metal deposition and lift-off is ruled out: even if the lift-off of very fine structures is possible, the edge of the remaining metal has an important roughness. Therefore our route was to start with the deposition of a thin film followed by a dry etching step that defined the gate geometry.

The gold way. The first attempts we made consisted in the deposition of a $20nm$ thick layer of gold on a Si/SiO_2 substrate, the etching being realized using a gallium Focused Ion Beam (FIB) in the team of Jacques Gierac at LPN, Marcoussis. Notably, this group is expert in cutting out 2D crystals [28]. Unfortunately, we were not able to reach our resolution target. As seen in Fig. 2.3 the triangular shape is not achieved, and although the rectangular gate seems correct, the gap between both gates is still too large ($> 50\,nm$) and the roughness is too high. Besides, we realized soon that such fine gold structures do not sustain a thermal treatment at $300°C$ needed to clean the sample. The FIB is a powerful technique but it would have demanded more development to optimize it to other materials. However a similar possibility would have been to use a Helium FIB. Using that it could be possible to etch thicker gold structures (a $100\,nm$ gold layer

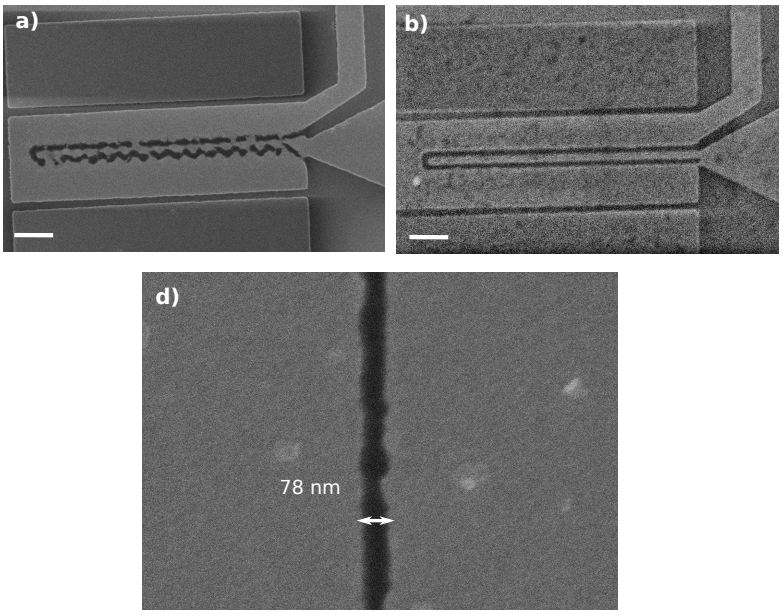

FIGURE 2.3: (a) Gold gate etched with a Gallium FIB targeting a sawtooth shape. (b) Gold gate etched with a Gallium FIB targeting a rectangular shape. (c) A single line etched with a Gallium FIB. The gap is varying around $\sim 50 - 80\,nm$. The scale bar is $400nm$ for (a) and (b).

is nearly insensitive to a temperature of $300°C$) with a better accuracy (see for example [29]).

Therefore we changed both the etching technique and the material. It appears that a conventional e-beam lithography ($20\,keV$) pushed to its ultimate resolution (thin layer of resist: $50\,nm$ PMMA, and exposure steps of $2\,nm$) enables the realization of very thin trenches in a resist, and that the gate material can be etched away efficiently using Reactive Ion Etching (RIE). Both equipments are available in the ENS clean room making the process development more efficient.

A quick review of ultimately thin metallic film properties This process has been tested on quite a few materials with little success. To summarize we are looking for a refractory material (even for very thin film) that does not react with H_2 but that can be etched either chemically or physically in RIE, provided that the RIE recipe does not etch the resist faster than the material. Here is a compilation of gate materials that have been tested:

- Palladium (evaporated Ti/Pd $1nm/15nm$) can be etched physically with Ar ions in RIE but it reacts with H_2 during the annealing.
- Niobium can be etched with SF_6 ions. For a $25nm$ thick Nb film deposited by sputtering, we measured a resistivity of $\sim 60\mu\Omega cm$ before annealing and $\sim 700\mu\Omega cm$

after annealing due to hydrogenation (and also its color and thickness have changed !).

- Graphite can be etched with an O_2 plasma and sustain the thermal treatment. However its deposition by the exfoliation method make the process random as we do not control its thickness. As a result a good calibration of the etching time was not achieved.

- Silicon On Insulator (SOI) obtained from the CEA-LETI is a thin layer (20 nm) of highly doped silicon. It is easy to etch, its flatness is very good as well as its resistance to annealing. However, SOI is still highly resistive (we measured $\sim$ 1800 $\mu\Omega cm$, but the usual value for this material is $\sim$ 360 $\mu\Omega cm$) and above all it is difficult to realize a good contact to the SOI gate due to the native oxide layer always present at the surface. This route is promising but was developed in parallel of tungsten which revealed simpler to use.

- Tungsten is a very refractory metal and it can be etched using SF_6 ions. A 20 nm film is deposited by sputtering at INSP by Loic Becerra. Its resistivity is $\sim$ 300 $\mu\Omega cm$

The best choice among the available materials is tungsten, an example of realization can be seen in Fig. 2.4. Nevertheless a fine tuning of the RIE parameters was necessary to etch completely and sharply the tungsten while some PMMA remains on the sample to protect the other areas. Finally, a gap width of 20 nm with little roughness was achieved in collaboration with Michael Rosticher and Jose Palomo from the ENS Physics department. For a complete description of the fabrication of the tungsten local bottom gate see appendix A. Let us emphasize that this choice is mainly dictated by our available equipment: the 20nm targeted accuracy requires to use a thin layer of PMMA that itself limits the etching time so that the gate material has to be thin. For example, with a 100keV e-beam we could reach the same resolution with a thicker PMMA and therefore have a thicker (meaning less resistive and less sensitive to annealing) material.

2.1.3 High mobility graphene: material

Exfoliated graphene The historical technique of exfoliation or micro-mechanical cleavage of bulk graphite is still widely used. It remains the technique that gives the highest mobility samples, but above all it allowed to explore the entire family of 2D materials (hBN, MoS_2, WS_2, $MoSe_2$, WSe_2, $MoTe_2$, Bi_2Se_3, Bi_2Te_3, black phophorus...) that raised much interest recently [2, 30–33]. Indeed it is the simplest technique to implement as one just needs to start with the bulk material and a piece of scotch tape. Moreover

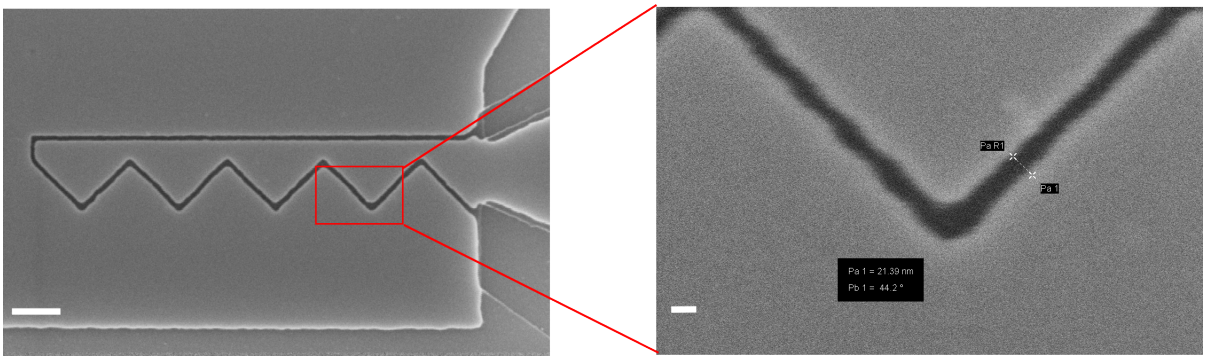

FIGURE 2.4: Local bottom gate in tungsten etched using an e-beam lithography followed by RIE etching. Left: the complete sawtooth gate. The scale is set by the white bar of 200 nm. Right: zoom onto the gap for which a resolution of 20 nm is achieved. The scale is set by the white bar of 20 nm.

one can easily choose the number of layers (a posteriori) which is critical as the material properties drastically depend on it. This technique relies on the weak Van der Waals interaction between layers which is comparable to the graphene-scotch tape and graphene-substrate interaction strength. Thus a small piece of graphite is stuck on the adhesive tape (Blue Low Tack tape *Semiconducor Equipment Corp*) then the tape is successively folded onto itself several times to peel away the graphite. Graphite is spread out on the tape and gets thinner. Finally the tape is put on a Si/SiO_2 substrate and removed leaving some graphite on the chip. One obtains a surface covered with flakes of various size and thickness. One of the great advantages of this technique is that the number of atomic layers can be identified with a simple optical microscope. Indeed, due to interferences between graphene and Si, provided that the SiO_2 layer has a suitable thickness, the optical contrast is enhanced, allowing to discriminate between a single layer and a bi-layer graphene, as shown in Fig. 2.5. Though, it has to be stressed that exfoliation is a random process, thus, in our fabrication process graphene cannot be deposited directly on the desired area, it has to be exfoliated somewhere and then transferred on the BN-local gate stack. Besides, this technique produces only small flakes, of a few μm^2 ($100\mu m^2$ at most) and is not suitable for systematic device characterization or industrial applications.

CVD graphene A very successful method to grow graphene is Chemical Vapor Deposition (CVD), demonstrated in 2008 by Yu et al. [9]. Graphene is grown from gaseous precursors on a metallic surface acting as a catalyst in a furnace at high temperature. The metallic catalyst can be chosen depending on the desired number of layers: Cu for monolayer, Ni for multilayer. The CVD graphene quality has experienced considerable improvement in the past few years, it now competes with the best exfoliated samples with very few defects and millimeter-size grains. Mobilities as high as $350,000\, cm^2/V/s$ have been achieved when it is used in combination with a hBN substrate [11]. At the

same time transfer techniques have also improved, even for large scale CVD, and it seems very promising for industrial applications. In this work we used CVD graphene grown on copper from 3 different origins:

- Commercial CVD graphene from *Graphene Supermarket*.
- Home grown CVD by Pascal Morfin. The CVD graphene is grown with an Aixtron reactor on a 99.999% pure and $100\mu m$ thick copper foil. The growth occurs at a temperature of $1020°C$, in an $CH_4/H_2/Ar$ atmosphere at $25\,mbar$ for 5 minutes.
- CVD from V. Bouchiat's group at Institut Néel in Grenoble [10]. Films are grown following an original method called *pulsed CVD*. It consists in the intermittent injection of the carbon precursor (CH_4) while H_2 is injected with a constant flux at $1000°C$. The advantage of this technique lies in the reduction of carbon by H_2 that saturates at Cu defects. In a standard growth this saturation leads to the formation of multilayer graphene around those defects. The pulsed CVD technique suppresses those multilayer patches leading to a more homogeneous graphene layer and in the end to a better mobility.

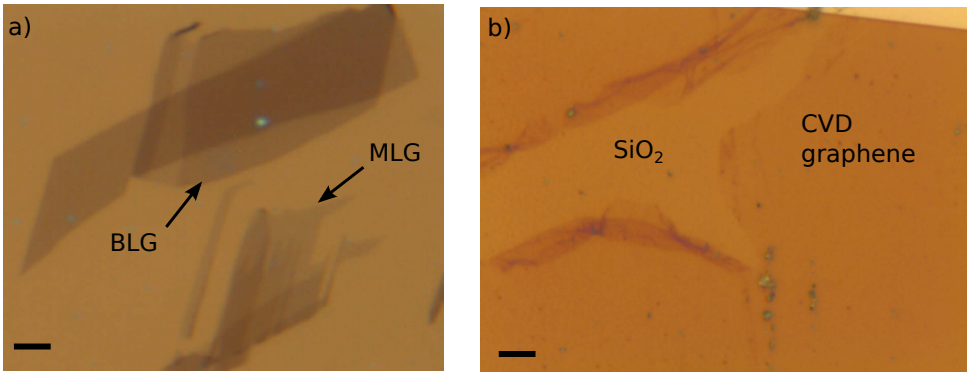

FIGURE 2.5: (a) optical image of exfoliated graphene on SiO_2. A monolayer (MLG) and a bilayer (BLG) graphene flakes are pointed out by the black arrows. One can clearly see the contrasts substrate-MLG and MLG-BLG. If needed it can be quantified by the grayscale of the picture. (b) Optical image of a LPA CVD graphene film transferred on SiO_2. The scale bar is $5\,\mu m$ for both images.

In each case it is delivered as a Cu foil covered with monolayer graphene that has to be transferred onto the desired substrate. First, PMMA is spin-coated on the foil, then Cu is gently etched away in an oxidant solution which leaves the PMMA-graphene stack floating at the surface of the solution. The stack is carefully rinsed off using deionized water before being "fished" with the target substrate (see Fig. 2.7-b). Finally, the PMMA is dissolved in acetone. Typically we obtain a 90% graphene coverage over $1\,cm^2$.

2.1.4 High mobility graphene: hBN substrate

The first samples with very high mobility were obtained with suspended graphene as the standard SiO_2 substrates bring many sources of scattering for Dirac Fermions especially due to its roughness and charge traps. Hexagonal boron nitride (hBN) is also a 2D material, thus atomically flat. It also has an hexagonal lattice with a 1.8% lattice constant mismatch with graphene, it is an insulator with a large bandgap ($6eV$), and the van der Waals interaction with graphene is very strong preventing the impurities to be trapped at the graphene-hBN interface [34]. In particular, the impurities tend to cluster in some area creating some bubbles. As can be seen on the AFM images of Fig. 2.6 these bubbles are linked with wrinkles. Obviously a device for Dirac Fermion optics should avoid the presence of such defects. Unfortunately it is more difficult to obtain a wrinkle free channel when working with a local bottom gate as the location of the device is decided prior to deposition.

In this work we used exfoliated hBN flakes from commercially available synthetic crystals (provider: HQ graphene).

Other substrates. hBN was not the only substrate used. Some characterization have been made directly on SiO_2 and a few devices have been made with Al_2O_3 as a gate dielectric. In that case, Al_2O_3 is deposited directly on the gates followed by the deposition of CVD graphene on top of Al_2O_3. The 10 nm thick layer of Al_2O_3 is either deposited by the successive evaporation and oxidation of 2 nm Al, or by the evaporation of a single 2 nm of Al followed by Atomic Layer Deposition (ALD) of Al_2O_3 (performed at LPN by Alan Durnez). The oxide obtained by ALD shows much better properties in terms of leaking current, breakdown voltage, residual doping and even mobility. ALD is a good technique for a fast and large scale characterization of new device geometries. Table 2.1.7 summarized the properties obtained for various graphene types and substrates.

2.1.5 High mobility graphene: transfers and cleaning

The transfer of 2D materials is a key step in the process of fabricating high quality devices. Considering the GoBN geometry, two transfer steps are necessary to fabricate a device: the transfer of hBN on top of the gates and the transfer of graphene on top of hBN. After each transfer a cleaning step is performed. In this work, various transfer techniques have been used:

Wet transfer. The wet transfer (or wedging transfer) was developed in Delft in 2010 [35], it was the first technique used to transfer graphene flakes. For a complete description of the wet transfer see Andreas Betz' thesis [36]. The process consists in exfoliating

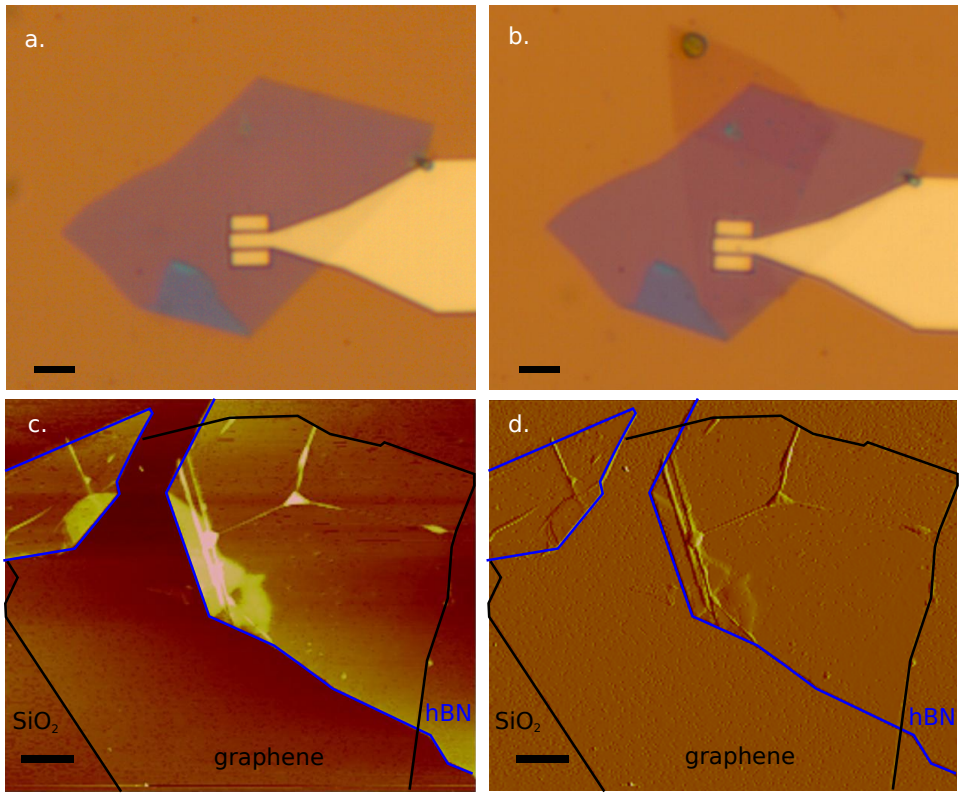

FIGURE 2.6: (a) Optical microscope image of a 7 nm thick hBN flake transferred on a local tungsten gate. (b) Optical microscope image of a graphene flake transferred on the hBN flake. For both optical images, the scale bar is 5 μm (c) Height sensor AFM scan of a graphene flake partly on SiO_2 and partly on hBN. The hBN thickness is 9.4 nm. The SiO_2-graphene step is 0.6 nm. We measured a roughness of 0.22 nm for graphene on SiO_2 and 0.15 nm for graphene on hBN. (d) Corresponding phase sensor. Looking carefully at the phase image, one can notice the improved flatness of graphene on hBN. However, the price to pay is the presence of wrinkles.For both AFM images, the scale bar is 1 μm.

graphene (or hBN) on a silicon chip and spin-coating a hydrophobic polymer on the chip. It is then immersed in water resulting for the graphene (or hBN) flakes to be lifted-off with the polymer film that floats on the water surface (see Fig. 2.7-a). By lowering the water level while monitoring the flake position one can precisely transfer the flake on the desired area. Unfortunately the wet conditions and the polymer used for the transfer bring many impurities which results in rather low mobilities.

Dry transfer. Numerous dry transfer techniques have been described recently [30, 33, 37]. For the fabrication of the GoBN1 and GoBN2 samples we used an all-dry technique inspired from the one developed at Delft [33]. In this technique, the flakes are directly exfoliated on a viscoelastic and transparent stamp. The stamp is adhered on a glass slide, it consists of a home made 1 mm thick layer of PDMS (Polydimethylsyloxane) covered by a layer of spin-coated copolymer (MMA-MAA). The flakes deposited on top of the copolymer are selected with an optical microscope (we checked we have a high enough

contrast to identify a monolayer by performing a Raman spectroscopy on a transferred flake). The stamp is turned upside down and attached to a XYZ micro-manipulator located on the optical axis of a long working distance optical microscope. The target substrate where one wants to transfer the 2D material flake is located below the stamp and attached to a XY stage. The stamp being transparent, one can focus successively on the flake and on the target substrate, and align the flake and the target area (in our case the gates) with a sub-micron precision. Then the stamp is carefully lowered to be finally brought into contact with the target substrate and gently pressed. The target substrate temperature is raised above the glass transition of the copolymer while the stamp is slowly peeled off. As a result, the copolymer sticks to the target substrate and remains with the flakes on the substrate (see Fig. 2.7-c). This technique takes advantage of the viscoelastic nature of the stamp which allows to fit the shape of a possibly patterned or tilted substrate. Thus a perfect flatness of both the stamp and the target substrate is not necessary to realize a good contact of the 2D flake with the substrate (metallic gate or hBN). Besides the low rigidity of the stamp reduces the stress applied on the flake during the transfer.

Pick-up transfer. The van der Waals pick-up technique, as developed in Columbia by Wang et al. [8], is the most recent and the most successful transfer technique as it allows multiple transfers for 2D material stacking without any contamination. In particular, the realization of hBN-encapsulated graphene has given access to ultra-clean graphene samples exhibiting a mobility only limited by phonons. Besides, this technique is now used in several groups to fabricate complex heterostructures involving also TMDs materials in addition to graphene and hBN. The principle is to use a viscoelastic stamp similar to the one presented above but instead of exfoliating onto the stamp, we start by exfoliating hBN flakes on a regular Si/SiO_2 substrate and we use the stamp to pick-up one "good" flake (size, thickness, flatness) that has been scanned by AFM previously. Having a hBN flake on the stamp, one can take advantage of the very strong van der Waals attraction between 2D materials by using it to pick up a graphene flake which will then stick to the hBN flake. The procedure can be reiterated to pick up another hBN flake on the bottom of the graphene flake. Finally the hBN/graphene/hBN stack can be deposited on any substrate by using a heater to melt the transferring polymer (Fig. 2.7-d). Therefore, the encapsulated graphene has never been in contact with a solvent nor with a polymer, and at the end of the fabrication it is protected from its environment by the top and bottom hBN flakes. However, a major drawback of this technique lies in the realization of the electric contact on the encapsulated graphene: there is no possible access for a top metallic contact. The solution found by Wang et al. consists in etching a trench in the stack to realize an edge contact [8]. It has been demonstrated in the same work that an edge contact can have a low contact resistance,

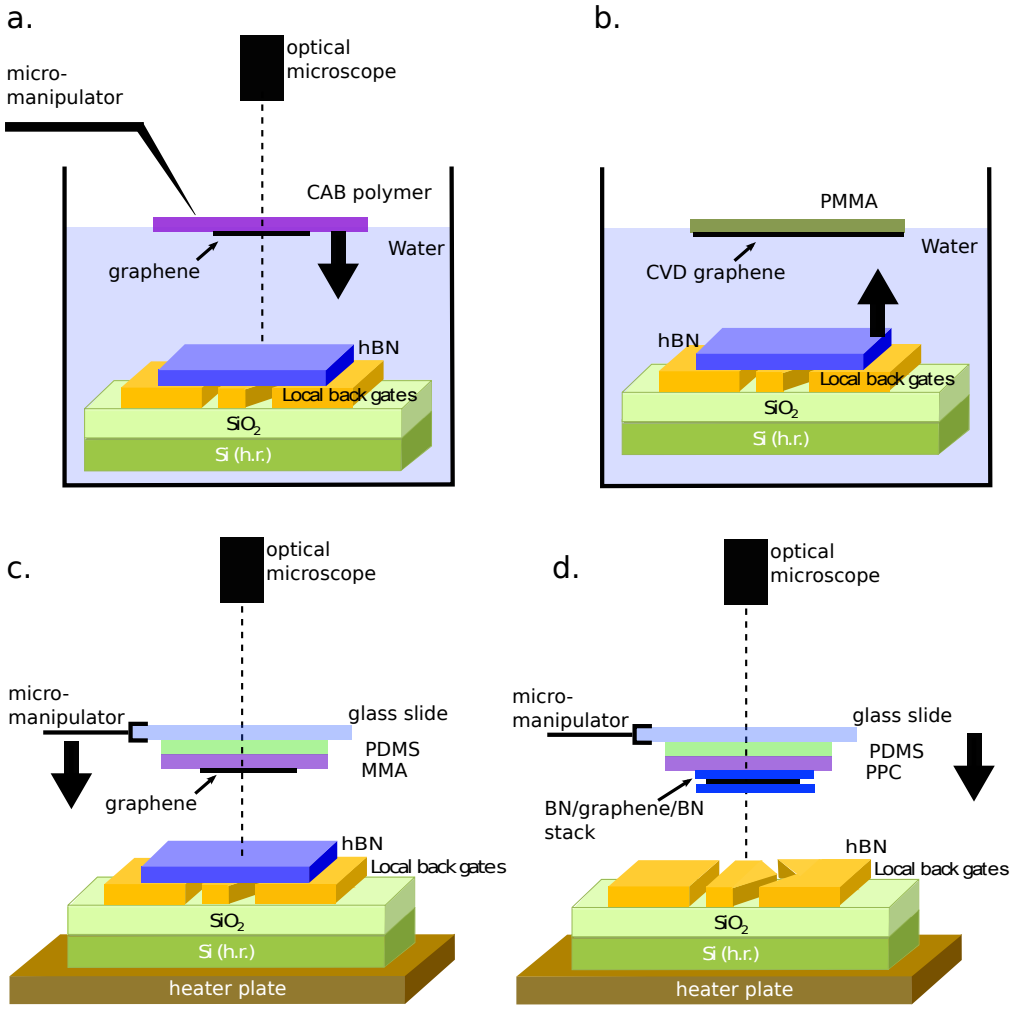

FIGURE 2.7: (a) Wet transfer technique: the cellulose acetate butyrate (CAB) polymer has been detached from the substrate taking away the graphene flake. Its position at the water surface is controlled with a tip while the water level is lowered by a pump. (b) CVD graphene transfer: The Cu foil has been dissolved, the remaining PMMA-graphene stack is fished by the targeted substrate. As the CVD sheet is much larger, we do not need the microscope nor the micro-manipulator for the alignment. (c) Dry transfer technique. (d) Pick-up technique (final step, the stack being realized previously). The large arrows indicate the moving parts and their direction during the transfer

however the reproducibility of good contact resistance is not achieved yet. As we need a very good contact resistance for high frequency devices we chose to work with non-encapsulated samples. In this work we used only the first step of this technique in the fabrication process of GoBN3, meaning we transferred a single hBN flake. Subsequently we transferred a CVD graphene film covering all the devices of the chip.

Annealing. The transfer techniques used in this work (CVD, wet, dry or pick-up) require the graphene to be into contact with a resist. Most of it is removed in acetone but we need a more efficient cleaning to access the high mobility. Consequently, we perform an annealing procedure to clean the hBN surface prior to the graphene transfer

and we perform another annealing step after the graphene transfer itself and before the contact deposition. The annealing process takes place in a tubular furnace at $300°C$ at atmospheric pressure and under a flow of 100 *sccm* of H_2 and 800 *sccm* of Ar for 2 hours. The H_2 gas removes efficiently the resist polymer residues but should be used with caution as it can also damage the graphene. Once the device fabrication is over we may need further cleaning of the free graphene surface that we perform inside the probe station: we can heat the samples up to $150°C$ under a vacuum of 1×10^{-5} $mbar$. In addition a current annealing at ~ 1 $A/\mu m$ can improve the device performance (Dirac point moves toward zero gate voltage and the on/off ratio increases)

2.1.6 Graphene contact

Making a good graphene contact is a very delicate process. As a result in this work we chose to follow the process developed by A. Betz in [36]: Standard e-beam lithography is used to define the contact area in a PMMA resist. A $50nm$ layer of Pd metal is deposited in an e-beam evaporator Plassys MEB 550S in Université Paris Diderot under a vacuum of a few 10^{-7} $mbar$. A significant improvement of the contact resistance is observed when one leaves the sample under high vacuum overnight prior to metal deposition. A more detailed review of contact resistance origin and state of the art will be presented in chapter 4.

2.1.7 Comments on the samples properties

During my thesis over a hundred devices have been fabricated with various graphene origins, substrates and transfer methods. Even though no systematic study was conducted, our main figure of merit, the mobility, is given for a selection of samples in Table 2.1.7. The mobility of our samples may seem low compared to the state of the art, however one has to keep in mind that the mobility is usually extracted from a quantum Hall effect measurement, a 4-point measurement or a transfer length measurement (see section 4.2.3) to avoid the contact resistance, and usually with bigger samples. On the contrary our devices are measured in a 2-point configuration and the mobility is extracted from the transfer curve so that the contact resistance has to be estimated and removed. Besides our devices are equipped with a local gate which can introduce more roughness and pollution. Finally they are short which implies their resistance is dominated by the contact resistance so it is more complicated to determine their intrinsic properties, they could also be more sensitive to resist residues near the contacts. This issue has also been pointed out in [14].

Samples	*graphene / transfer*	*substrate/transfer*	*size* L×W (μm^2)	*RT mobility* ($cm^2V^{-1}s^{-1}$)
GoBN1	exfoliated / dry	hBN / dry	1.4×1.6	12000
GoBN2	exfoliated / dry	hBN / dry	0.2×1.1	6000
GoBN3	CVD Bouchiat	hBN / pick-up	0.5×1.5	3500
GoAl0	CVD commercial	Al_2O_3 evaporated	0.5×1.5	1000
GoAl	CVD commercial	Al_2O_3 ALD	0.5×1.5	2000
Morfin	CVD LPA	SiO_2	1×2	3000

TABLE 2.1: Important parameters of the fabricated samples. The mobility is estimated from the transfer curve of a 2-points measurement taking into account the contact resistance, at room temperature. As expected, the mobility is better on hBN substrate. Besides, for a same substrate, we always observe a mobility degradation for smaller samples (also observed by [14]). This can come from a less well defined electrostatic environment, a dirtier graphene around the contacts, or simply a more difficult mobility extraction when the overall resistance is dominated by the contact resistance. Note that the dielectric breakdown voltage is around $1\ V/nm$ for all the dielectrics used here.

2.1.8 Coplanar waveguide

All our devices are embedded in an impedance matched coplanar waveguide in order to perform measurements in the radio-frequency range. Actually, the waveguide is fabricated prior to the hBN transfer to avoid unnecessary contamination. It is made of $250nm$ thick Joule evaporated Au. This large thickness is essential in case of probe measurements, as the probes strongly damage the metallisations. The shape of the waveguide has been carefully chosen to ensure a $50\ \Omega$-match all along the line that interpolates between the $100\ \mu m$ pitch of the probes and the micrometer size of the actual device. Some simulations using AppCAD have been performed to estimate both the metallisation width and the gap between the gate and source (as well as drain and source) electrodes. In addition we measured the transmission and reflection parameters of our coplanar waveguide in the throughline configuration. As one can see in Fig. 2.8-c we obtain a ~ 97 % transmission of the throughline with a relatively flat spectrum up to $40\ GHz$. The oscillations observed at high frequency result from a slight drift of the calibration (see next section).

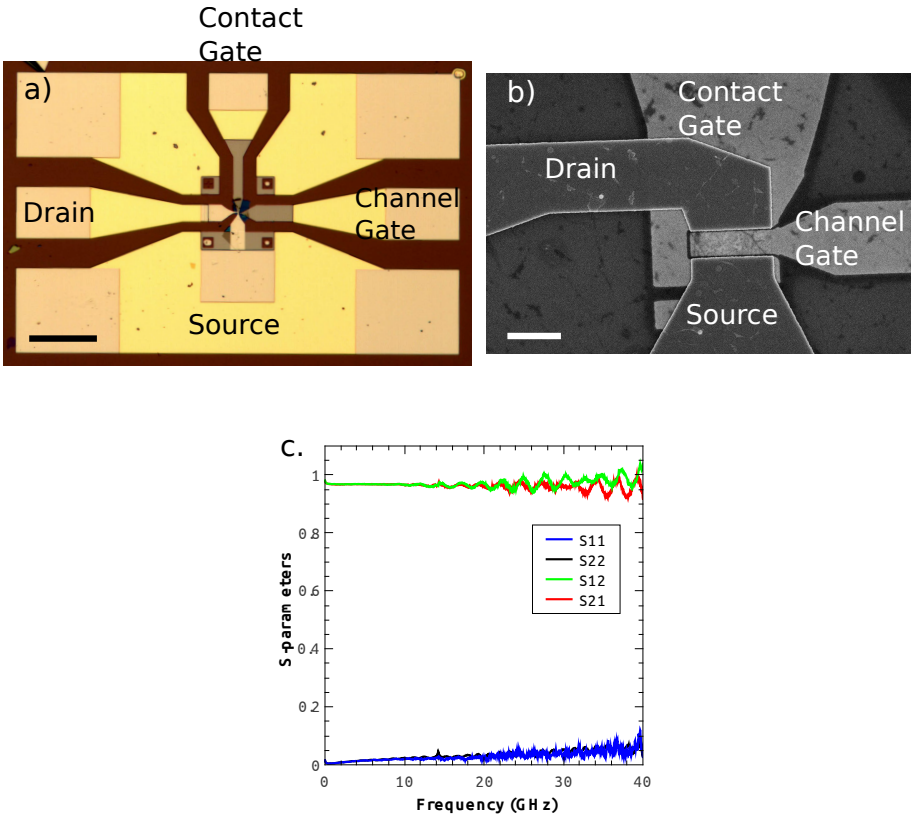

FIGURE 2.8: (a) Coplanar waveguide of a device with two gates (this is the sample GoBN3). The CPW is reinforced at the probe location. The active part of the device is located in a $100 \times 100\,\mu m^2$ square with alignment marks at the corners. The black scale bar is $100\,\mu m$. (b) SEM picture of the active part of the device. The white scale bar is $1\,\mu m$. (c) Module of the scattering parameter measured on a throughline with our CPW geometry. S12 and S21 are the frequency dependant transmission coefficients while S11 and S22 are the reflection coefficients (for both sides of the CPW).

2.2 Experimental setup

In that section we present our transport measurement setup. The devices are always characterized first in DC and at room temperature. However, the graphene surface being very sensitive to pollution from molecules in the air, the devices are characterized in vacuum at $1 \times 10^{-5}\,mbar$. To let us the possibility to go to cryogenic temperatures on one hand, and to perform measurements in the radio frequency (RF) range on the other hand, all measurements are carried out in a RF cryogenic Janis probe station (Fig. 2.9).

2.2.1 The Janis probe station

This probe station is designed to operate in a $0 - 40\,GHz$ frequency range, in vacuum ($1 \times 10^{-5}\,mbar$) and with variable temperature from $6\,K$ to $450\,K$ by means of helium circulation under a cold finger and heating of the sample holder. The station has 4 arms,

each of them being equipped with RF lines and RF probes. The RF probes consist of ground-signal-ground tips, with a pitch of $100\mu m$ between the tips (shown in Fig. 2.9). The probe positioning is performed through an optical window. In addition, we have an optical fiber mounted on a fifth arm that can be controlled with a XYZ stage within micrometer accuracy.

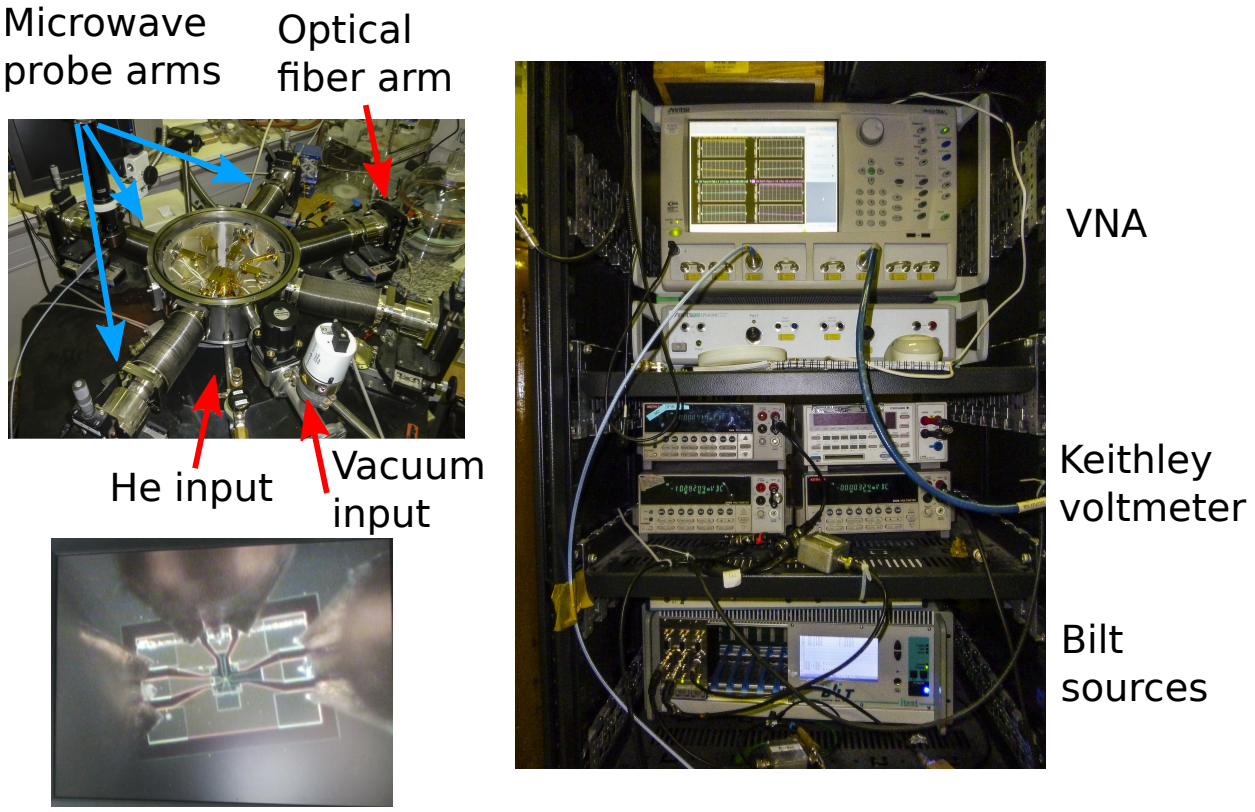

FIGURE 2.9: Top left: picture of the Janis probe station with the vacuum chamber open. Bottom left: picture of the device being measured. One can see the 3 RF probes on the CPW. Right: RF and DC measurement setup.

2.2.2 DC and radio frequency measurement

DC and AC actuations are provided to the probes through $500kHz-40GHz$ *Marki* bias-tees. The sample is DC biased using BILT DC sources and Keithley 2000 voltmeters in the voltage divider configuration for low bias measurements (Fig. 4.14) and in the voltage source configuration for high bias measurements. This enables us to measure the sample resistance and current as well as the possible leaking current through the gate dielectric to prevent dielectric breakdown. Most of the RF measurements are performed with a four port 70KHz-40GHz Anritsu Vector Network Analyser (VNA) providing the complex S-parameter matrix in the frequency range. The excitation level is kept below the thermal energy in order to preserve linear conditions, typically we apply $-27dBm \equiv 10mV$ (in a

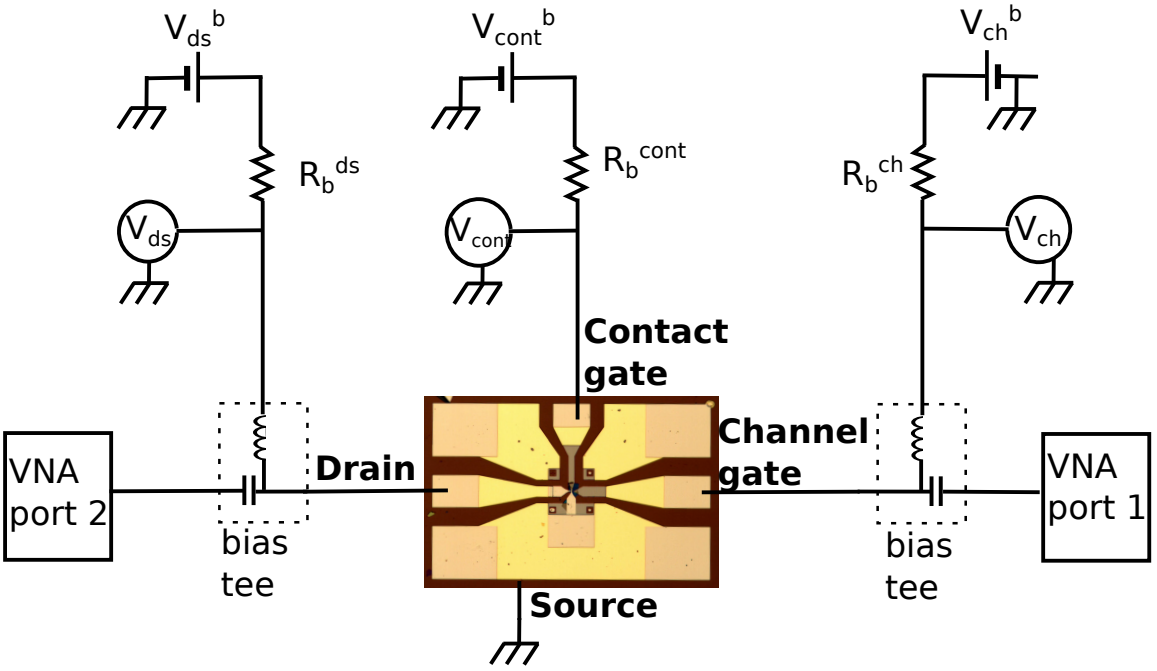

FIGURE 2.10: Schematic circuit diagram of the electrical setup with a double gate configuration. The drain side of the device is DC biased at V_{ds}^b with a BILT source through a bias resistance R_b^{ds}, and the actual drain source voltage V_{ds} is measured with a Keithley2000 voltmeter. Therefore, the drain-source current is $I_{ds} = (V_{ds}^b - V_{ds})/R_b^{ds}$. A similar circuit is used to bias the two gates. For RF measurements, each port of the VNA is connected through a bias tee to separate the high frequency signal from the DC actuation. (A third VNA port can be connected to the contact gate as well.)

50 Ω environment) at room temperature. The spectra are generally acquired with 1601 frequency points, averaged 5 times and within a resolution bandwidth of 1 kHz.

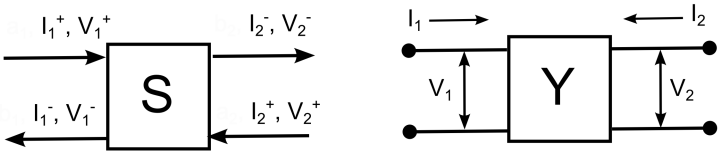

FIGURE 2.11

Principle of VNA measurements A good description of the measurement principle can be found in [36], here are the main points. A 2-terminal VNA measurement consists in measuring successively the reflected and the transmitted signal from both terminals. A signal is sent from the VNA to port i. At $x = 0$ a part of the signal is transmitted and another part is reflected:

$$V_i(\omega, x<0) = (V_i^+ e^{ikx} + V_i^- e^{-ikx})e^{-i\omega t} \quad (2.1)$$

$$V_j(\omega, x>0) = V_j^- e^{ikx} e^{-i\omega t} \quad (2.2)$$

Where V_i^+ is the amplitude of the voltage wave incident on port i, V_i^- is the amplitude of the voltage wave reflected from port i and V_j^- is the amplitude of the voltage wave transmitted to port j. Similarly for the currents:

$$I_i(\omega, x<0) = (I_i^+ e^{ikx} - I_i^- e^{-ikx})e^{-i\omega t} \quad (2.3)$$

$$I_j(\omega, x>0) = I_j^- e^{ikx} e^{-i\omega t} \quad (2.4)$$

So one should notice that the voltage wave is reflected keeping its sign (effective voltage at the input of the device):

$$V_i = V_i^+ + V_i^- \quad (2.5)$$

while the sign of the current is reversed (effective current at the input of the device):

$$I_i = I_i^+ - I_i^- \quad (2.6)$$

The output of the VNA consists in the 4 scattering parameters (S-parameters) for each frequency point. The S-parameter S_{12} (S_{21}) is the transmission coefficient from port 2 to port 1 (port 1 to port 2 respectively). The S-parameter S_{11} (S_{22}) is the reflection coefficient of port 1 (of port 2 respectively). They are defined as below (Fig. 2.11):

$$\begin{pmatrix} V_1^- \\ V_2^- \end{pmatrix} = \begin{pmatrix} S_{11} & S_{12} \\ S_{21} & S_{22} \end{pmatrix} \begin{pmatrix} V_1^+ \\ V_2^+ \end{pmatrix} \quad (2.7)$$

Besides, the S-parameters are complex values meaning that we have access to the phase of the transmitted and reflected signals. They can be converted in admittance parameters Y_{ij} following:

$$Y_{11} = \frac{1}{Z_0} \cdot \frac{(1-S_{11})(1+S_{22}) + S_{12}S_{21}}{(1+S_{11})(1+S_{22}) - S_{12}S_{21}} \quad , Y_{12} = \frac{1}{Z_0} \cdot \frac{-2S_{12}}{(1+S_{11})(1+S_{22}) - S_{12}S_{21}} \quad (2.8)$$

$$Y_{21} = \frac{1}{Z_0} \cdot \frac{-2S_{21}}{(1+S_{11})(1+S_{22}) - S_{12}S_{21}} \quad , Y_{22} = \frac{1}{Z_0} \cdot \frac{(1+S_{11})(1-S_{22}) + S_{12}S_{21}}{(1+S_{11})(1+S_{22}) - S_{12}S_{21}}$$

Which can also be expressed as:

$$\begin{pmatrix} I_1 \\ I_2 \end{pmatrix} = \begin{pmatrix} Y_{11} & Y_{12} \\ Y_{21} & Y_{22} \end{pmatrix} \begin{pmatrix} V_1 \\ V_2 \end{pmatrix} \quad , \tag{2.9}$$

where

$$Y_{ij} = \left(\frac{I_i}{V_j} \right)_{V_{k \neq j}=0} \qquad i, j = 1, 2 \tag{2.10}$$

Calibration In order to remove the spurious contributions from connectors, cables and probes (losses and dephasing) we perform a calibration following a Short-Open-Load-Through (SOLT) procedure on a commercially available calibration substrate. After this procedure the calibrated system has a virtual measurement reference plane located at the tip end. Further parasitic contributions can come from the CPW itself as dephasing through the access electrodes and parasitic capacitances between the pads. It can be removed using a *throughline structure*. This is a coplanar waveguide identical to the actual device except it is equipped with a continuous metalic line instead of a graphene transistor. The dephasing due to the propagation along the $600\mu m$ long waveguide is measured on the throughline. Generally it is on the order of:

$$\phi = \frac{\omega D}{v} \approx 2^{\circ} GHz^{-1} \tag{2.11}$$

Where $v \approx 1.2\ m/s$ is the speed of light in the system $air/SiO_2/Si$. It has to be noted that the effective CPW length depends on the tip positioning leading to a shorter $D \approx 400\ \mu m$.

We also make a device with the exact same geometry than the actual device but without graphene (called *open structure* or *dummy structure*). In that case, the measured signal corresponds to parasitic capacitances. In most cases, the parasitic capacitances are in parallel to the intrinsic ones meaning that a simple subtraction of the dummy Y-matrix from the device one allows to remove them. However, one has to keep in mind that this operation corresponds to a particular electrical model for a given device. For example it does not take into account losses in the access electrodes or series capacitances between the probes and the CPW. Those issues will be further discussed in the RF measurement chapter (6).

Chapter 3

The Klein tunneling transistor

In ballistic semiconductors the classical trajectory of electrons is similar to rays in geometrical optics. In optics, the manipulation of photons relies on interfaces between media of different indexes to make lenses and mirrors. Great efforts have been made the last few years to investigate the analogy between optics and electronic transport in two-dimensional electron systems such as GaAs-GasAlAs. For example, electron focusing was achieved using an electrostatic gate to mimic a lens behavior [38] or with a quantum point contact [39]. Similarly, quantum optic electronics is also an active research area [40]. In graphene, as for other semiconductors, the building block for electron manipulation is the p-n junction. Due to their chiral nature, the crossing of a p-n junction by Dirac Fermions (DF) has very particular properties [41, 42]. First, the pseudo-spin conservation is responsible for a total transmission of a normally incident electron. In other cases, the transmission probability depends on the incident angle, and the transmitted electron is refracted following a Snell-Descartes type law, but with a negative index. In graphene, large mean free paths are accessible thanks to the weak electron-phonon interaction, moreover electrostatic barriers are easy to induce thanks to the 2D nature of graphene. All those elements contribute to make graphene a very good candidate for optic electronics.

The aim of this chapter is to describe the working principle of the Klein Tunneling transistor [43]. This device has a triangular gate geometry to take advantage of the refraction at a p-n junction. It allows in principle to suppress the channel conductance at high densities. Although many proposals with similar geometries have been made, we try here to give the key principles toward the realization of a practical device.

I start by reviewing the progress made toward the realization of devices for Dirac Fermion optics, then I give the basic concepts useful to understand the physics of the p-n junction in graphene. Finally I explain the working principle of the Klein Tunneling transistor.

3.1 Transport in the ballistic regime: proposals and experiments

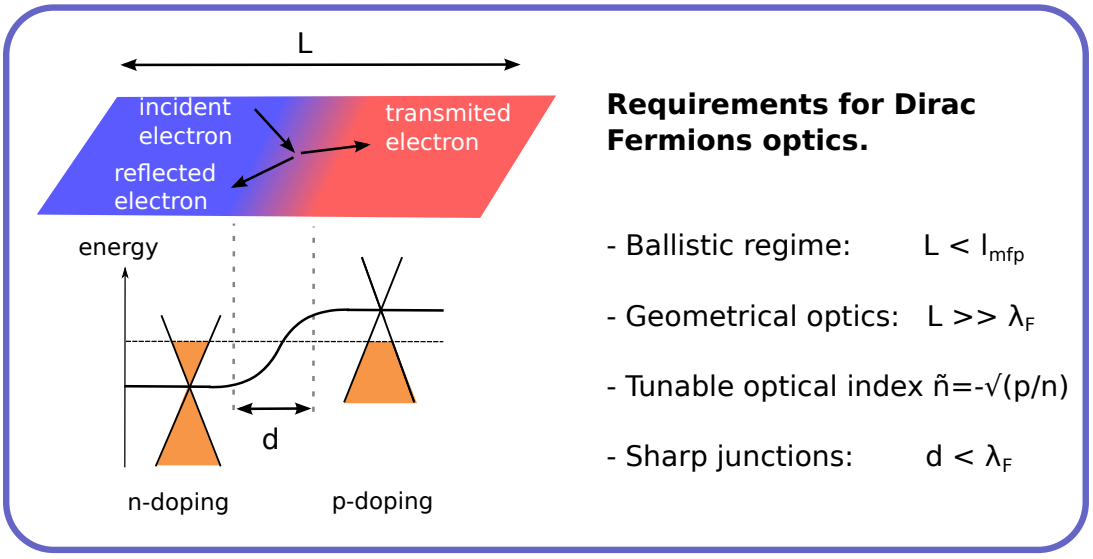

FIGURE 3.1

The requirements for Dirac Fermion optics from a technological point of view have already been mentioned in the previous chapter. It is worth reminding the main points (Fig. 3.1). First, the sample has to be ballistic meaning that the sample length L is smaller than the mean free path l_{mfp}[1]. Then, to be in the geometrical optics regime, the Fermi wavelength of Dirac Fermions at a given energy should be negligible with respect to the sample length, in order to avoid diffraction. Regarding the junction itself, one must be able to tune its transmission, meaning we should be able to control the doping p and n on both sides of the junctions. Finally, the sharpness of the junction defined by the length d to cross from the n-doped area to the p-doped area must be small with respect to λ_F to ensure good dynamics of the junction transmission. Let us give first a quick review on the graphene quality progress which is the real bottleneck for DF optics, before moving toward devices for DF optics.

The first transport measurements on graphene samples by Novoselov et al. in Manchester [2, 3] already exhibited high carrier mobilities, $\mu \simeq 5000\, cm^2/V/s$. Since then, the fabrication techniques have improved to reach mobilities higher than for any other materials. Higher mobility means longer mean free path, thus approaching the ballistic transport regime. This was first achieved in suspended samples, avoiding the roughness of SiO_2 substrates, with $\mu \simeq 200000\, cm^2/V/s$ [4, 5] but not practical for device implementation. Then the use of hexagonal boron nitride (hBN) as an atomically flat

[1] The sample may not be ballistic over its full length but it should be at least ballistic over the active part (the p-n junction, the p-n-p barrier...)

substrate for graphene allowed to work with supported samples with mobilities up to $\mu \simeq 100000\, cm^2/V/s$ [30] first, and then $\mu \simeq 500000\, cm^2/V/s$ [7, 8] by using hBN encapsulated graphene structures. At this point, the samples are generally smaller than the mean free path, which is illustrated for example by a negative bend resistance in the van der Pauw configuration [44] for samples of a few microns [7, 8]. Those improvements in graphene sample quality opened the way to the regime of Dirac Fermion (DF) optics: the first requirement for DF optics is to work with a transparent medium, i.e. to have a mean free path l_{mfp} larger than the sample length L.

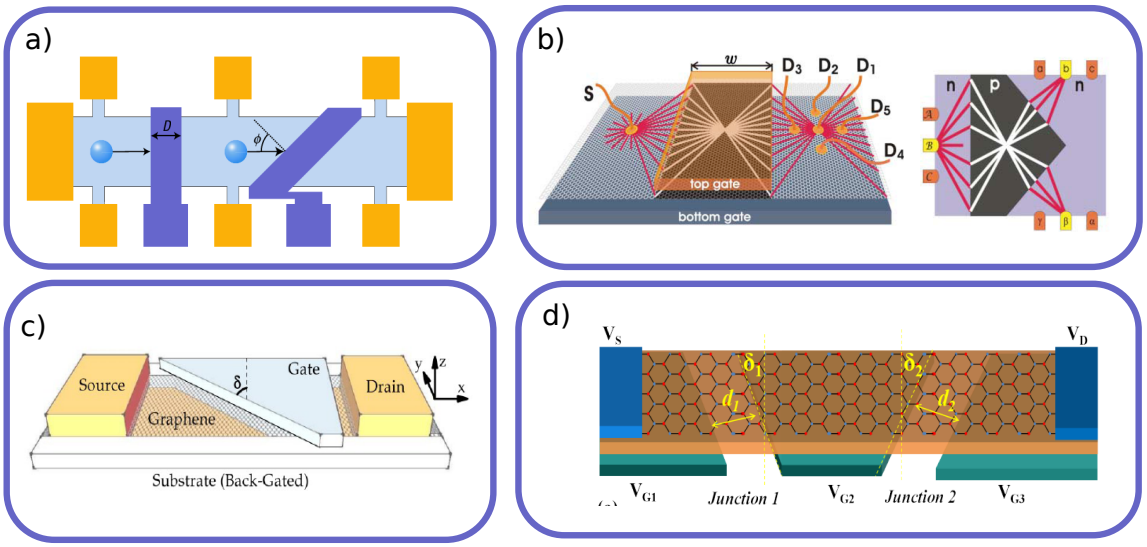

FIGURE 3.2: a) Proposal by Katsnelson, Novoselov and Geim [41] of a Klein tunneling experiment with tilted gates. b) Proposal by Cheianov, Fal'ko and Altshuler [45] of the graphene Veselago lens and a prism shaped beam-splitter with p-n-p barriers. c) Triangular gate for a graphene logic transistor [46]. d) Proposal by Sajjad and Gosh [47] to open a transmission gap with tilted gates.

Along with this increase of mobility, the peculiar properties of graphene p-n junction were investigated, generally with the combination of a remote back gate and a top gate to create a p-n-p barriers [48, 49]. In those first experiments, the junctions were smooth and the transport was not ballistic between the p-n and the n-p junctions. The observation of quantum interferences due to multiple reflections inside a p-n-p barriers [13, 50–52] (and predicted by [53]), namely Fabry-Pérot oscillations, gave a stronger evidence of the transmission properties of a p-n junction.

Let us focus now on graphene devices taking advantage of geometrical optics effects. One of the most striking properties of graphene is the total transmission of normally incident DF across a potential barrier regardless of its height. This effect is responsible for the graphene high mobility: a charged impurity cannot provoke a backscattering of DF. Yet it also prevents the realisation of graphene digital transistors: a regular electrostatic barrier cannot completely stop DFs. But that would be forgetting about

the refractive properties of a graphene p-n junction. As will be shown in more detail in the following section, the transmission of DF through a junction has an angular dependence, and in particular, it presents a critical angle above which no electrons are transmitted. Then, using tilted junctions in series, DF can be collimated first and then totally reflected by the second junction. This can be regarded as a polarizer-analyser geometry with respect to the pseudo spin degree of freedom. Thus one could suppress the channel conductance of a graphene transistor. This is the basic idea behind the *Klein tunneling transistor* [43] inspired by the early work of D. Torrin [54] in LPA. Following a similar route, a few proposals have been made to take advantage of the refraction/reflection effect [41, 45, 47, 55], along with experimental evidences of the angular dependent transmission [56–58]. Some emblematic devices inspired by optics have been realized: Taking advantage of the total reflection at a p-n junction allowed the authors of [59] to achieve electron guiding, realizing the electronic equivalent to optical fibers. More recently, focusing through a rectangular p-n-p barrier has been observed [60]. This demonstrates the Veselago lens proposal of Cheianov et al. [45] as it relies on the negative-index refraction of DF at a p-n junction.

Similarly to the Klein tunneling transistor presented in this thesis, other groups have proposed to use triangular shaped gates in order to open a transmission gap in graphene transistors [46, 61–65]. Those papers target digital applications with estimations of the ON/OFF ratio around $10^2 - 10^5$. We believe our approach to be more conservative in accounting for diffusive transport in the leads as well as diffraction effects. The ON/OFF ratio is more modest, the transconductance effect is significant and we target microwave electronic applications rather than logic transistors.

Besides, we want to stress the importance of the p-n junction sharpness (or length d). Experimentally, it is roughly given by the gate dielectric thickness. For instance, the use of suspended graphene [51] or remote gates [57] leads to very smooth junctions. As it will be shown later in this chapter, a smooth junction has a good angle selectivity but a poor transmission. The combination of a remote back gate and a top gate with a thin dielectric can lead to sharp junctions. For example the authors of [60] claim $d = 12\,nm$. The contact induced junction combined with a remote back gate also allows to study sharp junctions [13]. Our route is different, we target a transistor working in the radio frequency range. Hence we need at least two local gates and we need them to be close to each other at the $20\,nm$ scale, as presented in the fabrication section .

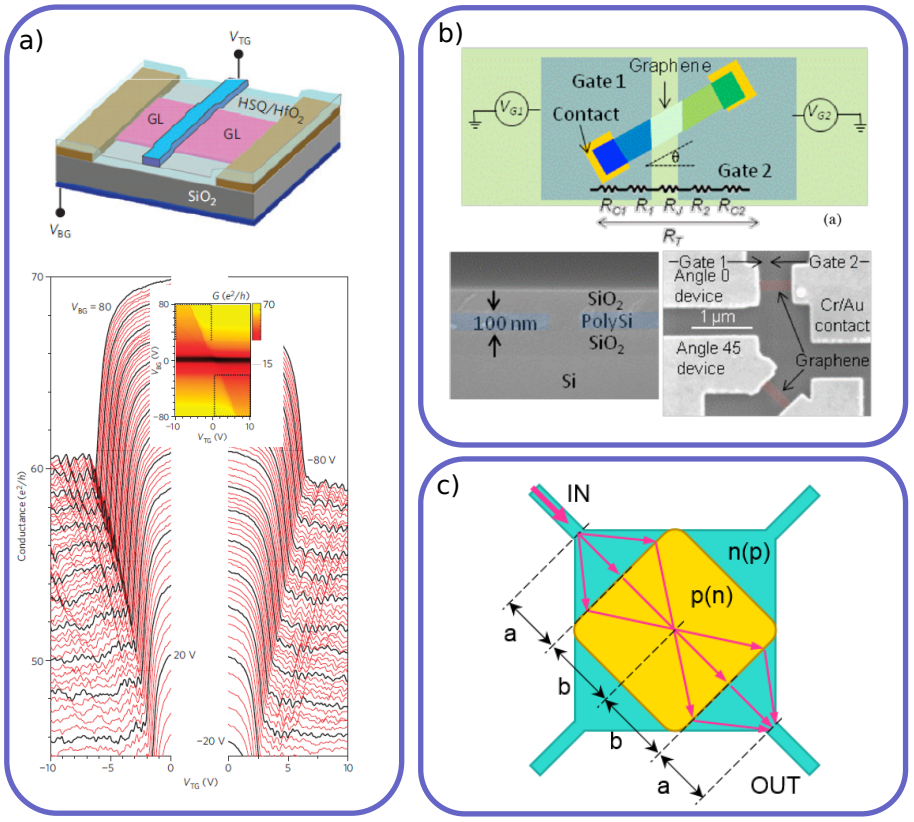

FIGURE 3.3: (a) Adapted from [50]. Conductance oscillations (Fabry-Pérot effect) inside the top gated area. (b) Adapted from [57]. Local split gates with buried highly doped silicon. Comparison of straight and tilted junction within a same flake or within a same CVD graphene grain to show the incidence angle dependence transmission. (c) Adapted from [60]. hBN encapsulated graphene with a combination of top and bottom gate is used. The top gated area plays the role of a negative refractive index medium. A current peak is observed in OUT terminal when the top gated and bottom gated area have opposite carrier densities which demonstrates the focusing effect of the top gate.

3.2 The p-n junction in graphene

3.2.1 Electron incident on a potential step

We describe here the situation of an electron in graphene incident on a potential step. This description is mainly based on the pedagogical review by P.E. Allain and J.N. Fuchs [19] where the reader can find more details if needed. The potential step is usually a consequence of a perpendicular electric field induced by a local gate, but it can alternatively be achieved by chemical doping from a metallic contact (see next chapter). We consider charge carriers at the Fermi level. If the Fermi level lies in the conduction band, the doping is said "n", the charge carriers are electron-like and their energy is positive. On the contrary, if the Fermi level is in the valence band the doping is said "p", the charge carriers are hole-like and their energy is negative. We are interested here in the case of a n-p junction as depicted in Fig. 3.4 (the p-n junction case is completely

symmetric). In that picture the band structure of graphene is shifted by the potential step while the Fermi level is constant. It results in a transition from a n-doped region to a p-doped region.

A particularly important property of the junction is its length d over which the change of potential occurs. Notably, the junction sharpness controls the transmission of the junction. To determine if the junction is sharp or smooth one has to compare d with the electronic wavelength λ_F. It is given by $\lambda_F = 2\sqrt{\pi/n}$ where n is the carrier density. In our accessible density range $n \sim 0.2 - 10 \times 10^{12} cm^{-2}$ it corresponds to $\lambda_F \sim 11 - 80\, nm$. The junction will be sharp when $d << \lambda_F$ and smooth when $d >> \lambda_F$. In that section we will distinguish both cases and give expressions for their transmission following [19, 41, 42]. Then we give a transmission expression calculated by [66] for a more realistic potential profile and which interpolates between sharp and smooth limits. Note also that the given transmissions are angle dependent. In a realistic device the total transmission of a junction will be given by integration over all incident angles.

Notations.

An electron of energy E and wave vector $\vec{k} = \big(k_x, k_y\big) = \frac{E}{\hbar v_F}\big(cos(\theta_i), sin(\theta_i)\big)$ is incident on a potential step of height V_0. The potential step is set at $x = 0$, it is translationally invariant in the y direction, θ_i is the angle between the normal and the incident ray as shown in Fig. 3.4. Note that due to the invariance of the potential along y direction the wavevector projection along y, k_y, is conserved.

$$V(x) = 0, \qquad -\infty < x < 0 \qquad (zone1) \tag{3.1}$$

$$V(x) = V_0, \qquad 0 < x < \infty \qquad (zone2) \tag{3.2}$$

In the area $x < 0$ the electron kinetic energy is $E_{kin} = E_1$ and for $x > 0$ $E_{kin} = E_2 = E_1 - V_0$. If $0 < E_1 < V_0$ then $E_2 < 0$ and we have indeed a n-p junction. In the case $V_0 < E_1$ then $E_2 > 0$ and it is a n-n' junction. We define the following wave vectors and associated angles:
Incident: $\vec{k_i} = \big(k_x, k_y\big) = \frac{E_1}{\hbar v_F}\big(cos(\theta_i), sin(\theta_i)\big)$
reflected: $\vec{k_r} = \big(k_{rx}, k_{ry}\big) = \frac{E_1}{\hbar v_F}\big(cos(\theta_r), sin(\theta_r)\big)$
transmitted: $\vec{k_t} = \big(k_{tx}, k_t y\big) = \frac{E_2}{\hbar v_F}\big(cos(\theta_t), sin(\theta_t)\big)$.

In Fig. 3.4 the black arrows correspond to the direction of propagation while the red arrows correspond to the wave vector direction. So one can notice the wavevector is reversed when going through the step (n-p case), but the direction of motion is preserved. In fact, in the n-doped region momentum direction and velocity direction are the same

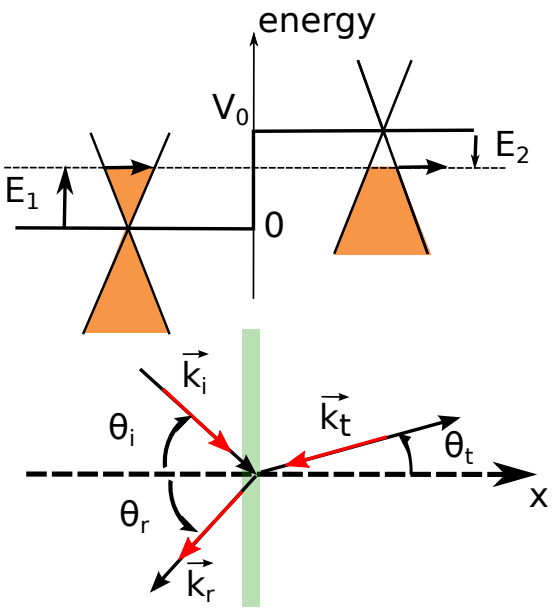

FIGURE 3.4: Sketch of an electron incident on an abrupt potential step and its corresponding band structure. The black arrows represent the direction of propagation and the red arrows represents the electron wavevector. The left region is n-doped so that momentum and propagation are in the same direction and the energy $E_1 > 0$. The right direction is p-doped, resulting in an energy $E_2 < 0$. The pseudo-spin conservation forces the electron to stay on the same branch of the band structure, therefore the momentum is reversed. However the direction of propagation is unchanged to ensure current conservation.

while in the p-doped region they are opposite. This is a peculiarity of Klein tunneling which is also highlighted in the band structure of Fig. 3.4: The black arrow indicates the direction of motion as well; the considered electron stays on the same branch of the band structure according to the pseudo-spin conservation; both energy and momentum change their sign; the direction of motion is conserved.

Anomalous refraction of Dirac Fermions.

From energy and k_y momentum conservation one obtains the Snell-Descartes law :
For reflection : $k_{rx} = -k_x$ and $\theta_r = -\theta_i$.
And for transmission : $k_{ty} = k_y$
Leading to :

$$E_1 sin(\theta_i) = E_2 sin(\theta_t) \tag{3.3}$$

This equation can be seen as as an analogue of Snell-Descartes refraction law from a medium of refraction index $\tilde{n}_1 \propto E_1$ to a medium of refraction index $\tilde{n}_2 \propto E_2 = E_1 - V_0$ which can be negative. Thus, for a n-p junction there is refraction into a medium of negative refraction index. Similarly to optics, if an electron is transmitted from a low doping region to a large doping region ($|E_1| < |E_2|$) then the electron is collimated ($\theta_t < \theta_i$). On the contrary, if $|E_1| > |E_2|$ the transmitted wave vanishes beyond a certain

critical incident angle θ_c defined as $sin\phi_c = \frac{V_0 - E_1}{E_1}$. Beyond this angle, an evanescent wave is created in the zone $x > 0$ and a total reflection is observed.

3.2.2 Angle dependant transmission of p-n junctions

3.2.2.1 Abrupt n-p step ($0 < E_1 < V_0$)

Still considering the optical analogy one can give an equivalent of the Fresnel law for the abrupt junction of Fig. 3.4. Let us write the wave function in zone left and right [19]:

$$\Psi_1 = e^{ik_y y}\left[e^{ik_x x}\begin{pmatrix}1\\ e^{i\theta_i}\end{pmatrix} + re^{-ik_x x}\begin{pmatrix}1\\ e^{-i\theta_i}\end{pmatrix}\right] \tag{3.4}$$

$$\Psi_2 = te^{ik_y y}e^{ik_{tx} x}\begin{pmatrix}1\\ -e^{i\theta_t}\end{pmatrix} \tag{3.5}$$

The continuity of the wave function in $x = 0$ leads to the transmission coefficient :

$$T(\theta_i) = 1 - |r|^2 = \frac{cos\theta_i cos\theta_t}{cos^2(\frac{\theta_i + \theta_t}{2})} \tag{3.6}$$

Where θ_t is given by the Snell-Descartes law 3.3. Thus for the normal incident case ($\theta_i = 0$) the probability to go through the step is

$$T(\theta_i = 0) = 1 \tag{3.7}$$

Let us notice that for a symmetric step $V_0 = 2 \times E_1$ (ie $E_1 = -E_2$) one has

$$T(\theta_i) = cos^2\theta_i \tag{3.8}$$

3.2.2.2 Sharp n-n' step ($V_0 < E_1$)

In this case the refraction law presents a positive index.

$$E_1 sin\theta_1 = (E_1 - V_0)sin\theta_t \tag{3.9}$$

And the formula (3.6) for the transmission coefficient T is still valid. Notice that the angle convention chosen does not take into account the sign of k_x. This leads to equivalent formula for both $E_1 < V_0$ and $E_1 > V_0$ and a stronger analogy with optics. But for a

more accurate description notice that in the case $E_1 < V_0$, k_x changes sign at x=0. For example at normal incidence $\theta_t = \theta_i + \pi$.

3.2.2.3 Smooth step

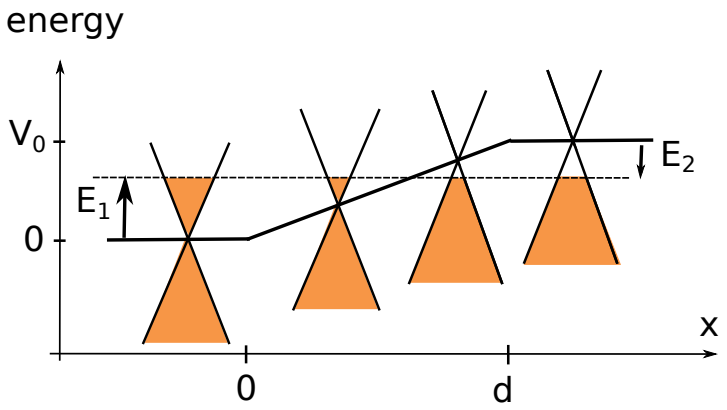

FIGURE 3.5: Potential profile of a smooth step of length d. The carrier density is vanishing at $x_c = E_1 d/V_0 = \frac{|k_i|}{|k_i|+|k_t|} d$.

We consider a smooth p-n junction (see figure 3.5). In that case, the junction length d is defined by the oblique potential zone. In that transition zone $0 < x < d$ the electrons energy is $E(x) = E_1 - V_0 x/d$. To go from n to p areas the Fermi level has to cross the charge neutrality point i.e. $E(x_c) = 0$ when $x_c = E_1 d/V_0 = \frac{|k_i|}{|k_i|+|k_t|} d$. The energy dispersion reads:

$$E(x) = \hbar v_F \sqrt{k_x^2(x) + k_y^2} \tag{3.10}$$

Since k_y is constant there is a classically forbidden zone defined by $k_x^2(x) = E(x)^2/(\hbar v_F)^2 - k_y^2 \leq 0$. Thus :

$$\frac{E_1 d}{V_0}(1 - sin(\theta_i)) \leq x \leq \frac{E_1 d}{V_0}(1 + sin(\theta_i)) \tag{3.11}$$

So the length of the forbidden zone is $2x_c sin\theta_i$. The electron has to tunnel across this zone to go through the junction. This leads to a transmission probability [42] :

$$T(\theta_i) \approx e^{-\pi k_y \times 2x_c sin^2\theta_i} \approx e^{-\pi \frac{2|k_i|^2}{|k_i|+|k_t|} d sin^2\theta_i} \tag{3.12}$$

The exponentially decreasing transmission of a smooth junction is similar to the well known case of p-n junctions in semiconductors. Except for normal incidence where the transmission is total. Therefore a smooth junction selects incident angles close to normal resulting in a stronger collimating effect than for sharp junctions. For an exact solution of such a smooth potential see also [67].

3.2.2.4 The interpolation function

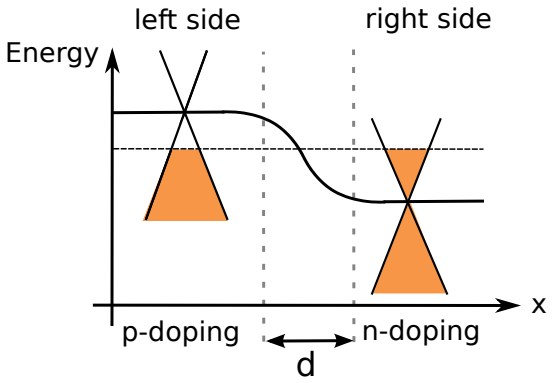

FIGURE 3.6: Fermi function-like doping profile assumed for the Cayssol's formula, in the case of a p-n junction.

Cayssol et al. have found a single interpolation formula giving the transmission T and matching the above sharp and smooth limits [66]. The authors of [66] assume a Fermi function-like potential step (shown in Fig. 3.6) and calculate an exact analytic formula for the transmission across such a potential step. This formula is very interesting from a practical point of view if one wants to estimate the transmission of a realistic p-n junction. Indeed the typical energy range of a graphene device corresponds to Fermi wavelengths extending over sharp and smooth regime. Moreover, the Fermi-like potential is probably more realistic than the smooth one of Fig. 3.5. The potential profile is given in terms of the wavevector by:

$$k_F(x) = k_i + \frac{k_t - k_i}{e^{-x/w} + 1} \tag{3.13}$$

Where w is a characteristic length of the junction which is not necessarily equals to the junction length d. To find the correspondence between the w and d length scales we calculate the transmissions with both formula in the limit of very smooth junctions ($d > 100nm$). We find a good agreement by taking $d \simeq 4.5w$. This value also corresponds to the 10-90% range of the Fermi step.

Finally, the solution of the Dirac equation with such a potential gives the transmission coefficient of Dirac Fermions across the potential step :

$$T = 1 - \frac{sinh(\pi w \kappa^{+-}) sinh(\pi w \kappa^{-+})}{sinh(\pi w \kappa^{++}) sinh(\pi w \kappa^{--})} \tag{3.14}$$

With $\kappa^{ab} = k_t - k_i + a k_{tx} + b k_{ix}$, and $a, b = \pm 1$.

3.2.2.5 Comparing the transmissions

One can compare the angular dependent transmission of the different regimes in Fig. 3.7 : the abrupt junction (red lines, formula (3.6)), the smooth junction for $d = 50\,nm$ (green lines, formula (3.12)) and Cayssol's transmission (blue lines, formula 3.3) for $d = 20\,nm$. The incident medium has a fixed doping $p = 3 \times 10^{12} cm^{-2}$ hence the Fermi wavelength is $\lambda_F \approx 20\,nm$. The transmission medium has a varying algebraic doping $n = sign(E) \times E^2/(\pi\hbar^2 v_F^2)$. Therefore a negative n actually corresponds to a p-doping. In Fig. 3.7-a. $n > p$ and there is no critical angle. As a result, the total transmission of the junction after integration over all incident angles is large. In Fig. 3.7-b. $n < p$ and there is a critical angle around 45° above which the transmission is vanishing. This leads to a low total transmission. This effect can also be interpreted in term of mode number : the mode number increases with the doping, and going from a large number of modes to a low number of modes leads to a poor transmission.

Let us now focus on the sharpness dependence of the transmission. One can notice that for the sharp junction the transmission is always larger. Similarly, the 20 nm long junction used for Cayssol's formula leads to a larger transmission than the smooth formula with $d = 50\,nm$. As already mentioned, it results in a stronger focusing for smoother junctions. Nevertheless, the refraction effect of Dirac Fermions at a potential barrier is more dramatic when the junction is sharp: As seen in Fig. 3.7 the contrast for $T(\theta)$ between the $n > p$ and $n < p$ cases is much more pronounced for sharp than smooth junctions. This property highlights the importance for us to work with junctions as sharp as possible. With the objective of realizing tunable barriers for Dirac Fermions we want to be able to close it efficiently (using the focusing effect) but also to open it with a good transparency.

Finally, Fig. 3.7-c. shows $T(n, \theta_i)$ calculated with the Cayssol's formula with $d = 20\,nm$. Let us notice the $T \sim 1$ in the $n < 0$ regime. This illustrates the much higher transmission of a p-p' junction. However, when $|n| < p$ there still is a critical angle and the total transmission is not maximum.

3.2.3 Conductance of p-n junctions

In the ballistic regime, the conductance is given by the Landauer-Büttiker formula :

$$G = \frac{4e^2}{h} \frac{W k_{F1}}{\pi} \mathcal{T} \tag{3.15}$$

Where $\frac{4e^2}{h}$ is the conductance quantum (for graphene there are two valley and two spin degrees of freedom), $\frac{W k_{F1}}{\pi}$ is the number of conduction modes and $\mathcal{T}$ is the transmission

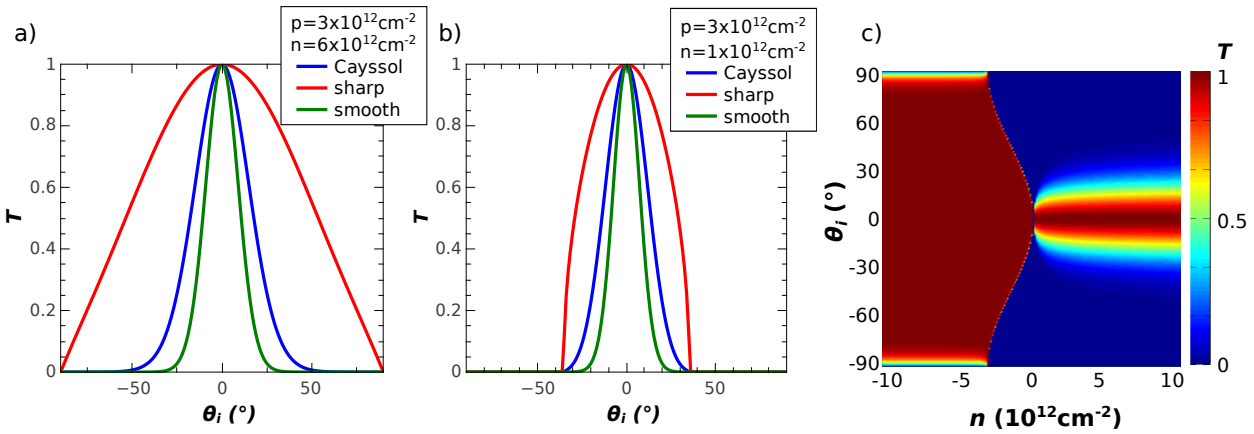

FIGURE 3.7: Angle dependent transmission of a p-n junction. The electron propagating in a medium doped at $p = 3 \times 10^{12} cm^{-2}$ is incident on a potential step with an angle θ_i and is transmitted into a n-doped medium. The transmission is calculated for an abrupt junction (red lines) a smooth junction with $d = 50\,nm$ (green lines) and using Cayssol's formula with $d = 20nm$ (blue lines). (a) $n = 6{\times}10^{12} cm^{-2} > p$ (b) $n = 1{\times}10^{12} cm^{-2} < p$. One can notice the presence of a critical angle in the case $n < p$ for which $T = 0$. (c) Color plot of $T(n, \theta_i)$ calculated with the Cayssol's formula and taking $d = 20\,nm$. Negative n values correspond in fact to a p-p' junction for which the transmission is ~ 1 for most angles.

of the junction. $\mathcal{T}$ is actually the total transmission obtained after integration of the angle dependant transmission $T(\theta_i)$ over all incident angles weighted by the angular density of states[2].

$$\mathcal{T} = \frac{1}{2} \int_{-\pi/2}^{\pi/2} \cos(\theta_i) T(\theta_i) d\theta \tag{3.16}$$

The total transmission $\mathcal{T}(n)$ and the junction conductance are plotted in Fig. 3.8, in the case of the Cayssol's formula with $d = 20nm$. One can notice the rather low transmission and conductance for the ambipolar junction ($n > 0$). Indeed, the conductance is mainly set by the smallest number of modes available in the unipolar regime : $\mathcal{T} \approx 1$ and the conductance is larger for $p = 3{\times}10^{12} cm^{-2}$ than for $p = 1{\times}10^{12} cm^{-2}$. Whereas in the p-n regime, the angle dependent transmission limits the conductance. Finally, Fig. 3.9 shows the junction length dependence of $\mathcal{T}$. For $p = 1 \times 10^{12} cm^{-2}$, the Fermi wavelength is larger than the junction length we can achieve with our fabrication techniques $d = 20nm$. This is the regime of sharp junctions where the transmission is rather large.

[2]Equivalent presentation: the Landauer formula reads $G = \frac{4e^2}{h} \Sigma T = \frac{4e^2}{h} \int_{-k_F}^{k_F} \frac{W}{2\pi} T(\theta_i) dk_y$ where the sum is over the transverse channels $k_y = k_F sin\theta_i$

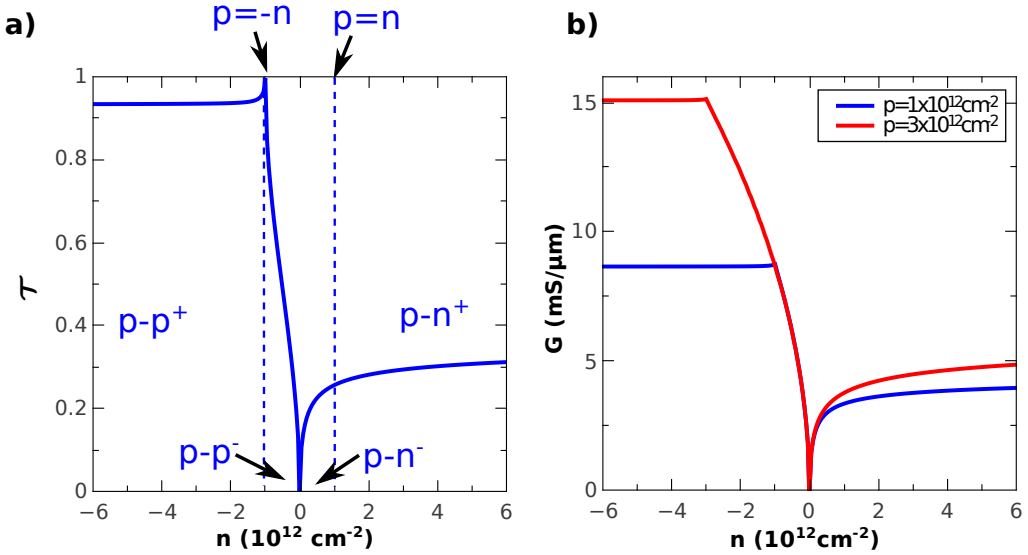

FIGURE 3.8: Total transmission (a) and conductance (b) of a p-n junction as a function of the algebraic doping $n = sign(E) \times E^2/(\pi\hbar^2 v_F^2)$ on the right side of the junction using Cayssol's formula with $d = 20nm$. The doping in the left area is set to $p = 1 \times 10^{12} cm^{-2}$ (blue line) and $p = 3 \times 10^{12} cm^{-2}$ (red line). One can notice the $\mathcal{T} = 1$ transmission when "$n = -p$". Four regions are identified by dotted lines in (a): the $p - p^+$ channel presents a large transmission, and the conductance is limited by the number of modes on the left side of the junction (p) ; the $p - p^-$ and $p - n^-$ are the regions where the transmission is limited by the low doping on the right side of the junction (n) ; the $p - n^+$ region corresponds to the Klein tunneling regime where the transmission is rather low due to the incident angle selection of the junction. Note that $n < -p$ and $n > p$ regions show relatively flat $T(n)$ and $G(n)$.

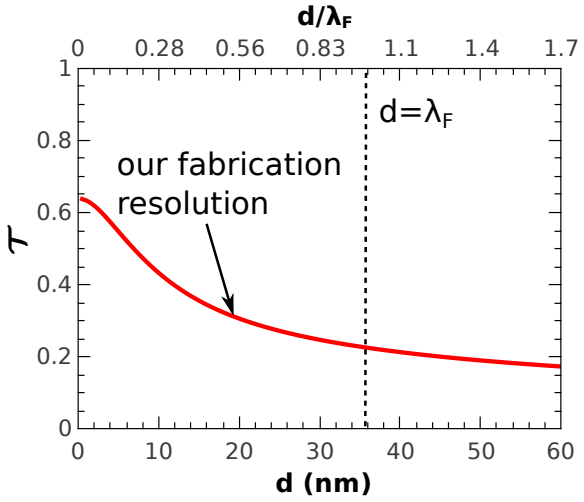

FIGURE 3.9: Effect of the junction length. The total transmission $\mathcal{T}$ is plotted as a function of the junction length d using Cayssol's formula. The doping is set to $p = 1 \times 10^{12} cm^{-2}$ and $n = 4 \times 10^{12} cm^{-2}$ (where the transmission is $\sim$ doping independent). The top axis d/λ_F gives a more general trend of the junction transmission (λ_F is given for the p region). For example, when p is increased, d/λ_F is increased as well and the transmission decreases.

3.3 The Klein tunneling transistor

By understanding the behavior of a simple p-n junction one can take advantage of this angle dependence to open and close the channel of a graphene transistor. We propose in this section a device geometry using the refractive effect of Dirac Fermions. We call that device the *Klein Tunneling Transistor* (KTT)[43]. An artist view of the KTT is shown in Fig. 3.10. The KTT consists of two junctions in series to make a p-n-p barrier. The doping p in the leads is fixed and n is varying. Working in the regime $p - n^+$ ($|n| > |p|$) the first junction has a relatively large transmission. It collects most of the incident electrons and focuses them. Therefore the role of the first junction is to select electrons close to $\theta_t = 0$. The second junction works in the regime $n^+ - p$ regime where total reflection can occur for oblique incidence. By tilting the second junction with respect to the first one, one enables reflecting most of the previously collimated electrons : their incidence angle is close to normal for the first junction but away from it for the second one.

The specific geometry we choose is the isosceles triangle. The base of the triangle is on the source side and the two other sides define the drain of the channel. The angle at the vertex is noted α. Intuitively one can say the best value for α is 45°. This specific angle maximises the chance of consecutive reflection on both faces. Imagine for example an electron normally incident on the basis, it is transmitted through the first junction and then has an incident angle of 45° on the second junction. It is completely reflected toward the other face of the second junction with again an incident angle of 45°. Finally, it is reflected back toward the source. A sketch of this is shown in Fig. 3.11-d for a more general case, where the incident angle is different from $\phi_1 = 0$

In the following we use Cayssol's formula to calculate the transmission probability across the junction. This is supported by the fact that a realistic junction will have a smoothness of roughly 20 nm which is not completely negligible beyond λ_F at any doping.

3.3.1 Transmission probability from scattering calculation

We use scattering theory to model the behavior of the KTT. We calculate the transmission probability of a triangular barrier and we deduce the corresponding transistor. Let us consider an electron incident from the source side of the device. It is characterized by a set of variables:

- The energy E_1 (which is equivalently defined by the wave vector $k_{F1} = E_1/\hbar v_F$ or the carrier density on the drain side p=k_{F1}^2/π)

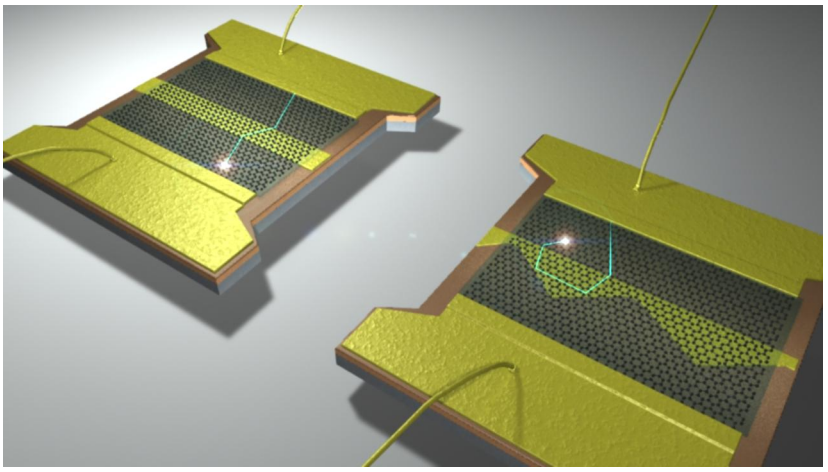

FIGURE 3.10: Artist view of the Klein tunneling transistor with its triangular gate (right) and a regular transistor with a rectangular gate (left). The trajectory of an electron is sketched on the figure to highlight the total reflection occurring in the triangular gate while the electron is transmitted through the rectangular gate.

- The y-intercept h of the electron incidence on the triangular potential on the source side.
- The incident angle ϕ_1.

The electron is then entering into the gated area and undergo consecutive reflections inside the gate area as pictured in figure 3.11-d. At each incidence on a side of the prism there is a change of trajectory and there is a probability for the electron to be transmitted outside of the prism. The trajectory is calculated using Snell-Descartes's laws. The transmission probability is calculated at each incidence using Cayssol's formula (3.3). We sum up intensities for each incidence to get both the total transmission toward the drain side and the total reflection toward the source side. We consider 20 reflections inside the prism which ensures a negligible probability for the electron to remain inside the prism.

Note that we sum up intensities and not complex amplitudes. This means that we neglect coherent effects and consider only a geometrical optic effect. It will be shown later with Green function simulations that coherent effects are indeed negligible.

Finally, assuming diffusive transport upstream of the barrier, the transmission probability is averaged over the all range of incident y-intercept h and incident angles (see (3.16)).

$$G = \frac{4e^2}{h}\langle T\rangle_{\phi_1,h} \tag{3.17}$$

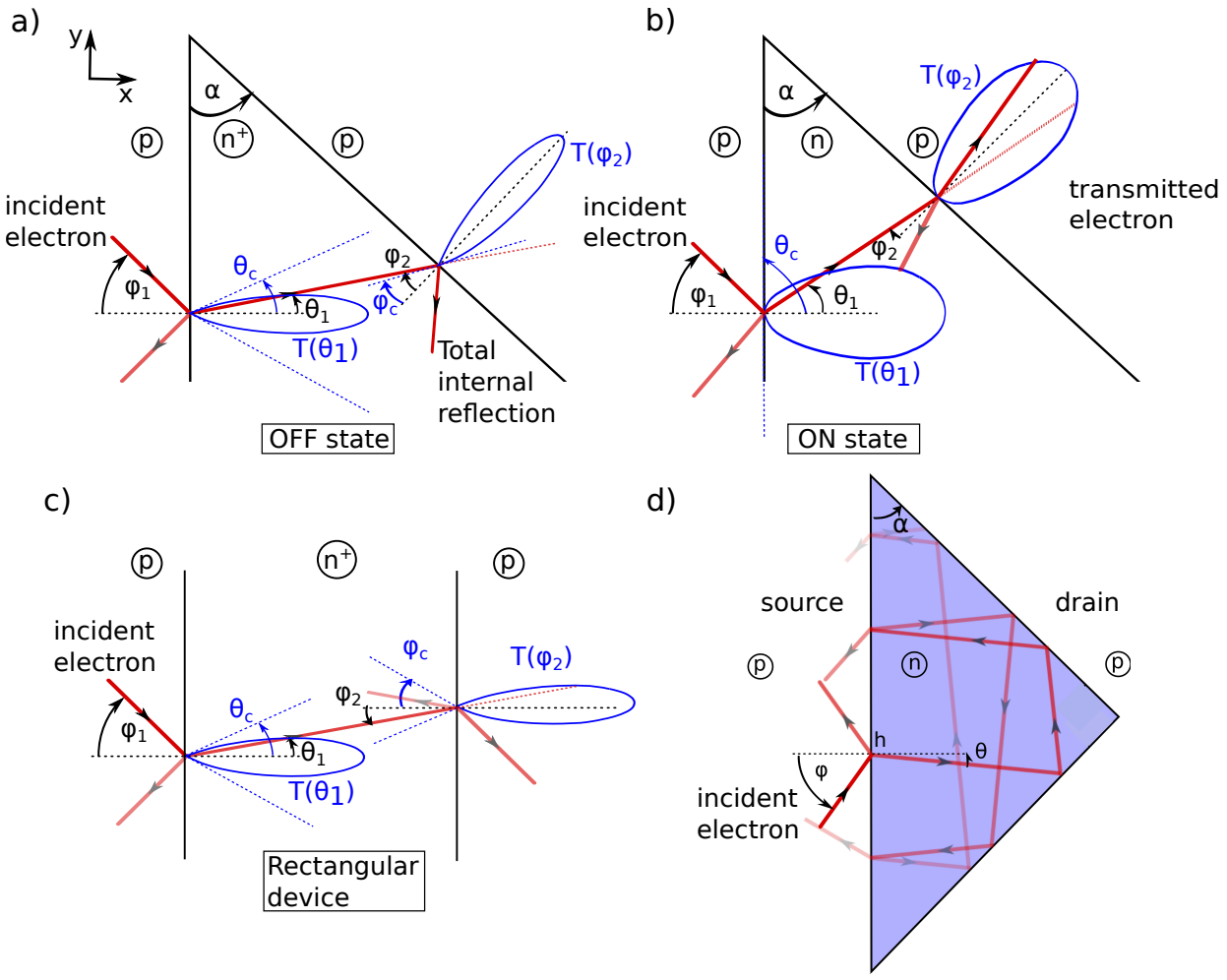

FIGURE 3.11: Electron trajectories (red lines) in the triangular gate area. (a) p-n^+-p regime. Regarding the first incidence on the p-n^+ junction: The optical index $\tilde{n}= -\sqrt{n/p}$ is large so the refraction is strong and the electrons are collimated. The blue lobe $T(\theta_1)$ represents the transmission amplitude as a function of the transmitted angle. θ_c is the critical angle over which no electrons are transmitted regardless of the incident angle. Regarding the second incidence at the n^+-p junction: The blue lobe $T(\phi_2)$ represents the transmission amplitude as a function of the incident angle. Here, most incident angles ϕ_2 are over the critical angle ϕ_c and there is no transmission. (b) p-n-p regime. The optical index is $\tilde{n}\sim -1$ so the transmission lobes are larger and the electrons can be easily transmitted through the two junctions. (c) Same situation than (a) but for a rectangular junction. The lobes are narrow but the electrons close to normal incidence are transmitted anyway. (d) Example of a computed electron trajectory with a number of 10 incidences.

The results of scattering calculations are plotted in Fig. 3.12. First of all, one can compare the conductance of a triangular barrier in the left panel of Fig. 3.12 with that of a rectangular barrier (Fig. 3.8). At low n, rectangular and triangular barriers show similar behavior up to $n \sim p$. Then, for the rectangular barrier the conductance saturates whereas for the triangular barrier a maximum is reached at $n \sim p$ followed by a reduction of the conductance. This decrease of $G(n)$ is a direct consequence of the refractive effects

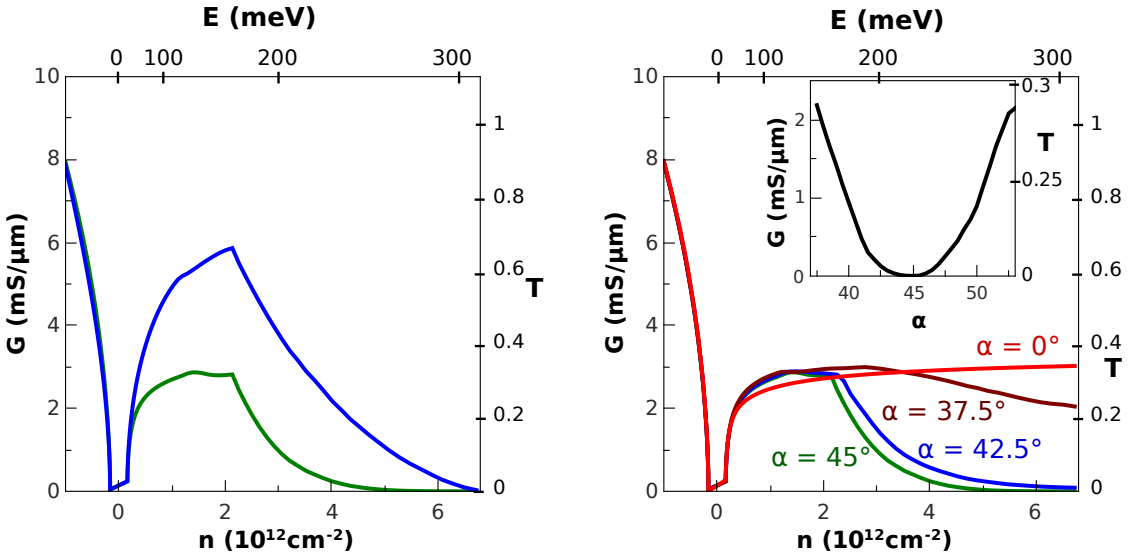

FIGURE 3.12: Results of the scattering calculations. Left: conductance and transmission of a triangular gate device with $d = 0$ sharp junctions (blue line) and $d = 20\,nm$ junctions (green line) respectively, with $p = 1 \times 10^{12}\,cm^{-2}$. We observe the refraction effect leading to a vanishing conductance at $n \sim 6 \times p$. Right: conductance and transmission with $d = 20\,nm$ junctions for different gate geometries, the opening angle of the prism varying from 45° to 0° (rectangular gate). Inset: conductance and transmission as a function of α for $n = 6 \times p$.

described above. Finally, the conductance completely vanishes at $n \sim 6 \times p$. The effect of the junction smoothness is shown as well : the same refractive effect is observed both for a $d = 0$ sharp junction (blue lines) and a $d = 20\,nm$ long junction (green line), the advantage of a sharper junction being to increase the ratio between the ON state at $n \sim p$ and the OFF state at $n \sim 6p$. The right panel of Fig. 3.12 shows the effect of the geometry of the triangular barrier. $G(n)$ curves are plotted for different prism angles α and in the inset one can see the $G(\alpha)$ at $n = 6p$. In accordance with our previous intuitive argument, we can say from the scattering calculations that the best geometry for the barrier is $\alpha = 45°$ (so it is a right triangle). Indeed, the vanishing conductance is quickly lost when α deviates from 45°.

3.3.2 Non equilibrium Green function simulations

The above description relies on the geometrical optics approximation where $\lambda_F << L$. In particular, diffraction effects are neglected and may drastically affect the total internal reflection. Besides, direct drain-source tunneling, dispersion effects arising from finite bias, as well as temperature effects have been neglected in the scattering approach. In order to quantify these effects, numerical simulations are performed by means of non-equilibrium Green function (NEGF) method.

The NEGF simulations have been performed by Salim Berrada, V Hung Nguyen and Philippe Dollfus at the Institute of Fundamental Electronics in Orsay. Their model is based on a tight binding Hamiltonian, giving a realistic description of graphene field effect transistors [68, 69]. In that model, the size of the sample is reduced compared to a realistic device in order to ensure reasonable calculation times. The transistor gate can be either rectangular or triangular to show the effect of geometry. For the rectangular gate, the simulated dimensions are $W = 80\,nm$, $L = 40\,nm$; and for the triangular gate they are $W = 80\,nm$, $L = 20 - 60\,nm$ which ensures a same gate area for both geometries. The junctions considered here are sharp ($d = 0$). The temperature is $300\,K$

The source side doping is set to $p = 2.3 \times 10^{12}\,cm^{-2}$. The NEGF simulation provides the transmission coefficient $T(\epsilon)$ through the device, ϵ being the carrier energy taking the zero energy reference at the charge neutrality point of the source. Two situations are considered : a low bias simulation $V_{ds} = 10\,mV$ (Fig.3.13-a and 3.14-a) allows direct comparison with (zero bias) scattering theory calculations as eV_{ds} is small compared to the Fermi energy ($E_F = \hbar v_F \sqrt{\pi * p} \simeq 0.15eV$). The high bias case is investigated for $V_{ds} = 200\,mV$ (Fig.3.13-b and 3.14-b) as eV_{ds} is larger than E_F. This case is more typical of transistor working conditions.

In Fig.3.13 $T(\epsilon)$ is displayed for the rectangular geometry (red lines) and the triangular geometry (blue lines) for the ON state $n \approx p$ of the transistor (dotted lines) and the OFF state $n \approx 6p$ (solid lines). In the ON state two minima of transmission appear corresponding to the CNP of the lead and the CNP of the barrier. The maximum of transmission lies between both CNPs, roughly at the Fermi energy of the lead, hence the current can flow through the device. In the OFF state, the barrier height is increased which means the CNP of the barrier is out of the range of Fig. 3.13. In the rectangular case a similar pattern to that of the ON state is expected with the exception that the transmission peak is broader and larger (not shown in the figure). For the triangular device, Klein tunneling effects take place at the asymmetric junctions and the transmission is strongly reduced around the Fermi level. As a consequence current is suppressed in the OFF state for a triangular transistor while it is increased for a rectangular transistor. In these figures, one should notice the oscillation of $T(\epsilon)$ for the rectangular device, it corresponds to the Fabry Pérot interferences inside the barrier. For the triangular device, oscillations are smaller, more complex but above all they are irrelevant for our model: they do not play any role in the geometrical refraction effect and they will be smoothed out by the integration. As a matter of fact we have neglected interference effects previously in the geometrical optics approach.

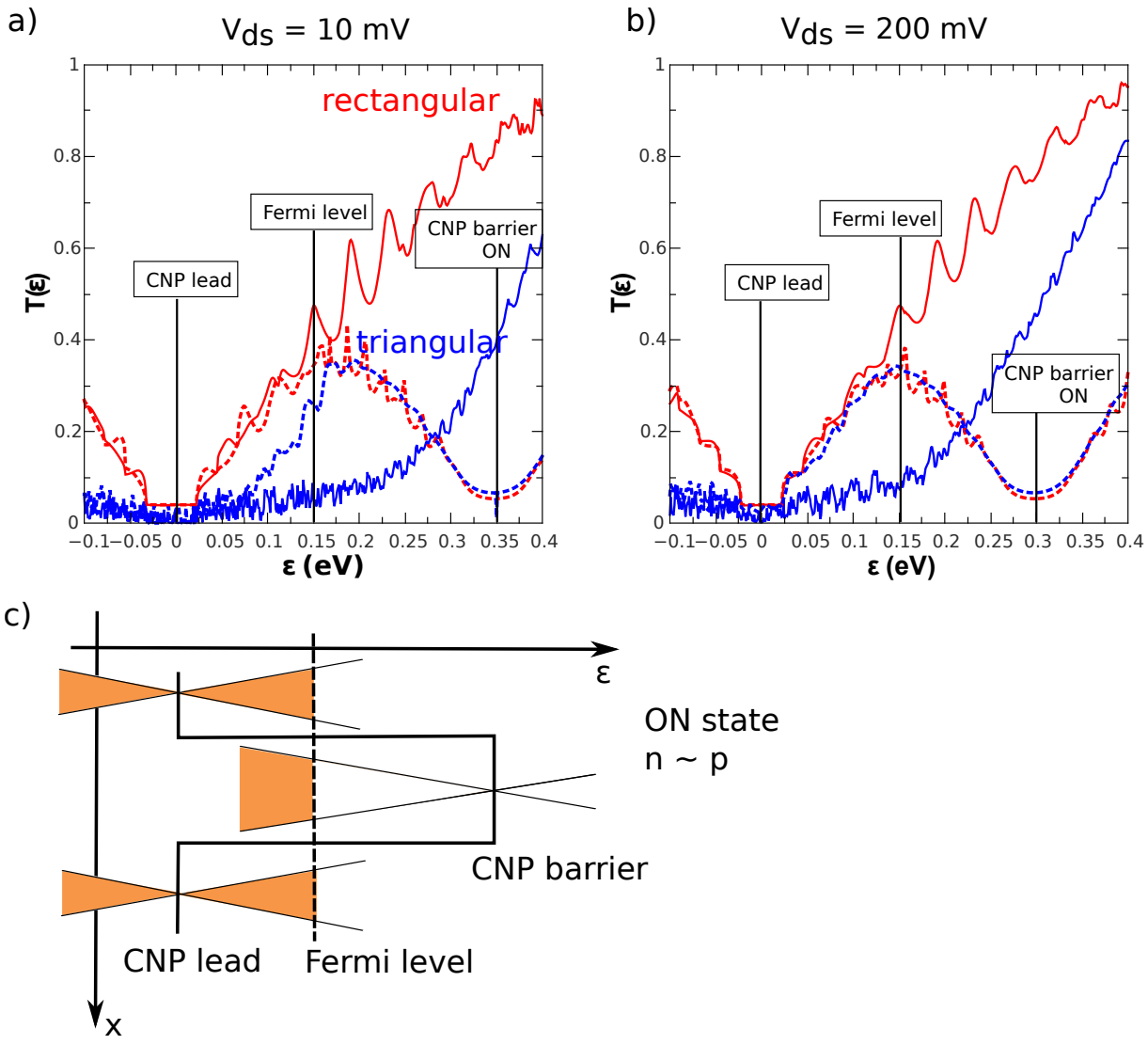

FIGURE 3.13: Transmission of the device from NEGF simulations as a function of the carrier energy ϵ for a given barrier height (from gate doping n) and a given Fermi level (p). We choose $\epsilon = 0$ at the CNP of the lead. Dotted lines (resp. solid lines) correspond to the ON state (resp OFF state). Red lines (resp. blue lines) correspond to the rectangular (resp. triangular) device. Panel (a) is for low bias ($10\,mV$), panel (b) is for high bias ($200\,mV$). They both show a similar transmission around the Fermi level in the ON state for rectangular and triangular devices while the transmission is suppressed in the OFF state for the triangular device only. (c) Band structure for the barrier in the ON state.

3.3.3 Results and interpretation

From the transmission, one can deduce the current flowing through the device with $I = \frac{4e^2}{h}\int_0^\infty T(\epsilon)(f_S(\epsilon) - f_D(\epsilon))d\epsilon$ where $f_S(\epsilon)$ (resp. $f_D(\epsilon)$) is the Fermi function for the source (resp. the drain). The current density I/W is shown in Fig. 3.14 as a function of gate doping n for rectangular (red line) and triangular (blue line) barriers. For the

sake of comparison, we also plot the results of scattering calculations for sharp junctions with dotted lines.

First of all we notice a close agreement between scattering theory and NEGF simulation for the rectangular barrier. Yet, only a qualitative agreement is obtained concerning the triangular barrier: the NEGF simulation clearly shows a transmission maximum around $n \sim p$ followed by a transmission decrease at higher densities, but without a total suppression of the OFF current. Nevertheless, the NEGF simulations show a better conductivity suppression with the refractive effect at high densities than at the Dirac Point where $\sigma_{min} \approx 4e^2/h$ (in the limit $W \lesssim L$ [13, 21]). In addition, the high bias ($V_{ds} = 200\,mV$) response is plotted in Fig. 3.14-b, and it also shows a suppression of the current at high densities. This result suggests that the Klein tunneling transistor could be used at high bias, for example as a high frequency amplifier.

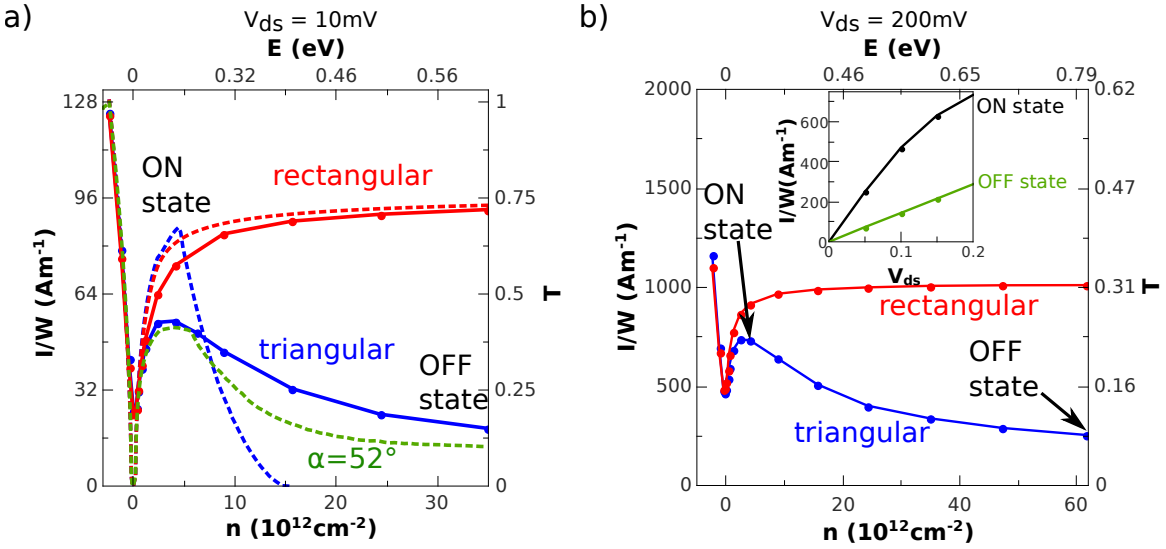

FIGURE 3.14: Influence of the barrier doping n on the current density I / W (and corresponding total transmission T) for (a) Vds = 10 mV and (b) Vds = 200 mV. Solid lines (resp. dotted lines) correspond to NEGF simulations (resp. scattering calculations), red lines (resp. blue lines) correspond to the rectangular (resp. triangular) device. In panel (a) the scattering calculation for the rectangular device with sharp junctions (red dotted line) is in good agreement with NEGF. The scattering calculation for the triangular device with a smooth junction $d = 10nm$ and opening angle $\alpha = 52°$ (green dotted line) is a way to take into account diffraction effects and compares well with NEGF simulations (blue solid line). Panel (b) inset: IV_{ds} characteristics of the triangular transistor in the ON state $n = 2 \times 10^{12} cm^{-2}$ (black line) and in the OFF state $n = 6 \times 10^{13} cm^{-2}$ (green line).

We attribute the disagreement between scattering calculations and NEGF simulation to diffraction effects. As a matter of fact, the NEGF simulations consider electronic waves which are sensitive to diffraction while the scattering approach stays within the geometrical optics approximation where all dimensions are large compared to the Fermi wavelength. Moreover, the NEGF simulation is performed here on a relatively small

device, the typical dimension is $L = 60\,nm$, whereas the typical wavelength at $n \sim 10\times10^{12}cm^{-2}$ is $\lambda_F \sim 10nm$. Therefore we expect a blurring on the order of $\lambda_F/L \sim 15\%$ of the geometrical angles. A way to estimate the diffraction effect with the scattering approach is to apply an uncertainty on the order of λ_F/L on the prism geometry. This is illustrated by plotting in Fig. 3.14 (green dotted line) the transmission of the triangular barrier calculated with an opening angle $\alpha = 52°$ which is a difference of 15% compared to the ideal $\alpha = 45°$; it follows roughly the numerical simulations comforting us in that interpretation.

3.3.4 Discussion

Scattering calculations and NEGF simulations represent two extreme cases between the macroscopic and the nanometric Klein tunneling transistor. In fact, the size of an actual device is size limited by the mean free path. Let us try to estimate the properties of a realistic device: Taking the state of the art hBN encapsulated graphene devices, the mean free path is on the order of 1 μm [8] at room temperature, therefore we choose $L = 500\,nm$. We set a lower doping $p \sim 0.5 \times 10^{12}\,cm^{-2}$ which gives an operating point at $n \sim 6p \sim 3 \times 10^{12}\,cm^{-2}$, thus $d \lesssim \lambda_F \sim 20 - 50\,nm << L$ satisfying the requirements for DF optics. In order to give a rough estimate of the KTT conductance with those parameters we simulate a gate with an opening angle of $\alpha = 43.2°$ (corresponding to $\lambda_F/L \sim 4\%$ in the gated area). It gives an ON/OFF ratio of ~ 50 and a minimum conductivity $\sigma_{min} \sim 3 \times 10^{-5}S$ below Dirac point conduction $4e^2/h \approx 1.5 \times 10^{-4}S$.

Still using those parameters we can evaluate the radio frequency (RF) properties of such a transistor. For the definition of the RF figures of merit, the relevant references and a related discussion the reader can refer to chapter 6. Considering a $10\,nm$ hBN dielectric thickness (thus the gate capacitance is $C_g = 3.7fF/\mu m^2$) we estimate the bias dependence of the transconductance per unit width $g_m V_{ds}^{-1}/W \approx 7mS\mu m^{-1}V^{-1}$, the voltage gain $AV_{ds}^{-1} = g_m V_{ds}^{-1}/g_{ds} \approx 3$ and the transit frequency $f_T V_{ds}^{-1} = g_m V_{ds}^{-1}/W/(2\pi C_g L) \approx 600\,GHzV^{-1}$, which compares very well with the state of the art graphene RF transistor. The maximum oscillation frequency f_{max} is more difficult to estimate (see equation (6.20)), but roughly, a 5-fold improvement in the conductance suppression should lead to a $\sqrt{5}$-fold improvement in f_{max}. The latter should be the most interesting feature of the KTT.

3.4 Conclusion and perspective

In this chapter we have presented a graphene device, the Klein Tunneling Transistor, whose working principle is based on the refractive properties of the graphene charge carriers at a potential barrier, to realize a tunable electrostatic barrier for Dirac fermions. We have used two distinct approaches: scattering calculations based on the geometrical optics approximation and non equilibrium Green function simulations, that give consistent results.

This device architecture could be used for quantum confinement, for example to achieve a single Dirac fermion pump for quantum optics experiments. It is also suited for microwave electronics.

Still, the fabrication of such a device is very demanding and we were not able to realize it yet. Our main issue was the rather low mobility ($3-10\times10^3 cm^2/V/s$) achievable with our fabrication techniques whereas one needs at least a mobility of $20\times10^3 cm^2/V/s$ to see the refractive effect. A possible solution is to use the hBN encapsulation of graphene with the Van-der-Waals pick up technique. However, this technique requires uncertain edge contacts with large contact resistances.

Let us notice that we focused our presentation on a double gate device for a full barrier tunability, but the triangular shape could be given by the contacting metal itself. The carrier density of the contacted graphene would be set by the doping from the metal while a local gate would tune the carrier density of the triangular channel. The next chapter will show how the doping of the contacted graphene can be tuned as well.

Chapter 4

A gated graphene contact

The physics of the contact between a metal and a semiconductor has been a major subject in the development of modern electronics, and it is still of great importance for both fundamental and technological issues. With the emergence of new 2D materials, the contact physics has to be revisited. From the scientific point of view first, the metal-graphene contact raises very interesting questions as its properties are intermediate between a semiconductor-metal contact and a metal-metal contact. Besides, the 2D nature of graphene strongly affects the usual screening that takes place near an interface. As a result, the contacting metal induces a doping in graphene beneath the metal, and there is a doping step building up at the contact edge. The direct consequence of this potential barrier is a relatively large contact resistance which is a major drawback for graphene electronic applications. Particularly, it is of high importance for radio frequency (RF) devices. Indeed, a graphene RF transistor should have a short channel to reach higher frequencies, but in that case, the channel contribution to the resistance becomes smaller than the contact contribution. Consequently, the total current modulation is reduced. The regime where contact dominates is called the "scaling limit" [70]. Reducing the contact resistance allows to push the scaling limit toward smaller scales and higher frequencies accordingly. Considerable efforts have been devoted in the community to determine what should be the "right" contacting metal and how it should be deposited, but no consensus has been reached yet.

Regarding now Dirac Fermion optics, we explained in the previous chapter how to take advantage of sharp potential steps in graphene to exploit the refractive effect of Klein tunneling. Dealing with a real device implies having some contacts on graphene, meaning that one already starts with at least two junctions. But above all we can use those *contact junctions* as the building blocks of Dirac Fermion optics devices. For that we exploit a singularity coming from the 2D nature of graphene: due to the absence of screening, the

Fermi level of contacted graphene is not pinned as it would be for a 3D conductor. This means there is room for an electrostatic tuning of the graphene doping level. The aim of this chapter is to present a new device architecture where a local gate is located just below the contact in order to tune the carrier density of the contacted graphene, another local back gate being dedicated to the channel. The spacing between both gates is kept as small as possible to induce a sharp junction between contacted graphene and graphene in the channel. Working with high mobility graphene and local back gates allows us to tune the carrier density on both sides of a sharp junction in the ballistic regime, thus we can use the model presented in the previous chapter to describe this junction. I start by quickly introducing the metal-graphene contact and reviewing the state of the art of low contact resistances. In a second part I present a theoretical description of how the carrier density of contacted graphene can be modulated despite the screening from the metal followed by a review of experimental works bringing evidences of contact tunability. Then I show the experimental results obtained with our new architecture first for a short channel device with exfoliated graphene on hBN, second for devices with CVD graphene on hBN.

4.1 The graphene contact

4.1.1 What is a metal-graphene contact

The contact between a metal and a 3D semiconductor induces a charge flow to equilibrate the Fermi levels on both sides of the metal-semiconductor junction. The relative shift of the semiconductor Fermi level is on the order of the difference between the two work functions. As a result there is a charge accumulation on both sides of the junction that may induce a depletion region in the semiconductor. This effect is known as the Schottky barrier. Then one has to solve the Poisson's equation to determine the length of the depletion region. Eventually, far from the contact, the Fermi level retrieve its initial position [71]. By contrast, in a metal-metal contact there is a larger carrier density and the electrons can screen efficiently the potential difference at the interface.

A major difference for graphene arises from its 2D nature: in the direction perpendicular to the graphene surface there is no charge that can screen the potential step at the interface. Horizontally, the graphene-metal contact is intermediate between the metal-metal and the semiconductor-metal cases. On one hand there is no bandgap in graphene so there is no depletion layer and thus no Schotkky barrier taking place at the interface. On the other hand, graphene has a small density of states and the charge exchange with the metal induces a shift of the Fermi level position. As a result, the graphene carrier

density is modified in the contact's vicinity. In an electronic transport experiment, the current flows in the graphene layer between two metallic electrodes. If there is a different carrier density in the contact area and in the bulk graphene then there is a junction at each contact. Depending on the work function difference between the metal and the graphene, the metal induced carrier density can be either n or p. Then, depending on the graphene sheet doping one can either have an unipolar or a bipolar junction at the contact, and a bipolar junction is more resistive than an unipolar one (as explained in the previous chapter).

This effect has been widely observed when measuring a graphene device resistance as a function of the gate voltage: the gate voltage tunes the bulk graphene carrier density from p to n while in the contact area the carrier density is pinned by the metal. This results in asymmetric transfer curves [13, 72, 73].

From a geometrical point of view, the above considerations suggest that the contact resistance is inversely proportional to the width of the contact but should be relatively independent of the contact length. It has been experimentally demonstrated that indeed the contact resistance is not proportional to the contact surface area but to its width, providing that the contact length is greater than $\sim 1\mu m$ [74]. As a result the contact resistance is always expressed in $\Omega\mu m$.

4.1.2 Imaging the contact

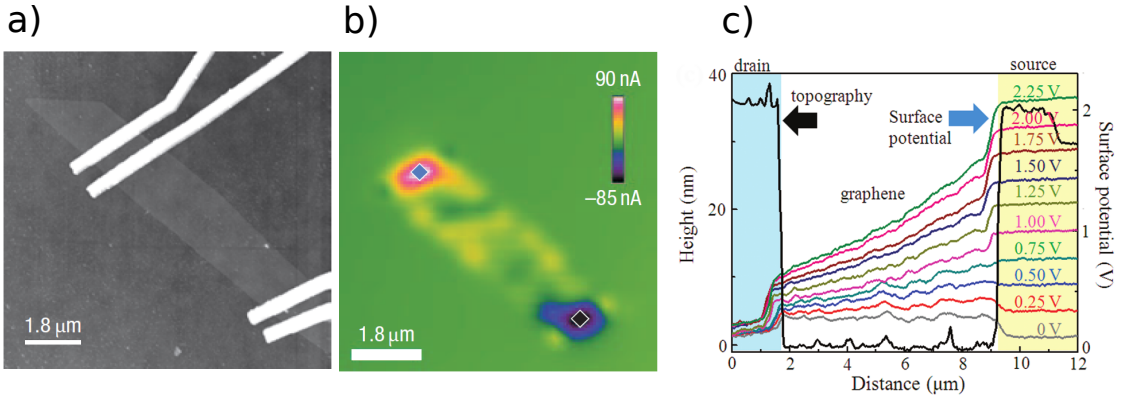

FIGURE 4.1: (a) Optical image of a contacted graphene flake (b) Photocurrent scanning experiment on the corresponding device. One can notice a much stronger current next to the contacts. Moreover, the current is reversed from one contact to another. This indicates the presence of a built in electric field between the free graphene area and the contacted area. Adapted from [25]. (c) Scanning Kelvin probe microscopy (SKPM) for a mapping of the graphene work function in the channel of a transistor, here for different drain-source voltages. One can notice the potential steps at the contacts that make the contact resistance visible. Here we also see the potential variation in the channel at high bias. Adapted From Yu et al. [75].

To provide a visual support of the metallic contact induced doping we show in Fig. 4.1 experiments that map the doping profile of graphene near a contact. Scanning photocurrent experiments efficiently detect potential steps in graphene. This technique was used to study the metal-graphene contact junction [25, 76]. Those experiments have shown the presence of a strong electric field close to the contact that corresponds to a doping difference between the bulk graphene and graphene in the contact area (see Fig. 4.1). According to photocurrent experiments [25, 76], the length of the p-n junction at the contact would extend over at least 100 nm. This result presents a strong contrast with our own findings. The contact junction is probably reduced in the case of local gating of the channel which is the very idea of our device. In addition the use of a bottom gate allows us to reduce the ungated access area of the channel. Similarly, the electric potential of graphene in the channel and around the contact can be scanned using a scanning Kelvin probe microscopy (SKPM). An illustration [75] is shown in Fig. 4.1. It also shows a potential step when approaching the contact, and the step length seems to be on the order of 100 nm.

4.1.3 A quest toward low contact resistance

A large contact resistance is a performance killer for future graphene devices. Therefore, many routes to lower the contact resistance have been explored. The first parameter to tune is of course the metal itself, but for the same metal the contact resistance values vary from one sample to another. Thus, the process conditions, (type of resist, metal deposition technique...) matter as well. Without claiming to be exhaustive, we summarize some low contact resistance achievements in table 4.1.3. In [77] for example, the authors claim an improvement of 40% in the contact resistance when graphene is encapsulated between a top and a bottom contact.

Our route is to tune the contact induced carrier density with a local gate in order to reduce in situ the resistance of the contact junction.

Author	*metal*	*contact type*	*temperature* K	R_c $\Omega\mu m$
Xia [78]	Pd	top	6	110
Xia [78]	Pd	top	300	185
Xia [79]	Ti	top	300	430
Zhong [80]	Pd	top	$78-300$	100
Sordan[a]	Au	top with holes	300	90
Franklin [77]	Ti/Pd $(0.5/30nm)$	top and bottom	300	260
Wang [8]	Cr/Pd $(1/15nm)$	edge contact	$4-300K$	140
Meric [14] rf	Pd	top	300	950
This work	Pd	top	300	$150-300$
This work	Pd	top	10	$75-100$

TABLE 4.1: State of the art contact resistance. [a]private communication.

4.2 Theory of contact gating

When metal and graphene are brought into contact, there is a charge exchange to achieve a chemical and electrostatic equilibrium. As a result, there is a balance between the electrochemical potential of graphene and that of the contacting metal. However, the density of states in the metal is much larger than in graphene, thus the metal acts as a reservoir that sets the electrochemical potential μ^*, which is determined by the work function W_m and the potential V_m of the contacting metal as:

$$\mu^* = -W_m - eV_m \tag{4.1}$$

By gauge invariance we can set $V_m = 0$. The electrochemical potential of graphene follows that of the metal, resulting in a shift of its Fermi Level as well as its electrical potential. We note $\Delta E_F = E_F - E_{Dirac}$ the Fermi energy shift with respect to the Dirac point E_{Dirac}. It is related to the carrier density n by $n = sign(\Delta E_F)\frac{\Delta E_F^2}{\pi\hbar^2 v_F^2}$. Then V_{gr} is the electrostatic potential of graphene and W_{gr} is the work function of intrinsic graphene. Close to the contact, the equality of electrochemical potential reads (see also Fig. 4.2):

$$\mu^* = -W_m = -W_{gr} + \Delta E_F - eV_{gr} \tag{4.2}$$

Away from the contact, V_{gr} and ΔE_F re-equilibrate to reach $\Delta E_F = 0$ (neutrality) and $V_{gr} = 0$, when graphene is naturally undoped, as depicted in Fig. 4.2. Therefore we have in the channel $\mu^* = -W_{gr}$. By contrast, using an electrostatic gate allows a full control of the doping profile (Fig. 4.2).

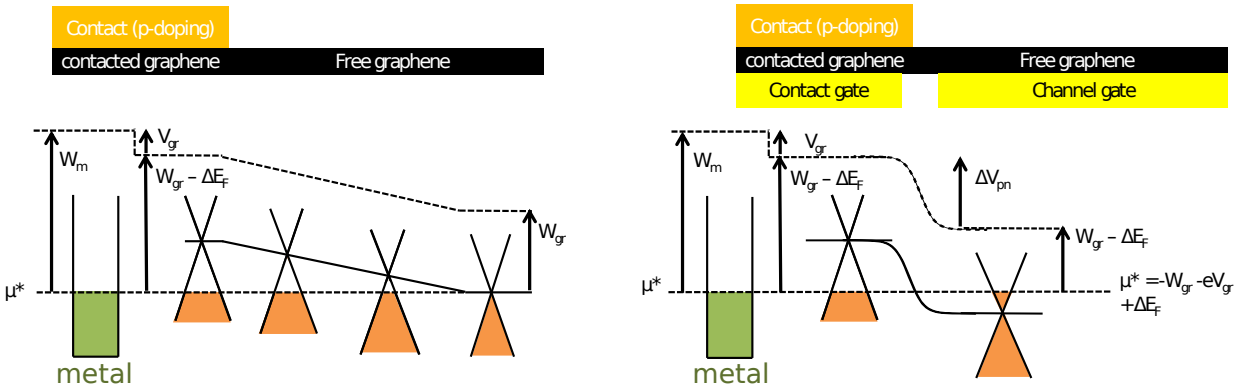

FIGURE 4.2: Graphene doping profile at the metal graphene interface. *Left*: Long screening length in the absence of gating (100 *nm* according to [76]). *Right*: The contact gate controls the contact doping thanks to the absence of vertical screening and the channel gate sets the channel doping. The p-n junction length between contact and channel areas is controlled by the gate geometry.

In this section, we start by describing the field effect doping of graphene in the channel. In particular we emphasize the difference between local and remote gating. Then, we present how one can use field effect to control the carrier density of contacted graphene.

4.2.1 Graphene gating

We consider a gate electrode separated from graphene by a thin hBN flake of thickness t_{BN}. In the standard classical picture, this gate just acts as a plate capacitor that sets the charge (thus the carrier density n) of graphene, the charge carriers being provided by the contact (therefore essential for the gating effect):

$$n = \frac{C_g(V_g^0 - V_{DP})}{e} = \frac{CV_g}{e} \tag{4.3}$$

Where $C_g = \epsilon_0\epsilon_{BN}/t_{BN}$ is the parallel plate capacitance per unit area, $V_g = V_g^0 - V_{DP}$ is the gate voltage measured from Dirac Point (DP), i.e. V_{DP} is the gate voltage one has to apply to induce a charge neutrality in graphene. The fact that in most cases $V_{DP} \neq 0$ results from the presence of chemical doping, for example lithography resist residues, but in the case of graphene with free surface, it can also arise from molecular adsorption. We should point out that the experimental V_{DP} varies a lot from one sample to another and within the same sample it varies throughout the measurement history. Those impurities can be removed by thermal or current annealing of the sample. Our process usually induces a p-doping ($V_{DP} > 0$), but after efficient cleaning we usually recover $V_{DP} \approx 0$.

In fact, formula 4.3 is an approximation that does not take into account the finite (and small) density of state of graphene near the Dirac point. For the sake of simplicity we will take as a reference of electrochemical potentials:

$$\mu^* + W_{gr} = \Delta E_F - eV_{gr} = 0 \tag{4.4}$$

This is true far away from the contact for a clean graphene sheet. We will deal with graphene close to a metallic contact in the next section.

From Gauss' theorem we obtain the electrostatic relation between the charge on graphene and the voltage across the gate dielectric[1]:

$$C_g(V_{gr} - V_g) = ne = -sign(E_F)e\frac{\Delta E_F^2}{\pi\hbar^2 v_F^2} \tag{4.5}$$

Then combining (4.5) and (4.4) one obtains:

$$C_g(\Delta E_F - eV_g) = -sign(E_F)e^2\frac{\Delta E_F^2}{\pi\hbar^2 v_F^2} \tag{4.6}$$

Defining a characteristic energy ϵ_c,

$$\epsilon_c = \frac{C_g\pi\hbar^2 v_F^2}{2e^2}, \tag{4.7}$$

Eq. (4.6) becomes:

$$sign(\Delta E_F)\Delta E_F^2 + 2\epsilon_c\Delta E_F - 2\epsilon_c eV_g = 0 \tag{4.8}$$

Whose solution is:

$$\Delta E_F = sign(eV_g) \times \epsilon_c\left(\sqrt{1 + 2\frac{|eV_g|}{\epsilon_c}} - 1\right) \tag{4.9}$$

Two regimes can be considered:

- The high doping regime $|eV_g| >> \epsilon_C$, where

$$\begin{aligned}\Delta E_F &= \epsilon_C\sqrt{2\frac{|eV_g|}{\epsilon_c}} \\ &= \hbar v_F\sqrt{\pi\frac{C_g V_g}{e}},\end{aligned}$$

[1] If $\Delta E_F > 0$ then the doping is n, meaning that the charge on graphene is negative. It corresponds to a gate voltage $V_g > 0$.

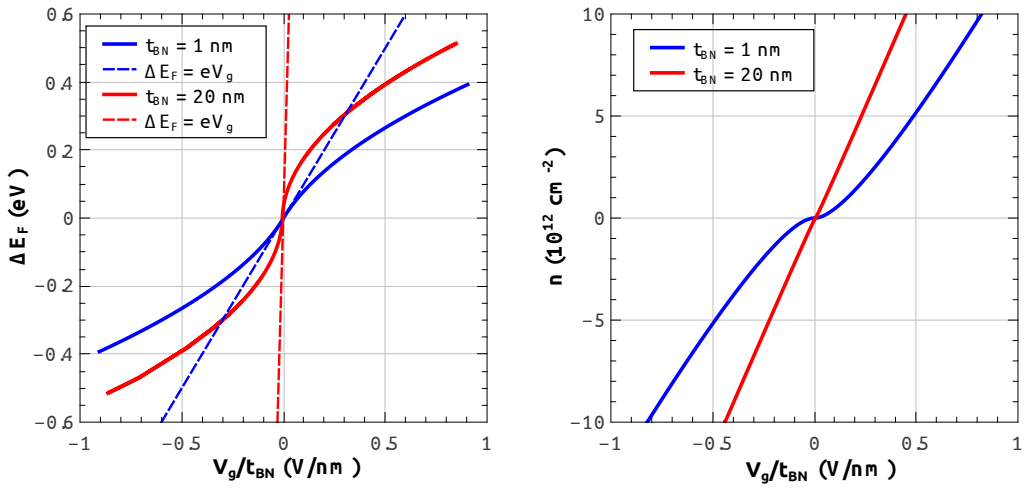

FIGURE 4.3: Simulated Fermi level (left) and carrier density (right) as a function of the gate induced electric field in the limit of very thin dielectric thickness (blue curves) and for larger dielectric thickness (red curves). The range over which the dotted lines and the ΔE_F curves overlap defines the unscreened regime where $|eV_g| << \epsilon_c$

and

$$n = \frac{\Delta E_F^2}{\pi \hbar^2 v_F^2} = \frac{C_g V_g}{e}. \tag{4.10}$$

We retrieve the capacitor plate formula of Eq. (4.3) of the classical metallic regime.

- The low doping regime where $|eV_g| << \epsilon_c$

$$\Delta E_F \simeq eV_g \tag{4.11}$$

Therefore, in that regime, the gate directly sets the chemical potential of graphene. This is the so called quantum capacitance regime [26, 81, 82].

We notice that ϵ_c represents the screening energy scale of the system. In the $|eV_g| << \epsilon_c$ regime there are too few electrons to screen the electric field of the gate and graphene is transparent from the electrostatic point of view. In that case, the chemical potential just follows the gate electrostatic potential. This regime is experimentally accessible in the case of very thin gate dielectric as $\epsilon_c \propto C_g \propto 1/t_{BN}$. On the contrary, when $|eV_g| >> \epsilon_c$, the graphene electrons can efficiently screen the electric field from the gate, and the graphene acts as a metallic plate of a capacitor. The evolution of ΔE_F and n in both regimes is shown in Fig. 4.3. We plot them as a function of the gate induced electric field (instead of the usual gate voltage). Therefore, the difference between the red and blue curves in Fig. 4.3 illustrates the effect of the screening constant ϵ_c. In the case $t_{BN} = 20\,nm$, we have $\epsilon_c = 7\,meV$ and the plate capacitor approximation is almost always valid. On the contrary, if $t_{BN} = 1\,nm$, we have $\epsilon_c = 150\,meV$ and we clearly see

the regime where $\Delta E_F \simeq eV_g$. As a result we get a carrier density and a Fermi level lower than the one expected from a classical model. In particular, one can see that the gate has only a very poor control on the carrier density close to the Dirac point.

This crossover can be seen in a capacitance measurement from which one can deduce the quantum capacitance [26, 81, 82]. Indeed, the quantum capacitance is a direct measure of the density of states as it is described below. This approach where the total gate capacitance is modelled as the geometrical capacitance in series with the quantum capacitance C_Q, is strictly equivalent to the approach shown above. First the quantum capacitance is defined (at $T = 0$) as:

$$C_Q = \frac{2e^2 \Delta E_F}{\pi \hbar^2 v_F^2} = \frac{C_g \Delta E_F}{\epsilon_c} \tag{4.12}$$

And the carrier density is evaluated using the capacitor plate model with the total capacitance $C_t = \frac{C_Q C_g}{C_Q + C_g}$:

$$n = \frac{C_Q C_g}{C_Q + C_g} \frac{V_g}{e} = \frac{\Delta E_F}{\Delta E_F + \epsilon_c} \frac{C_g V_g}{e} \tag{4.13}$$

Replacing n by its energy formulation leads to formula (4.8).

We note that ϵ_c essentially depends on C_g. For a typical BN thickness of 10 nm we get $C_g = 3.5\, fF/\mu m^2$ and $\epsilon_c = 15\, meV$ which is small compared to the energy resolution of our measurements. Indeed the addition of the temperature ($\approx 25\, meV$ at room temperature) and the typical residual density from impurities (also $\approx 25\, meV$) are combining to make the quantum capacitance effect negligible for the channel of a transistor. On the other hand this effect is observable in a graphene contact as described in the following section.

4.2.2 Contact gating

In this part I present a model that explains how the carrier density of contacted graphene can be tuned by field effect. It relies on two very basic principles (electrochemical equilibrium and Maxwell-Gauss equation) and has been introduced for the first time by Giovannetti et al. in 2008 [83]. This model was supported by ab-initio calculations and was followed by a more detailed paper [84] on this subject. Let now us focus on the contact area where ΔE_F can be affected by the presence of the metal. We recall the equality of electrochemical potentials:

$$\mu^* = -W_m = -W_{gr} + \Delta E_F - eV_{gr} \tag{4.14}$$

At first sight one could think that a perfect contact imposes its electrostatic potential as well as its chemical potential. In that case the Fermi level $\Delta E_F = W_m - W_{gr}$ would be pinned by the contact.

If we consider now that only the electrochemical potential is set by the contact and that the balance between ΔE_F and V_{gr} is free to change, we can improve the previous equation but now by replacing $V_{gr} = (-W_{gr} + \Delta E_F + W_m)/e$ in (4.5). This is equivalent to replacing V_g by $eV_g - (W_m - W_{gr})$. We see that we expect a shift in the CNP gate voltage given by the difference in work functions between graphene and metal. For example for Pd, $W_{Pd} - W_{gr} \approx 5.5 - 4.5\,eV = 1\,eV$, one should apply $+1\,V$ on the gate to compensate the doping by the contact. In other words, graphene is naturally p-doped around Pd. On the other hand, for Al, $W_{Al} - W_{gr} \approx 4.0 - 4.5\,eV = -0.5\,eV$, graphene is naturally n-doped. However, this simple description is not complete; first it neglects screening effects from the contact which depend strongly on the distance between metal and graphene. Secondly, Giovannetti et al. have shown that there is a metal-graphene chemical interaction in addition to the work function difference [83]. From now on we will note ΔW the effective work function difference between metal and graphene that includes this chemical interaction.

We follow the work by Giovannetti to understand the metal-graphene contact. A metal-graphene interface is described as a tunnel junction, where charges can flow through an ideally small resistance R_{mg} in parallel with a large capacitance C_{dl}. This simple model explains well how the equality of electrochemical potentials does not lead to equality of electrostatic and chemical potential necessarily. Indeed, even if charges can flow through the junction there is still a charge accumulation on both sides of that junction that forms an electrical double layer over a microscopic distance t_{dl} and sets the value of the capacitance $C_{dl} = \epsilon_0/t_{dl}$. As a result there is a built-in potential drop across the junction that is sensitive to field effect and that can be tuned by a gate. Let us consider a graphene area which is just underneath the metallic contact. We note C_{cont} the geometrical capacitance per unit area of the gate devoted to the contact (the value of the capacitance is the same as before since the dielectric thickness is unchanged). The electrostatic relation reads:

$$C_{cont}(V_{gr} - V_g) + C_{dl}(V_{gr} - V_m) = ne = -sign(E_F)e\frac{\Delta E_F^2}{\pi\hbar^2 v_F^2} \tag{4.15}$$

That has to be combined with

$$\Delta W = -\Delta E_F + eV_{gr} \tag{4.16}$$

to give

$$\Delta W + \Delta E_F - \frac{C_{cont}}{C_{cont}+C_{dl}} eV_g = -sign(E_F)e^2 \frac{\Delta E_F^2}{\pi\hbar^2 v_F^2 (C_{cont}+C_{dl})} \tag{4.17}$$

The characteristic energy constants of the system are:

$$\epsilon_c = (C_{cont}+C_{dl})\frac{\pi\hbar^2 v_F^2}{2e^2}, \tag{4.18}$$

and,

$$\epsilon_W = \frac{C_{cont}}{C_{cont}+C_{dl}} eV_g - \Delta W \tag{4.19}$$

That leads to

$$sign(E_F)\Delta E_F^2 + 2\epsilon_c \Delta E_F - 2\epsilon_W \epsilon_c = 0 \tag{4.20}$$

And finally

$$\Delta E_F = sign(\epsilon_W) \times \epsilon_c \left(\sqrt{1 + 2\frac{|\epsilon_W|}{\epsilon_c}} - 1\right) \tag{4.21}$$

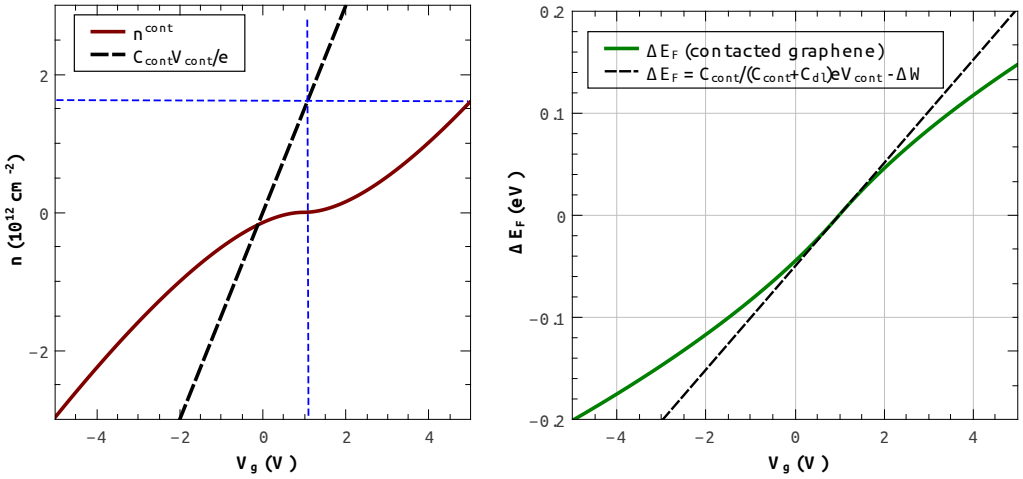

FIGURE 4.4: Calculated ΔE_F and n^{cont} as a function of the gate voltage V_{cont} in the case of contacted graphene with a work function difference $\Delta W = 50\,meV$ and a metal-graphene distance $t_{dl} = 0.2\,nm$ (and a gate capacitance calculated with $15nm$ BN thickness)

This formula is similar to (4.9). However in addition to the gate voltage shift due to ΔW we should emphasize that ϵ_c can be very large due to the large value of the double layer capacitance C_{dl}. Consequently the screening by a metallic contact is much stronger than in the channel. If we take a typical graphene-metal separation distance $t_{dl} = 0.3\,nm$ from Giovannetti's ab initio calulations, we find $C_{dl} = 30 fF/\mu m^2$ while the geometrical capacitance is $C_g = 3.5\,fF/\mu m^2$. Therefore we end up with $\epsilon_c = 136\,meV$. Then ϵ_c has

to be compared with ϵ_W which is also controlled by the ratio C_g/C_{dl}. Both effects work together to put the graphene area under the contact in the unscreened regime for a wide range of gate voltages. This can be seen in Fig. 4.4 where the calculated density n^{cont} strongly deviates from the classical one $C_g V_g/e$, and the calculated ΔE_F is linear for $V_g \sim 0 \rightarrow 2\,V$ hence in the $\epsilon_W < \epsilon_c$ regime. Nevertheless, the aim of this chapter is to show that a modulation is possible as we will see in the following section reviewing the state of the art in this specific domain and in the last section about my experimental results.

4.2.3 State of the art of the remote contact gating

Following the theoretical paper by Giovannetti and co-workers [83], a few experimentalist groups made attempts to find evidence of contact doping modulation and to provide some values of the metal induced doping. They always rely on the presence of a remote back gate tuning at the same time both channel and contact graphene. Basically two different principles are used: either the contact resistance is measured by the Transfer Length Method (TLM) where measuring samples of various lengths provides the contact resistance as a function of back gate voltage or a combination of top and remote back gate is used, and in that case, the contact doping effect is extracted from the transfer characteristic asymmetry or from the observation of a "secondary Dirac Point" that corresponds to contact neutrality.

TLM measurement of the contact resistance

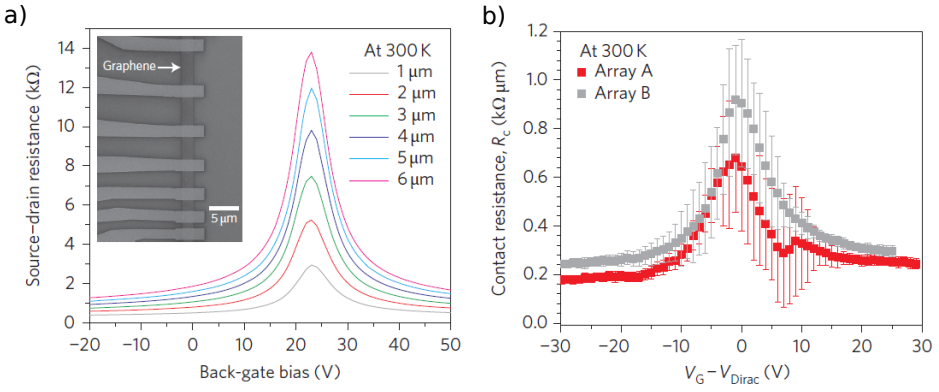

FIGURE 4.5: TLM measurement by [78]. The contact resistance R_c is extracted from the y-intercept of the resistance as a function of the sample length. Contact properties are extracted from the $R_c(V_g)$ curve

In [78], Xia and co-workers are using TLM to extract the contact resistance of an exfoliated single layer graphene sample with Pd contacts as a function of back gate voltage. They use an analysis based on [66] to estimate the contact transmission (they assume

a contact junction length of $d = 40\,nm$) and use [83] to extract the contact properties (metal induced doping and metal-graphene distance). A graphene-metal distance of $0.1\,nm$ is found corresponding to a renormalisation of the work function difference of $\Delta_C \simeq 0.9\,eV$ accounting for the chemical interaction between graphene and metal orbitals. In our notation it corresponds to $\Delta W = 200\,meV$. They measure a contact resistance of $R_c = 110\,\Omega\mu m$ at $6\,K$ which is close to the Landauer limit and compatible with Giovannetti's predictions. A strong signature of contact doping modulation would be the observation of a secondary Dirac point in the transfer curve arising when the contacted graphene is brought to neutrality by the back gate. However, according to the authors, the large energy broadening due to the metal smears out the second resistance peak, preventing its experimental observation.

Similar measurements have been conducted by Zhong et al. [80]. The authors argue that their good contact evaporation conditions (Pd purity of 99.95% and high vacuum $1 \times 10^{-8}\,mbar$) allows them to obtain a lower contact resistance $\leq 100\,\Omega\mu m$ with a good reproducibility. They observe a strong asymmetry in the p-n branches of the transfer curve which is, from my analysis, due to a larger junction length, as well as a secondary Dirac point. If we apply Giovannetti's model to their results and if we assume a typical (but process dependent) double layer thickness of $0.1\,nm$ we find a Pd effective work function of $\Delta W = 50\,meV$ in accordance with our own measurement (see section 4.3).

Top and remote back gates

A combination of top gate and back gate with no ungated area is used by Knoch and colleagues [85] to investigate the remote gating of Pd contacts. Indeed, this geometry gives access to a broad doping range for both contact and channel areas. On one hand, figure 4.6 shows a set of top gate transfer curves for given back gate voltages. Apart from the shift of the transfer curves, the change in the asymmetry demonstrates the reversal of the contact polarity: a lower resistance on the $V_{tg} < V_{Dirac}$ side indicates a p-doping of the contacts while a lower resistance on the $V_{tg} > V_{Dirac}$ side indicates a n-doping. On the other hand, Figure 4.6-b shows the remote back gate transfer curves at given top gate voltages. Here, the back gate tunes at the same time the channel and contact doping. The main peak corresponds to the regular charge neutrality point of the channel while a smeared second peak is observed corresponding to the charge neutrality at the contact. The occurrence of this second peak at a different V_{BG} reflects both a chemical doping by the metallic contact specific to the contact area and a different field effect efficiency from the back gate to the channel and to the contact as explained in the previous section. From the second peak position, the authors deduce a metal induced doping smaller than $100\,meV$, according to them, this doping is too small to be observed with a single gate

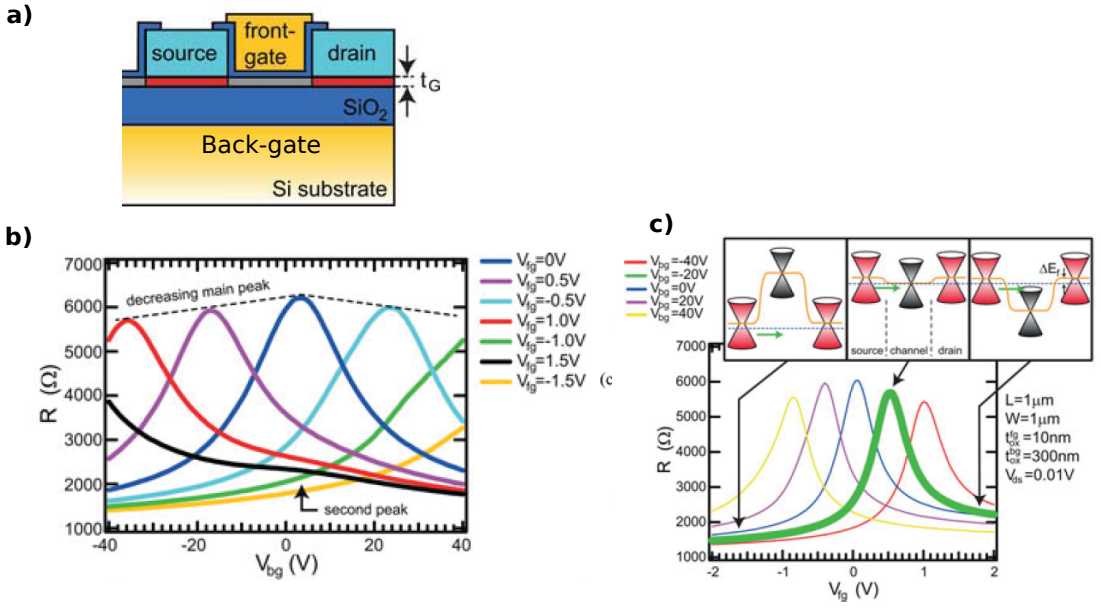

FIGURE 4.6: (a) Side view of a device with top and remote back gates (adapted from [85]). (b) The back gate voltage is tuned, for various top gate voltages a second resistance peak is observed suggesting the contact neutrality. (c) The top gate voltage is tuned for various back gate voltages, the asymmetry reversal points out a polarity reversal of contacted graphene.

where both resistance peaks would overlap. Having a second gate that tunes the contact doping while a top gate sets the channel carrier density is then necessary.

Fano factor measurement

The noise of a graphene p-n junction has been calculated theoretically in [66] and [67]. As it has been shown before, a contact can act as a p-n junction, thus investigating the noise of a 2 terminal graphene device provides additional information on the contact properties.

Such an experiment, where the Fano factor is measured in RF, has been performed recently in a suspended graphene sample [86] with Au contacts. The contact-channel resistance is estimated assuming a trapezoidal p-n barrier in the ballistic regime and using Klein tunneling transmission calculations by Sonin et al.[67]. The contact doping is estimated from Giovannetti's model. Experimental data fits well the model. Obtained parameters: renormalized work function $\Delta W = 18\, meV$, barrier length: $d = 20\, nm$, double layer capacitance: $C_{dl} = 190\, fF/\mu m^2$ (thus a double layer thickness of $0.1\, nm$) while the gate capacitance is $C_g = 5 \times 10^{-2}\, fF/\mu m^2$. This translates in our notation to a screening constant $\epsilon_c \approx 400\, meV$ which is much greater than $\epsilon_W \propto \frac{C_g}{C_{dl}} eVg \propto 2.5 \times 10^{-4} eV_g$. Thus tuning of the contact doping is limited due the fact that gating is

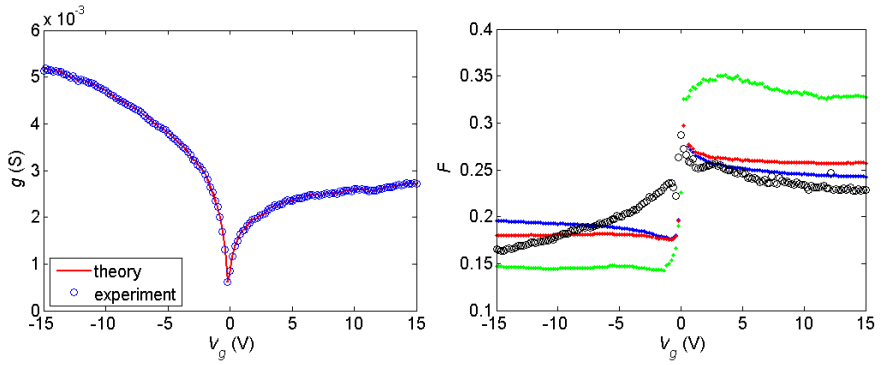

FIGURE 4.7: From Laitinen et al. [86]. Left: Conductance of a suspended sample fitted with contact doping model and Klein junction at the contact. Right: Measured (black circle) and calculated (diamonds) Fano factor of the contact junction at finite bias. The calculated Fano factors are shown for junction length of $d = 1, 20$, and $100\,nm$ (blue, red, green respectively)

Author	metal	contact polarity	Induced doping (meV)	Metal-graphene distance (nm)	Junction length (nm)	ϵ_c (meV)
Xia [78]	Pd	p	~ 200	0.1	40	
Xia [79]	Ti	n			40	
Zhong [80]	Pd	p	50			
Laitinen [86]	Au	p	18	0.1	20	400
GoBN1	Pd	p	70		70	
GoBN2	Pd	p	50	2	30	28
GoBN3	Pd	p	10	0.3	30	140

TABLE 4.2: Contact gating review

remote. Via DC measurement, a single gate makes a direct extraction of both chemical doping and double layer capacitance difficult. However a rf measurement that provides the Fano factor as a function of V_g gives an additional information. Laitinen et al. use the information from the Fano factor to extract the junction length d, which removes a fitting parameter for the zero bias conductance.

Table 4.2.3 summarizes the relevant contact properties from the litterature and from my own measurements (see below).

4.3 The gated contact transistor (GoBN2)

In this section we present the measurements made on a transistor made of exfoliated, graphene and equipped with independent and local channel and contact gates (shown in

Fig. 4.8). The channel length is reduced to 200 nm to approach ballistic transport. Consequently, the device resistance is mainly dominated by the contact junction resistance. The contact gate (same for source and drain) located just underneath the contacts will allow to tune the carrier density of the contacted graphene. The consequences will be visible in the transport properties and in particular in the tuning of the contact junction transmission. Thus we will be able to use the model presented above to extract some of the Pd contact properties such as the double layer capacitance, the effective work function difference between Pd and graphene and the junction length.

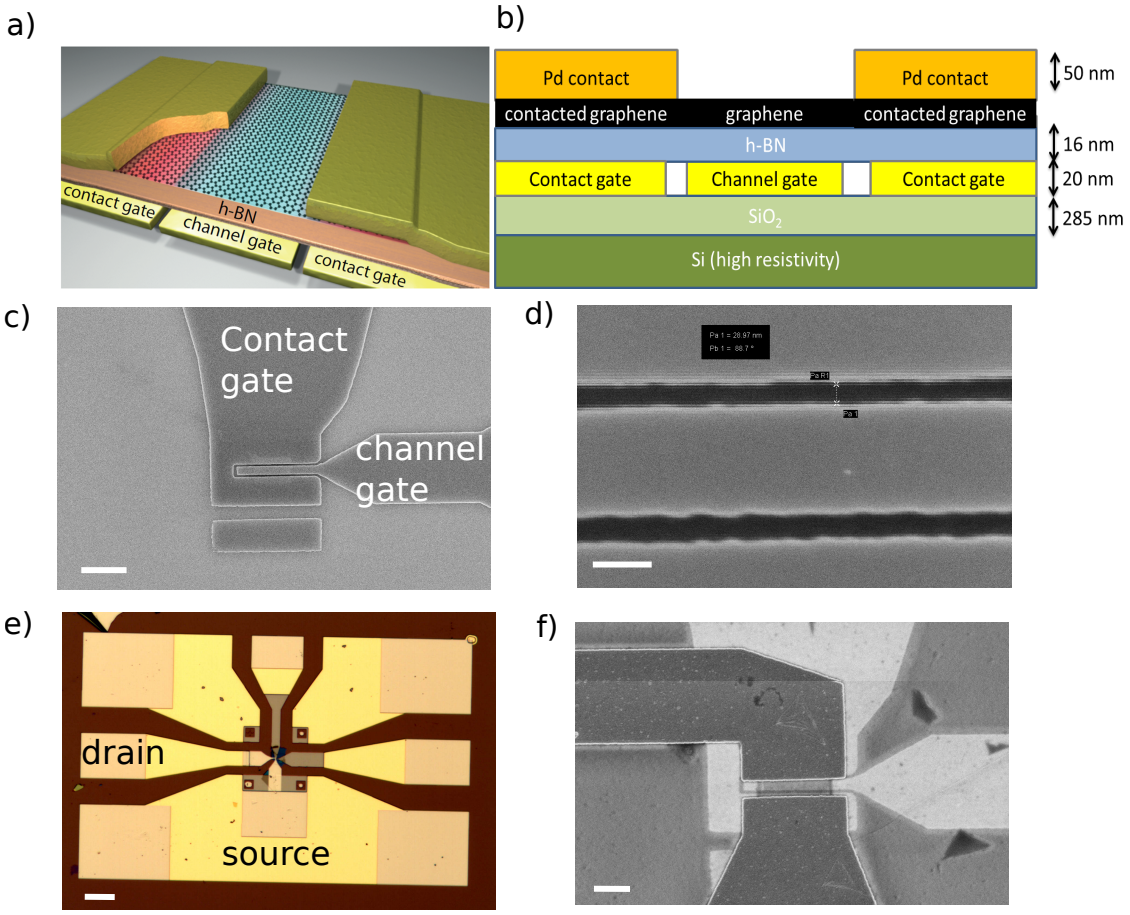

FIGURE 4.8: (a) Artist view of the device GoBN2. The change of color of graphene in the channel and underneath the contact reflects the contact induced doping. (b) Side view of the device. (c) TEM image of the gates before hBN and graphene deposition. The white scale bar is 1 μm. (d) Zoom of (c) centered on the channel gate. The gap between both gates is 30 nm. The white scale bar is 100 nm. (e) Optical image of the device in its coplanar waveguide. The white scale bar is 50 μm (f) SEM image of the contacted device. The graphene channel can be seen in gray, its dimensions are $L = 200\,nm$, $W = 1.1\,\mu m$. The white scale bar is 500 nm.

4.3.1 Device presentation and setup

As explained in the fabrication section 3.1 the local bottom gates are made out of a 20 nm thin tungsten film that is etched to define a 30 nm gap between the two gates. The dry transfer technique is used to transfer successively a 16 nm hBN flake and a monolayer graphene flake. A furnace annealing step ($300°C$ under Ar/H_2) is performed after each transfer to remove the MMA residues. The device is contacted with 50 nm thick Pd leads whose edges lie in the gap between the contact and channel gates as depicted in Fig. 4.8. A final annealing step is performed in the Janis probe station at 440 K and 1×10^{-5} $mbar$ prior to measurement. The channel length and width are $L = 200\,nm$ and $W = 1.1\,\mu m$ respectively. As seen in Fig. 4.8-e the device is embedded in a three port coplanar waveguide to allow further RF characterization.

The sample is DC biased using three BILT DC sources and three Keithley 2000 voltmeters in the voltage divider configuration. This allows to measure the sample resistance and current as well as the possible leaking current through the gate dielectric. We note V_{ch}, V_{cont} and V_{ds} the channel gate, contact gate and drain to source DC voltages respectively.

4.3.2 Experimental DC results

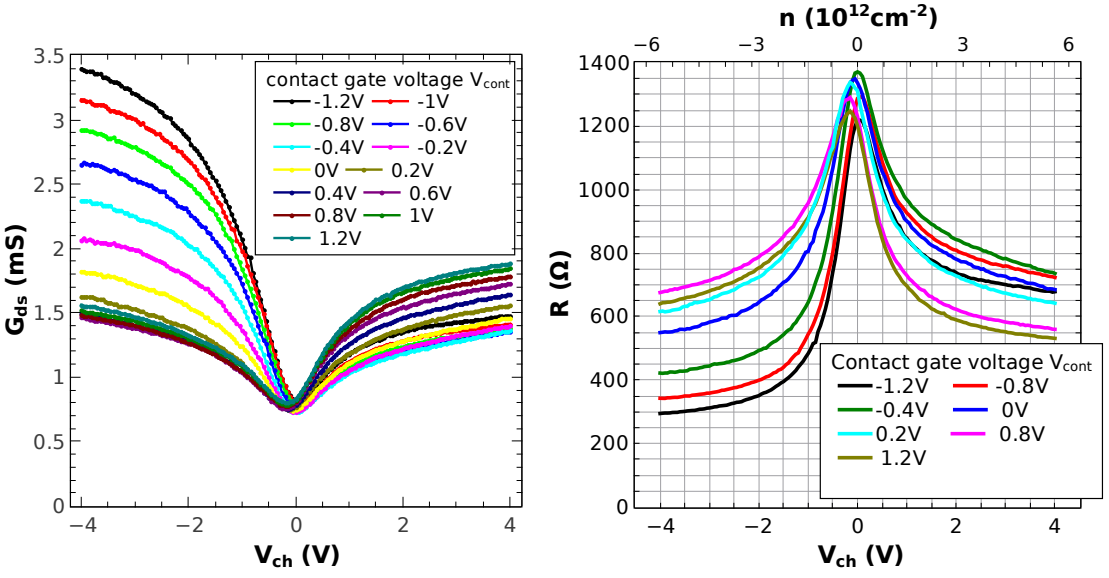

FIGURE 4.9: Transfer curves of GoBN2. Conductance (left) and resistance (right) as a function of the channel gate voltage for various contact gate voltages. The Dirac point is around zero gate voltage and the peak is sharp indicating a good device quality. We observe a large tunability of the conductance with V_{cont}, which demonstrates the efficiency of our contact gate.

This part is dedicated to DC measurements of the device resistance at room temperature as a function of the channel gate and contact gate voltages, V_{ch} and V_{cont} respectively. First we show in Fig. 4.9 the conductance $G(V_{ch})$ and the resistance $R(V_{ch})$ of the device for contact gate voltages $V_{cont} = -1.2 \rightarrow 1.2\,V$. The transfer curve $G(V_{ch})$ (or $R(V_{ch})$) is typical of a high mobility device with a charge neutrality point located near $V_{ch} = 0$ and with an ON/OFF ratio that is large for such a short channel transistor [13] (the corresponding density range is $n = -5.8 \times 10^{12}\,cm^{-2}$ to $n = +5.8 \times 10^{12}\,cm^{-2}$). But the main feature of this measurement is the efficient modulation of conductance induced by the contact gate away from charge neutrality. $G(V_{ch})$ is tuned by a factor 2.3 for $V_{ch} < 0$ and 1.3 for $V_{ch} > 0$. By contrast, there is only a small variation of G near the Dirac point which points out a channel dominated resistance with finite mobility. Regarding the position of the CNP, it is not modulated by V_{cont} which confirms the independence of both gates and differs from previous investigations using a combination of remote back gate and local top gate [80].

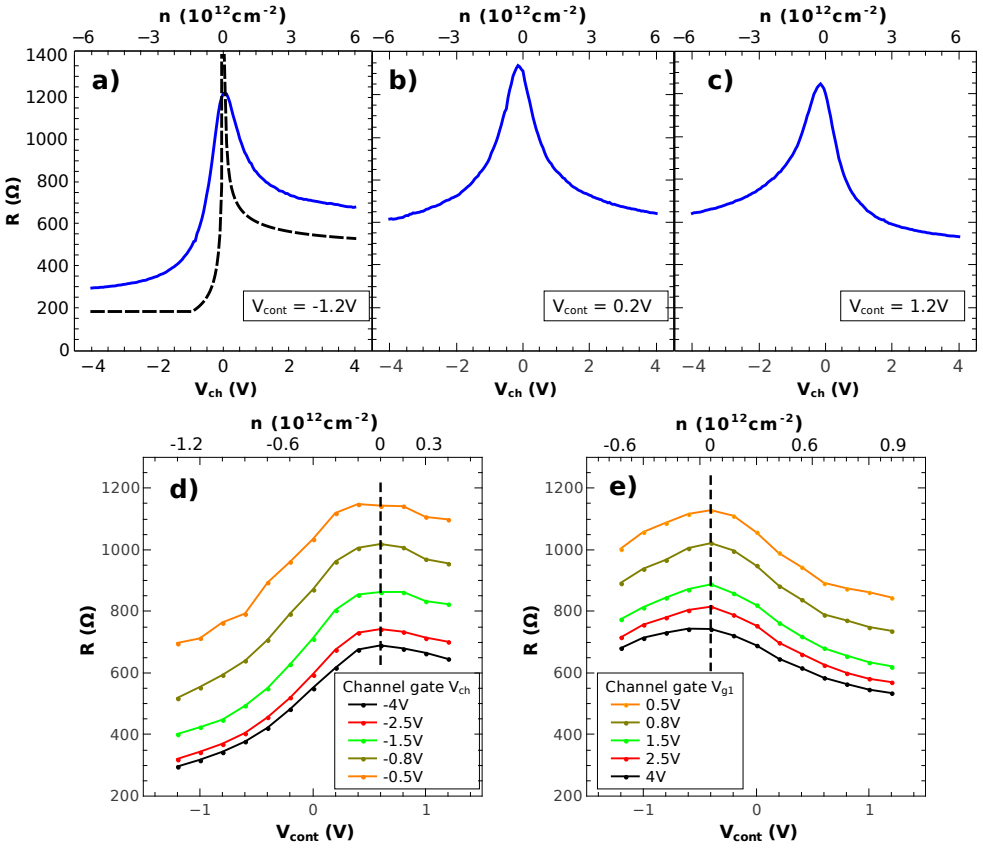

FIGURE 4.10: Typical resistance transfer curves for a subset of contact gate voltages. The asymmetry of curves in panels a) and c) reflects the p and n doping of the contact respectively ; the symmetry of the curve in panel b)suggests a neutral contact. The dotted line in panel a) represents the transfer curve expected for a fully ballistic device. Panels e) and f): Device resistance as a function of contact gate voltage for channel gate voltages $V_{ch} = -4V \rightarrow -0.5\,V$ and $V_{ch} = +4V \rightarrow +0.5\,V$ (from bottom to top) respectively.

Let us focus on the transfer curves for three representative contact gate voltages (Fig. 4.10 top panel). We now plot the resistance in order to separate the serial contributions of the contact junctions and the channel. At $V_{cont} = -1.2V$ the transfer curve is asymmetric suggesting a p-doping of the contact as the device is less resistive when the channel is p-doped ($V_{ch} < 0$). The asymmetry level can be changed gradually up to $V_{cont} = +0.2\,V$ where the transfer curve is symmetric. For higher contact gate voltages the asymmetry is reversed suggesting a n-doping of the contacts as can be seen in Fig. 4.10-c for $V_{cont} = +1.2\,V$. This first result demonstrates that the gated contact geometry allows for an extensive control over the doping of graphene in the contact area. As discussed in section 4.2.2 (Eq. (5.19)), tuning the contact gate voltage is like changing the natural doping induced by the metallic contact. For example $V_{cont} > +0.2\,V$ emulates a low n-doping metal as titanium and would give a maximum transconductance on the $V_{ch} > 0$ side. On the other hand applying a negative V_{cont} strengthens the p-doping nature of Pd and lowers the contact resistance in the p-doped regime. In Fig. 4.10-a we reach a minimum resistance $R = 300\,\Omega$ corresponding to a contact resistance $R_c \lesssim 150\,\Omega\mu m$ per contact that compares well with the best achievements presented in table 4.1.3. For comparison, we plot with a dotted line (Fig. 4.10-a) the expectation in the ballistic case where the total resistance reduces to a ballistic p-n-p barrier (with a contact doping p set at $1.7 \times 10^{12}\ cm^{-2}$). The theoretical curve shows an asymmetry which is consistent with the measured one, $\Delta R(V_{ch} = \pm 4V, V_{cont} = -1.2V) \simeq 400\Omega$. The main deviation is an overall resistance shift of $\simeq 110\Omega$ that we attribute to an additional (and not tunable) metal-graphene resistance ($R_{mg} \simeq 55\Omega$ per contact). At the CNP a diffusive contribution from the channel will have to be accounted for as well as smearing by thermal effect and residual charge density.

As we deal with a dual gate transistor we can also plot the data as a function of the contact gate voltage $R(V_{cont})$ in Fig. 4.10 d) and e) for various channel gate voltages. Those curves show directly the effect of the contact gate on the total resistance, they show a maximum and an asymmetry typical of a standard transfer curve and demonstrate the ambipolar behavior of our gated contact. Note that those curves cannot be obtained with a remote back gate that tunes channel and contact altogether and for which the evidence of contact neutrality relies on the existence of a smeared second peak. Again, the positions of the maxima are independent of V_{ch} (given a channel polarity) confirming the independence of the two gates. The $R(V_{cont})$ curves are mainly shifted upward when V_{ch} is approaching charge neutrality due to finite carrier mobility in the channel. One can notice that the contact gate voltage range is limited to $\pm 1.2V$ due to gate leakage at higher voltages. We attribute this different behavior to a possible weakening of the hBN dielectric underneath the contact during the metal evaporation. Finally, the entire set of data is displayed as a color plot of $R(V_{ch}, V_{cont})$ in Fig. 4.11 (left panel). Simulation

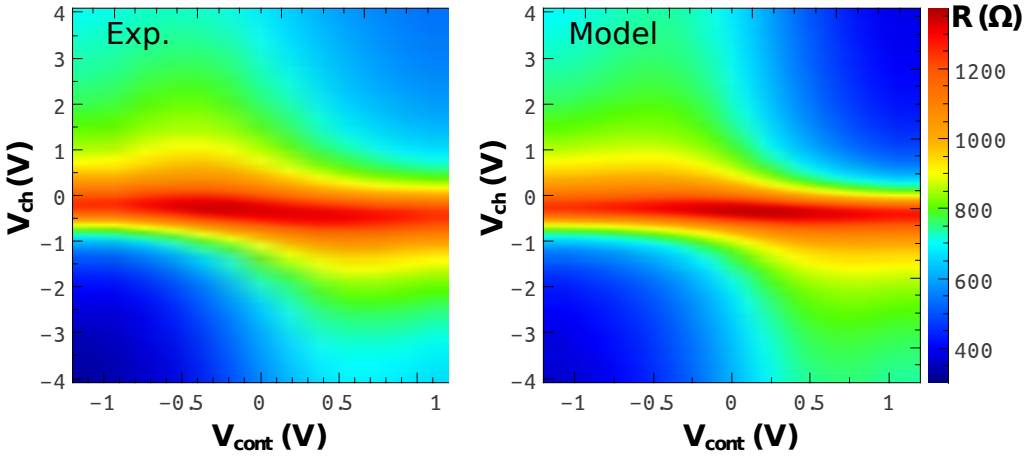

FIGURE 4.11: Left: Color map of the device resistance as a function of contact and channel gate voltages. Right: Corresponding simulation using the fitting model and parameters.

results are displayed in the right panel in an attempt to reproduce $R(V_{ch}, V_{cont})$ features. The simulation relies mainly on the contact gating theory presented above and the junction transmission presented in the previous chapter. It will be applied to the case of the GoBN2 sample in the next subsection.

4.3.3 Device modelling and interpretation

This subsection aims to precise the modelling that leads to the simulated color plot of Fig. 4.11-(right panel). We assume two contact junctions at drain and source, whose doping is calculated on the contacted side using the model presented in 4.2.2. Before using Cayssol's formula to calculate the transmission of such a junction, it is important to check that the potential profile with a Fermi-like shape assumed in our p-n junction model is realistic in our geometry. We do that with finite elements electrostatic simulation:

Electrostatics simulation

We use a finite elements solver, COMSOL Multiphysics, to solve the Poisson equation and to calculate the 2d electrical potential map created by the 3 electrodes at the junction area (Fig. 4.12-a). The electrode edges are rounded to a radius curvature of 1 nm. The computation was done for a sub-domain size comprised between 0.04 nm and $2nm$. A cut in the color plot along the x-axis gives the potential variation across the junction (Fig. 4.12-b blue line). From this we extract the characteristic length scale $d \approx 30nm$ for the 10-90% extension of the potential step. In practice this length is determined by the lithography limited gap between the contact gate and the channel gate. This length has to be compared with the typical Fermi wavelength within the measurement range which

varies from 15 nm to 50 nm. Therefore, the potential step length lies in the relatively sharp regime where the junction transmission is very sensitive to this length. In order to accurately model the transmission we need a formula accounting for the junction length dependence. It should be noted that this simulation neglects graphene screening and corresponds to the specific case where $\epsilon_W << \epsilon_c$ which is relevant at low doping and particularly in the contact area (see theoretical section). Nevertheless we are mainly interested in the general aspect of the potential step giving its width and in comparison with a Fermi-like function.

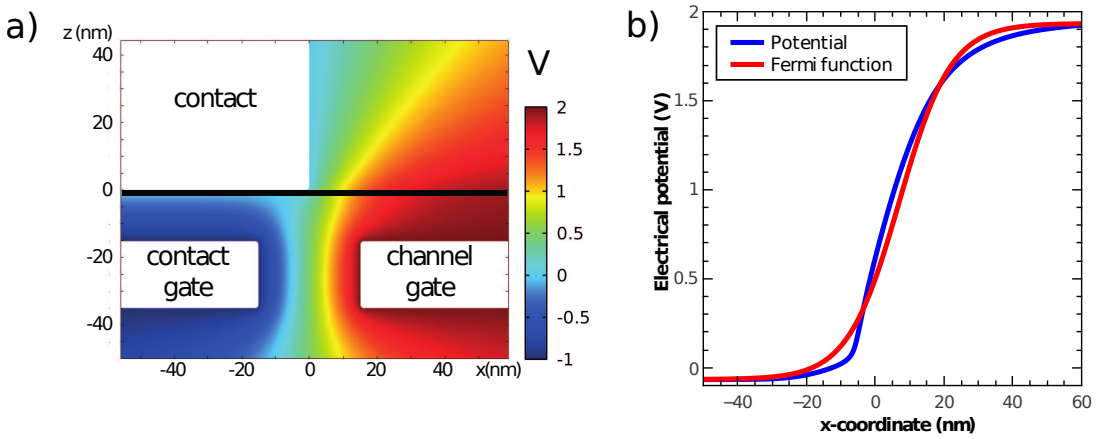

FIGURE 4.12: Panel a) Electrical potential map of the device at the contact junction from finite element simulation for two typical channel and contact gate voltages, $V_{cont} = -1V$ and $V_{ch} = +2V$, the contact being at $V_{source} = 0V$. The graphene layer is located at z = 0. Panel b) Horizontal cut of the potential through the junction together with a Fermi like function. The $10-90\%$ range is within $d \approx 30nm$.

Transmission of the junction

We consider the transmission of the contact junction from the area underneath the metal to the channel area. The COMSOL simulations tell us we can assume within good approximation the shape of the electrostatic potential to be Fermi-Dirac like equation (Fig. 4.12-b red line):

$$V(x) = V_{gr}^{cont} + \frac{V_{gr}^{ch} - V_{gr}^{cont}}{e^{-x/w} + 1} \tag{4.22}$$

Taking this potential profile allows us to use the formula by Cayssol et al. [66] giving the exact transmission T of the corresponding potential step for any junction length $d \approx 4.5w$ as explained in chapter 3.

Proceeding as explained in section 3.2 we can calculate the contact junction transmission and deduce its conductance.

$$G_K(\Delta E_F^{cont}, \Delta E_F^{ch}) = \frac{4e^2}{h} \frac{W k_F^{cont}}{\pi} \mathcal{T}(\Delta E_F^{cont}, \Delta E_F^{ch}), \tag{4.23}$$

where doping the levels of graphene in the contact and channel areas ($\Delta E_F^{cont}(V_{cont})$ and $\Delta E_F^{ch}(V_{ch})$ respectively) are estimated from the model presented previously (in 4.2.2).

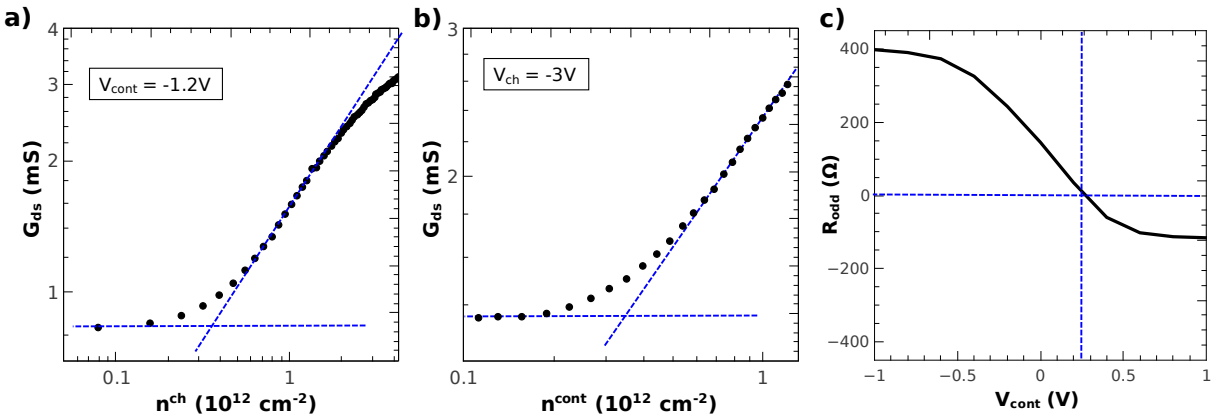

FIGURE 4.13: (a) Device conductance as a function of the channel carrier density in a logarithmic scale. The intercept of the two dotted lines gives an estimate of the residual carrier density in the channel n_0^{ch}, following the method of ref. [52]. (b) Idem but for the carrier density in the contact area. (c) Odd part of the resistance $R_{odd} = R(V_{ch}) - R(-V_{ch})$ at $V_{ch} = \pm 4\,V$ as a function of the contact gate voltage. The slope of the linear part is related to C_{dl} while the x-intercept is related to ΔW.

This conductance is convoluted with a Gaussian function accounting for residual density and thermal averaging in both V_{cont} and V_{ch} direction:

$$Gauss^{cont,ch} = \frac{1}{\sqrt{\pi} t_{cont,ch}} \exp - \left(\frac{E_F^{cont,ch}}{t_{cont,ch}} \right)^2 \tag{4.24}$$

Where $t_{cont,ch} = \hbar v_F \sqrt{\pi \cdot n_0^{cont,ch}}$ is the energy width of the Gaussian function related to the residual density $n_0^{cont,ch}$ of contact and of channel areas respectively. They can be estimated by plotting $G(n)$ in logarithmic scale as in Fig. 4.13-a,b.

Final electrical model and fit

Our model is based on a lumped element model as described in Fig. 4.14. The two contact junctions are sketched with a K symbol (standing for Klein junction); they lie at the source and drain of the device and are presumed to be identical, $R_K = G_K^{-1}$. Transport is assumed to be incoherent within the channel, which implies that we simply add up resistances of both contact junctions.

As our device is not ballistic over its full length, we assume a diffusive channel of dimensions $L = 200\,nm$ and $W = 1.1\,\mu m$. The resistance of the channel is calculated using $R_{ch} = \frac{L}{W n_{ch} e \mu}$ with a constant mobility μ and a carrier density given by

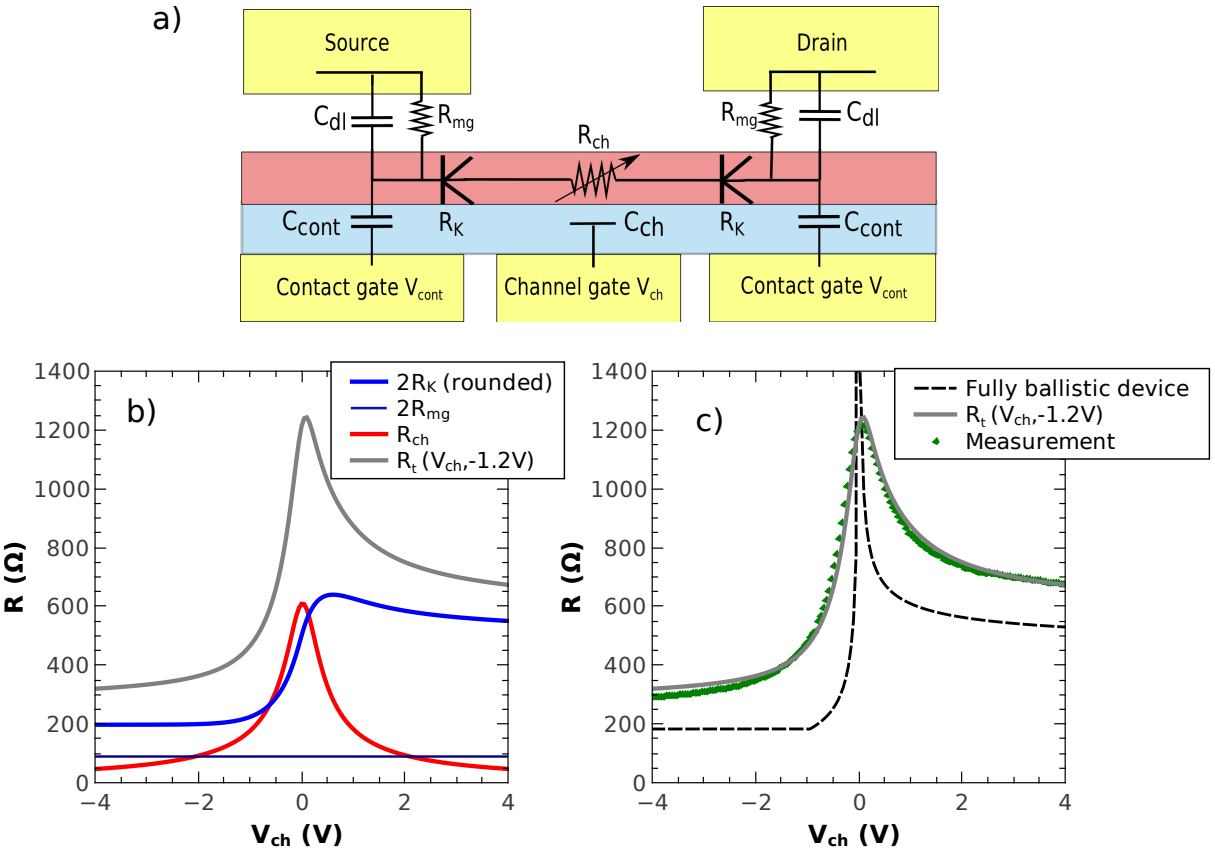

FIGURE 4.14: (a) Electrical sketch of the device. (b) Different contributions to the total resistance R_t (gray line): two contact junction resistance $2R_K$ (thick blue line), diffusive channel resistance R_{ch} (red line) and additive (constant) contact resistance $2R_{mg}$ (thin dark blue line). (c) $R(V_{ch}, V_{cont} = -1.2V)$ data point (green diamonds) fitted using our model (R_t: gray line). The dotted line represents the contact junction resistance without Gaussian broadening.

$n_{ch} = \sqrt{(n_0^{ch})^2 + C_{ch}V_{ch}/e}$, where n_0^{ch} is a residual carrier density. Thus the total resistance is given by:

$$R_t(V_{ch}, V_{cont}) = 2R_{mg} + 2R_K(V_{ch}, V_{cont}) + R_{ch}(V_{ch}) \tag{4.25}$$

We have now all the ingredients we need to propose an accurate model interpreting the measurement. A priori we have a large number of unknown parameters in the model: d, ΔW, C_{dl}, R_{mg}, n_0^{ch}, n_0^{cont} and μ. As already mentioned, the junction length $d = 30nm$ is determined from the COMSOL simulation. Let us enumerate the number of observables in our measurement:

- In the $R(V_{ch})$ curves we have a resistance peak around the charge neutrality. Considering the amplitude of the peak and its width we have two observables which are related to the mobility μ and the residual density n_0^{ch}.

- In the $R(V_{ch})$ curves, away from neutrality, the resistance tends toward a constant value. It gives one observable which is related to R_{mg}.
- Considering the asymmetry of the $R(V_{ch})$ curves as a function of V_{cont}, we plot the odd part of the resistance: $R_{odd} = R(V_{ch}) - R(-V_{ch})$ in Fig. 4.13-c. $R_{odd}(V_{cont})$ is roughly linear, so that we have two more observables: the x-intercept and the slope, that are related to ΔW and C_{dl}.
- Finally, the width of the $R(V_{cont})$ peak resistance gives a final observable which is related to the contact residual density n_0^{cont}.

So we have as many observables as unknown parameters.

From a practical point of view, the residual densities are determined from the log-log plots of the conductance of Fig. 4.13 following the method of ref. [52], $n_0^{ch} = n_0^{cont} = 3.5 \times 10^{11} cm^{-2}$. Moreover there is a relationship between ΔW and C_{dl}: the neutrality of graphene underneath the contact is reached when $V_{cont} = 0.2V$ (symmetric curve in Fig. 4.10), therefore $\Delta E_F^{cont}(V_{cont} = 0.2V) = 0 \Leftrightarrow \epsilon_W(V_{cont} = 0.2V) = 0$, leading to

$$0 = \frac{C_{cont}}{C_{cont} + C_{dl}} eV_{cont} - \Delta W \tag{4.26}$$

$$\Delta W = \frac{0.2V \cdot eC_{cont}}{C_{cont} + C_{dl}} \tag{4.27}$$

So we end up with three fitting parameters for a 2D plot : C_{dl}, μ and R_{mg}.

The fit gives $R_{mg} = 55\Omega$, $\mu = 6000 cm^2 V^{-1} s^{-1}$ and $C_{dl} = 4.5 fF/\mu m^2$ which corresponds to $\Delta W = 55\, meV$.

Interpretation and partial conclusion

Regarding the contact properties, the most interesting outputs of the model are C_{dl} and ΔW that allow us to calculate the screening constant

$$\epsilon_c = (C_{cont} + C_{dl}) \frac{\pi \hbar^2 v_F^2}{2e^2} = 28\, meV \tag{4.28}$$

and the tunable energy scale

$$\epsilon_W = \frac{C_{cont}}{C_{cont} + C_{dl}} eV_g - \Delta W \approx 0.32 \times eV_{cont} + 0.05\, eV \tag{4.29}$$

Therefore we work mainly in the screened regime where $\epsilon_W \gg \epsilon_c$. From this we deduce our accessible energy range in the gated area: $\Delta E_F^{cont} = -130 \rightarrow 110\, meV$, which corresponds to a carrier density range of $n^{cont} = -1.25 \times 10^{12} \rightarrow 0.9 \times 10^{12}\, cm^{-2}$. By comparison, in the channel our energy window is $\Delta E_F^{ch} = \pm 260\, meV$ corresponding to

$n^{ch} = \pm 5.5 \times 10^{12}\, cm^{-2}$. The value of ΔW in itself is of great interest as it determines the natural doping level of contacted graphene for a given metal and therefore will guide the choice of the contacting metal depending on the application: large ΔW for a low contact resistance (RF transistors for example), positive or negative ΔW for p-type or n-type transistors (operating point at positive or negative gate voltage respectively), low ΔW if one wants to operate near charge neutrality or to create a barrier (for example the KT transistor described in chapter 3 could be made from patterned contact with low p-doping level), asymmetric contacts with positive and negative ΔW for non-opposite photocurrent generation at the contacts, etc. It has to be specified that reported values of Pd doping show a relatively large scattering [78, 80, 85] and appear to be even more distant from the ab initio predictions [83, 84]. In fact the choice we made for the definition of ΔW does not lead to the pure Pd work function. Actually it represents the effective work function difference between graphene and Pd. For example, the presence of PMMA residues on graphene affects its work function. In addition if we refer to the work by Giovannetti we have to take into account a graphene-metal chemical interaction ($\Delta_c \approx 0.9\, eV$ in [83]) that depends itself very strongly on the metal-graphene distance. Therefore a thin layer of residual resist on the graphene can change ΔW a lot. Regarding now the double layer capacitance value $C_{dl} = 4.5\, fF/\mu m^2$, it corresponds to a metal-graphene distance of $2\, nm$ which is much larger than the DFT prediction in [83, 84] or the previously reported values [78, 80, 85, 86]. We attribute this discrepancy to the slight shift between the contact edge and the inter-gate gap. Indeed there is a short non-contacted graphene area on top of the contact gate as can be seen in Fig. 4.8-f. It leads to a strong reduction of metal screening which is accounted for a larger metal-graphene distance that means a smaller C_{dl} or a smaller ϵ_c. The large contact gate modulation that we observed in this particular sample probably benefits from this small imperfection. The next section will deal with a similar sample and it will show a lower modulation and a more realistic graphene-metal distance. Nevertheless, a gated contact transistor geometry with slightly backward contacts with respect to the inter-gate gap proves itself to be more efficient if one wants to implement a device with a tunable contact resistance.

Finally we can comment on the value obtained for the channel mobility: $\mu = 6000 cm^2 V^{-1} s^{-1}$. It corresponds to a mean free path in excess of $50\, nm$ which is consistent with our working hypothesis of a ballistic contact junction and a diffusive channel. Moreover, for a charge injection within a few tens of nanometers from the contact edge, it confirms also that we can neglect any diffusive propagation in the contact area. This analysis is reinforced by the low temperature measurement showing Fabry Pérot oscillations (see below in Fig. 4.15).

4.3.4 Low temperature measurement

A measurement run at $6K$ is performed in the Janis probe station to check the low temperature properties of the device. The poor mechanical stability of the probes at low temperature prevents exhaustive measurements. As a result, only a few transfer curves have been acquired as the one shown in Fig. 4.15-a). First we observe a higher resistance peak in the $R(V_{ch})$, consistent with a lower thermal broadening. Interestingly, some low frequency resistance oscillations are observed away from the Dirac point. These kind of oscillations have been reported several times in high mobility devices at low temperature [13, 50–52] and are usually attributed to Fabry Pérot interferences where electrons are experiencing multiple reflections between two barriers.

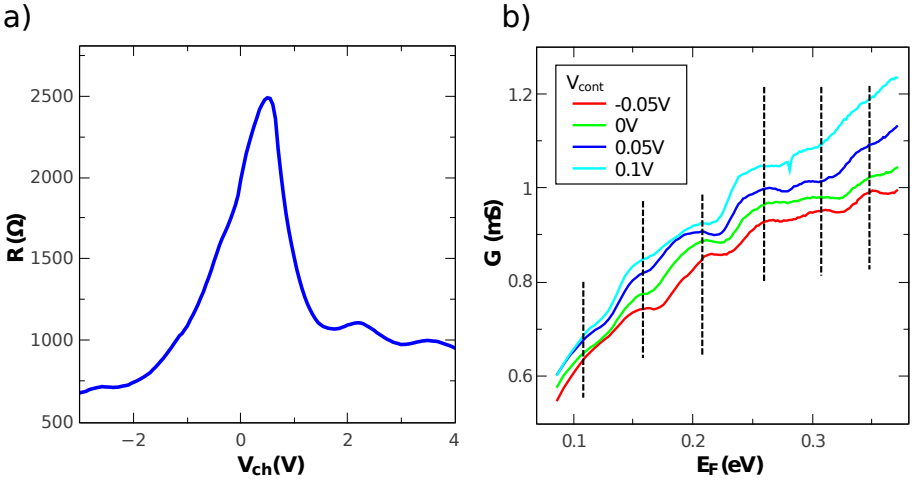

FIGURE 4.15: Device GoBN2 measured at 6 K. (a) Resistance as a function of the channel gate voltage for $V_{cont} = 0$. Fabry Pérot oscillations observed on the n-side. (b) Conductance as a function of the channel Fermi energy for $V_{cont} = -0.05 \rightarrow 0.1V$ from bottom to top. Several oscillations are identified by the vertical dotted lines (maxima of the red curve). A period of 50 meV is observed, that corresponds to a 40 nm cavity.

Conductance resonances are expected whenever

$$\lambda_F = 2NL \tag{4.30}$$

$$k_F = N\pi/L \tag{4.31}$$

$$E_F = \hbar v_F k_F = \hbar v_F N\pi/L \tag{4.32}$$

$$\Delta E_F = \hbar v_F \pi/L \approx \frac{2}{L}\, eV, \tag{4.33}$$

where N is an integer and L in nm.

First on a regular transfer curve, two resistance peaks are visible with a very good contrast separated by $\Delta E_F \approx 70meV$. Thus the corresponding cavity length is $L = \pi\hbar v_F/\Delta E_F \approx 30\, nm$. From Eq. (4.33) however, one can see that it is more convenient

to plot the conductance as a function of the Fermi energy. Fig. 4.15-b shows $G(E_F)$ for various contact gate voltages; it gives more numerous and regular oscillations. We extract $\Delta E_F \approx 50\,meV$, hence $L = 40\,nm$. The $30-40\,nm$ observed length corresponds well to the misalignment of the contact gate with the inter-gate gap. So the observed oscillation is consistent with a cavity defined by a barrier at the contact edge and another barrier at the channel gate edge on the drain side. It also defines a lower boundary for the mean free path. We do not observe faster oscillations that would correspond to the 200 nm length of the device, therefore the channel is not fully ballistic. Let us emphasize that we directly plot the measured conductance, we do not need in this case to differentiate $G(V_{ch})$ to get a good contrast of the interferences.

4.3.5 Dynamical properties of the gated contact

If one wants to operate a transistor at RF frequencies it is necessary to be equipped with local gates. Thus even if the DC gating effect of a graphene contact has been observed before with remote gates, this work enables us for the first time to drive a contact gate at high frequency. Here we show that our contact gate is still active in the GHz range, meaning that its transconductance is preserved up to a few GHz. The main frequency limitation of our geometry is extrinsic, it originates from the high resistivity of the thin tungsten gates.

VNA measurement Using the Janis probe station in a 3 probe configuration we measure the scattering matrix elements between the channel gate and the drain, and between the contact gate and the drain, up to 20 GHz and extract the admittance parameters of the device (see chapter 6 for more details). Note that we have to apply a relatively large DC drain-source bias $V_{ds} \gtrsim 100\,mV$ to observe a transconductance effect. Being limited by the gate resistivity, we limit ourselves to the $0.1-3\,GHz$ range and we deduce the transconductance for both channel gate $g_m^{ch} = \partial I/\partial V_{ch}$ and contact gate $g_m^{cont} = \partial I/\partial V_{cont}$. Surprisingly, g_m^{ch} and g_m^{cont} are of the same order of magnitude and both compare well with graphene FET standards [12, 82, 87] ($g_m/W \sim 0.25\,mS\mu m^{-1}$) as seen in Fig. 4.16-a. One should note that g_m^{cont} depends strongly on the operating conditions (V_{ch},V_{cont},V_{ds}). Indeed, for a given V_{cont}, g_m^{cont} can be tuned from positive to negative when changing V_{ch}. This can also be observed in DC and in a pulse measurement (Fig. 4.10 and 4.16-b respectively)

The high contact gate transconductance value suggests that a transistor can be operated by the contact gate only. In that geometry, a thin DC channel gate would be sufficient to set the channel doping. A large contact gate (whose size is not limited by the channel length) would command the drain source current acting on the contact resistance. This

geometry would maximize the transit frequency, as the channel can be short, but above all it would maximize the power gain frequency by keeping a low gate resistance (see chapter 6 for the description of a RF transistor).

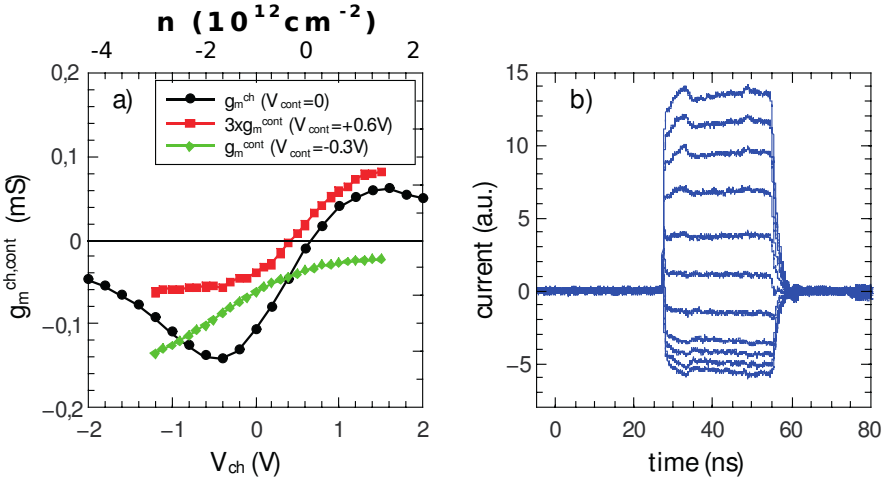

FIGURE 4.16: Finite bias operation of the contact gated transistor. (a) RF transconductance measurements for channel gating: black circles for $V_{ds} = 300\,mV$, $V_{cont} = 0V$, and for two typical contact gating conditions: green diamonds for $V_{ds} = 300\ mV$, $V_{cont} = -1V$, red squares for $V_{ds} = 100mV$, $V_{cont} = 0.6V$. (b) drain current temporal trace under contact-gate pulses of amplitude $\lesssim 90mV$ for $V_{ds} = 120\ mV$, $V_{ch} = -1 \rightarrow 1\,V$ (top to bottom), $V_{cont} = -0.2\,V$.

Pulse measurements

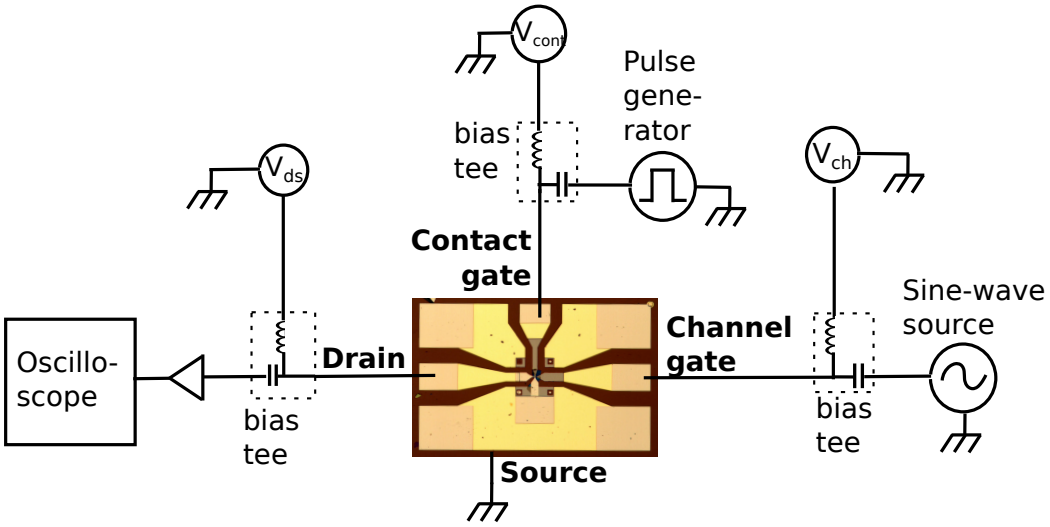

FIGURE 4.17: Schematic of the electric circuit in the pulse measurement configuration. The contact gate is actuated by a nanosecond pulse and the channel gate by a GHz sine-wave ; the drain-source current variation is amplified and acquired with an oscilloscope. This is the situation of Fig. 4.18-a. A DC bias is applied at each port through the bias tees

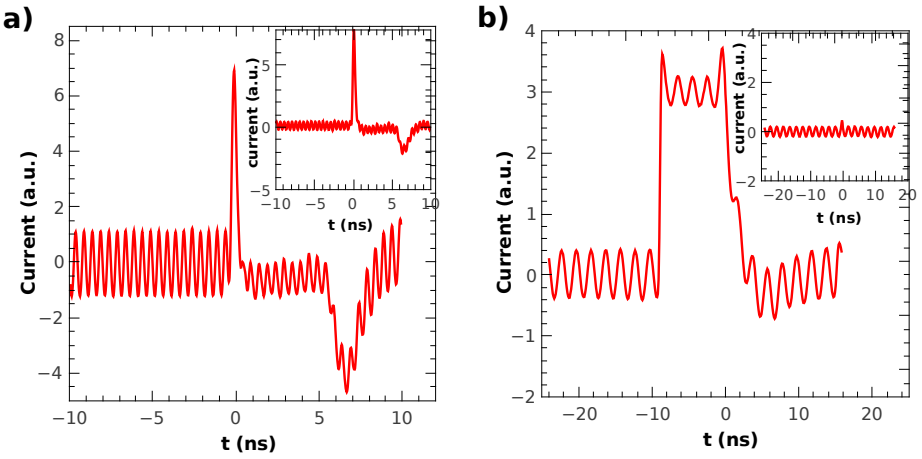

FIGURE 4.18: Finite bias operation of the contact gated transistor. (a) Drain current modulation under combined sine-wave channel gate excitation at $2\,GHz$ and $5\,ns$ pulsed contact gate actuation (see Fig. 4.17). The DC biases are $V_{cont} = 0\,V$, $V_{ds} = 150\,mV$. Inset: same conditions but at zero DC bias ($V_{ds} = 0$) ; the sine amplitude indicates the crosstalk level. (b) Drain current modulation under combined $10\,ns$ pulsed channel gate actuation and $0.5\,GHz$ sine-wave contact gate. The DC biases are $V_{ch} = -0.1\,V$, $V_{cont} = 0\,V$, $V_{ds} = 150\,mV$. Inset: same conditions but at $V_{ds} = 0$; the sine amplitude indicates the crosstalk level.

As an example of application we drive the contact gate with short pulses using a pulse generator *Picosecond - Pulse Labs*. The resulting drain current variation is amplified by a *Miteq* amplifier ($35\,dB$-$0.1 \rightarrow 2\,GHz$) and detected with a fast oscilloscope *Tektronix-DPO* ($16\,GHz$-$100\,GSample/s$). Fig. 4.16-b shows the oscilloscope trace of the drain current when a $30\,ns$ voltage pulse is sent to the contact gate while the channel gate DC bias varies from p to n doping. We notice a sign reversal of the current when the channel polarity is changed. What is observed here is the contact gate transconductance as we measure the current variation in response to a V_{cont} variation. The sign can be understood by looking at the DC $R(V_{cont})$ of Fig. 4.10: at $V_{cont} = -0.2\,V$, the slope of $R(V_{cont})$ changes sign when the channel polarity is reversed.

Having 2 gates, we can operate both of them at high frequency to create new functionalities. As an illustration we apply a $2\,GHz$ sinus-wave on the channel gate and a short pulse on the contact gate (schematic of Fig. 4.17 and measurement of Fig. 4.18-a). The output sine signal is strongly modulated by the pulsed contact gate voltage, meaning that the channel transconductance can be switched ON and OFF by the contact gate. The residual signal observed in the OFF state corresponds to the capacitive crosstalk between gate and drain at $V_{ds} = 0$[2] as shown in the inset of Fig. 4.18. We show as well the reversed operation where the contact gate is driven by a sinus-wave and the channel gate is pulsed (Fig. 4.18-b). Again, the capacitive crosstalk signal is shown in inset. In

[2] At $V_{ds} = 0$ there is no transconductance so the observed sine-wave is the direct capacitive coupling between the gate and drain electrodes.

the current arbitrary units, the signal peak to peak amplitude in the ON state is 0.8, it is 0.5 in the OFF state and 0.4 in the crosstalk, so we have a good efficiency of our RF switch. Choosing other bias conditions, we can also have the output signal magnified during the pulse duration.

This demonstration that the contact gate is active at high frequency is important in terms of the application of our new architecture. The graphene contacts are no longer a drawback but can be used for new functionalities. For instance we can imagine an optoelectronic device where the photocurrent is generated at the contact junctions and modulated by asymmetric contact gates.

4.4 The gated contact transistor with CVD graphene (sample GoBN3)

As already mentioned, a large scale and reliable graphene production technique is essential for applications. Chemical vapor deposition (CVD) of graphene is a solution as the quality of CVD graphene is improving regularly. It is then important to test the compatibility of our GoBN technology with CVD graphene. In addition, the fabrication process is much simpler with CVD than with exfoliated graphene as a single transfer CVD transfer allows to cover many devices. As a result we obtain a much better yield within one fabrication run: a rate of 6 out of 9 devices were successfully contacted and measured, against ~ 1 out of 10 for exfoliated graphene.

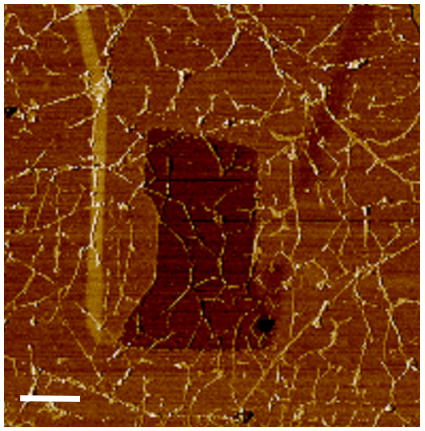

FIGURE 4.19: AFM image (phase mode) of the etched graphene channel (darker brown) before contact deposition(device GoBN3-4x1). Some wrinkles (white lines) are visible on the graphene. Elsewhere the white lines correspond to different depths of the partially etched BN, the graphene wrinkles played the role of a shadow mask during the O_2 etching. The white scale bar is $1\mu m$.

4.4.1 Sample presentation

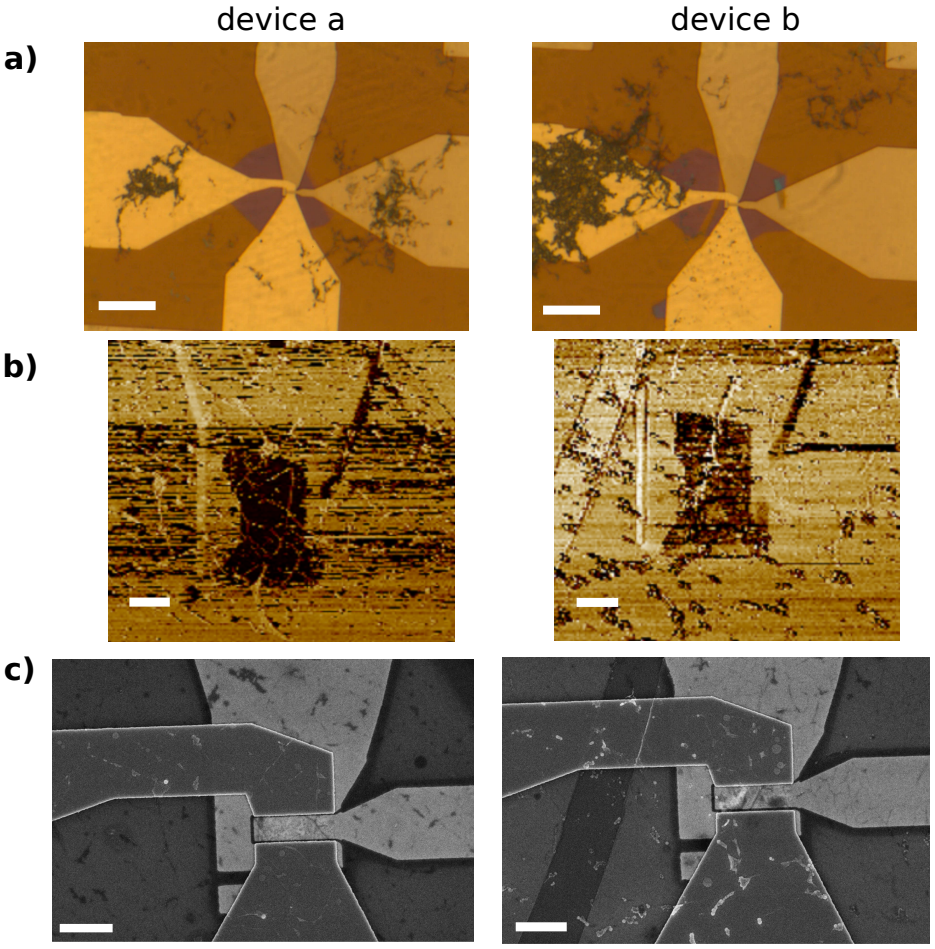

FIGURE 4.20: (a) optical pictures of devices GoBN3-4x2 and GoBN3-1x2. One can notice the remains of folded CVD graphene outside the BN flake. White scale bar: 10 μm. (b) AFM images (phase mode) of the two devices before contact deposition. One can notice the presence of a few graphene wrinkles. White scale bar: 1 μm. (c) SEM images of the devices. The channel of device 4x2 appears much cleaner than the one of 1x2. White scale bar: 1 μm. Device dimensions: $L = 500\,nm$, $W = 1.5\,\mu m$ and $t_{BN}^{4\times2} = 15\,nm$, $t_{BN}^{1\times2} = 12\,nm$.

Devices with a similar geometry are fabricated using hBN flakes as gate dielectric and CVD graphene. hBN flakes are transferred on local contact and channel tungsten gates using the van der Waals pick-up technique [8]. This step is followed by an annealing of the sample at $300°C$ with Ar/H_2 atmosphere to remove resist residues. CVD graphene is provided by the group of V. Bouchiat (Institut Néel, Grenoble) and is transferred on the wafer in wet conditions [10] at LPA. Another annealing procedure is performed after the transfer. Contacts are made of 50 nm evaporated Pd. Note that the channel dimensions slightly differ from the previous sample: for GoBN3 we have $L = 500\,nm$ and $W = 1.5\,\mu m$. AFM scans of the devices are performed systematically once the channel

has been defined by O_2 etching but before contact deposition. On the phase channel a good contrast between BN and graphene is observed. Unfortunately, many devices exhibit wrinkles or defects in the channel like the device GoBN3-4x1 in Fig. 4.19. Two other devices GoBN3-4x2 and GoBN3-1x2 are shown in Fig. 4.20

4.4.2 DC measurement: Contact gate effect at room temperature

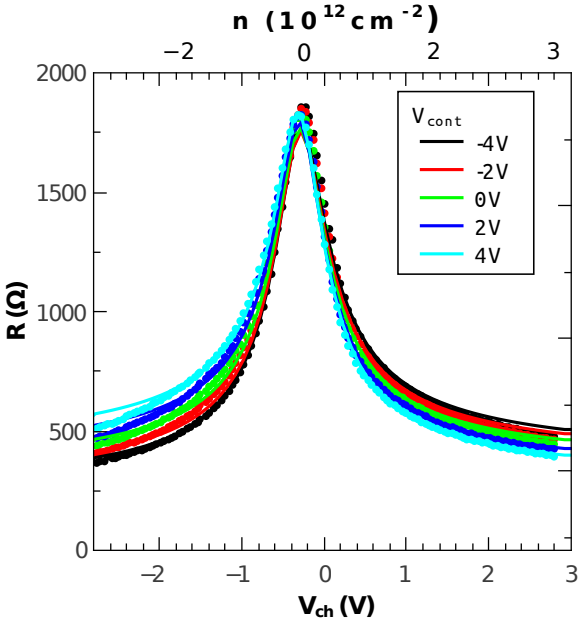

FIGURE 4.21: Device GoBN3-4x2. $R(V_{ch})$ at room temperature fitted by the contact gating model. The result of the model is: $R_K = 105\ \Omega\mu m$, $R_{mg} = 75\ \Omega\mu m$, $\mu = 3500 cm^2/V/s$, $\Delta W \simeq 10\ meV$ and $t_{dl} = 0.3\ nm$. (sample dimensions $L = 500\ nm$, $W = 1.5\ \mu m$, $t_{BN}^{4\times2} = 15\ nm$)

We focus here on two devices, 4x2 and 1x2, showing typical properties of gated contact transistors. As explained in the previous section, DC measurements are carried out to extract $R(V_{ch})$ for various V_{cont} which is shown in Fig. 4.21 and 4.22. Those samples show good modulation with the contact gate although it seems less impressive than GoBN2 studied in the previous section. The most obvious reason comes from the longer channel and lower sheet mobility for the CVD samples. Thus there is a larger contribution from the channel resistance. Nevertheless the absolute modulation is not negligible: $\Delta R \approx 140\,\Omega$ for device 4x2 $\Delta R \approx 230\,\Omega$ for sample 1x2. Let us look deeper into the data of sample 4x2 in Fig. 4.21. We see the asymmetry reversal of $R(V_{ch})$ when the contact gate is tuned over $V_{cont} = -4 \rightarrow +2\,V$, suggesting the polarity reversal of contacted graphene. The symmetric curve is obtained for $V_{cont} \approx 0V$, pointing out a very small doping induced by Pd. The smaller resistance variation with V_{cont} indicates a higher screening constant ϵ_c that is the result of a shorter metal-graphene distance t_{dl}. The model presented earlier is applied to this sample. At $V_{cont} = -4V$ the total contact

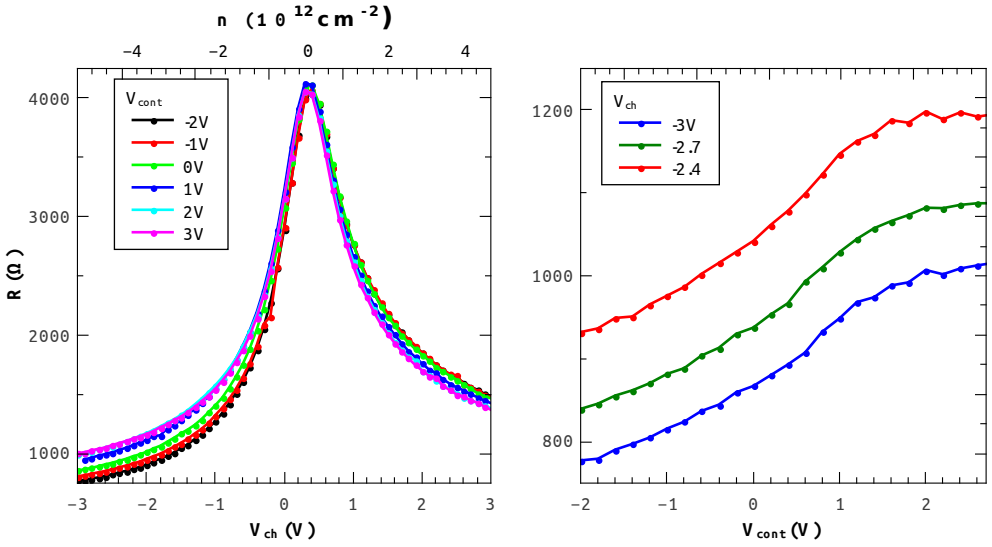

FIGURE 4.22: Transfer curves of Device GoBN3-1x2 as a function of channel gate voltage (left panel) and contact gate voltage (right panel). We observe a maximum of the $R(V_{cont})$ curve, suggesting that the contact neutrality is reached. The measured resistance remains much higher than in Fig. 4.21 indicating a lower sample quality. (sample dimensions $L = 500\,nm$, $W = 1.5\,\mu m$, $t_{BN}^{1\times2} = 12\,nm$)

resistance is $R_c = 240\,\Omega$ namely $180\,\Omega\mu m$ per contact. It is divided into the Klein tunneling resistance $R_K = 105\,\Omega\mu m$ and an additive contact resistance $R_{mg} = 75\,\Omega\mu m$. Besides, the mobility is estimated at $\mu = 3500 cm^2/V/s$. Concerning the contact doping properties, we extract $\Delta W \simeq 10\,meV$ and $t_{dl} = 0.3\,nm$ which is indeed much lower than that of GoBN2. The corresponding double layer capacitance is $C_{dl} = 30\,fF\mu m^{-2}$ which is an order of magnitude larger than $C_{cont} = 2\,fF\mu m^{-2}$. Thus the screening constant is $\epsilon_c = 140\,meV$, and the tunable energy scale is

$$\epsilon_W = \frac{C_{cont}}{C_{dl} + C_{cont}} eV_{cont} + \Delta W \simeq 0.045 eV_{cont} + 0.01\,eV, \tag{4.34}$$

expressed in eV with V_{cont} in V. So ϵ_W varies from $-170\,meV$ to $190\,meV$. Therefore, this device operates in both screened and unscreened regimes, and the carrier density below the contacts is modulated as $n_{cont} \approx \pm 1 \times 10^{12}\,cm^{-2}$.

In accordance with the images of Fig. 4.20 device GoBN3-1x2 shows some degraded characteristics: it has a higher contact resistance (baseline at $\sim 800\,\Omega$) and a higher channel resistance ($R(V_{ch}) \sim 4000\Omega$ at Dirac point) indicating a lower mobility. However a good modulation with contact gate is observed and $R(V_{cont})$ has a maximum, indicating that we reach neutrality in the contacted area.

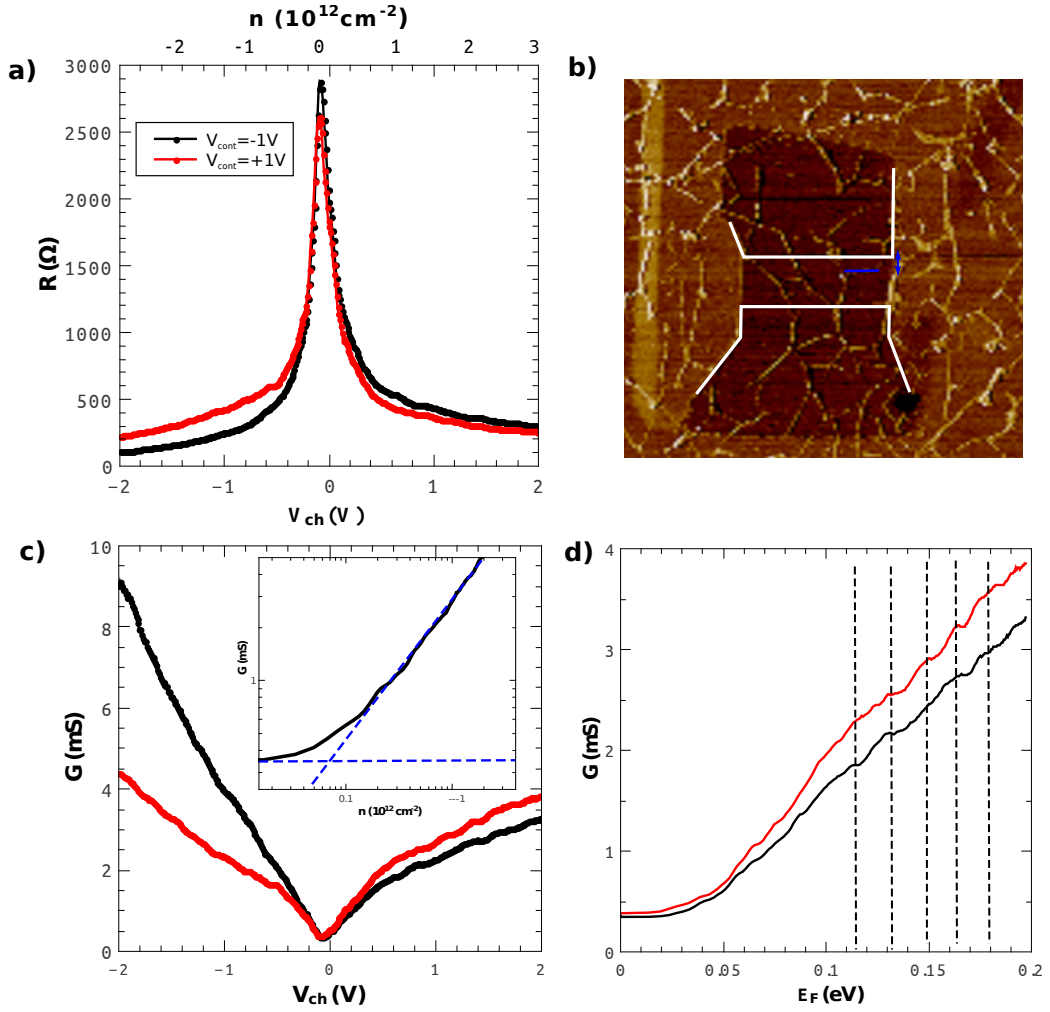

FIGURE 4.23: 10 K measurement on device GoBN3-4x2. Sample dimensions: $t_{BN}^{4\times1} = 15\,nm$, $L = 500\,nm$, $W = 1.5\,\mu m$. (a) Transfer curve $R(V_{ch})$ for $V_{cont} = -1V$ (black line) and $V_{cont} = +1V$ (red line) (b) Phase signal of the AFM scan of the channel. The contact edge position is shown with white lines. The blue line highlights a wrinkle that could be one barrier of the Fabry-Pérot cavity (the scale is set by the contact distance of 0.5 μm) (c) Same as (a) but for the conductance. Inset: $G(n_{ch})$ in logarithmic scale to determine the residual density $n_0 \approx 7 \times 10^{10}\,cm^{-2}$. (d) Conductance in the n-doped regime as a function of the Fermi level energy. The dashed lines identify conductance peaks with a spacing of $\approx$ 16 meV which corresponds to the resonances in a cavity whose length is $\approx 129nm$.

4.4.3 Low temperature measurement

A measurement of the GoBN3 sample was carried out in the Janis probe station at $10^{-5}\,mbar$ and 10 K. Looking at the transfer curves of device 4×1 in Fig. 4.23, one can notice first the amazing improvement in the channel gate modulation (now a factor ~ 10), the sharpness of the resistance peak ($n_0 \approx 7 \times 10^{10}\,cm^{-2}$ determined from the $log\,G$ vs $log\,n$ plot in the inset of Fig. 4.23) and the minimum resistance (100 Ω) which implies a very low contact resistance ($R_c \sim 75\,\Omega\mu m$). This resistance value suggests that

we now deal with a quasi-ballistic device as this is what we expect in the ballistic regime when the transport is coherent through the sample.

$$R_K = (\frac{4e^2}{h}\frac{\sqrt{\pi n}W}{\pi})^{-1} = 54\,\Omega \tag{4.35}$$

When $n = 2 \times 10^{12} cm^{-2}$. Another signature of ballistic transport is observed through Fabry-Pérot oscillations. They are rather weak due to a good contact transparency. Even though different frequencies seem to be mixed, we can identify some periodic conductance peaks indicated by the dashed lines in Fig. 4.23. The spacing between peaks is $\Delta E_F \approx 16 meV$ which corresponds to a cavity length of $\approx 129nm$. To understand that cavity length one has to come back to the AFM image of sample 4×1 (Fig. 4.19) that shows a few wrinkles in the channel. Oscillations are less visible for $V_{cont} = -1V$ and V_{ch} on the p-doping side, which is consistent with a higher transmission of the contact junction on that side. For $V_{cont} = +1V$, conductance is low and the oscillations are visible on both sides, indicating a low transmission barrier at the contacts, this suggests that the contacted graphene is close to neutrality for $V_{cont} = +1V$. From those observations and the cavity length of $\approx 129nm$, we assume that the observed Fabry Pérot oscillations are the result of reflections between a contact and a wrinkle. The cavity is depicted in Fig. 4.19 between the contact edge in white and the wrinkle in blue. From this we can estimate a lower boundary for the carrier mobility: $\mu = l_{mfp} e v_F / E_F > 12800\, cm^2/V/s$ at $E_F = 100\, meV$. Nevertheless, some faster oscillations but with lower contrast suggest that the mobility could be higher.

The minimum conductivity that we measure is $\sigma^{min} = 1.16 \times 10^{-4} S$ which is higher than the theoretical value of $4e^2/(\pi h)$ [21, 22] but smaller than $4e^2/h$ in accordance with the W/L ratio [23].

4.5 Variations around the gated contact (GoAl samples)

In collaboration with Thales Research & Technology and Michael Rosticher (ENS) we fabricated and measured a series of devices based on the same split local back gate in tungsten but at a larger scale. In order to avoid tedious and uncertain flakes transfers and looking for more reproducibility we used wafer scale fabrication techniques: the dielectric is now made out of aluminium oxide deposited by Atomic Layer Deposition and graphene is obtained using CVD (from Graphene Supermarket). Using those techniques we were able to obtain many more devices in each fabrication run. This allowed us to play with the geometry of the devices and in particular to vary the position of the contacts with respect to the gates. Two particular geometries will be shown here, the shifted contacts and the backward contacts.

We can start with a comment about the dielectric quality of Al_2O_3 versus hBN. In Fig. 4.24 we plot the drain-current temporal trace under contact gate pulse actuation for both dielectrics in the experimental conditions described in section 4.3.5. The current relaxation observed in the case of Al_2O_3 indicates the presence of interface charges with slow dynamics (typically 100 ns) [88, 89]. Those interface charges are also responsible for gate hysteresis effects. They are not present in hBN which is thus a more stable

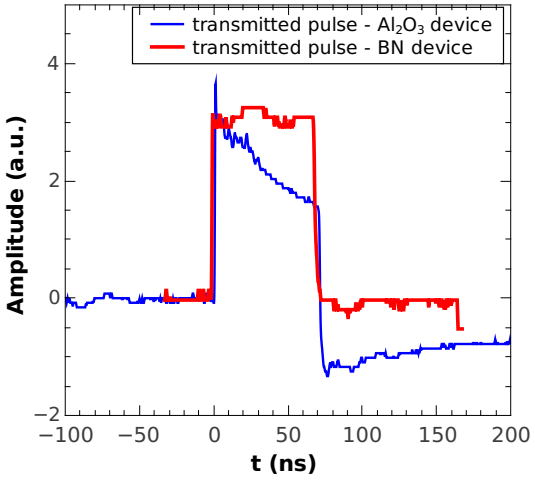

FIGURE 4.24: Drain current temporal trace measured with an oscilloscope under pulsed contact gating using h-BN (red line) and Al_2O_3 (blue line) for the gate dielectric. The slow current decrease in the case of Al_2O_3 is reminiscent of an interface charge relaxation effect. This measurement confirms the superiority of hBN as a dielectric.

4.5.1 The shifted contact (sample GoAl1)

The device GoAl1 has an inter-gate gap which is purposely set at the middle of the channel (Fig. 4.25-c). The source and drain contact edges are each located on top of a different gate electrode. Therefore, this device has 3 junctions in series: 2 contact junctions (which are not symmetric) and another junction in the channel. This makes the analysis of the transport properties more complex. In addition it has to be mentioned that the graphene mobility is much lower in this case as both the dielectric and the graphene itself are not optimized for high mobility. Thus the measured resistance is dominated by the mobility limited sheet resistance and the contribution of the junction is more elusive. Another factor that we could take into account is that the dielectric takes the shape of the gate electrodes and thus there is an air gap in the inter-gate space, where graphene is suspended (over $\sim 10nm$).

Figure 4.26-a shows the transfer curve of GoAl1 $R(V_{g1})$ for different V_{g2} ($g1$ being the former channel gate and $g2$ the former contact gate). Unfortunately, the $g2$ gate is leaking

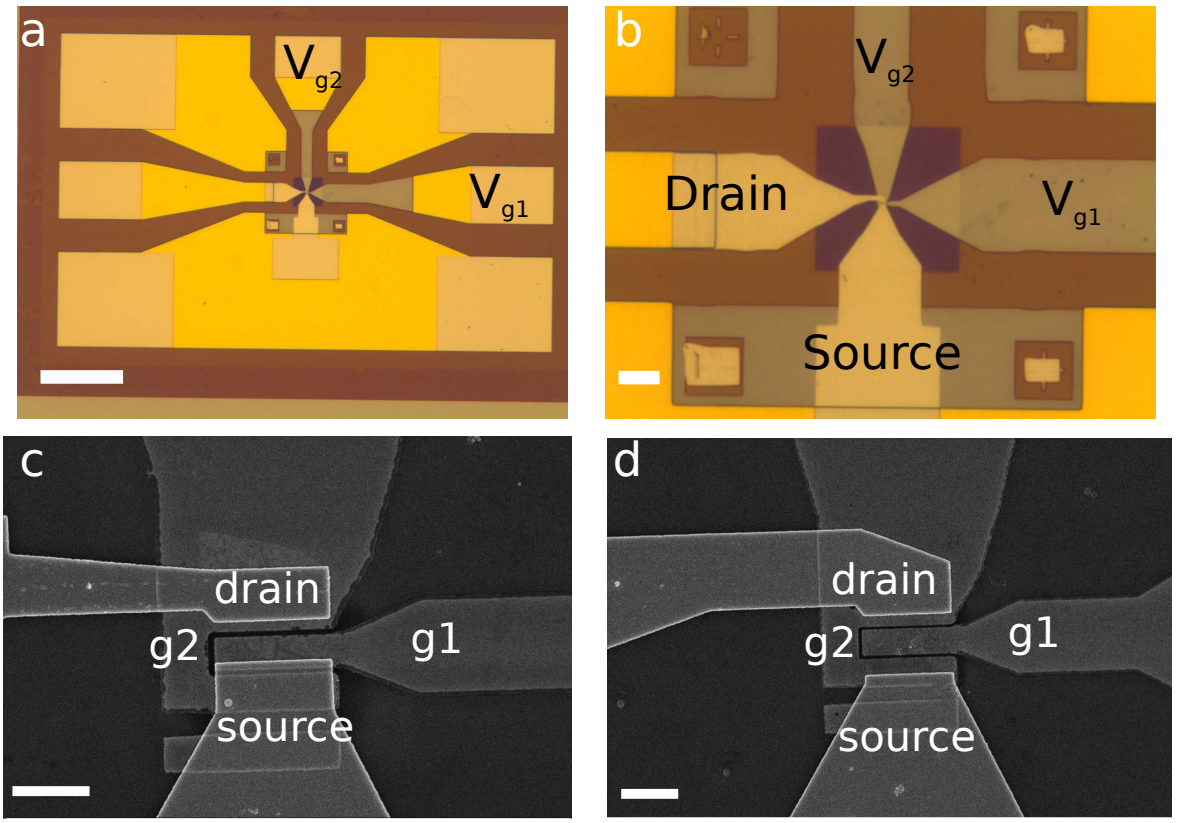

FIGURE 4.25: Graphene on Al_2O_3 ALD with local split gates. (a) coplanar waveguide with 3 terminal. White scale bar: 100 μm. (b) zoom on the active area. The blue square corresponds to the Al_2O_3 deposited, the gate tungsten electrodes are on the top right and the palladium contacts are on the bottom left. White scale bar: 10 μm. (c) SEM image of the shifted contact GoAl1. (d) SEM image of the backward contact GoAl2. White scale bar: 1 μm.

at $V_{g2} > 0.6V$ which limits our working range. First we notice that the $R(V_{g1})$ curves are mainly shifted when tuning V_{g2}. Second, we note that with our particular process graphene is naturally p-doped. As a result, the CNP lies at $V_{g1} \approx +2V$ (for the $g1$ area), similarly the resistance increases with V_{g2} which also indicates a CNP at positive voltage although no maximum is visible when varying V_{g2} (the voltage range is too small). We do not aim to fully analyse those data, but we can make a few qualitative remarks: it seems that the effect of our dual gate geometry is essentially to tune independently the carrier density (n_1 and n_2) of two distinct areas in series ($g1$ and $g2$ respectively). However, the transfer characteristic is not symmetric and it shows a shoulder for $V_{g1} < 2V = V_{DP}$. This deviation from the standard transfer curve is a sign of the presence of two asymmetric junctions at both ends of the $g1$ area. On one side we have the sharp contact junction studied before but here the carrier density of contacted graphene is tuned by the same gate that controls the $g1$ area. On the other side there is a smoother junction, defined by the inter-gate gap whose transmission is controlled by both V_{g1}

and V_{g2}. The transition from a flat $R(V_{g1})$ for $V_{g1} < -2V$ to the shoulder could be set by the transition from $n_1 < n_2 \rightarrow n_1 > n_2$. Defining R_{K1}, R_{K2} and R_{K12} to be the resistances from the contact junction on the $g1$ side, on the $g2$ side, and between $g1$ and $g2$ respectively we can write the total resistance:

$$R(V_{g1}, V_{g2}) = R_{K1} + \frac{L}{W}(C_{Al_2O_3} V_{g1} \mu)^{-1} + R_{K12} + \frac{L}{W}(C_{Al_2O_3} V_{g2} \mu)^{-1} + R_{K2} \quad (4.36)$$

Where $C_{Al_2O_3}$ is the gate capacitance and $\mu \approx 2000 cm^2/V/s$ is the sheet carrier mobility.

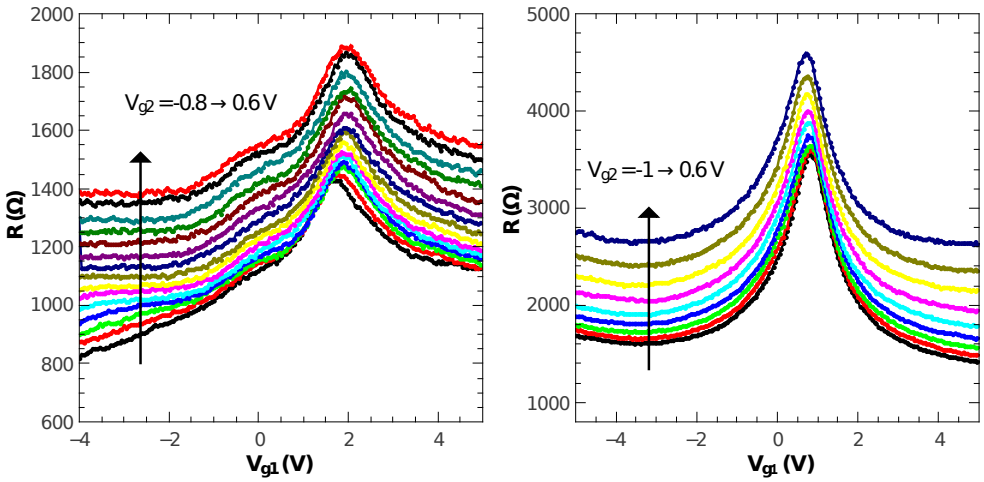

FIGURE 4.26: Left panel: GoAl1 device with shifted contact. Right panel: GoAl2 device with backward contact. In both cases the curves are mainly shifted upward when the second gate is tuned which is attributed to a finite mobility effect of the graphene sheet.

4.5.2 The backward contact (sample GoAl2)

GoAl2 has both contacts lying on top of the former contact gate (Fig. 4.25-d). Therefore there are two symmetric contact junctions and two symmetric junctions ($g2 \rightarrow g1$ and $g1 \rightarrow g2'$) in the channel. The device is symmetric, and accordingly the transfer curves shown in Fig. 4.26-right are indeed symmetric. Again, the main feature of this measurement is the shifting of the curves when V_{g2} is tuned, indicating transport properties limited by diffusion in areas with different carrier densities. The origin of the onset of a secondary resistance peak at negative V_{g1} is not clear and could for example be due to the bending of the suspended graphene through the inter-gate gap.

4.6 Conclusion and perspectives

In this chapter we have introduced a new architecture for a graphene transistor: the gated contact. Having a specific gate for the contact and having this gate very close to the contacted graphene opens new perspectives of applications for graphene devices. In DC, the contact polarity is fully controlled by the contact gate, the metal induced doping can be enhanced to lower the contact resistance or compensated to achieve contact neutrality, it can even be reversed. The device transport properties are well understood with standard contact gating and p-n junction transmission models. In addition, we have demonstrated that the contact gate can be actuated at GHz frequencies with a transconductance comparable to usual channel gating.

Pushing the RF gated transistor further, we could break the scaling limit by having only a contact gate to actuate the transistor hence not limited by the length of the channel gate. This contact gate could also prove to be useful for optoelectronic devices where the photocurrent is often generated at the asymmetric contact junctions. To this end, the asymmetric GoAl devices, presented in the last section, could be of great interest. Indeed, it is a way to introduce a sharp p-n junction which is electrostatically controlled in the channel of a graphene transistor. It has been shown several times that a photocurrent is generated around a p-n junction [25, 76] through the photoelectric or the photo-thermo electric effect. Here we could take advantage of the short channel, the sharp and tunable junction, and the fact that our devices are embedded in a coplanar waveguide to study fast photocurrent generation [90]. In particular, asymmetric contacts are generally used to generate a non-compensated current at both contacts, here, the asymmetry level is directly controlled by V_{g1} and V_{g2}. We have started some preliminary photo-rf transport experiments with those devices, unfortunately the optical part of our setup is not yet optimized and the optical power incident on the device was too low to allow for photocurrent detection.

In the longer term, the gated contact could be implemented in an electronic quantum optics experiment for single electron sources [40].

Chapter 5

Velocity saturation in local gate devices

In a transistor, the current saturation may have two origins. One is the pinch-off effect that occurs when the depletion region appears at the drain side of a semiconductor device. The other is when the current saturation is actually due to carrier velocity saturation which is a consequence of the phonon scattering. It is the one that generally prevails in graphene. In this chapter we aim to address the subject of the high bias regime, that is to say high drain source voltage ($V_{ds} \gtrsim 100\,mV$). In this regime and for high mobility samples, current saturation occurs, but with a peculiar aspect due the local nature of the gating and related to the bias-induced doping profile in the channel.

Let us start with an experimental observation. In figure 5.1 we plot the I-V characteristics and the differential resistance $r(V_g) = \frac{dV_{ds}}{dI}$ (differentiated numerically or directly extracted from a small signal measurement at finite frequency) at various V_{ds} for two types of devices: graphene on hBN with a remote back gate [1] (left panel) and graphene on hBN with a local bottom gate (right panel, device GoBN3-4x2 of section 4.4.2).

First, we notice a trend toward current saturation in the I-V characteristics when V_{ds} increases. This sublinear behavior is also reflected in the increase of the differential resistance with V_{ds} for certain V_g. This effect is generally attributed to scattering by optical phonons which are triggered at high bias due to their rather high energy $\hbar\Omega$ [91–96]. A debated question arises here: whether the relevant optical phonon are the graphene intrinsic ones ($\hbar\Omega_{gr} \approx 150\,meV$ [97]) or those of the substrate ($\hbar\Omega_{SiO_2} \approx 55\,meV$, $\hbar\Omega_{hBN} \approx 100\,meV$ [95]). This is illustrated by the graphene phonon spectrum and the hBN infrared spectroscopy of Fig. 5.2.

[1] The data is extracted from measurements by A. Betz [36]. The sample is a $L \times W = 2.2 \times 2.7\,\mu m^2$ graphene flake on hBN, the Si substrate is used as a gate with a dielectric thickness of $1\,\mu m$

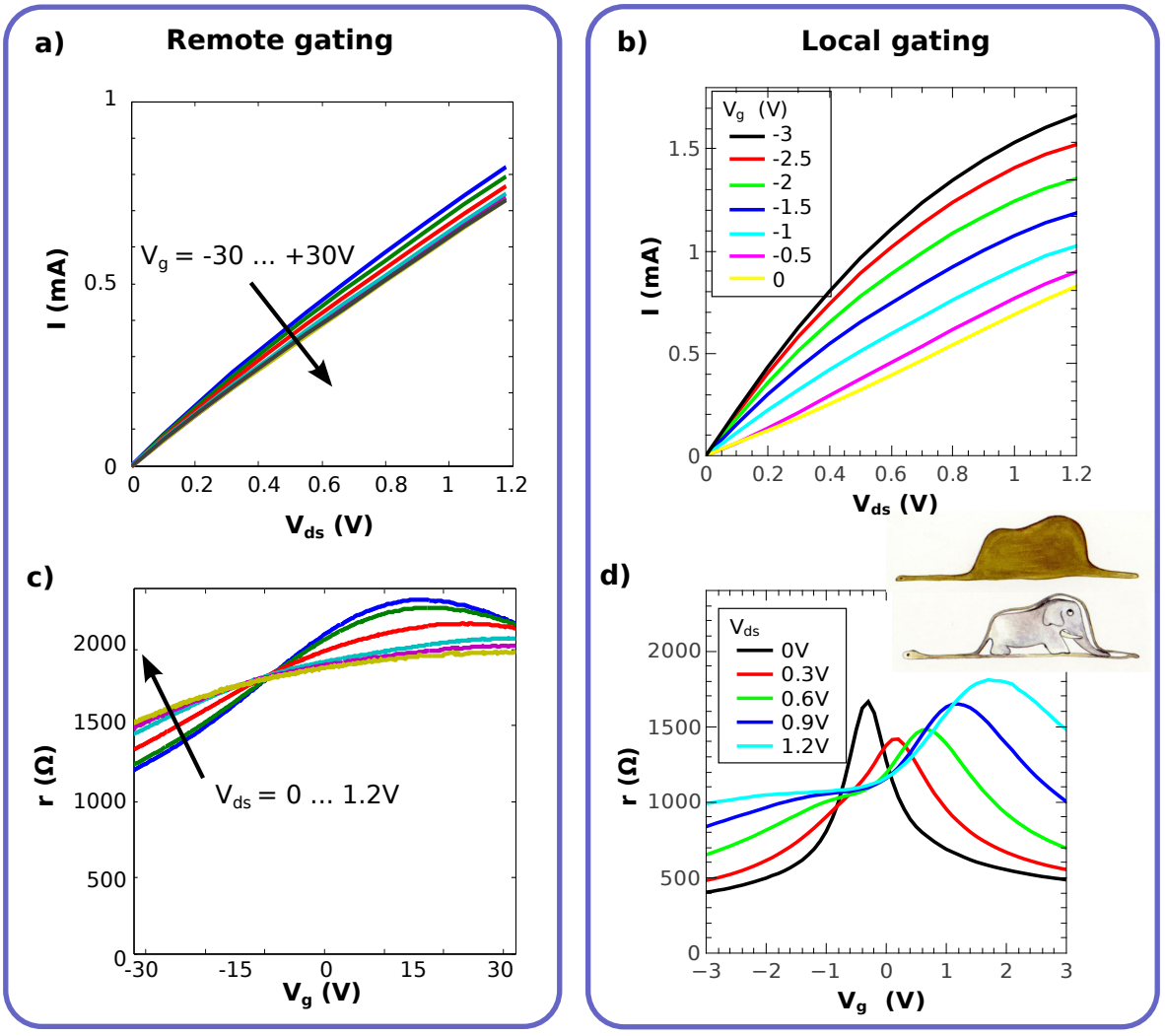

FIGURE 5.1: Observation of high biased samples. The left panel is adapted from [36] with a graphene sample $L \times W = 2.2 \times 2.7\ \mu m^2$ on hBN with a remote (silicon substrate/$1\mu m$ SiO_2) back gate. (a) I-V characteristic for several gate voltages. (c) Differential resistance $r = \frac{dV_{ds}}{dI}$ as a function of gate voltage for increasing bias voltages $V_{ds} = 0 \rightarrow 1.2V$. Right panel: measurements performed on sample GoBN3-4x2 ($L \times W = 0.5 \times 1.5\ \mu m^2$, see section 4.4.2), with a local gate. (b) I-V characteristics for various gate voltages. Thanks to a good mobility, the I-V curves show a trend to saturation. (d) Differential resistance $r(V_g)$ for $V_{ds} = 0 \rightarrow 1.2V$. The "boa digesting an elephant" shape is a characteristic feature of a locally gated device

Secondly, we observe a peculiar differential resistance $r(V_g)$ curve shape at high V_{ds} for the local gate device (Fig. 5.1-d), which is different from the one observed for the remote gate device (Fig. 5.1-c). This particular shape, that we are going to call "a boa digesting an elephant" (and not a hat) is characteristic of local gate devices. For those devices the quantum capacitance effect is not negligible and the gate cannot set a homogeneous carrier density in the channel. As a result, when driven at high bias, the device may present a localized charge neutrality point (CNP) in the channel (analog to the "pinch-off" effect in MOSFET) whose position depends on (V_g, V_{ds}) [91]. Therefore our GoBN

geometry is well suited to study both effects. In order to separate them we distinguish three domains: in the range $V_g = -3 \rightarrow -1\,V$ of Fig. 5.1-d the channel is unipolar p and the prominent mechanism is the optical phonon scattering, in the range $V_g = -1 \rightarrow 2\,V$ the channel is bipolar and the main resistance contribution comes from the bias induced CNP in the channel. For $V_g > 2\,V$, the channel is unipolar n.

As we shall see in chapter 6, those high bias phenomena turn out to be of great importance for the realization of graphene radio frequency (RF) transistors as both large V_{ds} and local gates are needed to achieve high transconductances. On one hand, the device speed is limited by the carrier saturation velocity $v_{sat} = (2/\pi)\hbar\Omega v_F/E_F$ that depends on the optical phonon energy involved in the scattering mechanism. On the other hand the increase of the differential resistance (hence the current saturation) leads to enhanced voltage gains and ultimately to a higher power gain cut-off frequency f_{max}.

In the present chapter, we focus on the physical phenomena underlying the high bias curves in Fig. 5.1-b and d. We first present a simple model (inspired from [98]) describing the scattering by optical phonon. We use it to analyse our experimental results and single out the most prominent scattering mechanism (intrinsic optical phonon or substrate phonon). Finally we integrate this mechanism to a model for the heterogeneous doping profile in the channel to explain the "boa digesting an elephant" shape of the transfer curve at high bias.

5.1 Current saturation by optical phonon scattering

5.1.1 Introduction and overview

In graphene, acoustic phonons interact weakly with electrons, they are relevant at low field and their effect is visible in high mobility samples. At room temperature, the intrinsic graphene resistivity is limited by acoustic phonon scattering corresponding to a mobility of $\mu = 2 \times 10^5\ cm^2/V/s$ [8, 102]. The low acoustic phonon-electron interaction is responsible for the exceptional conductivity of graphene and the fact that its room temperature mobility exceeds that of any other semiconductor. At moderate fields, acoustic phonons control the out-of-equilibrium electronic temperature [103, 104]. But at very high field ($V \sim 1V/\mu m$), the scattering by optical phonons becomes predominant [96, 105]. The graphene intrinsic optical phonons energy threshold is $\hbar\Omega_{gr} \approx 150\,meV$; they have been identified as the main source of relaxation at high energy by means of shot noise thermometry in suspended bilayer graphene by Laitinen et al. [96]. However,

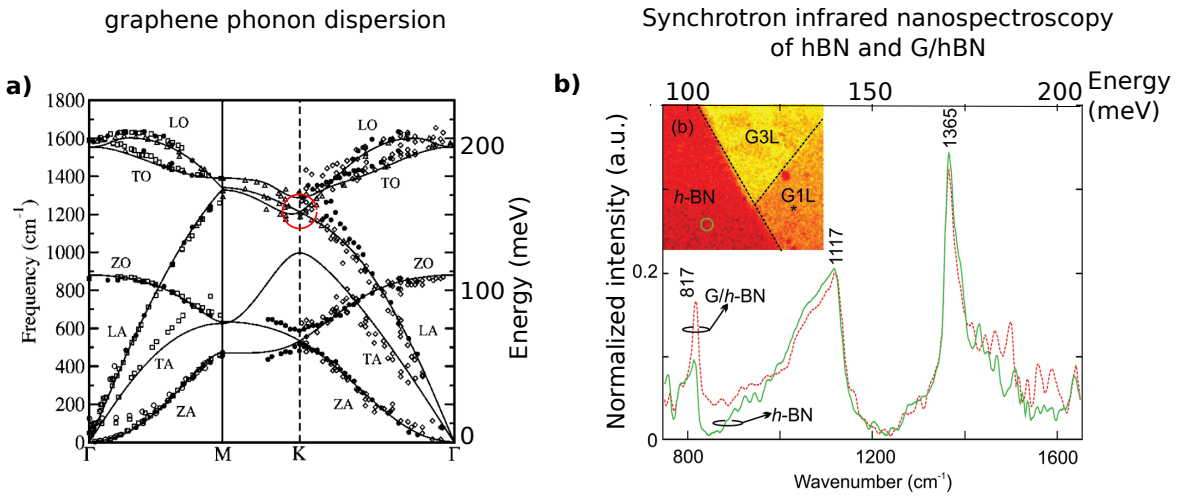

FIGURE 5.2: (a) Phonon dispersion and electron energy loss spectroscopy data for graphene (ref. [99]). The main optical phonon scattering mechanism is due to the longitudinal optic (LO) phonons at the K point (red circle), that is to say $\hbar\Omega_{gr} \approx 150\,meV$. (b) Infrared nanospectroscopy of hBN and graphene on hBN from ref. [100]. A low energy peak is observed at $817\,cm^{-1} = 101.3\,meV$ which corresponds to the surface phonon of hBN relevant for electronic transport. This surface phonon energy can be derived from the LO phonon energy [95, 101].

for supported samples, the measured saturation velocities $v_{sat} = (2/\pi)\hbar\Omega v_F/E_F$[2], where E_F is the graphene Fermi level energy, are lower than the intrinsic optical phonon limit, pointing out a lower energy of the phonon responsible for scattering [91, 92, 94, 95, 102] (except for [93]). Consequently, the scattering by the substrate's optical phonons, called remote phonons or surface polar phonons (SPP) is invoked. Indeed, the impact of substrate phonons on the electronic transport in semiconductors is well known since 1972 [106, 107], and it was soon considered in the case of graphene by Fratini and Guinea [108]. As a result, the saturation velocity must depend on the substrate, for example, it should be lower for graphene on SiO_2, for which $\hbar\Omega_{SiO_2} \approx 59\,meV$ than for graphene on hBN $\hbar\Omega_{hBN} \approx 100\,meV$ [95]. We show in Fig. 5.2-a the graphene phonon spectrum where the characteristic energy can be identified for the longitudinal optic phonon at the K point. We show as well in Fig. 5.2-b, a spectroscopy measurement by Barcelos et al. [100] indicating a surface phonon mode of hBN at $\simeq 100\,meV$.

We are aware of numerous saturation velocity measurements and analysis for SiO_2 [91–95], but very few for hBN [109]. Our study is therefore important to identify the saturation mechanisms specific to graphene on hBN substrate that will limit the performance of such transistors.

[2]Related to the saturation current by $I_{sat} = nev_{sat}W$, where n is the graphene carrier density and W is the sample width.

Substrates	SiO_2	Al_2O_3	HfO_2	*Sapphire*	*Diamond*	*SiC*	*hBN*
ϵ_r	3.9^a	7.4^a	11.7^a	9^a	5.5	9.7^b	4.1^b
$\hbar\Omega$ *(meV)*	58.9^b	55^c	21.6^b	$\approx 48^d$	165^e	116^b	101.7^b

TABLE 5.1: Dielectric constants ϵ_r and surface phonon energies $\hbar\Omega$ of usual graphene substrates and gate dielectrics. A high ϵ_r dielectric is an advantage in term of gating efficiency, but more important is the value of $\hbar\Omega$ as it determines the saturation velocity. From this, the diamond, SiC and hBN seem to be the best substrates (note however that diamond and SiC cannot be used with local bottom gating).
[a] *private communication from D. Neumaier, AMO.* [b]Ref. [95]. [c]Ref. [110]. [d]Ref. [111]. [e]Ref. [112].

In [93] (see Fig. 5.3-a) the current saturation is investigated for graphene on SiO_2 with a remote back gate. The contact resistance issue is solved by using a four-point measurement. The data is compared to a model based on the Boltzmann equation including impurity and optical phonon scattering. The energy of the graphene intrinsic optical phonon $\hbar\Omega = 149\,meV$ is taken as an input of the model and fits well the data. In [91], (see Fig. 5.3-c) graphene on SiO_2 is considered as well, but with local gating. As a result there is "kink" in the I-V characteristic (also in Fig. 5.3-b). This effect is related to the "elephant" effect observed above: it is due to a non-uniform doping profile in the channel at high bias. For a certain couple of values (V_g,V_{ds}) the CNP is localized in the channel, and an increase in V_{ds} just shifts the CNP position without changing the device resistance. At higher V_{ds}, the channel is unipolar again and a nearly linear $I(V_{ds})$ is restored (this will be further discussed in section 5.2). So it is important to distinguish the current saturation from optical phonon scattering and the current saturation from a bipolar channel. Nevertheless, in [91], the authors claim that they can take into account this effect in their analysis of the I-V curve, and they extract a relevant phonon energy of $\hbar\Omega = 54\,meV$ thus very close to the SiO_2 phonon energy. However it is worth noting that the definition used to extract $\hbar\Omega$ is not consistent with other studies [92–95] by a factor $2/\pi$ (see also Eq. (5.7)). Finally, to our knowledge, one single current saturation measurement of graphene on hBN has been reported so far [109], that is plotted in Fig. 5.3-b. The author extract a relevant phonon energy $\hbar\Omega = 40\,meV$ significantly far from the hBN phonon energy of $100\,meV$. However, the same comments as above can be made concerning the analysis.

5.1.2 Theoretical elements of optical phonon scattering

Here we present a model to describe the current saturation observed in our samples. As there is still a debate on the relevant phonon responsible for scattering we note $\hbar\Omega$ the

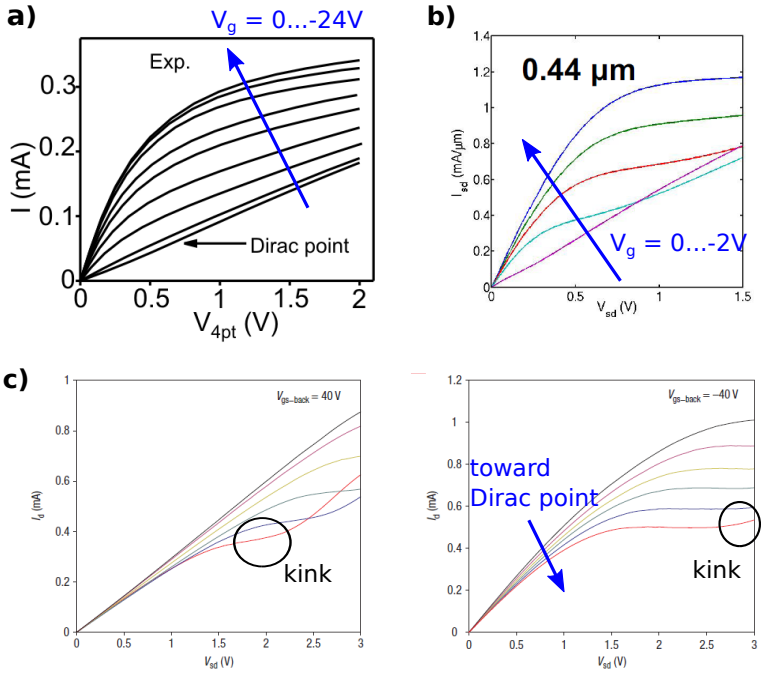

FIGURE 5.3: (a) Current saturation measurement for graphene on SiO_2 by Barreiro et al. [93]. Sample size: $L = 1.3\mu m$, $W = 0.35\mu m$. The current is measured in a four-point configuration, thus avoiding contact resistance effect and for various remote back gate voltages V_g. (b) Current saturation measurement for graphene on hBN by Meric et al. [109]. Sample size: $L = 0.44\mu m$. The current is measured within a 2-points configuration and with a local gate. The light blue curve shows a "kink" effect, characteristic of a local gated device, for which the current nearly saturates around $V_{ds} \sim 0.5 \rightarrow 1\,V$ before increasing again at $V_{ds} > 1\,V$. This effect is a sign of a bipolar channel (as explained in [91]). Note that for both measurement the maximum current density is around $1\,mA/\mu m$ (c) Current saturation measurement from [91]. The left plot is taken at lower density to show the kink effect. The right plot is taken at higher density to ensure an unipolar channel and extract the optical phonon energy, but the kink is also observed at $V_{sd} = 3V$.

phonon energy whose value should settle the question about its nature.

To model the scattering by optical phonon we rely on a simple heuristic model which has been introduced in the case of the Carbon Nanotube by Yao et al. [98] and for graphene in [93] and in [113] where it is supported by Monte Carlo simulations. In that model, one considers the graphene electrons being accelerated by an electric field $\mathcal{E}$ and it is assumed that once an electron reaches the energy of the optical phonon (or of the SPP) it is stopped and emits a phonon. Thus the phonon emission occurs when the electric field work is equal to the phonon energy:

$$e\mathcal{E}l_\Omega = \hbar\Omega \tag{5.1}$$

$$l_\Omega = \frac{\hbar\Omega}{e\mathcal{E}} \tag{5.2}$$

Where l_Ω is the scattering length associated with the emission of an optical phonon.

In the case of ballistic graphene, where the optical phonons would be the only source of scattering, this would lead to a conductance [114]:

$$G^0 = \frac{4e^2}{h}\frac{k_F W}{\pi}\frac{l_\Omega}{L + l_\Omega} \tag{5.3}$$

Where L is the sample length and we assume $L >> l_\Omega$. Besides we have $\mathcal{E} = V_{ds}/L$. From Eqs. (5.2) and (5.3) we get

$$G^0 = \frac{4e^2}{h}\frac{k_F W}{\pi}\frac{\hbar\Omega}{eV_{ds}}, \tag{5.4}$$

which gives a saturation current:

$$I_{sat} = \frac{4e^2}{h}\frac{k_F W}{\pi}\frac{\hbar\Omega}{e} \tag{5.5}$$

$$= \frac{2ek_F W\Omega}{\pi^2} \tag{5.6}$$

We can estimate this current. If the main source of scattering comes from the intrinsic graphene optical phonons then $\hbar\Omega \approx 150 meV$. Thus $I_{sat} = 1.3 mA/\mu m$ at $n = 10^{12} cm^{-2}$ and $I_{sat} = 3.2\, mA/\mu m$ at $n = 6 \times 10^{12} cm^{-2}$ (this is the maximum density at which we measured the saturation). On the contrary, if the dominant scatterers are the phonons of the substrate, in the case of hBN: $\hbar\Omega \approx 100\, meV$. Which leads to $I_{sat} = 0.9\, mA/\mu m$ at $n = 10^{12} cm^{-2}$ and $I_{sat} = 2.1 mA/\mu m$ at $n = 6\times 10^{12} cm^{-2}$. Note that in [93] it is specified that the I_{sat} formula is valid only for $E_F \geq \hbar\Omega/\sqrt{2}$, that is to say $n \geq 0.4 \times 10^{12} cm^{-2}$

Velocity saturation This saturation can also be expressed in terms of carrier velocity saturation v_{sat} using $I_{sat} = nev_{sat}W$. Which gives:

$$v_{sat} = \frac{2}{\pi}\frac{\hbar\Omega}{E_F} \times v_F \tag{5.7}$$

Here, one should be careful with the $2/\pi$ pre-factor which was "forgotten" in [91, 115] and which changes the calculated value of Ω when the measured quantity is I_{sat}.

In the high bias limit, even for a diffusive device the smallest scattering length would be the one associated with optical phonons, we therefore expect an actual saturation current of the order of the estimations above. Theoretically its value should allow us to discriminate between the intrinsic phonons and the SPP. However we never observe a full saturation of the current and we need to include scattering by impurities for a more accurate description.

Accounting for impurity scattering

The impurity mean free path is given by

$$l_e = \frac{2}{\pi}\mu\hbar\sqrt{\pi n}/e \tag{5.8}$$

We then use Matthiessen's rule to add the different sources of scattering (see Fig. 5.4):

$$\frac{1}{l_{scat}} = \frac{1}{l_e} + \frac{1}{l_\Omega}, \tag{5.9}$$

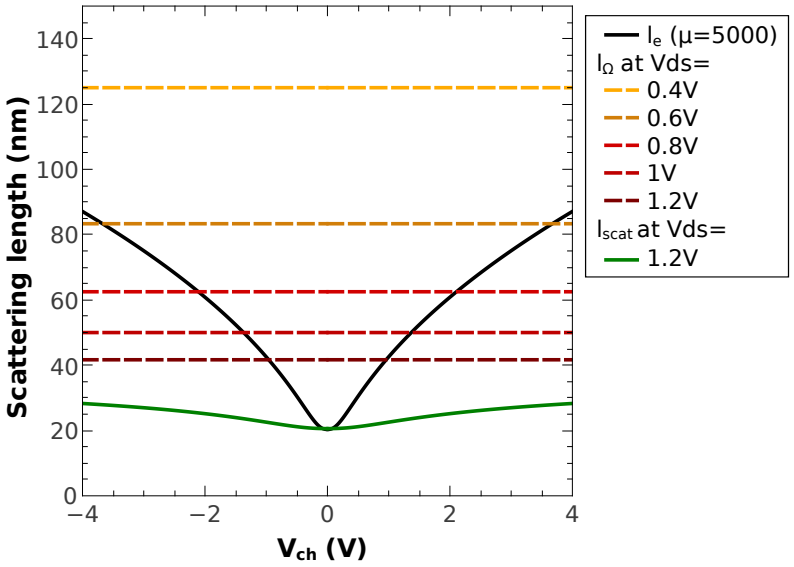

FIGURE 5.4: Comparison between the impurity scattering length l_e from Eq. (5.8) (black line) and the optical phonon scattering length l_Ω for different bias voltages using Eq. (5.2) (dotted lines). The total scattering length obtained with the Matthiessen's rule is plotted with a dark green solid line at high bias (phonon limited).

and the sample conductance is now given by [114]:

$$G = \frac{4e^2}{h}\frac{k_F W}{\pi}\frac{l_{scat}}{L + l_{scat}} \tag{5.10}$$

Which can be expressed as a resistance:

$$R = \frac{h\pi}{4e^2 k_F W}(1 + L(\frac{1}{l_e} + \frac{1}{l_\Omega})) \tag{5.11}$$

$$= \frac{h\pi}{4e^2\sqrt{\pi n}W}(1 + \frac{eL}{\frac{2}{\pi}\mu\hbar\sqrt{\pi n} + \frac{eV_{ds}}{\hbar\Omega}} \tag{5.12}$$

$$= \frac{h\pi}{4e^2 k_F W} + \frac{L}{Wne\mu} + \frac{h\pi}{4e^2 k_F W}\frac{eV_{ds}}{\hbar\Omega} \tag{5.13}$$

We can easily identify the three terms in that expression: The first term is the ballistic resistance, the second term is the well known diffusive term while the third term corresponds to the calculation above where the only source of scattering are the optical

phonons, this is the term responsible for saturation. A convenient experimental way to extract the saturation current is to write [98]:

$$R = R_0 + \frac{V_{ds}}{I_{sat}} \tag{5.14}$$

Where R_0 contains the first 2 terms of Eq. 5.13 plus (in experimental conditions) the contact resistance. Measuring $R(V_{ds})$ one obtains a linear behavior where the constant term gives information on the impurity scattering (hence the mobility) and the contact resistance while the slope gives information on the optical phonon energy. This is therefore a good way to decouple the optical phonon contribution from other scattering sources.

Equivalently, taking Eq. 5.13, neglecting the ballistic term ($\frac{h\pi}{4e^2 k_F W}$) and using the previously calculated velocity saturation v_{sat} one could express the current as:

$$I = \frac{V_{ds}}{R} = Wne\frac{\mu V_{ds}/L}{1 + \mu V_{ds}/(Lv_{sat})} \tag{5.15}$$

As a conclusion of this theoretical section we note that the effect of a low mobility is mainly to increase the treshold voltage of saturation and to blur the transition toward the current saturation regime. It explains why current saturation is only observed in high-mobility samples. If the mobility is too low, the sample burns before showing a saturation effect.

5.1.3 Experimental results

In Fig. 5.5 we show our experimental results at high bias obtained on the graphene on hBN sample GoBN3-4x2 already presented in section 4.4. Several devices have been measured and show similar results, GoBN3-4x2 being chosen for its low contact resistance. In this experiment, the contact gate is DC biased at a large negative value $V_{cont} = -2\,V$ to further reduce the contact resistance on the p-doping side. We apply a large DC bias across the channel while probing the small signal device conductance at RF frequency. The measurement takes place in the Janis probe station at $8\,K$. The S-parameters are measured from $70\,kHz$ to $20\,GHz$ with an excitation level of $-30dBm \equiv 7\,mV$. The complex impedances (Y parameters) are extracted (see section 6.1.2 and in particular Eq. 6.4) and from the real part of $Y22$ one directly obtains the small signal conductance of the device $g_{ds} = r^{-1}$. First one can verify in Fig. 5.5 that $g_{ds}(f)$ is flat between $70\,kHz$ and $\sim 3\,GHz$. We average over that range to get an accurate value of $r = 1/g_{ds}$ which is therefore the differential resistance mentioned above. From here we can go back to the

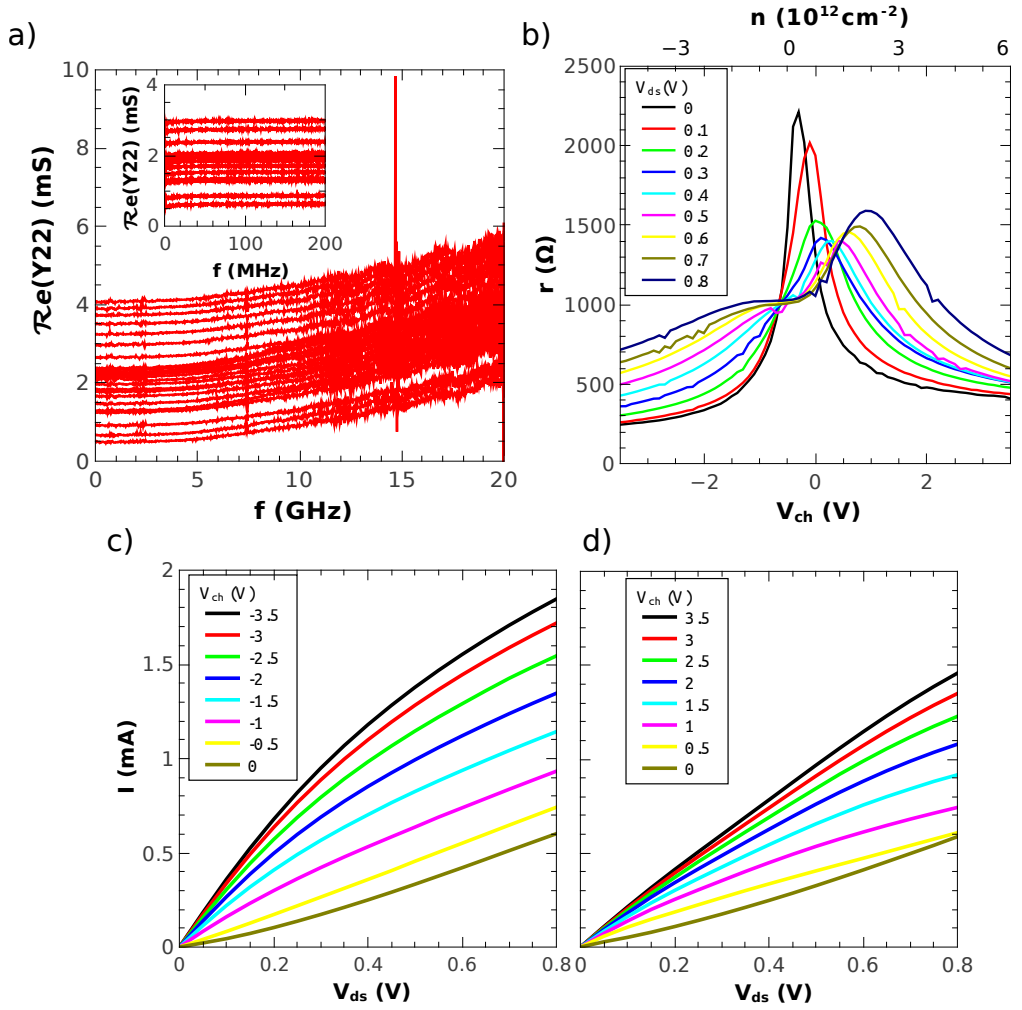

FIGURE 5.5: High bias measurement on sample GoBN3-4x2 ($L = 0.5\,\mu m$, $W = 1.5\,\mu m$, $t_{hBN} = 15\,nm$) at $T = 8\,K$. (a) VNA measurement of the small signal channel conductance $\Re(Y22) = g_{ds}(f)$ as a function of frequency in the range $70\,kHz \rightarrow 200\,MHz$ (inset) and up to $20\,GHz$ (main panel). (b) Differential resistance r extracted from panel (a) by averaging $\Re(Y22)^{-1}$ over the flat frequency range $70\,kHz \rightarrow 3\,GHz$, as a function of gate voltage V_{ch} for various biases V_{ds}. (c) I-V characteristics for $V_{ch} < 0$. (d) I-V characteristics for $V_{ch} > 0$. We observe a trend toward saturation at high densities, and a slight change of curvature near the Dirac point.

total current in the device by integrating g_{ds}:

$$I(V_{ds}) = \int_0^{V_{ds}} g_{ds} dV \tag{5.16}$$

The calculated current I is consistent with the one measured at DC, but the differential resistance measured in RF is more accurate than the DC one, which is obtained through numerical differentiation. $I(V_{ds})$ and $r(V_{ch})$ are displayed in Fig. 5.5. One can notice again the elephant shape of $r(V_{ch})$ and the trend toward saturation of $I(V_{ds})$. We first investigate the saturation due to optical phonons so we focus on the homogeneous p-doped regime to avoid being disturbed by the elephant head. Moreover, the contact

resistance is lower on that side. As already mentioned, there is a shift of the CNP gate voltage when increasing V_{ds} that can be seen in the color plot of $r(V_{ch}, V_{ds})$ in Fig. 5.6. To ensure a constant average carrier density while increasing V_{ds}, we take some oblique cuts in the data, parallel to the black line of Fig. 5.6.

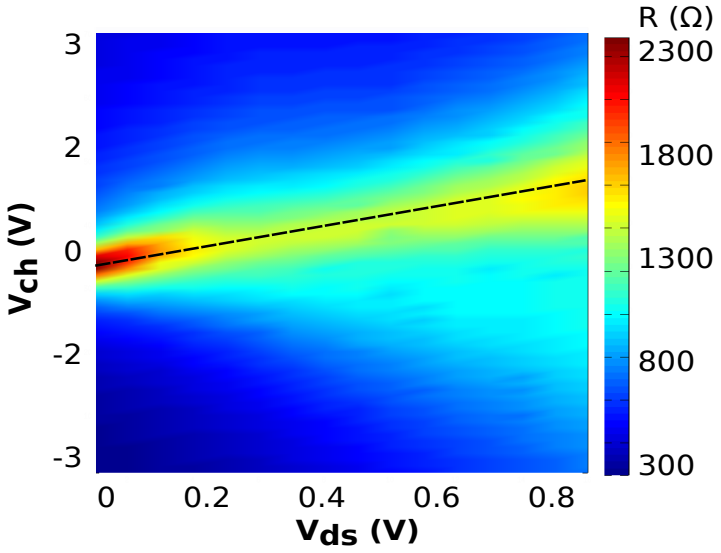

FIGURE 5.6: Color plot of the differential resistance $r(V_{ch}, V_{ds})$. The shift of the Dirac point gate voltage with respect to V_{ds} is emphasized by the black dotted line.

From the theoretical section we know that it is convenient to plot V_{ds}/I as a function of V_{ds} to extract the phonon energy. Following oblique cuts parallel to the dotted line of Fig. 5.6, we replot $I(V_{ds})$ and $V/I(V_{ds})$ for various gate voltages $V_{ch} < 0$ in Fig. 5.7. As predicted by the model, we observe a linear behavior of V_{ds}/I above the $V_{ds} < 0.3\,V$ region which is a regime where acoustic phonon scattering contribute significantly. We also plot in Fig. 5.7 the curves (solid lines) obtained from the fit of the data with (see Eq. 5.13):

$$\frac{V_{ds}}{I} = 2R_c + \frac{L}{Wne\mu} + \frac{h\pi}{4eW\sqrt{\pi n}}\frac{V_{ds}}{\hbar\Omega} \tag{5.17}$$

The gate voltage range is restricted to $-3.2 \rightarrow -1.4\,V$ to stay in the large doping regime where the model is valid. The only fitting parameter is the phonon energy $\hbar\Omega$. The contact resistance $2 \times R_c = 100\,\Omega$ (determined from 4.4.3) and the mobility $\mu = 3500\,cm^2/V/s$ are extracted independently from the gated contact model in 4.4.2. We obtain a very good agreement with the model over a broad V_{ds} and V_{ch} range by taking $\hbar\Omega = 105\,meV$. This value sets the energy scale of the dominant scattering mechanism at high bias. It is consistent with the energy of the surface polar phonons of hBN.

Nevertheless, we do not reach the full saturation and the current stays below the asymptotic I_{sat}. As an illustration, in Fig. 5.8 we plot the measured drift velocity

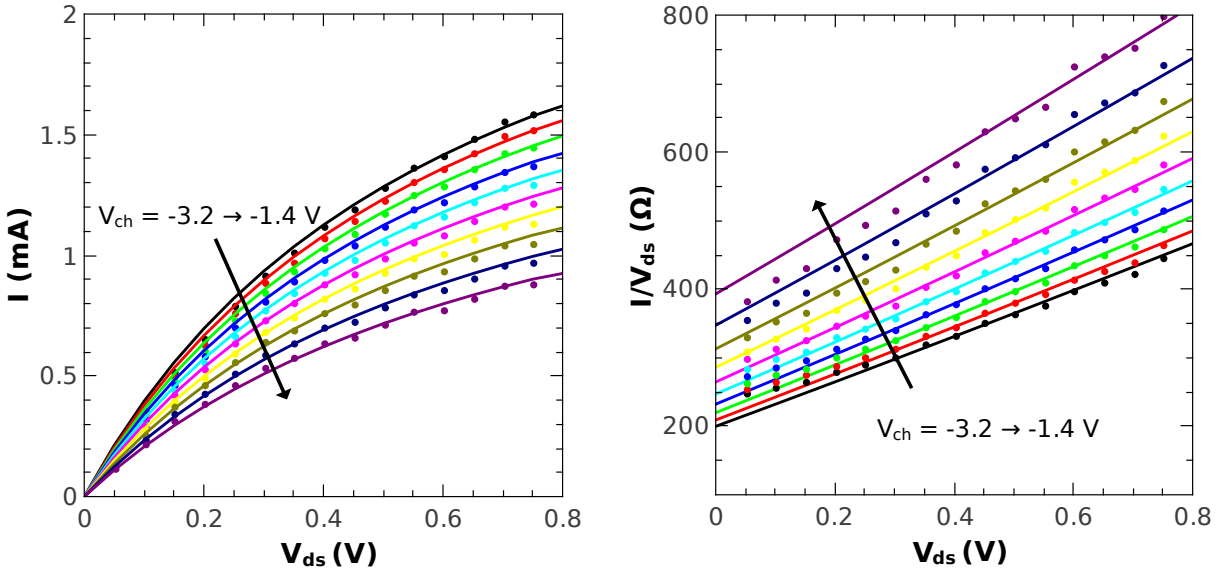

FIGURE 5.7: $I(V_{ds})$ and $V/I(V_{ds})$ following parallels of the oblique dotted line of Fig. 5.6 to ensure a nearly constant carrier density. The dots are experimental points, the solid lines are plotted from Eq. (5.17) using $\hbar\Omega$ as a single fitting parameter. In the right panel, the $V/I(V_{ds})$ data shows a good agreement with the expected linear behavior for $V_{ds} > 0.25\,V$.

$v_d = I/(neW)$, first as a function of V_{ds} to see the tendency to saturation and second as a function of the carrier density n to compare with the saturation velocity $v_{sat} = (2/\pi)\hbar\Omega v_F/E_F$ expected when $\hbar\Omega = 105\,meV$. An extrapolation of the model at higher V_{ds} (or equivalently with a higher mobility) shows a full saturation and higher drift velocities.

5.1.4 Partial conclusion

From the trend toward saturation of the I-V characteristics we were able to extract an energy scale for the inelastic scattering mechanism of $\hbar\Omega = 105 \pm 5\,meV$. To our knowledge, this is the first time that such a value, close to the energy of the hBN surface phonon is measured. It suggests that for graphene on hBN, the dominant scattering mechanism at high bias is the scattering by remote phonons of the substrate. This value is important for the design of future graphene RF transistor as it will set the the saturation velocity limit hence the speed of the transistor. Let us notice that our reference value $\hbar\Omega_{hBN} \approx 101.7\,meV$ [95] stands for a semi-infinite hBN, whereas in our measurement, the hBN thickness is $15\,nm$. An interesting further study would be to estimate the phonon energy for different thickness of the hBN dielectric for which $\hbar\Omega$ may deviate as it was shown by Fischetti et al. [107] in the case of Si. The critical thickness is related to the spatial extent of the remote phonon evanescent wave, which

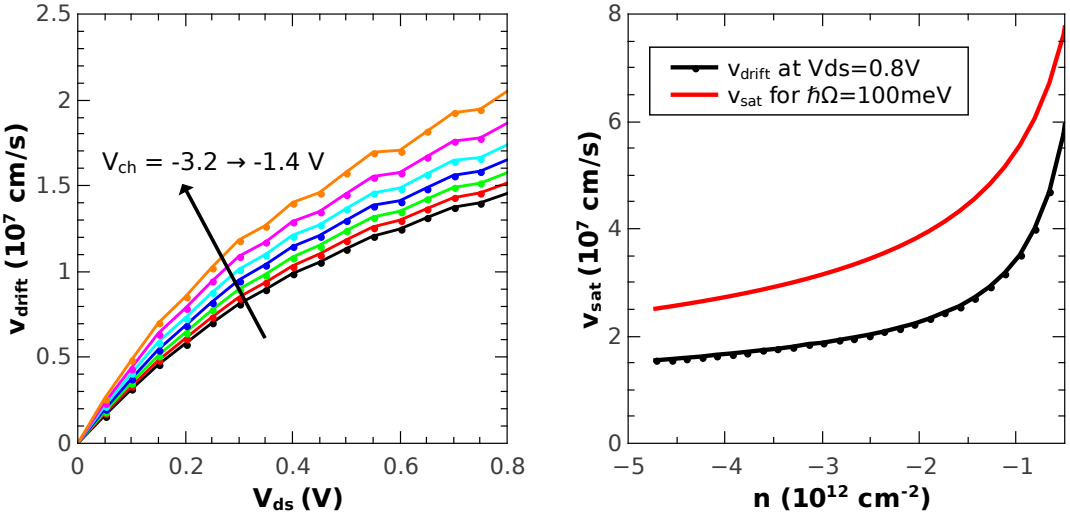

FIGURE 5.8: Left panel: Data of Fig. 5.7 replotted in terms of drift velocity $v_d = I/(neW)$ (without fit). Right panel: Maximum measured drift velocity at $V_{ds} = 0.8\,V$ compared to the saturation velocity one would expect for a full saturation by hBN remote phonon scattering (Eq. (5.7)), as a function of the carrier density n. The low density region is not plotted as (5.7) is no longer valid for $|n| < 0.4 \times 10^{12} cm^{-2}$

would be $\approx 6\,nm$ for hBN according to Viljas [116]. The effect of the remote phonons is also important in terms of energy relaxation of hot electrons. For example, it has been pointed out in [101], that the substrate phonon will limit the photocurrent generated in optoelectronic devices. Finally, the remote phonons will play a role in graphene plasmonic devices to form hybrid plasmon-phonon modes [117].

5.2 Bias induced doping profile

Let us return to the "elephant" shape of the differential resistance of Fig. 5.1-d which is specific to locally gated devices. As already mentioned, this effect comes from a non-uniform carrier density in the channel, related to the quantum capacitance effect or equivalently to inhomogeneous screening effects. However, the remote phonon scattering also has to be accounted for, to explain the overall shape of the high bias transfer curve.

In this section we combine the screening effect (or quantum capacitance) introduced in section 4.2.2 with the scattering by the remote phonons of hBN in order to propose a simple model reproducing the "boa digesting an elephant".

5.2.1 Modelling the potential profile

Applying an electrostatic potential to the drain electrode changes the electrochemical potential landscape of graphene in the channel. The electrochemical potential difference between source and drain is equal to V_{ds}. We assume this potential is varying linearly in the channel. The new electrochemical equilibrium equation depending on the x position in the channel reads:

$$\Delta E_F(x) + eV_{gr} = -eV_{ds} \times \frac{x}{L} \tag{5.18}$$

Following the procedure developed in the previous chapter, this equation is combined with the electrostatic one: $n(x)e = C_g(V_{gr} - V_g)$ to calculate $\Delta E_F(x)$.

$$\Delta E_F = sign(\epsilon_W) \times \epsilon_c(\sqrt{1 + 2\frac{|\epsilon_W|}{\epsilon_c}} - 1) \tag{5.19}$$

With

$$\epsilon_c = C_g \frac{\pi\hbar^2 v_F^2}{2e^2} \tag{5.20}$$

and

$$\epsilon_W(x) = eV_g - eV_{ds} \times \frac{x}{L} \tag{5.21}$$

Resulting in an inhomogeneous ΔE_F within the channel. This effect is sketch in Fig. 5.9. Simulations using $\Delta E_F(x)$ as calculated above are shown in Fig. 5.10. We observe here that ΔE_F is almost homogeneous in the channel at large doping. At lower doping its variation is stronger and ΔE_F is no longer linear with x. Starting from an n-doped channel and decreasing V_g, we first reach neutrality at the drain side, then we have a local neutral area whose location is shifted toward the source. At this point the channel is ambipolar. Further decrease of V_g leads finally to a p-doped channel.

ΔE_F is converted into the local carrier density:

$$n(x) = \sqrt{(\frac{\Delta E_F^2}{\pi\hbar^2 v_F^2})^2 + n_0^2} \tag{5.22}$$

Here we have to take into account the residual carrier density n_0. But for high biased samples, the electronic temperature can rise up to $800\,K$ [103] and the resulting thermal broadening that depends on V_{ds} has to be accounted for as well. We propose to write the residual carrier density as the sum of an impurity contribution term and a hot electron term: $n_0 = n_{imp} + n_{th}$, with:

$$n_{th} = \alpha V_{ds}^{4/3} \tag{5.23}$$

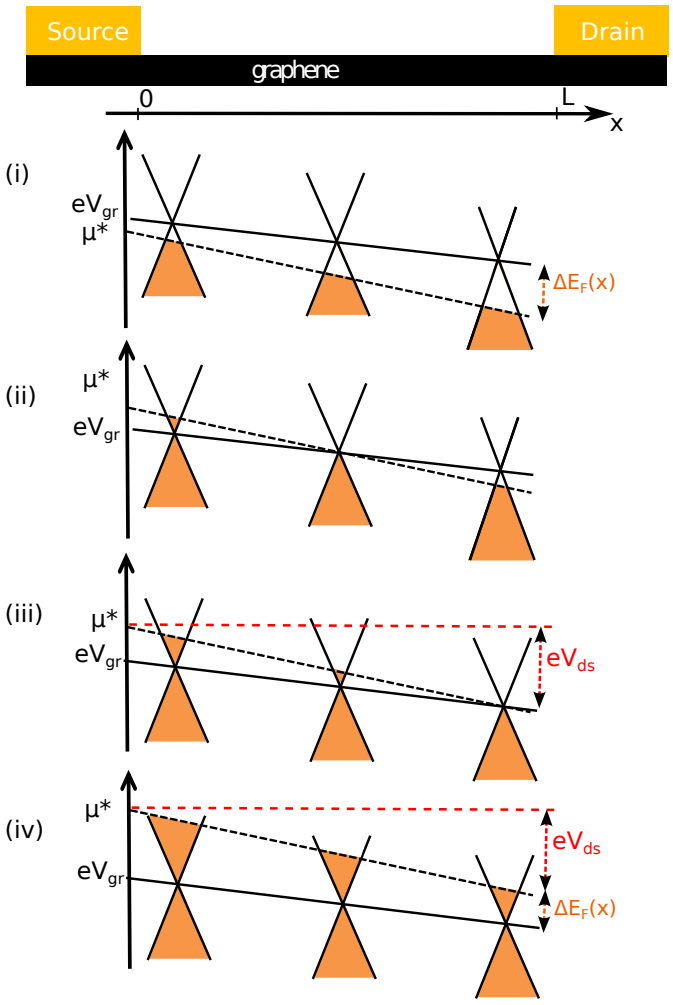

FIGURE 5.9: Potential profile in the channel at high bias for increasing gate voltages from top to bottom. In (i) the gate voltage is negative and the channel is unipolar p. In (ii) the CNP has entered into the channel from the source side, the channel is bipolar. Here, tuning the gate voltage has little effect on the total resistance which translates into a relatively flat $R(V_{ch})$ around $V_{ch} = 0V$. In (iii) the Dirac point leaves the channel area at the Drain side. (iv) The gate voltage is positive and the channel is unipolar n.

Where α is a constant. The 4/3 exponent of V_{ds} comes from the supercollision cooling regime of undoped graphene [104] where the electronic temperature scale as[3]: $T_e^3 \propto V^2$ and $n \propto T_e^2$.

[3]At high bias and low doping the Joule power obeys $V^2/(RLW) = AT_e^3$ where the pre-factor $A \propto n$ and the resistance $R \propto 1/n$ so AR is constant. We take a typical value from [104]: $AR = 1.3 \times 10^3 V^2 m^{-2} K^{-3}$. Then we convert it in carrier density using: $n_{th} \sim \frac{\Delta E_F^2}{\pi\hbar^2 v_F^2} = \frac{(k_B T_e)^2}{\pi\hbar^2 v_F^2} = \frac{k_B^2}{\pi\hbar^2 v_F^2} \frac{1}{(ARWL)^{2/3}} V^{4/3}$. So that $\alpha \approx 4.4 \times 10^{15}/(10^{12} WL)^{2/3} = 5.3 \times 10^{12} cm^{-2} V^{-4/3}$ for our sample dimensions $L = 0.5\mu m$, $W = 1.5\mu m$. (We do not intend here to quantitatively describe that effect but just to give an insight into the bias dependent broadening.)

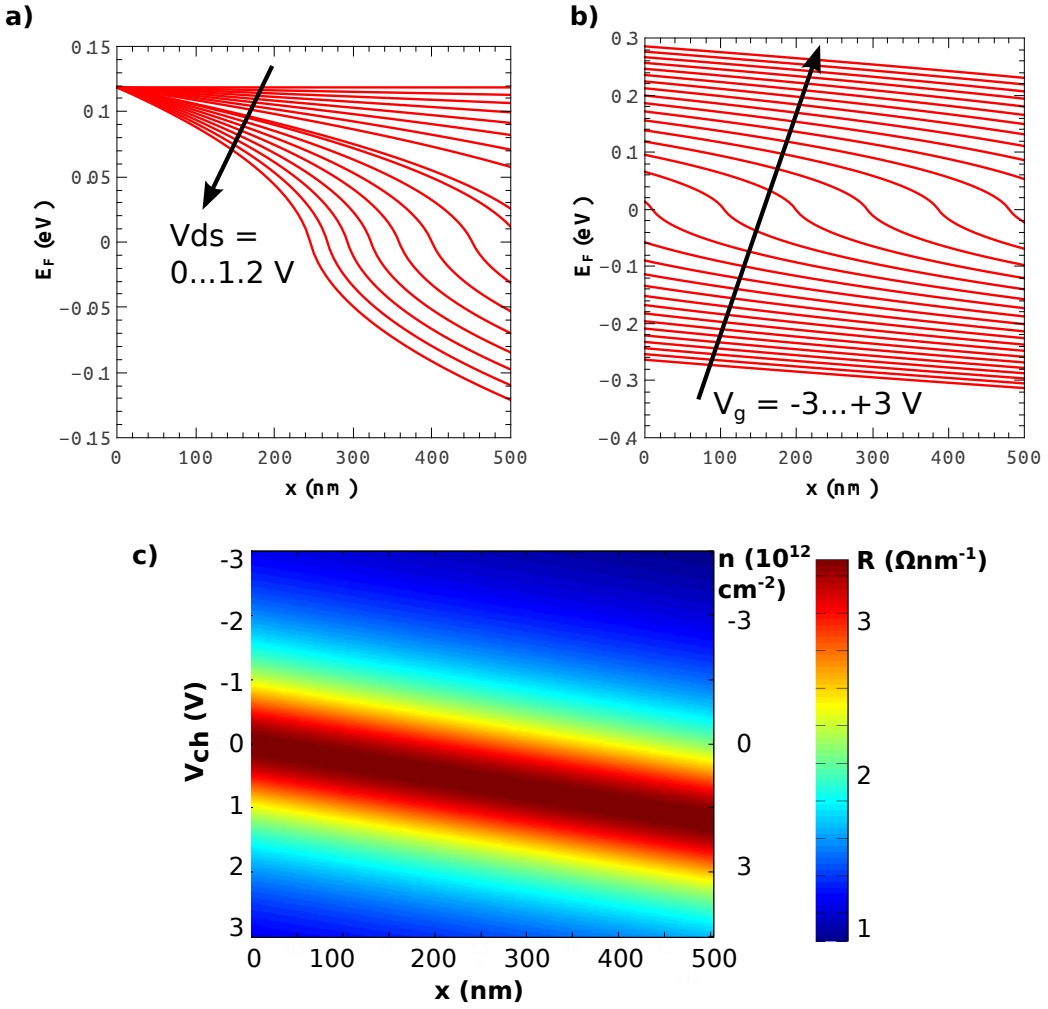

FIGURE 5.10: Simulated $\Delta E_F(x)$ along the channel, (a) $V_{ds} = 0 \to 1.2\,V$ at $V_g = 0.6\,V$ and (b) for $V_g = -3 \to 3V$ at $V_{ds} = 1\,V$; with $t_{BN} = 10nm$. (a) At low bias ΔE_F is homogeneous in the channel, but when increasing V_{ds} a bipolar channel can be reached. (b) Away from the CNP, $\Delta E_F(x) \sim constant$, but when getting closer to the CNP an bipolar channel can be reached as well. (c) 2d map of the local resistivity as a function of the x-position along the channel and the gate voltage V_{ch} for a bias voltage $V_{ds} = 1.2\,V$.

The total resistance of the device is the integration over x of this resistivity.

5.2.2 Combining potential profile and scattering

We write again the scattering by impurities and optical phonons.

The impurity mean free path is:

$$l_e(x) = \mu\hbar\sqrt{\pi n(x)}/e \tag{5.24}$$

And the optical phonon mean free path is given by:

$$l_\Omega(x, V_{ds}) = \frac{\hbar\Omega}{eV_{ds}}L \tag{5.25}$$

The total mean free path is given by the Matthiessen's rule:

$$\frac{1}{l_{scat}} = \frac{1}{l_e} + \frac{1}{l_\Omega} \tag{5.26}$$

Thus the local resistance is

$$r(x) = \frac{\pi h}{4e^2 W\sqrt{n(x)\pi}} \frac{dx}{l_{scat}(x)} \tag{5.27}$$

We finally integrate over x to find the total resistance of the channel.

$$R_{ds} = \int_0^L r(x) \tag{5.28}$$

Equivalently we calculate the differential resistance r_{ds} from $I_{ds} = V_{ds}/R_{ds}$ and $r_{ds} = dV_{ds}/dI_{ds}$.

5.2.3 Results and discussion

The results of this model are plotted in Fig. 5.11. We do not aim to fit our experimental data exactly but only to be able to retrieve the overall shape of the high bias transfer curve. The simulated sample has a size $L = 500\,nm$, $W = 1.5\,\mu m$ and a typical mobility $\mu = 5000\,cm^2/V/s$. The phonon energy is taken at $\hbar\Omega = 100\,meV$.

First we plot the differential resistance r_{ds} from our model using a dielectric thickness $t_{hBN} = 300\,nm$ (top panel of Fig. 5.11), hence with a remote gate, in order to stress the importance of t_{hBN} for the "elephant shape". Basically, the effect of the bias is to blur the resistance peak due to a thermal effect and to increase the resistance at higher densities due to phonon scattering. Then we plot the simulated r_{ds} with $t_{hBN} = 15\,nm$ in the middle panel of Fig. 5.11. A negative (positive) bias shifts the resistance peak toward negative (positive) gate voltages respectively. For comparison, in the bottom panel we plot the measured differential resistance for both negative and positive bias voltages. The lack of symmetry between $V_{ds} < 0$ and $V_{ds} > 0$ is probably due to a contact resistance effect. Finally, we also plot in Fig. 5.12 the 2D plot of the differential resistance as a function of the gate voltage and the bias voltage from the experimental data (left panel) and from the model (right panel).

The model captures the main features of experimental data. We argue that with the ingredients of the model introduced in this section we obtain a good understanding of the physics of a graphene on hBN transistor driven at high bias. This is important in terms of RF applications:

- One wants to maximize the current flowing through the device in order to maximize the transconductance. This is achieved by using a substrate with high energy surface phonons which translates into a large saturation velocity.
- A large velocity saturation also leads to a faster transistor, the current gain cut-off frequency being $f_T = v_{drift}/(2\pi L)$ (L is the channel length).
- The small signal resistance must be large in order to increase the voltage gain of a transistor. This generally comes from the phonon induced current saturation, but one can also engineer the density profile to take advantage of the "Dirac pinch-off" effect and further increase the differential resistance. Note as well that a good mobility allows to reach the saturation regime at lower bias, hence to reduce the transistor's consumption and hot electron effects.

To illustrate the relevancy of velocity saturation for graphene electronics we finally plot in Fig. 5.13 (a) the I-V curve of a typical MOSFET and (b) the simulated I-V curve of our graphene transistor. In the simulation we just push V_{ds} further and increase the mobility to $\mu = 15 \cdot 10^3\, cm^2/V/s$ to show the full saturation regime. Here, the graphene transistor and the MOSFET show very similar properties, with a linear regime followed by the current saturation, the main difference being the absence of current suppression for graphene, which is not a drawback for high frequency electronics. Thanks to the high mobility of graphene on hBN, there is a fast increase of I_{ds} at low bias, and thanks to the hBN high energy surface phonon, the current reaches values as large as $I_{ds} \approx 2mA\mu m^{-1}$. The full current saturation in Fig. 5.13-b is reached thanks to the combination of the scattering by the hBN surface phonons and to the "Dirac pinch off" effect described above.

In the next chapter we drive our devices in the current saturation regime and we show measurement in the $0 - 20\, GHz$ range to attest their performances as RF transistors.

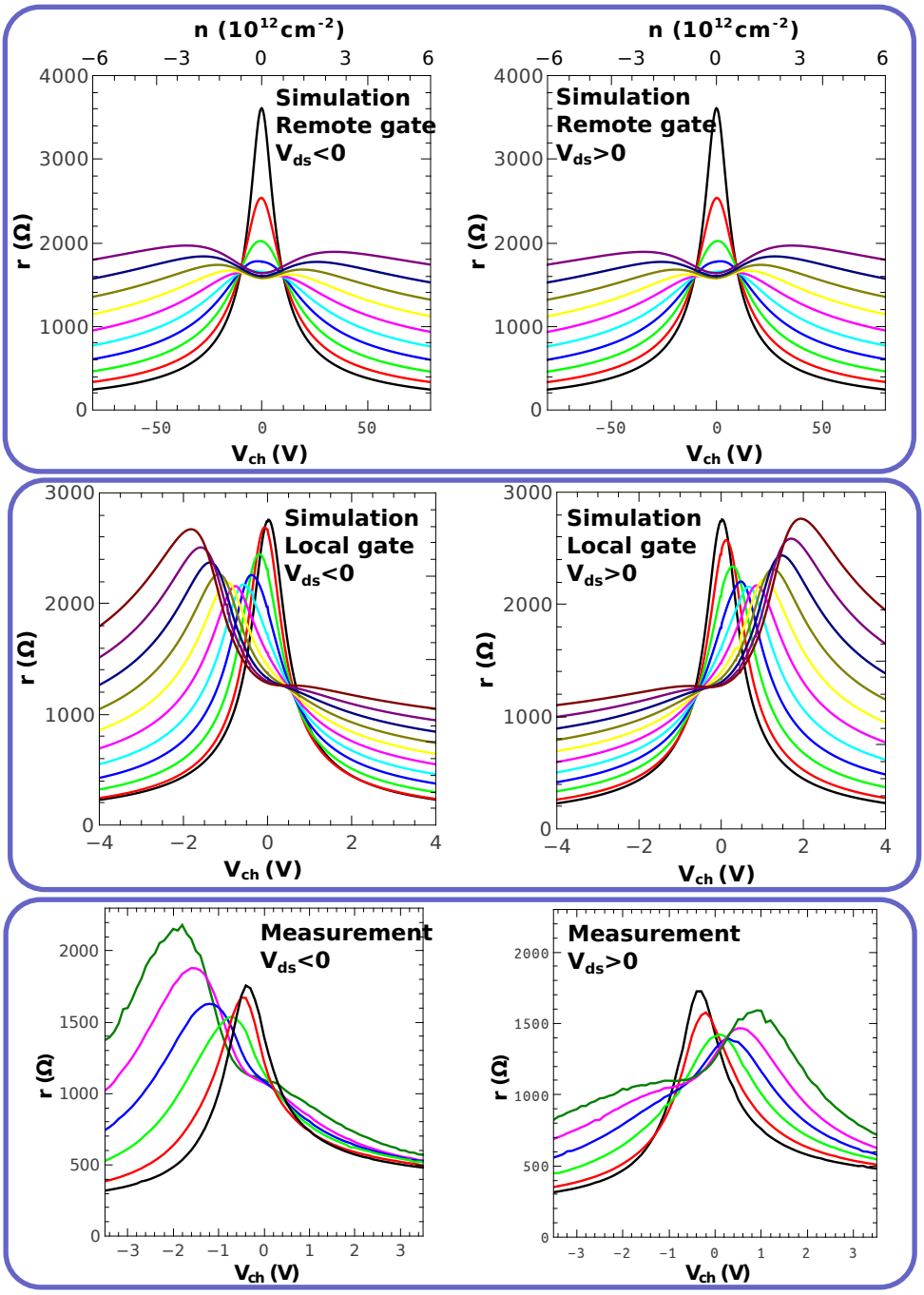

FIGURE 5.11: Differential resistance calculated with our model for remote and local gating (top and middle panel respectively) with a bias voltage $V_{ds} = -0.8 \rightarrow 0V$ (left) and $V_{ds} = 0 \rightarrow 0.8V$ (right). The model includes the scattering by the hBN phonons and the quantum capacitance effect. Bottom panel: experimental data from sample GoBN3-4x2 taken at room temperature. ($L = 500\,nm$, $W = 1.5\,\mu m$)

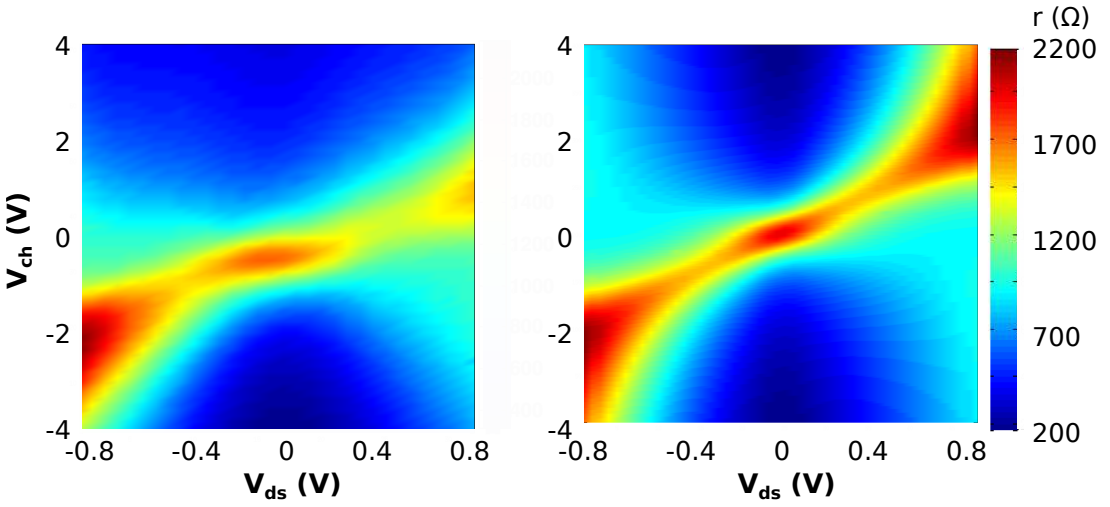

FIGURE 5.12: Differential resistance from experimental data (left panel) and simulation (right panel). The maximum resistance of the simulation has been normalized.

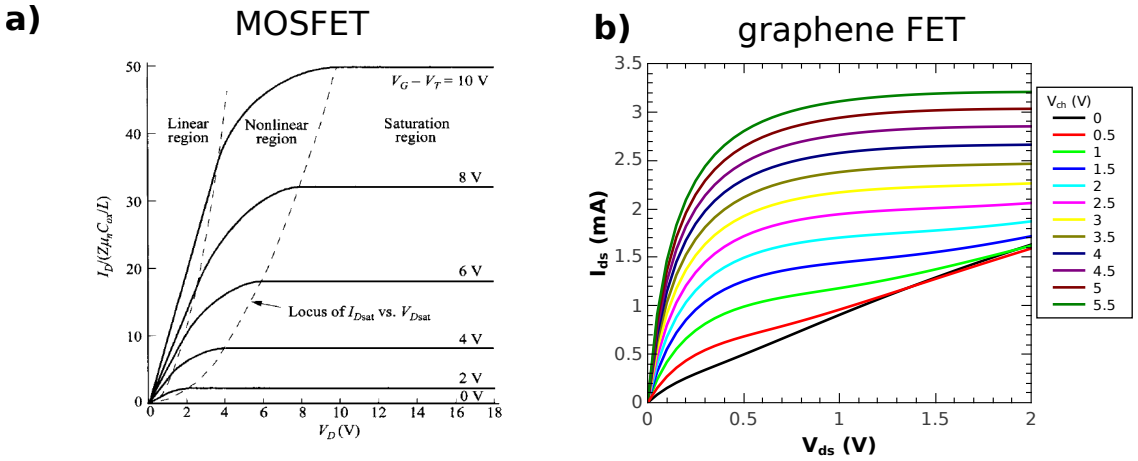

FIGURE 5.13: (a) Typical I-V curves of a MOSFET from [71]. (b) Simulated I-V curves of a graphene transistor ($L = 500\,nm$, $W = 1.5\,\mu m$). The simulation parameters are identical to those of Figs. 5.11 and 5.12 except that the mobility $\mu = 15 \cdot 10^3\,cm^2/V/s$ and $V_{ds} = 0-2V$ have been pushed further in that simulation. The current saturation is as good for the graphene transistor as for the MOSFET. The I-V curves of the graphene transistor show ideal properties for a FET: there is a fast increase of the current, thanks to the high mobility, and a saturation thanks to the scattering by the remote phonons of hBN

Chapter 6

Application: the RF transistor

The use of graphene in radio frequency (RF) electronics has raised a great deal of interest since the first attempts to make field effect transistors working at GHz frequencies ([91] and [118]). Indeed, the high carrier mobility and the high Fermi velocity of graphene should make it possible to realize transistors with cut-off frequencies in the sub-THz range. However, real devices operate at high bias where the mobility decreases and the drift velocity saturates.

In this last chapter, relying on the high bias properties discussed in the previous chapter, we show the potential of our GoBN devices for application as RF transistors.

Very few RF transistors with graphene on hBN have been measured so far [14]. Although our samples are not fully optimized to compete with the state of the art graphene RF transistors[1], it is interesting to see what is gained using an hBN substrate. Here we take advantage of the current saturation shown in the previous chapter to maximize the power gain cut-off frequency f_{max}.

6.1 The graphene RF transistor

6.1.1 A quick review

The past few years have seen a race for obtaining graphene RF transistor operating at higher frequency [12, 13, 82, 118, 119]. But we need to specify what we mean by operating frequency. There are two main figure of merits for RF transistors: the current gain cut-off frequency also called transit frequency f_T and the power gain cut-off frequency f_{max}. f_T

[1] In particular our sample width $W = 1.5\,\mu m$ is not sufficient to ensure a large transconductance. Moreover our tungsten gate electrode has a large resistivity, limiting the device performance in term of power gain.

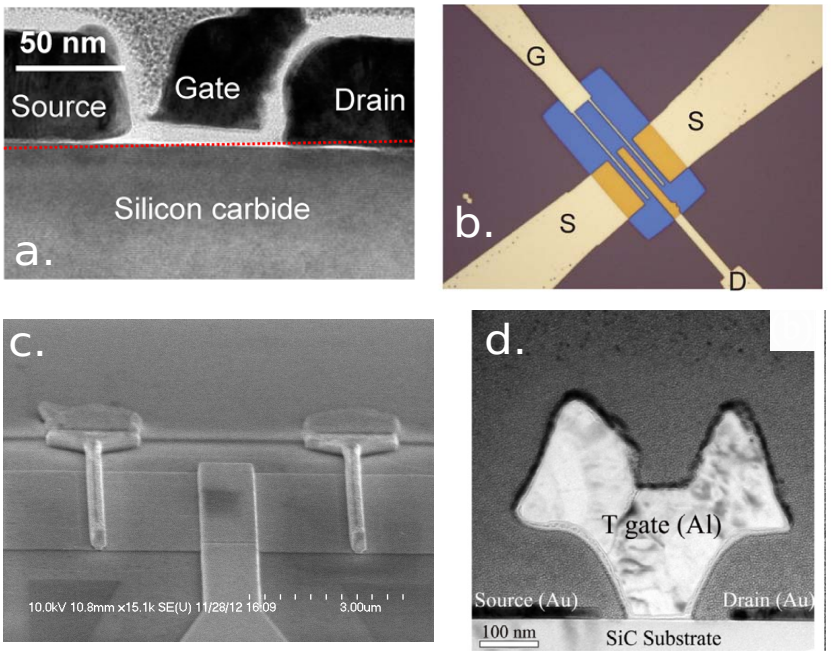

FIGURE 6.1: (a) TEM cross section of the world-record $f_T = 350GHz$ transistor [13]. Note the very short channel and very thin dielectric thickness. (b) Graphene on hBN RF transistor [14] achieving $f_{max} = 34\,GHz$. Note the non-gated access area in the channel that suggests there is a room for improvement. (c) Epitaxial graphene RF transistor with T-gates $f_{max} = 74\,GHz$ after de-embedding. (d) TEM cross section of the world-record $f_{max} = 105\,GHz$ transistor [16] using an "ultra clean self aligned process" with T-gates.

was the first figure of merit to be investigated for graphene. Rapid progress was made and f_T up to $350GHz$ were obtained [13] (Fig. 6.1-a) for devices with a short channel and a thin dielectric. Nevertheless, f_T is mostly useful in terms of digital applications as it sets the speed of logical operations, but the low ON/OFF ratio of graphene transistors does not allow such operations. f_{max} is a more important figure of merit for analog devices, for example for low noise amplifiers, which are a more realistic application of graphene. f_{max} depends more critically on parasitic capacitances and resistances of the device but above all it requires current saturation as will be shown later. As a result, reported f_{max} values remain low. Several routes can improve f_{max}: in [14] hBN substrate is used to improve current saturation and $f_{max} = 34\,GHz$ is obtained (Fig. 6.1-b). In [15], T-gates and self aligned contacts are used to reduce the gate resistance and spurious capacitances. Besides the authors use a Si-C substrate which has high energy optical phonons $\hbar\Omega_{SiC} = 115\,meV$. They obtain $f_{max} = 70\,GHz$ (Fig. 6.1-c). Combining self aligned fabrication, low contact resistance, very thin dielectric ($t_{Al_2O_3} = 6\,nm$), and above all low gate resistance thanks to T-gates ($R_G = 2.2\Omega$), the authors of [16] hold the record with $f_{max} = 105\,GHz$ (Fig. 6.1-d).

6.1.2 Definitions and figures of merit

At high frequency, we describe the transistor with the small signal model [120]. The equivalent electrical circuit of the transistor is shown in Fig. 6.2. The intrinsic elements (the channel resistance $r_{ds} = 1/g_{ds}$, the gate to drain capacitance C_{gd}, the gate to source capacitance C_{gs} and the transcondutance g_m are within the green dotted line area). The extrinsic elements are the gate, drain and source electrode's access resistances R_G, R_D and R_S respectively and the parasitic capacitances C^0_{gs}, C^0_{gd} and C^0_{ds}, within the red dotted line area.

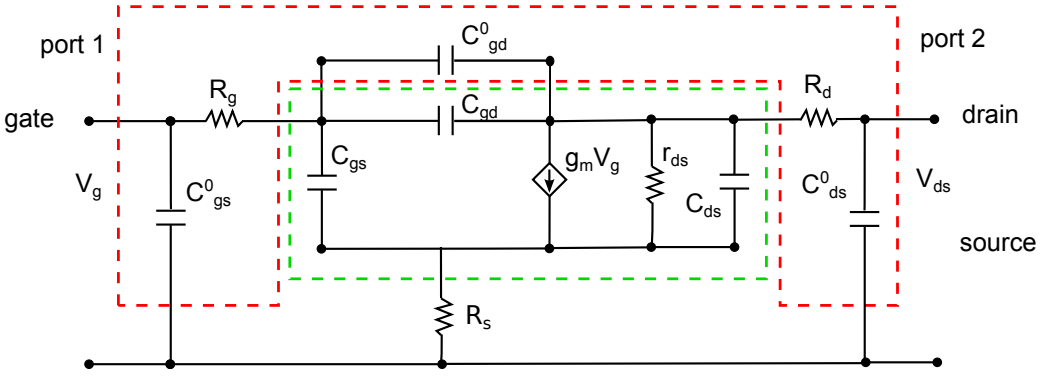

FIGURE 6.2: Small signal equivalent circuit of a graphene transistor. The green dotted line delimits the intrinsic electrical lumped elements of our transistor while the red dotted line delimits the extrinsic elements (noted with a superscript 0).

From a VNA measurement we have direct access to the Y parameters (see section 2.2.2), which are related to the device parameters using $Y_{ij} = \frac{I_i}{V_j}_{V_i=0}$. Here are the intrinsic Y parameters:

$$Y_{11}(\omega) = j(C_{gs} + C_{gd})\omega \tag{6.1}$$

$$Y_{21}(\omega) = g_m - jC_{gd}\omega \tag{6.2}$$

$$Y_{22}(\omega) = g_{ds} + j(C_{gd} + C_{ds})\omega \tag{6.3}$$

$$Y_{12}(\omega) = jC_{gd}\omega \tag{6.4}$$

However one may want to take into account some of the extrinsic elements which can be useful to understand the measured spectrum:

$$Y_{11}(\omega) = \frac{R_g(C_{gs}+C^0_{gs}+C_{gd}+C^0_{gd})^2\omega^2 + j(C_{gs}+C^0_{gs}+C_{gd}+C^0_{gd})\omega}{1+R_g^2(C_{gs}+C^0_{gs}+C_{gd}+C^0_{gd})^2\omega^2} \quad (6.5)$$

$$Y_{21}(\omega) = g_m - j(C_{gd}+C^0_{gd})\omega \quad (6.6)$$

$$Y_{22}(\omega) = g_{ds} + j(C_{gd}+C^0_{gd}+C_{ds}+C^0_{ds})\omega \quad (6.7)$$

$$Y_{12}(\omega) = \frac{-R_g(C_{gd}+C^0_{gd})^2\omega^2 - j(C_{gd}+C^0_{gd})\omega}{1+R_g^2(C_{gd}+C^0_{gd})^2\omega^2} \quad (6.8)$$

The transconductance g_m The device transconductance is defined as below:

$$g_m = \frac{\partial I}{\partial V_g} \quad (6.9)$$

In the diffusive regime the current is expressed as

$$I = ne\mu\frac{W}{L}V_{ds}, \quad (6.10)$$

with $n = \frac{CV_g}{e}$, where $C = \epsilon_0\epsilon_r/t_{hBN}$ is the gate capacitance per unit area. Therefore

$$g_m = \frac{\partial(ne\mu WV_{ds}/L)}{\partial V_g} \quad (6.11)$$

$$= Ce\mu\frac{W}{L}V_{ds} \quad (6.12)$$

So to maximize g_m one must work with a high mobility sample, with a short length L and large width W, at large bias voltage and with a thin dielectric. However, at large bias a saturation of g_m is observed. It is related to the current saturation as the upper limit for the current is $I_{sat} = neWv_{sat}$. Thus, at $n = 10^{12}\,cm^{-2}$, for $C = 2.3\,mF\cdot\mu m^{-2}$ (our sample) and considering scattering by the surface phonons of hBN ($\hbar\Omega = 100meV$, see section 5.1), one obtains:

$$g_m/W = \frac{C\Omega}{\pi^{3/2}\sqrt{n}} \approx 0.6\,mS\mu m^{-1} \quad (6.13)$$

This upper limit for g_m is still larger than typical measured $g_m \approx 0.25mS\,\mu m$ in the literature [12, 14, 15, 82, 121] and in this work. That can be explained by the fact that the full current saturation is never reached.

Current gain The current gain is defined as below:

$$H = \frac{I_1}{I_2} = \frac{Y21}{Y11} = \frac{g_m - jC_{gd}\omega}{j(C_{gd}+C_{gs})\omega} = \frac{g_m}{j(C_{gs}+C_{gd})\omega} - \frac{C_{gd}}{C_{gd}+C_{gs}} \quad (6.14)$$

With $\frac{C_{gd}}{C_{gd}+C_{gs}}$ generally equals to 1/2. f_T is defined as the maximum frequency at which $|H| > 1$, therefore the intrinsic f_T reads:

$$f_T = \frac{g_m}{2\pi(C_{gs} + C_{gd})} \tag{6.15}$$

With g_m and $C_g \propto LW/t_{BN}$, one has to minimize the channel length L and the dielectric thickness to increase f_T. Measurements show a clear $1/L$ dependence of f_T [13].

A more realistic expression of f_T accounting for spurious contribution in a real device is [122]:

$$f_T = \frac{g_m/2\pi}{(C_{gs} + C_{gd} + C^0_{gs} + C^0_{gd})(1 + (R_S + R_D)g_{ds}) + (C_{gd} + C^0_{gd})g_m(R_D + R_S)} \tag{6.16}$$

The intrinsic f_T is directly related to the transit time of the carriers through the gate length, so it is a way to measure the actual drift velocity:

$$f_t = \frac{v_{drift}}{2\pi L} \tag{6.17}$$

This method is used in [123] to extract v_{drift}. The difficulty here is to accurately remove the parasitic capacitances.

Finally we point out that generally $C_{gd} \approx C_{gs}$ (if the device is symmetric) so that in the limit $f >> f_T$, one has $H \to 1/2$.

Voltage gain

The voltage gain A reads:

$$A = \frac{g_m}{g_{ds}} \tag{6.18}$$

In graphene transistors, A is generally below 1. One can see that we need to go into the current saturation regime to decrease g_{ds} in order to increase A.

Power gain As already mentionned, an important figure of merit for RF transistors is the maximum oscillation frequency f_{max} which corresponds to the cut-off frequency of the power gain. Formally, its definition relies on the Mason's gain U [120]:

$$U = \frac{|Y21 - Y12|^2}{4(\Re(Y11)\Re(Y22) - \Re(Y21)\Re(Y12)} \tag{6.19}$$

And one has $U(f_{max}) = 1$. The f_{max} formula is therefore defined as below:

$$f_{max} = \frac{f_T}{2\sqrt{(R_G + R_S)g_{ds} + 2\pi f_T C_{gd} R_G}} \tag{6.20}$$

The important parameters usually limiting f_{max} are the gate electrode resistance R_G and the channel resistance $r_{ds} = 1/g_{ds}$. Indeed, with our thin and resistive tungsten gate, we can estimate $R_G \sim 300\Omega$ which is of the order of the low bias channel resistance. In addition the access resistance R_S also accounts for the contact resistance of $\sim 100\Omega$ so that we end up with $f_{max} <\sim f_T$. Therefore the key to increase f_{max} is to have a saturating current increasing r_{ds}.

About de-embedding The de-embedding procedure consists in removing the parasitic capacitances by measuring an open structure similar to the device but without graphene. The corresponding Y parameters (Y_{open}) would only contain the imaginary part with the C^0_{gs} and C^0_{gd} capacitances. Then, the subtraction $Y - Y_{open}$ for all Y-parameters would lead to the intrinsic Y. However, this works only if one can neglect the spurious gate resistance R_G and access drain and source resistances R_D and R_S. Nevertheless, this procedure is efficient to estimate the intrinsic f_T. In principle, f_{max} should be less sensitive to de-embedding as it is mostly limited by R_G.

6.2 Experimental results

6.2.1 The RF measurement

Here I present a set of data from measurements on sample GoBN-4x2 (presented in section 4.4.2). As a reminder, the sample's dimensions are $L = 0.5\,\mu m$, $W = 1.5\,\mu m$ and $t_{BN} = 15\,nm$; its mobility is $\mu = 3500\,cm^2/V/s$. This sample is equipped with a contact gate which is tuned at $V_{cont} = -4\,V$ in order to minimize the contact resistance to $\sim 180\,\Omega\mu m^{-1}$. The S-parameters are acquired between 20 MHz and 20 GHz after SOLT calibration. They are converted in Y parameters as explained in section 2.2.2. A first operation is performed on those spectra that consists in removing the propagative phase due to the finite length of the coplanar wave guide. We apply $S_{ij} \rightarrow S_{ij}e^{j\phi}$ with:

$$\phi = D\omega/v_p \tag{6.21}$$

Where $v_p = 1 \times 10^8 m/s$ is the phase velocity for a CPW on Si/SiO_2 substrate, and $D = 400\mu m$ is the CPW length between the probes. This dephasing is also directly measured on a through line device to confirm this estimation.

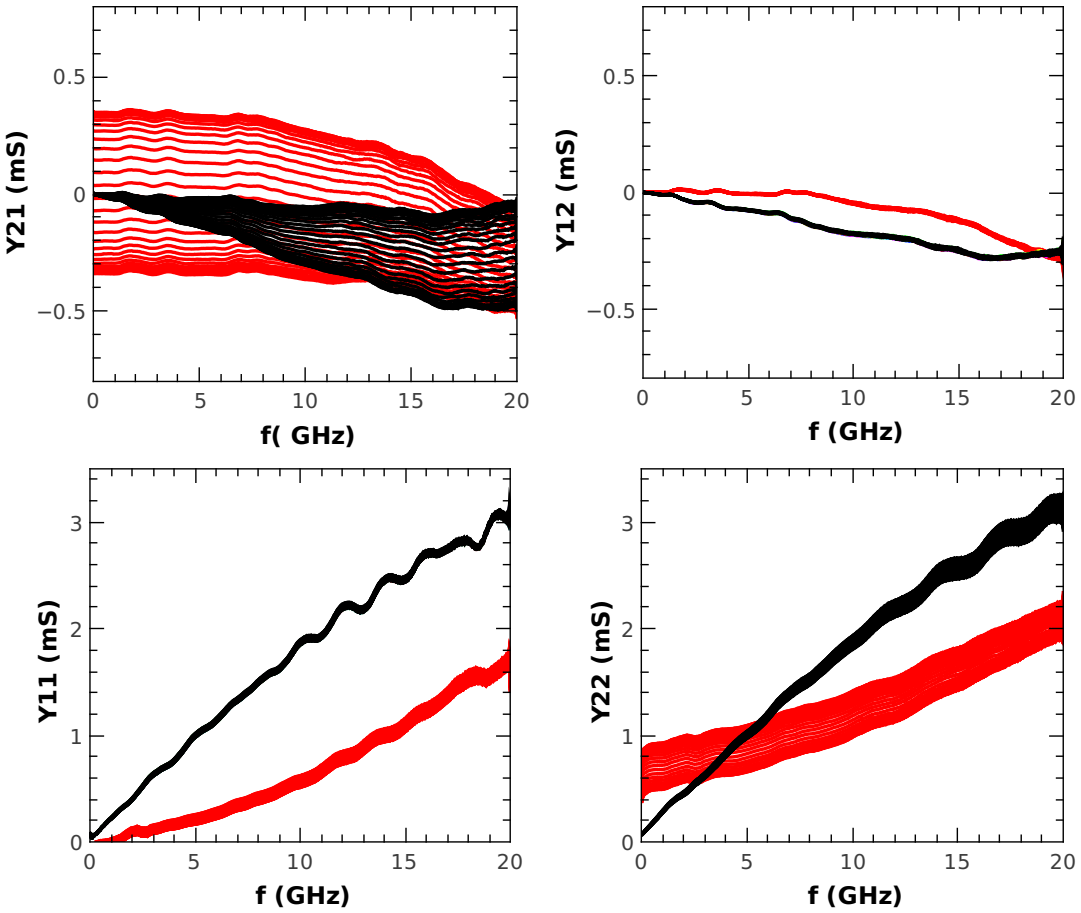

FIGURE 6.3: VNA measurement of the complex admittance parameters. The spectrum are the de-embedded Y-parameters ($Y - Y_{open}$), supposedly intrinsic, for various gate voltages. The red lines stand for the Y real parts and the black lines for the Y imaginary parts. The $\Re(Y21)$ spectra reflect the variation of the transconductance, $\Re(Y22)$ reflects the channel conductance. The $\Im(Y21)$ spectrum is linear and its slope corresponds to the gate capacitance. The slope of $\Im(Y11)$ and $\Im(Y22)$ is higher suggesting a remaining contribution of the parasitic capacitance.

The corrected spectra are shown in Fig. 6.3 with red lines for real parts and black lines for imaginary parts, and for the gate voltages $V_{ch} = -3 \rightarrow +3V$. One can notice a strong gate dependence for $\Re(Y21)$, which corresponds to the transconductance g_m. As well the low frequency part of $\Re(Y22)$ is finite and it varies with the gate voltage ; it corresponds to g_{ds}. On the contrary, neither $\Re(Y11)$ nor $\Re(Y12)$ show gate dependence in accordance with formulas 6.4. They show a parabolic behavior corresponding to a capacitance and a resistor in series. Accordingly Y11 is fitted with formula 6.8 to estimate the gate resistance: $R_G = 150\,\Omega$ (see Fig. 6.4-d). Concerning the imaginary parts, they are linear and their slopes give the capacitance values. One can see similar magnitudes for Y21 and Y12 on one hand and Y11 and Y22 on the other hand. Indeed, the capacitance extracted from $\Im(Y11)$ (or $\Im(Y22)$) is $C_{gs}+C^0_{gs}+C_{gd}+C^0_{gd} \sim C_{ds}+C^0_{ds}+C^0_{gd}+C_{gd} \sim 30\,fF$ (see fit

Fig. 6.4-d) while the capacitance extracted from $\Im(Y12)$ (or $\Im(Y21)$) is $C_{gd}+C^0_{gd} \sim 3\,fF$ (fit not shown). The variation observed in $\Im(Y21)$ is probably due to a phase rotation [2].

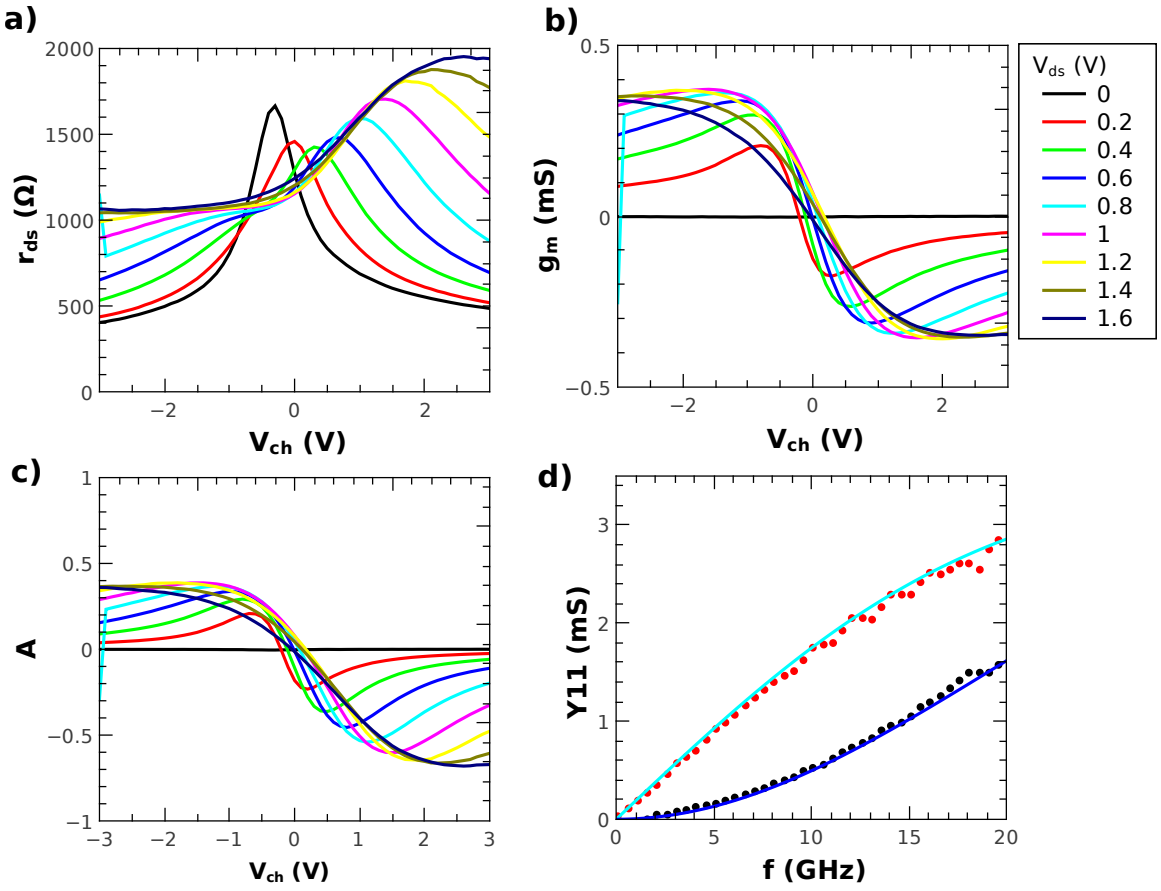

FIGURE 6.4: Quantities extracted from Fig. 6.3. (a) Small signal resistance (b) transconductance and (c) voltage gain as a function of the gate voltage, for bias voltages $V_{ds} = 0 \to 1.6\,V$. (d) Y11 spectra real (blue line) and imaginary (red line) parts fitted with Eq. 6.8 (solid lines). The fit gives $R_G = 150\,\Omega$ and $C_{gs}+C^0_{gs}+C_{gd}+C^0_{gd} = 30\,fF$

Fig. 6.4 shows $g_m(V_{ch})$, $r_{ds}(V_{ch})$ and $A(V_{ch})$ for bias voltages $V_{ds} = 0 \to 1.6V$. One can recognise the elephant shape of $r_{ds}(V_{ch})$ associated with the current saturation. g_m changes sign when going from p to n doping. It has two extrema around $n = \pm 2.2 \times 10^{12}\,cm^{-2}$, but one can notice a slightly larger value on the p-side $g_m = 0.38\,mS$ due to a lower contact resistance. Besides g_m saturates around $V_{ds} \approx 1\,V$. The voltage gain is more asymmetric, reflecting the "elephant shape". We obtain a maximum of $A = 0.68$ on the n-side where the saturation current effect dominates.

The current gain H and Mason's gain U are plotted in logarithmic scale in Fig. 6.5 before and after de-embedding for the higher bias voltage $V_d = 1.6V$ and at $V_{ch} = 2V$. H shows

[2] This variation is not due to quantum capacitance effect. If it was the case we would observe a variation on the other channels as well. Besides the quantum capacitance is large beyond the geometrical one due to a rather large t_{BN}.

a clear $1/f$ dependence. f_T is improved from $1.9\,GHz$ before de-embedding to $9.3\,GHz$ after de-embedding. The slope of U is slightly stronger than the expected $20dB/decade$ before de-embedding, but the $1/f^2$ behavior is restored after de-embedding. As well, f_{max} is improved from $3\,GHz$ before to $7\,GHz$ after de-embedding.

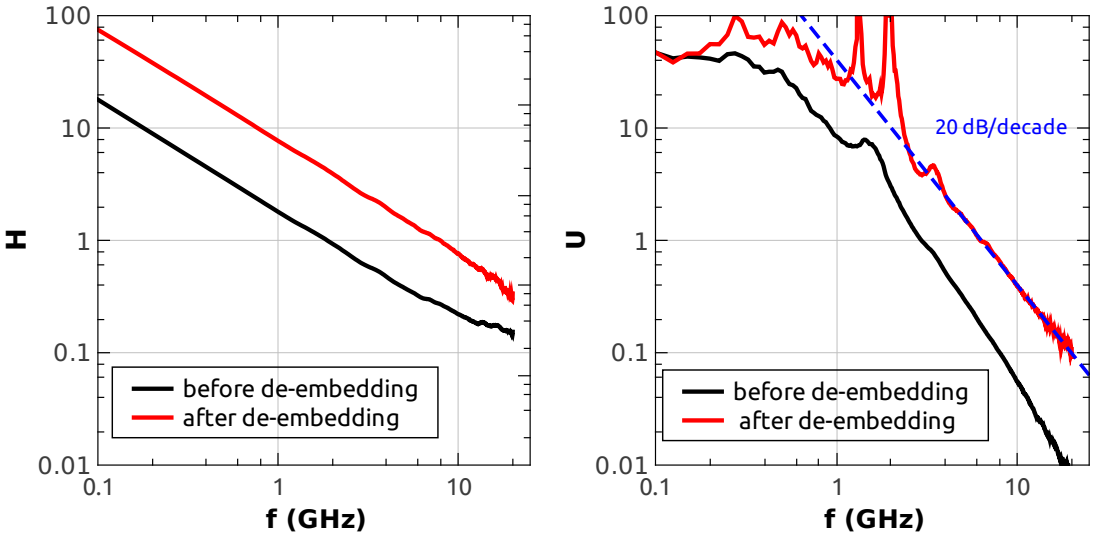

FIGURE 6.5: Spectra of the current gain $H = I_1/I_2 = Y_{21}/Y_{11}$ (left panel) and Mason's gain U (right panel) before and after de-embedding. $H(f)$ follows a $1/f$ dependence while $U(f)$ follows a $1/f^2$ dependence. f_T (f_{max}) is determined from the intersection of $H(f)$ ($U(f)$) with $H = 1$ ($U = 1$) respectively.

$f_T(V_{ch}, V_{ds})$ and $f_{max}(V_{ch}, V_{ds})$ are plotted in a color plot in Fig. 6.6. One can notice that f_T mainly follows g_m and f_{max} mainly follows A, as expected. The V_{ch} asymmetry can be explained as follow: f_T depends essentially on g_m and therefore is higher on the low contact resistance side ($V_{ch} < 0$) while f_{max} benefits from the saturation on the $V_{ch} > 0$ side. As a result it seems that applying a negative bias would allow us to benefit both from the saturation and the low contact resistance on the $V_{ch} < 0$ side (see also Fig. 5.11).

6.2.2 Results and discussion

Before de-embedding we obtain $f_T = 1.9GHz$ and $f_{max} = 3GHz$. It is interesting to note that we obtain a larger value for f_{max} than for f_T contrasting with most results on that subject, and despite our particularly large gate resistance. This can be explained by our relatively small channel width W leading to low a g_m, hence a low f_T. Apart from that we have a relatively large channel length L and dielectric thickness t_{BN}. It results in parasitic capacitances larger than the intrinsic ones and contributes to the reduction of f_T. As an illustration let us calculate the expected extrinsic f_T taking $(C_{gs} + C_{gd} + C^0_{gs} + C^0_{gd}) =$

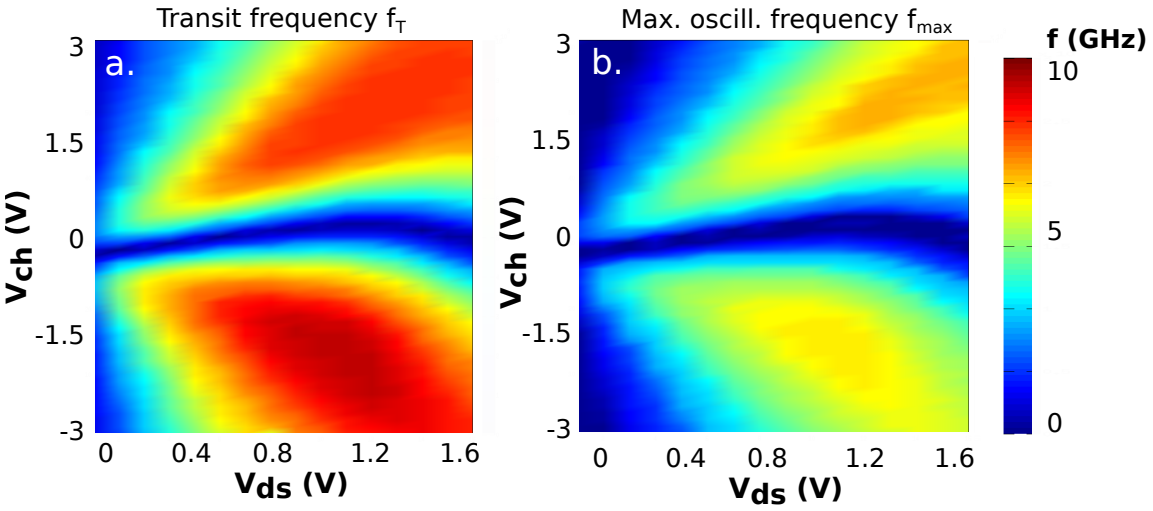

FIGURE 6.6: Bias voltage and gate voltage dependence of f_T (left panel) and f_{max} (right panel). The best f_{max} is obtained around $V_{ch} = 1.7\,V$, $V_{ds} = 1.3\,V$. A better value may have been obtained for negative V_{ds} and negative V_{ch} for which the contact resistance is lower.

30 fF and $(C_{gd} + C^0_{gd}) = 3\,fF$ extracted from the imaginary part of Y11 and Y12 respectively (while the intrinsic capacitance is $C_{gd} \approx C_{gs} = \epsilon_0\epsilon_r LW/t_{BN} = 1.8\,fF$) and access and contact resistances $R_D + R_S \approx 250\Omega$. Using formula 6.16 we obtain $f_T \approx 1.8\,GHz$, very close to the measured value. On the contrary, f_{max} benefits from the pronounced saturation of the current. We use formula 6.20 with $R_G = 150\Omega$ and $r_{ds} = 2000\Omega$ to estimate $f_{max} = 2.5\,GHz$.

After de-embedding we obtain $f_T = 9.2GHz$, well below the expected $f_T = g_m/(2\pi C_{gs}) = 32\,GHz$. We explain this discrepancy by the delicate de-embedding when we try to remove extrinsic contributions larger than the intrinsic ones. Surprisingly, f_{max} is improved by the de-embedding. Although it is usually poorly sensitive to this procedure, it probably benefits here from the reduction of the large parasitic capacitance.

Even though we do not beat the state of the art f_T and f_{max}, our measurements show the potential of the GoBN technology for RF electronics: the use of hBN provides a good mobility and high energy substrate phonons. In the I-V characteristics this translates into a steep slope of $I(V_{ds})$ followed by a large current saturation. In addition the use of a contact gate can reduce the contact resistance. These first results can be improved by optimizing the device geometry: the use of buried thick gold electrodes will reduce the gate resistance which is the main limitation for f_{max}. Similarly, using a double gate geometry and wider channels will improve f_{max} as well. This has been implemented in a new generation of GoBN devices by Mohamed Boukhicha at Laboratoire Pierre Aigrain. A picture of the device as well as some preliminary results are shown in Fig. 6.7.

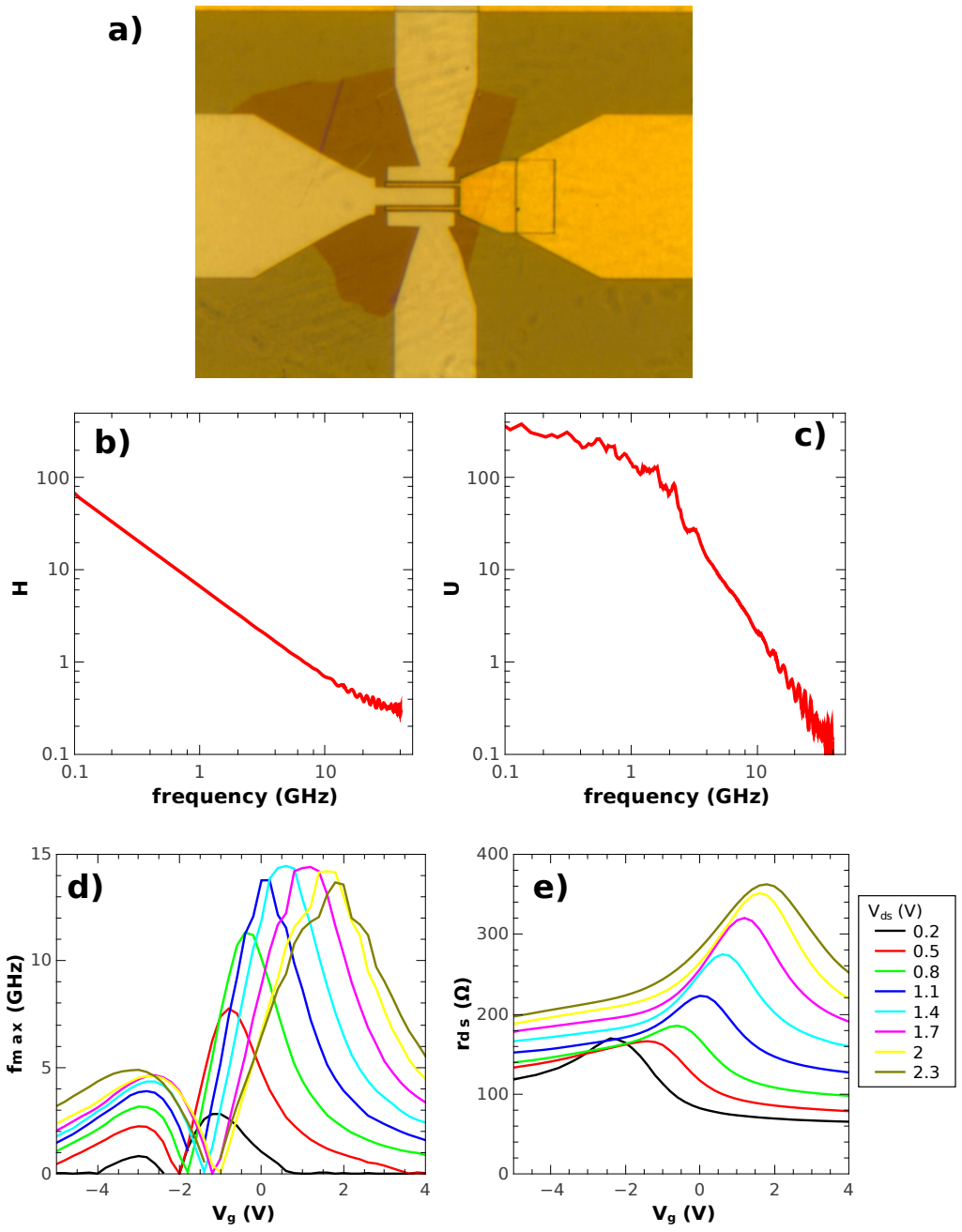

FIGURE 6.7: (a) Optimized graphene RF transistor with thick (200 nm) Au double gates ($W = 10\ \mu m$, $L = 300\ nm$) fabricated by M. Boukhicha. (b) Current and (c) Mason gains at $V_g = 1\ V$ and $V_{ds} = 1.5\ V$ without de-embedding. We obtain $f_t \approx 7\,GHz$ and $f_{max} \approx 14\,GHz$ (d) f_{max} and (e) r_{ds} as a function of the gate voltage for $V_{ds} = 0 \rightarrow 2.3\ V$. The device is driven on the low contact resistance side and with positive V_{ds} to take advantage of the pinch-off effect ($V_g = 1\ V$, $V_{ds} = 1.5\ V$).

Chapter 7

Conclusion and perspectives

In this thesis, we have discussed the realization and the operation of graphene on hexagonal boron nitride on nanostructured bottom gate devices that efficiently control the doping profile of graphene for high frequency electronics. We have developed the fabrication methods allowing us to induce sharp potential steps in graphene, based on precise e-beam lithography and dry etching of a 20 nm-thin tungsten film followed by the dry transfer of hBN and graphene. We discussed the use of this technology for the realization of a *Klein tunneling transistor*, which can switch ON and OFF a graphene channel transmission taking advantage of the refraction properties of Dirac fermions at a p-n junction. This technology was first implemented experimentally in a gated contact transistor for which we demonstrated a full doping tunability of the contacted graphene area. For this device, the Klein tunneling transmission of the contact junction is modulated at GHz frequencies from the contact gate making possible the realization of graphene transistors breaking the scaling limit. We investigated as well the high bias properties of our devices. We observed the current saturation and identified two different mechanisms that are specific to our technology: the scattering by the surface polar phonons of the hBN substrate and a non-uniform doping profile arising for locally gated devices only, both leading to a Dirac pinch-off. Finally, all those effects have been implemented for the assessment of our devices as radio frequency transistors.

This work opens many perspectives for Dirac fermion electronics. In the short-term we are expecting an experimental realization of the *Klein tunneling transistor* using the van der Waals pick-up technique for a hBN encapsulated device. As well we should be able to demonstrate a high frequency transistor based on the GoBN technology with a cut-off frequency f_{max} above $100 GHz$. In the longer term, graphene is considered as the model-system for Dirac fermion electronics, but this physics will also be investigated in other systems. For example, there is a 2D Dirac fermion gas living at the surface of topological

insulators, and the graphene issues can be revisited in these materials. In topological insulators this is the real spin which is locked to the momentum. As in graphene, it results in high mobility samples and the Klein tunneling effect should also be observed for the surface states at a p-n junction. The issue of the Dirac fermion-phonon interaction is fascinating as well since in topological insulator the scattering should be dominated by the intrinsic surface phonon of the material instead of the substrate remote phonons in graphene.

Regarding graphene itself, there is still a large scope of physics to investigate. The next graphene device generation could rely on plasmonics for optoelectronic applications in the terahertz range. The technology developed in this work will prove useful to realize a plasma resonance transistor (Fig. 7.1), as a bottom local gate array of a carefully chosen periodicity can induce plasmons of a given wavevector that can couple to a THz field.

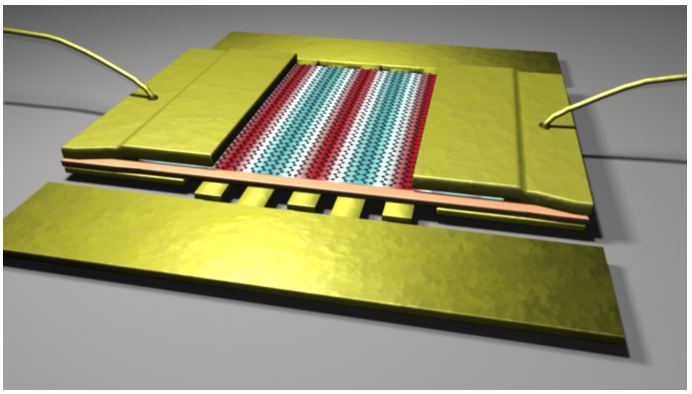

FIGURE 7.1: Artist view of a plasma resonance transistor with an array of local interdigitated bottom gates for THz detection.

Appendix A

Fabrication processes

step	*description*	*tool(s)*	*notes*
1	substrate preparation	acetone & IPA & ultrasounds	10 min
1b	substrate preparation	*Harrick* plasma oven	5 min O_2 plasma, 200 W, P $\lesssim$ 20 μbar
2	tungsten deposition	sputtering (at INSP)	20 nm
3	substrate preparation	acetone & IPA & ultrasounds	10 min
3b	substrate preparation	*Harrick* plasma oven	5 min O_2 plasma, 200 W, P $\lesssim$ 20 μbar
4	spin coating	spin coater & PMMA	30 s, 4000 rpm, 4000 rpm/s, PMMA *AZ6* (diluted) $\rightarrow$ 50 nm
5	baking	heater plate	6 min, 165 ° C
6	e-beam lithography **fine structure**	*Raith e-Line*	7.5 μm aperture, 20 kV, 900 μC/cm^2, 2 nm step
7	developing	MIBK & IPA	30 s MIBK/30 s IPA
8	etching tungsten	RIE	SF_6 (6 mT - 10 W - 75 s) / O_2 100 mT-30 W-20 s

9	spin coating	spin coater & PMMA	30 s, 4000 rpm, 4000 rpm/s, PMMA $AZ6$ (diluted) $\rightarrow 50\,nm$
10	baking	heater plate	6 min, 165 ° C
11	e-beam lithography **large structures**	*Raith e-Line*	7.5 μm aperture, 20 kV, 240 μC/cm^2, 10 nm step
12	developing	MIBK & IPA	30 s MIBK/30 s IPA
13	etching tungsten	RIE	SF_6 6 mT-10 W-75 s/ O_2 100 mT-30 W-20 s
14	spin coating	spin coater & PMMA	30 s, 4000 rpm, 4000 rpm/s, PMMA $AZ6$ $\rightarrow\sim 500\,nm$
15	baking	heater plate	12 min, 165 ° C
16	e-beam lithography (CPW)	*Raith e-Line*	120 μm aperture, 20 kV, 320 μC/cm^2, 100 nm step
17	developing	MIBK & IPA	90 s MIBK/30 s IPA
17	evaporation	home made Joule evaporator	Cr 2 nm/Au 200 nm 0.1 nm/s 10^{-5} $mbar$
18	lift-off	acetone & IPA	acetone 20min 50°C / IPA 30s
19	**hBN deposition**	dry transfer technique	
20	annealing	home made furnace	Ar 800 $sccm$/H_2 100 $sccm$ 300°C 2 $hours$
21	**graphene deposition**	dry transfer technique or CVD transfer technique	
22	spin coating	spin coater & PMMA	30 s, 4000 rpm, 4000 rpm/s, PMMA $AZ6$ $\rightarrow\sim 150\,nm$
23	baking	heater plate	10 min, 165 ° C
24	e-beam lithography - **graphene etching**	*Raith e-Line*	7.5 μm aperture, 20 kV, 300 μC/cm^2, 10 nm step
25	developing	MIBK & IPA	75 s MIBK/30 s IPA

26	etching graphene	RIE	O_2 50 mT-60 W-10 s
27	lift-off	acetone & IPA	acetone 2 h RT / IPA 30 s
28	annealing	home made furnace	Ar 800 $sccm/H_2$ 100 $sccm$ 300°C 2 $hours$
29	spin coating	spin coater & PMMA	30 s, 4000 rpm, 4000 rpm/s, PMMA $AZ6$ $\rightarrow\sim$ 150 nm
30	baking	heater plate	10 min, 165 ° C
31	e-beam lithography - **graphene contact**	*Raith e-Line*	7.5 μm aperture, 20 kV, 200 μC/cm^2, 10 nm step
32	developing	MIBK & IPA	90 s MIBK/30 s IPA
33	evaporation	e-gun evaporator Plassys MEB 550S	Pd 50 nm 0.2 nm/s $\cdot 10^{-7}$ $mbar$ (better if vacuum over night)
34	lift-off	acetone & IPA	acetone 4 h RT / IPA 30 s
35	annealing	Janis probe station	$10^{-5} mbar$ 130°C 2 $hours$

Table A.2: Complete GoBN process.

Appendix B

Sample GoBN1

B.1 Device presentation

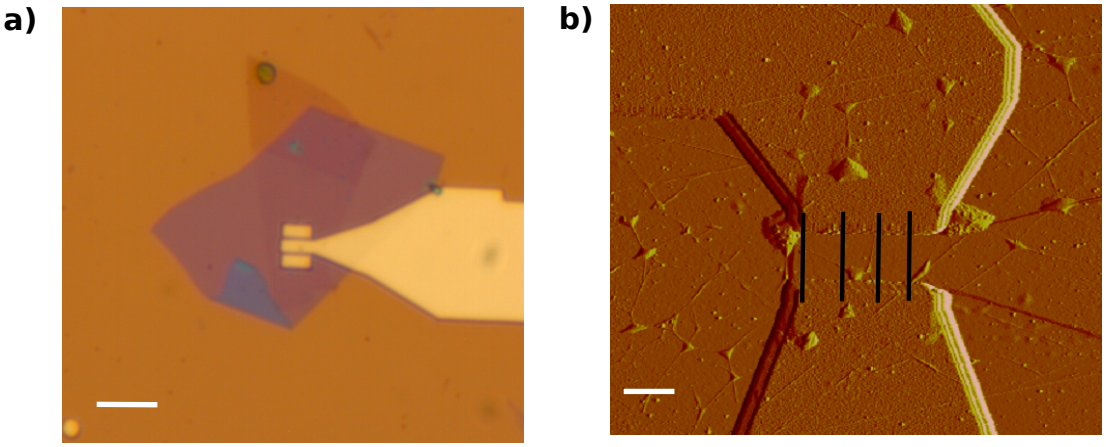

FIGURE B.1: (a) Optical image before the contact deposition and channel etching. The white scale bar is $5\,\mu m$. (b) AFM scan of the contacted device. The black lines indicate the position of the channels etching. The white scale bar is $1\,\mu m$.

The sample GoBN1 is the prototype of the GoBN technology. It consists of a single tungsten gate on a SiO_2/Si substrate, over which a $7\,nm$ thick hBN flake and a monolayer graphene flake have been successively deposited with a dry transfer technique. An annealing step in a furnace at $300°C$ in H_2 and Ar atmosphere for 2 hours is performed after each transfer. The graphene flake is etched in two rectangular channels to avoid a wrinkle at the center of the flake (see Fig. B.1). The overall dimensions are $W = 1.6\,\mu m$ and $L = 1.4\,\mu m$. It is contacted by Pd electrodes.

B.2 DC measurement

Figure B.2 shows the transfer characteristic of the device at ambient conditions. The very sharp resistance peak is the sign of a large mobility device. The asymmetric resistance is due to contact doping by the Pd metal. A lower resistance on the p side (negative gate voltage) indicates a p doping by the Pd contact. We attribute the large offset resistance (750 Ω) to an additional contact resistance in series (R_{mg} in chapter 4).

Therefore we can use the model of chapter 4 to fit the data. We assume ballistic junctions at the contact with a fixed doping n_{cont} induced by the Pd metal. The channel is assumed to be diffusive: $R_{ch} = \frac{L}{Wn_1e\mu}$. The fitting parameters are the channel mobility, the Pd induced doping n_{cont} and the contact junction length d. We obtain $\mu = 12000\,cm^2V^{-1}s^{-1}$, $n_{cont} = 3.10^{12}cm^{-2}$ and $d = 70\,nm$. In addition we account for a broadening due to the residual carrier density of $n_0 = 3.10^{11}cm^{-2}$.

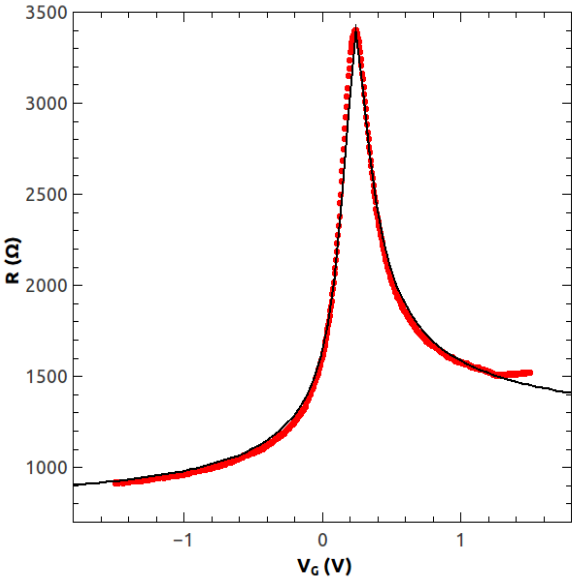

FIGURE B.2: Transfer characteristic of GoBN1 (red dots) fitted by the contact junction model (black line). A mobility of $\mu = 12000\,cm^2V^{-1}s^{-1}$ is extracted.

The good device mobility shows the potential of the GoBN technology for Dirac fermion optics experiments.

Appendix C

Samples characteristics

Samples	*graphene / transfer*	*substrate/transfer*	*size* L×W (μm^2)	*dielectric* (nm)	*RT mobility* ($cm^2V^{-1}s^{-1}$)
GoBN1	exfoliated / dry	hBN / dry	1.4×1.6	7	12000
GoBN2	exfoliated / dry	hBN / dry	0.2×1.1	15	6000
GoBN3 4×1	CVD Bouchiat	hBN / pick-up	0.5×1.5	15	3500
GoBN3 4×2	CVD Bouchiat	hBN / pick-up	0.5×1.5	15	3500
GoBN3 1×2	CVD Bouchiat	hBN / pick-up	0.5×1.5	12	1200
GoAl	CVD commercial	Al_2O_3 ALD	0.5×1.5	12	2000

TABLE C.1: Fabrication techniques, dimensions and mobility of devices discussed in this thesis. All devices have tungsten bottom gates. GoBN1 is the prototype of the GoBN technology and has a single gate. GoBN2 and GoBN3 have contact and channel gates. GoAl have split gates as well but the contact position is shifted.

Appendix D

List of acronyms

AFM:	Atomic fore microscope
ALD:	atomic layer deposition
CAB:	cellulose acetate butyrate
CNP:	Charge neutrality point
CPW:	Coplanar waveguide
CVD:	Chemical vapor deposition
DC:	direct current
ENS:	Ecole Normale Supérieure
FET:	Field effect transistor
hBN:	Hexagonal boron nitride
GoBN:	Graphene on boron nitride
GoAl:	Graphene on aluminium oxide
HEMT:	High electron mobility transistor
KTT:	Klein tuneling transistor
LPA:	Laboratoire Pierre Aigrain
MOSFET:	Metal-oxide-semiconductor field effect transistor
PMMA:	Poly methyl methacrylate
RF:	Radio frequency
RIE:	Reactive ion etching
SPP:	surface polar phonon
VNA:	Vector network analyser

Appendix E

Publication list

Graphene

1. **Q. Wilmart**, S. Berrada, D. Torrin, V. Hung Nguyen, G. Feve, J.-M. Berroir, P. Dollfus and B. Placais, "A Klein-tunneling transistor with ballistic graphene", *2D Materials* **1**, 1, 011006 (April 2014).

2. **Q. Wilmart**, A. Inhofer, M. Boukhicha, W. Yang, M. Rosticher, P. Morfin, N. Garroum, G. Feve, J.-M. Berroir, and B. Placais, "Gated-contact graphene transistor at gigahertz frequencies", *under referring.*

3. **Q. Wilmart**, A. Inhofer, M. Boukhicha, W. Yang, M. Rosticher, P. Morfin, V. Bouchiat, G. Feve, J.-M. Berroir, and B. Placais (preliminary author list). "Velocity saturation in graphene by Dirac pinch-off", *in preparation.*

4. E. Pallecchi, **Q. Wilmart**, a. C. Betz, S.-H. Jhang, G. Feve, J.-M. Berroir, S. Lepillet, G. Dambrine, H. Happy and B. Placais, "Graphene nanotransistors for RF charge detection", *Journal of Physics D: Applied Physics* **47**, 9, 094004 (2014).

5. D. Brunel, S. Berthou, R. Parret, F. Vialla, P. Morfin, **Q. Wilmart**, G. Feve, J-M. Berroir, P. Roussignol, C. Voisin and B. Placais, "Onset of optical-phonon cooling in multilayer graphene revealed by RF noise and black-body radiation thermometries", *J. Phys.: Condens. Matter* **27**, 164208 (2015).

In collaboration

6. A. Hemamouche, A. Morin, E. Bourhis, B. Toury, E. Tarnaud, J. Mathe, P. Guegan, A. Madouri, X. Lafosse, C. Ulysse, S. Guilet, G. Patriarche, L. Auvray, F.

Montel, **Q. Wilmart**, B. Placais, J. Yates and J. Gierak, "FIB patterning of dielectric, metallized and graphene membranes: A comparative study", *Microelectronic Engineering* **121**, 8791 (June 2014).

7. A. C. Betz, S. Barraud, **Q. Wilmart**, B. Placais, X. Jehl, M. Sanquer and M.F.G. Zalba, "Thermionic charge transport in CMOS nano-transistors", *Applied Physics Letter* **104**, 4, 043106 (2014).

Internship at NTT Atsugi, Japan (2010)

8. I. Mahboob, **Q. Wilmart**, K. Nishiguchi, A. Fujiwara, and H. Yamaguchi, "Wideband idler generation in a GaAs electromechanical resonator" *Physical Review B* **84**, 11 (2011).

9. I. Mahboob, **Q. Wilmart**, K. Nishiguchi, A. Fujiwara, and H. Yamaguchi, "Tuneable electromechanical comb generation" *Applied Physics Letters* **100**, 11 (2012).

Bibliography

[1] A. A. F. K.S. Novoselov, A. K. Geim, S. V. Morozov, D. Jiang, Y. Zhang, S. V. Dubonos, I. V. Grigorieva, "Electric Field Effect in Atomically Thin Carbon Films", *Science* **306**, nº 5696, 666–669 (October 2004), ISSN 0036-8075.

[2] K. S. Novoselov, A. K. Geim, S. V. Morozov, D. Jiang, M. I. Katsnelson, I. V. Grigorieva, S. V. Dubonos and A. A. Firsov, "Two-dimensional gas of massless Dirac fermions in graphene", *Nature* **438**, nº 7065, 197–200 (November 2005), ISSN 0028-0836.

[3] K. S. Novoselov, D. Jiang, F. Schedin, T. J. Booth, V. V. Khotkevich, S. V. Morozov and A. K. Geim, "Two-dimensional atomic crystals", *Proceedings of the National Academy of Sciences* **102**, nº 30, 10451–10453 (July 2005), ISSN 0027-8424.

[4] X. Du, I. Skachko, A. Barker and E. Y. Andrei, "Approaching ballistic transport in suspended graphene", *Nature Nanotechnology* **3**, nº 8, 491–495 (August 2008), ISSN 1748-3387.

[5] K. I. Bolotin, K. J. Sikes, J. Hone, H. L. Stormer and P. Kim, "Temperature-Dependent Transport in Suspended Graphene", *Physical Review Letters* **101**, nº 9, 096802 (August 2008), ISSN 0031-9007.

[6] C. R. Dean, a. F. Young, I. Meric, C. Lee, L. Wang, S. Sorgenfrei, K. Watanabe, T. Taniguchi, P. Kim, K. L. Shepard and J. Hone, "Boron nitride substrates for high-quality graphene electronics.", *Nature nanotechnology* **5**, nº 10, 722–6 (October 2010), ISSN 1748-3395.

[7] A. S. Mayorov, R. V. Gorbachev, S. V. Morozov, L. Britnell, R. Jalil, L. a. Ponomarenko, P. Blake, K. S. Novoselov, K. Watanabe, T. Taniguchi and a. K. Geim, "Micrometer-scale ballistic transport in encapsulated graphene at room temperature.", *Nano letters* **11**, nº 6, 2396–9 (June 2011), ISSN 1530-6992.

[8] L. Wang, I. Meric, P. Y. Huang, Q. Gao, Y. Gao, H. Tran, T. Taniguchi, K. Watanabe, L. M. Campos, D. A. Muller, J. Guo, P. Kim, J. Hone, K. L. Shepard and C. R. Dean, "One-Dimensional Electrical Contact to a Two-Dimensional Material", *Science* **342**, nº 6158, 614–617 (November 2013), ISSN 0036-8075.

[9] Q. Yu, J. Lian, S. Siriponglert, H. Li, Y. P. Chen and S.-S. Pei, "Graphene segregated on Ni surfaces and transferred to insulators", *Applied Physics Letters* **93**, nº 11, 113103 (2008), ISSN 00036951.

[10] Z. Han, A. Kimouche, D. Kalita, A. Allain, H. Arjmandi-Tash, A. Reserbat-Plantey, L. Marty, S. Pairis, V. Reita, N. Bendiab, J. Coraux and V. Bouchiat, "Homogeneous Optical and Electronic Properties of Graphene Due to the Suppression of Multilayer Patches During CVD on Copper Foils", *Advanced Functional Materials* **24**, nº 7, 964–970 (February 2014), ISSN 1616301X.

[11] L. Banszerus, M. Schmitz, S. Engels, J. Dauber, M. Oellers, F. Haupt, K. Watanabe, T. Taniguchi, B. Beschoten and C. Stampfer, "Ultrahigh-mobility graphene devices from chemical vapor deposition on reusable copper", *Science Advances* **1**, nº 6, e1500222–e1500222 (July 2015), ISSN 2375-2548.

[12] Y.-M. Lin, C. Dimitrakopoulos, K. A. Jenkins, D. B. Farmer, H.-Y. Chiu, A. Grill and P. Avouris, "100-GHz Transistors from Wafer-Scale Epitaxial Graphene", *Science* **327**, nº 5966, 662–662 (February 2010), ISSN 0036-8075.

[13] Y. Wu, K. a. Jenkins, A. Valdes-Garcia, D. B. Farmer, Y. Zhu, A. a. Bol, C. Dimitrakopoulos, W. Zhu, F. Xia, P. Avouris and Y.-M. Lin, "State-of-the-art graphene high-frequency electronics.", *Nano letters* **12**, nº 6, 3062–7 (June 2012), ISSN 1530-6992.

[14] I. Meric, C. R. Dean, N. Petrone, L. Wang, J. Hone, P. Kim and K. L. Shepard, "Graphene Field-Effect Transistors Based on BoronNitride Dielectrics", *Proceedings of the IEEE* **101**, nº 7, 1609–1619 (July 2013), ISSN 0018-9219.

[15] Z. Guo, R. Dong, P. S. Chakraborty, N. Lourenco, J. Palmer, Y. Hu, M. Ruan, J. Hankinson, J. Kunc, J. D. Cressler, C. Berger and W. a. de Heer, "Record maximum oscillation frequency in C-face epitaxial graphene transistors.", *Nano letters* **13**, nº 3, 942–7 (March 2013), ISSN 1530-6992.

[16] Z. Feng, C. Yu, J. Li, Q. Liu, Z. He, X. Song, J. Wang and S. Cai, "An ultra clean self-aligned process for high maximum oscillation frequency graphene transistors", *Carbon* **75**, 249–254 (August 2014), ISSN 00086223.

[17] A. K. Geim and K. S. Novoselov, "The rise of graphene.", *Nature materials* **6**, nº 3, 183–191 (2007).

[18] A. H. Castro Neto, N. M. R. Peres, K. S. Novoselov and A. K. Geim, "The electronic properties of graphene", (2009).

[19] P. E. Allain and J. N. Fuchs, "Klein tunneling in graphene: optics with massless electrons", *The European Physical Journal B* **83**, nº 3, 301–317 (October 2011), ISSN 1434-6028.

[20] D. R. Cooper, B. DAnjou, N. Ghattamaneni, B. Harack, M. Hilke, A. Horth, N. Majlis, M. Massicotte, L. Vandsburger, E. Whiteway and V. Yu, "Experimental Review of Graphene", *ISRN Condensed Matter Physics* **2012**, 1–56 (2012), ISSN 2090-7400.

[21] J. Tworzydo, B. Trauzettel, M. Titov, A. Rycerz and C. W. J. Beenakker, "Sub-Poissonian Shot Noise in Graphene", *Physical Review Letters* **96**, nº 24, 246802 (June 2006), ISSN 0031-9007.

[22] R. Danneau, F. Wu, M. F. Craciun, S. Russo, M. Y. Tomi, J. Salmilehto, A. F. Morpurgo and P. J. Hakonen, "Evanescent Wave Transport and Shot Noise in Graphene: Ballistic Regime and Effect of Disorder", *Journal of Low Temperature Physics* **153**, nº 5-6, 374–392 (December 2008), ISSN 0022-2291.

[23] Y. Wu, V. Perebeinos, Y.-m. Lin, T. Low, F. Xia and P. Avouris, "Quantum Behavior of Graphene Transistors near the Scaling Limit", *Nano Letters* **12**, nº 3, 1417–1423 (March 2012), ISSN 1530-6984.

[24] L. Wang, I. Meric, P. Y. Huang, Q. Gao, Y. Gao, H. Tran, T. Taniguchi, K. Watanabe, L. M. Campos, D. a. Muller, J. Guo, P. Kim, J. Hone, K. L. Shepard and C. R. Dean, "One-dimensional electrical contact to a two-dimensional material.", *Science (New York, N.Y.)* **342**, nº 6158, 614–7 (November 2013), ISSN 1095-9203.

[25] E. J. H. Lee, K. Balasubramanian, R. T. Weitz, M. Burghard and K. Kern, "Contact and edge effects in graphene devices", *Nature Nanotechnology* **3**, nº 8, 486–490 (August 2008), ISSN 1748-3387.

[26] J. Xia, F. Chen, J. Li and N. Tao, "Measurement of the quantum capacitance of graphene", *Nature Nanotechnology* **4**, nº 8, 505–509 (August 2009), ISSN 1748-3387.

[27] F. Schedin, a. K. Geim, S. V. Morozov, E. W. Hill, P. Blake, M. I. Katsnelson and K. S. Novoselov, "Detection of individual gas molecules adsorbed on graphene", *Nature Materials* **6**, n° 9, 652–655 (September 2007), ISSN 1476-1122.

[28] A. Hemamouche, A. Morin, E. Bourhis, B. Toury, E. Tarnaud, J. Mathé, P. Guégan, A. Madouri, X. Lafosse, C. Ulysse, S. Guilet, G. Patriarche, L. Auvray, F. Montel, Q. Wilmart, B. Plaçais, J. Yates and J. Gierak, "FIB patterning of dielectric, metallized and graphene membranes: A comparative study", *Microelectronic Engineering* **121**, 87–91 (June 2014), ISSN 01679317.

[29] M. Ananth, L. Stern, D. Ferranti, C. Huynh, J. Notte, L. Scipioni, C. Sanford and B. Thompson, "Creating nanohole arrays with the helium ion microscope", (2011).

[30] C. R. Dean, a. F. Young, I. Meric, C. Lee, L. Wang, S. Sorgenfrei, K. Watanabe, T. Taniguchi, P. Kim, K. L. Shepard and J. Hone, "Boron nitride substrates for high-quality graphene electronics.", *Nature nanotechnology* **5**, n° 10, 722–6 (October 2010), ISSN 1748-3395.

[31] L. A. Ponomarenko, A. K. Geim, A. A. Zhukov, R. Jalil, S. V. Morozov, K. S. Novoselov, I. V. Grigorieva, E. H. Hill, V. V. Cheianov, V. I. Falko, K. Watanabe, T. Taniguchi and R. V. Gorbachev, "Tunable metalinsulator transition in double-layer graphene heterostructures", *Nature Physics* **7**, n° 12, 958–961 (October 2011), ISSN 1745-2473.

[32] a. K. Geim and I. V. Grigorieva, "Van der Waals heterostructures", *Nature* **499**, n° 7459, 419–425 (July 2013), ISSN 0028-0836.

[33] A. Castellanos-Gomez, M. Buscema, R. Molenaar, V. Singh, L. Janssen, H. S. J. van der Zant and G. a. Steele, "Deterministic transfer of two-dimensional materials by all-dry viscoelastic stamping", *2D Materials* **1**, n° 1, 011002 (April 2014), ISSN 2053-1583.

[34] a. V. Kretinin, Y. Cao, J. S. Tu, G. L. Yu, R. Jalil, K. S. Novoselov, S. J. Haigh, a. Gholinia, a. Mishchenko, M. Lozada, T. Georgiou, C. R. Woods, F. Withers, P. Blake, G. Eda, a. Wirsig, C. Hucho, K. Watanabe, T. Taniguchi, a. K. Geim and R. V. Gorbachev, "Electronic Properties of Graphene Encapsulated with Different Two-Dimensional Atomic Crystals.", *Nano letters* (Mai 2014), ISSN 1530-6992.

[35] G. F. Schneider, V. E. Calado, H. Zandbergen, L. M. K. Vandersypen and C. Dekker, "Wedging Transfer of Nanostructures", *Nano Letters* **10**, n° 5, 1912–1916 (Mai 2010), ISSN 1530-6984.

[36] A. Betz, "Elastic and inelastic scattering in graphene studied by microwave transport and noise", (2012).

[37] P. J. Zomer, S. P. Dash, N. Tombros and B. J. van Wees, "A transfer technique for high mobility graphene devices on commercially available hexagonal boron nitride", *Applied Physics Letters* **99**, n° 23, 232104 (2011), ISSN 00036951.

[38] J. Spector, H. L. Stormer, K. W. Baldwin, L. N. Pfeiffer and K. W. West, "Electron focusing in two-dimensional systems by means of an electrostatic lens", *Applied Physics Letters* **56**, n° 13, 1290 (1990), ISSN 00036951.

[39] H. van Houten, C. W. J. Beenakker, J. G. Williamson, M. E. I. Broekaart, P. H. M. van Loosdrecht, B. J. van Wees, J. E. Mooij, C. T. Foxon and J. J. Harris, "Coherent electron focusing with quantum point contacts in a two-dimensional electron gas", *Physical Review B* **39**, n° 12, 8556–8575 (April 1989), ISSN 0163-1829.

[40] E. Bocquillon, V. Freulon, F. D. Parmentier, J. M. Berroir, B. Plaçais, C. Wahl, J. Rech, T. Jonckheere, T. Martin, C. Grenier, D. Ferraro, P. Degiovanni and G. Fève, "Electron quantum optics in ballistic chiral conductors", *Annalen der Physik* **526**, n° 1-2, 1–30 (January 2014), ISSN 00033804.

[41] M. I. Katsnelson, K. S. Novoselov and a. K. Geim, "Chiral tunnelling and the Klein paradox ingraphene", *Nature Physics* **2**, n° 9, 620–625 (August 2006), ISSN 1745-2473.

[42] V. Cheianov and V. Falko, "Selective transmission of Dirac electrons and ballistic magnetoresistance of n-p junctions in graphene", *Physical Review B* **74**, n° 4, 041403 (July 2006), ISSN 1098-0121.

[43] Q. Wilmart, S. Berrada, D. Torrin, V. Hung Nguyen, G. Fève, J.-M. Berroir, P. Dollfus and B. Plaçais, "A Klein-tunneling transistor with ballistic graphene", *2D Materials* **1**, n° 1, 011006 (April 2014), ISSN 2053-1583.

[44] I. van der Pauw, *A method of measuring specific resistivity and Hall effect of discs of arbritary shape.*, vol. 13 (1958).

[45] V. V. Cheianov, V. Fal'ko and B. L. Altshuler, "The focusing of electron flow and a Veselago lens in graphene p-n junctions.", *Science (New York, N.Y.)* **315**, n° 5816, 1252–5 (March 2007), ISSN 1095-9203.

[46] C. Pan and A. Naeemi, "Device- and system-level performance modeling for graphene P-N junction logic", in "Thirteenth International Symposium on Quality Electronic Design (ISQED)", pages 262–269, IEEE (March 2012), ISBN 978-1-4673-1036-9.

[47] R. N. Sajjad and A. W. Ghosh, "Manipulating Chiral Transmission by Gate Geometry: Switching in Graphene with Transmission Gaps", *ACS Nano* **7**, nº 11, 9808–9813 (November 2013), ISSN 1936-0851.

[48] R. V. Gorbachev, A. S. Mayorov, A. K. Savchenko, D. W. Horsell and F. Guinea, "Conductance of p-n-p graphene structures with "air-bridge" top gates.", *Nano letters* **8**, nº 7, 1995–9 (July 2008), ISSN 1530-6984.

[49] N. Stander, B. Huard and D. Goldhaber-Gordon, "Evidence for Klein Tunneling in Graphene p-n Junctions", *Physical Review Letters* **102**, nº 2, 026807 (January 2009), ISSN 0031-9007.

[50] A. F. Young and P. Kim, "Quantum interference and Klein tunnelling in graphene heterojunctions", *Nature Physics* **5**, nº 3, 222–226 (February 2009), ISSN 1745-2473.

[51] P. Rickhaus, R. Maurand, M.-h. Liu, M. Weiss, K. Richter and C. Sch, "Ballistic interferences in suspended graphene", pages 1–15 (2013).

[52] M. Oksanen, A. Uppstu, A. Laitinen, D. J. Cox, M. Craciun, S. Russo, A. Harju and P. Hakonen, "Single- and multi-mode Fabry-P erot interference in suspended graphene", pages 1–6 (2013).

[53] A. Shytov, M. Rudner and L. Levitov, "Klein Backscattering and Fabry-Pérot Interference in Graphene Heterojunctions", *Physical Review Letters* **101**, nº 15, 156804 (October 2008), ISSN 0031-9007.

[54] D. Torrin, *Nanotransistor de graphene*, master thesis, Ecole Normale Suprieure, Laboratoire Pierre Aigrain (2010).

[55] R. N. Sajjad and A. W. Ghosh, "High efficiency switching using graphene based electron optics", *Applied Physics Letters* **99**, nº 12, 123101 (2011), ISSN 00036951.

[56] R. N. Sajjad, S. Sutar, J. U. Lee and A. W. Ghosh, "Manifestation of chiral tunneling at a tilted graphene pn junction", pages 1–5 (2012).

[57] S. Sutar, E. S. Comfort, J. Liu, T. Taniguchi, K. Watanabe and J. U. Lee, "Angle-dependent carrier transmission in graphene p-n junctions.", *Nano letters* **12**, nº 9, 4460–4 (September 2012), ISSN 1530-6992.

[58] A. Rahman, J. W. Guikema, N. M. Hassan and N. Marković, "Angle-dependent transmission in graphene heterojunctions", *Applied Physics Letters* **106**, n° 1, 013112 (January 2015), ISSN 0003-6951.

[59] J. R. Williams, T. Low, M. S. Lundstrom and C. M. Marcus, "Gate-controlled guiding of electrons in graphene", *Nat Nano* **6**, 222225.

[60] G.-H. Lee, G.-h. Park and H.-j. Lee, "Observation of negative refraction of Dirac fermions in graphene", *Nature Physics* (September 2015), ISSN 1745-2473.

[61] S. Tanachutiwat and J. U. Lee, "Reconfigurable Multi-Function Logic Based on Graphene P-N Junctions", *Design Automation Conference (DAC), 2010 47th ACM/IEEE* pages 883–888 (2010).

[62] T. Sohier and B. Yu, "Ultralow-voltage design of graphene PN junction quantum reflective switch transistor", *Applied Physics Letters* **98**, n° 21, 213104 (2011), ISSN 00036951.

[63] M. S. Jang, H. Kim, Y.-W. Son, H. A. Atwater and W. A. Goddard, "Graphene field effect transistor without an energy gap", *Proceedings of the National Academy of Sciences* **110**, n° 22, 8786–8789 (Mai 2013), ISSN 0027-8424.

[64] S. Miryala, M. Montazeri, A. Calimera, E. Macii, M. Poncino, P. Torino and A. G. Junction, "A Verilog-A Model for Reconfigurable Logic Gates Based on Graphene pn-Junctions", *Proceedings of the Conference on Design, Automation and Test in Europe* **2**, n° 1, 2–5 (2013).

[65] V. Tenace, A. Calimera, E. Macii, M. Poncino, P. Torino and A. G. P.-n. Junction, "Pass-XNOR Logic : A new Logic Style for P-N Junction based Graphene Circuits", .

[66] J. Cayssol, B. Huard and D. Goldhaber-Gordon, "Contact resistance and shot noise in graphene transistors", *Physical Review B* **79**, n° 7, 075428 (February 2009), ISSN 1098-0121.

[67] E. Sonin, "Effect of Klein tunneling on conductance and shot noise in ballistic graphene", *Physical Review B* **79**, n° 19, 195438 (Mai 2009), ISSN 1098-0121.

[68] S. Berrada, "Etude Théorique de Nouveaux Concepts de Nano-Transistors en Graphène", (2014).

[69] A. Alarcon, V.-h. Nguyen, S. Berrada, D. Querlioz, J. Saint-Martin, A. Bournel and P. Dollfus, "Pseudosaturation and Negative Differential Conductance in Graphene Field-Effect Transistors", *IEEE Transactions on Electron Devices* **60**, n° 3, 985–991 (March 2013), ISSN 0018-9383.

[70] Y. Wu, V. Perebeinos, Y.-m. Lin, T. Low, F. Xia and P. Avouris, "Quantum behavior of graphene transistors near the scaling limit.", *Nano letters* **12**, n° 3, 1417–23 (March 2012), ISSN 1530-6992.

[71] S. Sze and N. Kwok, "Physics of Semiconductors Devices", (2007).

[72] B. Huard, N. Stander, J. Sulpizio and D. Goldhaber-Gordon, "Evidence of the role of contacts on the observed electron-hole asymmetry in graphene", *Physical Review B* **78**, n° 12, 121402 (September 2008), ISSN 1098-0121.

[73] K. Nagashio and A. Toriumi, "Density-of-States Limited Contact Resistance in Graphene Field-Effect Transistors", *Japanese Journal of Applied Physics* **50**, n° 7, 070108 (July 2011), ISSN 0021-4922.

[74] K. Nagashio, T. Nishimura, K. Kita and a. Toriumi, "Contact resistivity and current flow path at metal/graphene contact", *Applied Physics Letters* **97**, n° 14, 143514 (2010), ISSN 00036951.

[75] Y.-j. Yu, Y. Zhao, S. Ryu, L. E. Brus, K. S. Kim and P. Kim, "Tuning the Graphene Work Function by Electric Field Effect", *Nano Letters* **9**, n° 10, 3430–3434 (October 2009), ISSN 1530-6984.

[76] F. Xia, T. Mueller, R. Golizadeh-Mojarad, M. Freitag, Y.-m. Lin, J. Tsang, V. Perebeinos and P. Avouris, "Photocurrent Imaging and Efficient Photon Detection in a Graphene Transistor", *Nano Letters* **9**, n° 3, 1039–1044 (March 2009), ISSN 1530-6984.

[77] A. D. Franklin, S.-j. Han, A. A. Bol and V. Perebeinos, "Double Contacts for Improved Performance of Graphene Transistors", *IEEE Electron Device Letters* **33**, n° 1, 17–19 (January 2012), ISSN 0741-3106.

[78] F. Xia, V. Perebeinos, Y.-m. Lin, Y. Wu and P. Avouris, "The origins and limits of metalgraphene junction resistance", *Nature Nanotechnology* **6**, n° 3, 179–184 (March 2011), ISSN 1748-3387.

[79] F. Xia, V. Perebeinos, Y.-m. Lin, Y. Wu and P. Avouris, "The origins and limits of metal-graphene junction resistance.", *Nature nanotechnology* **6**, n° 3, 179–84 (March 2011), ISSN 1748-3395.

[80] H. Zhong, Z. Zhang, B. Chen, H. Xu, D. Yu, L. Huang and L. Peng, "Realization of low contact resistance close to theoretical limit in graphene transistors", *Nano Research* **8**, n° 5, 1669–1679 (Mai 2015), ISSN 1998-0124.

[81] S. Droscher, P. Roulleau, F. Molitor, P. Studerus, C. Stampfer, K. Ensslin and T. Ihn, "Quantum capacitance and density of states of graphene", *Applied Physics Letters* **96**, n° 15, 152104 (2010), ISSN 00036951.

[82] E. Pallecchi, C. Benz, a. C. Betz, H. V. Lohneysen, B. Placais and R. Danneau, "Graphene microwave transistors on sapphire substrates", *Applied Physics Letters* **99**, n° 11, 113502 (2011), ISSN 00036951.

[83] G. Giovannetti, P. Khomyakov, G. Brocks, V. Karpan, J. van den Brink and P. Kelly, "Doping Graphene with Metal Contacts", *Physical Review Letters* **101**, n° 2, 026803 (July 2008), ISSN 0031-9007.

[84] P. A. Khomyakov, G. Giovannetti, P. C. Rusu, G. Brocks, J. van den Brink and P. J. Kelly, "First-principles study of the interaction and charge transfer between graphene and metals", *Physical Review B* **79**, n° 19, 195425 (Mai 2009), ISSN 1098-0121.

[85] J. Knoch, Z. Chen and J. Appenzeller, "Properties of Metal–Graphene Contacts", *IEEE Transactions on Nanotechnology* **11**, n° 3, 513–519 (Mai 2012), ISSN 1536-125X.

[86] A. Laitinen, S. Paraoanu, M. Oksanen, F. Monica, S. Russo, E. Sonin and P. Hakonen, "Klein tunneling, contact doping, and pn -interfaces in gated suspended graphene", pages 1–9 (2015).

[87] I. Meric, C. R. Dean, K. a. Jenkins, J. Hone and K. L. Shepard, "High-frequency performance of graphene field effect transistors with saturating IV-characteristics", *2011 International Electron Devices Meeting* pages 2.1.1–2.1.4 (December 2011).

[88] Y. G. Lee, C. G. Kang, U. J. Jung, J. J. Kim, H. J. Hwang, H.-J. Chung, S. Seo, R. Choi and B. H. Lee, "Fast transient charging at the graphene/SiO[sub 2] interface causing hysteretic device characteristics", *Applied Physics Letters* **98**, n° 18, 183508 (2011), ISSN 00036951.

[89] E. a. Carrion, A. Y. Serov, S. Islam, A. Behnam, A. Malik, Feng Xiong, M. Bianchi, R. Sordan and E. Pop, "Hysteresis-Free Nanosecond Pulsed Electrical Characterization of Top-Gated Graphene Transistors", *IEEE Transactions on Electron Devices* **61**, n° 5, 1583–1589 (Mai 2014), ISSN 0018-9383.

[90] D. Schall, D. Neumaier, M. Mohsin, B. Chmielak, J. Bolten, C. Porschatis, A. Prinzen, C. Matheisen, W. Kuebart, B. Junginger, W. Templ, A. L. Giesecke and H. Kurz, "50 GBit/s Photodetectors Based on

Wafer-Scale Graphene for Integrated Silicon Photonic Communication Systems", *ACS Photonics* **1**, n° 9, 781–784 (September 2014), ISSN 2330-4022.

[91] I. Meric, M. Y. Han, A. F. Young, B. Ozyilmaz, P. Kim and K. L. Shepard, "Current saturation in zero-bandgap, top-gated graphene field-effect transistors", *Nature Nanotechnology* **3**, n° 11, 654–659 (November 2008), ISSN 1748-3387.

[92] M. Freitag, M. Steiner, Y. Martin, V. Perebeinos, Z. Chen, J. C. Tsang and P. Avouris, "Energy Dissipation in Graphene Field-Effect Transistors", *Nano Letters* **9**, n° 5, 1883–1888 (Mai 2009), ISSN 1530-6984.

[93] A. Barreiro, M. Lazzeri, J. Moser, F. Mauri and A. Bachtold, "Transport Properties of Graphene in the High-Current Limit", *Physical Review Letters* **103**, n° 7, 076601 (August 2009), ISSN 0031-9007.

[94] V. E. Dorgan, M.-H. Bae and E. Pop, "Mobility and saturation velocity in graphene on SiO[sub 2]", *Applied Physics Letters* **97**, n° 8, 082112 (2010), ISSN 00036951.

[95] V. Perebeinos and P. Avouris, "Inelastic scattering and current saturation in graphene", *Physical Review B* **81**, n° 19, 195442 (Mai 2010), ISSN 1098-0121.

[96] A. Laitinen, M. Kumar, M. Oksanen, B. Plaçais, P. Virtanen and P. Hakonen, "Coupling between electrons and optical phonons in suspended bilayer graphene", *Physical Review B* **91**, n° 12, 121414 (March 2015), ISSN 1098-0121.

[97] M. Lazzeri, C. Attaccalite, L. Wirtz and F. Mauri, "Impact of the electron-electron correlation on phonon dispersion: Failure of LDA and GGA DFT functionals in graphene and graphite", *Physical Review B* **78**, n° 8, 081406 (August 2008), ISSN 1098-0121.

[98] Z. Yao, C. L. Kane and C. Dekker, "High-Field Electrical Transport in Single-Wall Carbon Nanotubes", *Physical Review Letters* **84**, n° 13, 2941–2944 (March 2000), ISSN 0031-9007.

[99] N. Mounet and N. Marzari, "First-principles determination of the structural, vibrational and thermodynamic properties of diamond, graphite, and derivatives", *Physical Review B* **71**, n° 20, 205214 (Mai 2005), ISSN 1098-0121.

[100] I. D. Barcelos, A. R. Cadore, L. C. Campos, A. Malachias, K. Watanabe, T. Taniguchi, F. C. B. Maia, R. Freitas and C. Deneke, "Graphene/h-BN plasmonphonon coupling and plasmon delocalization observed by infrared nano-spectroscopy", *Nanoscale* **7**, n° 27, 11620–11625 (2015), ISSN 2040-3364.

[101] T. Low, V. Perebeinos, R. Kim, M. Freitag and P. Avouris, "Cooling of photoexcited carriers in graphene by internal and substrate phonons", *Physical Review B* **86**, n° 4, 045413 (July 2012), ISSN 1098-0121.

[102] J.-H. Chen, C. Jang, S. Xiao, M. Ishigami and M. S. Fuhrer, "Intrinsic and extrinsic performance limits of graphene devices on SiO2", *Nature Nanotechnology* **3**, n° 4, 206–209 (April 2008), ISSN 1748-3387.

[103] a. C. Betz, F. Vialla, D. Brunel, C. Voisin, M. Picher, a. Cavanna, a. Madouri, G. Fève, J.-M. Berroir, B. Plaçais and E. Pallecchi, "Hot Electron Cooling by Acoustic Phonons in Graphene", *Physical Review Letters* **109**, n° 5, 056805 (August 2012), ISSN 0031-9007.

[104] A. C. Betz, S. H. Jhang, E. Pallecchi, R. Ferreira, G. Fève, J.-M. Berroir and B. Plaçais, "Supercollision cooling in undoped graphene", *Nature Physics* **9**, n° 2, 109–112 (December 2012), ISSN 1745-2473.

[105] D. Brunel, S. Berthou, R. Parret, F. Vialla, P. Morfin, Q. Wilmart, G. Fève, J.-M. Berroir, P. Roussignol, C. Voisin and B. Plaçais, "Onset of optical-phonon cooling in multilayer graphene revealed by RF noise and blackbody radiation thermometries", *Journal of Physics: Condensed Matter* **27**, n° 16, 164208 (April 2015), ISSN 0953-8984.

[106] S. Q. W. Mahan and G. D., "Electron Scattering from Surface Excitations", *Physical Review B* **6**, n° 12 (1972).

[107] M. V. Fischetti, D. A. Neumayer and E. A. Cartier, "Effective electron mobility in Si inversion layers in metaloxidesemiconductor systems with a high-κ insulator: The role of remote phonon scattering", *Journal of Applied Physics* **90**, n° 9, 4587 (2001), ISSN 00218979.

[108] S. Fratini and F. Guinea, "Substrate-limited electron dynamics in graphene", *Physical Review B* **77**, n° 19, 195415 (Mai 2008), ISSN 1098-0121.

[109] I. Meric, C. Dean, A. Young, J. Hone, P. Kim and K. L. Shepard, "Graphene field-effect transistors based on boron nitride gate dielectrics graphene b) c) AuPd BN 2 u m 1 u m m graphene", pages 556–559 (2010).

[110] A. Konar, T. Fang and D. Jena, "Effect of high-k gate dielectrics on charge transport in graphene-based field effect transistors", *Physical Review B* **82**, n° 11, 115452 (September 2010), ISSN 1098-0121.

[111] S. C. Lee, S. S. Ng, H. A. Hassan, Z. Hassan and T. Dumelow, "Surface phonon polariton responses of hexagonal sapphire crystals with non-polar and

semi-polar crystallographic planes", *Optics Letters* **39**, nº 18, 5467 (September 2014), ISSN 0146-9592.

[112] Y. Wu, Y.-m. Lin, A. a. Bol, K. a. Jenkins, F. Xia, D. B. Farmer, Y. Zhu and P. Avouris, "High-frequency, scaled graphene transistors on diamond-like carbon", *Nature* **472**, nº 7341, 74–78 (April 2011), ISSN 0028-0836.

[113] T. Fang, A. Konar, H. Xing and D. Jena, "High-field transport in two-dimensional graphene", *Physical Review B* **84**, nº 12, 125450 (September 2011), ISSN 1098-0121.

[114] S. Datta, *Electronic Transport in Mesoscopic Systems*, Cambridge Univ. Press (1998).

[115] S.-J. Han, A. V. Garcia, S. Oida, K. a. Jenkins and W. Haensch, "Graphene radio frequency receiver integrated circuit.", *Nature communications* **5**, 3086 (January 2014), ISSN 2041-1723.

[116] J. K. Viljas and T. T. Heikkilä, "Electron-phonon heat transfer in monolayer and bilayer graphene", *Physical Review B* **81**, nº 24, 245404 (June 2010), ISSN 1098-0121.

[117] T. Low and P. Avouris, "Graphene Plasmonics for Terahertz to Mid-Infrared Applications", (2014).

[118] Y.-m. Lin, K. A. Jenkins, A. Valdes-Garcia, J. P. Small, D. B. Farmer and P. Avouris, "Operation of Graphene Transistors at Gigahertz Frequencies", *Nano Letters* **9**, nº 1, 422–426 (January 2009), ISSN 1530-6984.

[119] C. Benz, M. Thurmer, F. Wu, Z. Ben Aziza, J. Mohrmann, H. V. Lohneysen, K. Watanabe, T. Taniguchi and R. Danneau, "Graphene on boron nitride microwave transistors driven by graphene nanoribbon back-gates", *Applied Physics Letters* **102**, nº 3, 033505 (2013), ISSN 00036951.

[120] F. Schwierz, "Graphene transistors.", *Nature nanotechnology* **5**, nº 7, 487–96 (July 2010), ISSN 1748-3395.

[121] E. Pallecchi, Q. Wilmart, a. C. Betz, S.-H. Jhang, G. Fève, J.-M. Berroir, S. Lepillet, G. Dambrine, H. Happy and B. Plaçais, "Graphene nanotransistors for RF charge detection", *Journal of Physics D: Applied Physics* **47**, nº 9, 094004 (2014), ISSN 0022-3727.

[122] F. Schwierz, H. Wong and J. Liou, *Nanometer CMOS*, Pan Stanford Publishing (2010).

[123] H. Wang, A. Hsu, D. S. Lee, K. K. Kim, J. Kong and T. Palacios, "Delay Analysis of Graphene Field-Effect Transistors", pages 1–3 (2011).